A THEORETICAL STUDY OF REACTION AND DIFFUSION IN MICROSTRUCTURED MATERIALS

Thesis by

Michael Loewenberg

In Partial Fulfillment of the Requirements

for the Degree of

Doctor of Philosophy

California Institute of Technology

Pasadena, California

1988

(Submitted May 19, 1988)

ACKNOWLEDGEMENTS

I'd like to thank some of the people who have helped me to reach this goal. First of all my advisor, George Gavalas: I have learned (am learning) a lot from you. Although its not always obvious, I have share your view that simplicity is elegant but not at the cost of clarity. I appreciate/respect your approach to research; you've been a good mentor. I would also like to thank Gary Leal and John Brady for expressing an interest in me and advising me with career plans.

I've enjoyed my friendships with fellow graduate students and have learned a lot from many conversations with several of them including: Ed Ascoli and Ardith El-Kareh (the best mathematicians I've known – thanks for your help), Chris Guske and Robin Horrell (my previous officemates and good friends who were frequently subjected to discussions on my research and contributed many thoughtful ideas), Suk-Woo Nam (my most recent officemate with whom I had several useful collaborations including the thermodynamic implications of tedious work. Michael Prairie (whose inadvertent accomplishment seems to have been a proof by example that good science doesn't imply compulsiveness–you're also a good friend and a kcufhctib), Joe Vallino (who exemplified brilliance through eccentricity), Herman Yee, Steve Strand and Jim Killory (the smartest guys I know — clear evidence of bugs in the system), Ken Reardon (my friend who helped me persevere by demonstrating that hard work brings success and the best of bakeries), Yiannis Levendis (who has taught me much about the other side of life: experiments; I hope we continue to interact and enjoy further Pyrrhic victories), Brent Shanks and Scott Northrop (friends with whom I've had many enjoyable/useful discussions), and many others... Before arriving at Caltech, I'd never have thought it possible to concentrate so many smart and interesting people in one place. The most amazing

thing about the experience: after a lot of hard work, learning is more enjoyable now than ever. I appreciate the students and faculty who have made this experience a good one.

I would like to thank Lark (and Nicci-nose) for taking the time to know me and for valuing this accomplishment. Thanks also for tolerating me during the trying time which accompanied my finishing. I look forward to our future together.

I'd like to thank my parents; without them, I wouldn't be here for a few reasons... I hope this compensates for dropping out of high school to become a cook at Sambo's. I'd like to thank Deb and Rich, my sister and brother who always accepted and supported me. Youngest, but not least, I want to acknowledge Sarah, the smartest person I know, for being an excellent niece and making me look forward to being a father very much.

I am grateful for the support provided by fellowships from the National Science Foundation and LINK Foundation.

to my family

ABSTRACT

A fundamental study of heterogeneous reaction and diffusion in random, microstructured materials has been conducted. A detailed, ensemble averaging approach has been developed for the analysis of diffusion-controlled reactions. The method was used to determine the reactant flux into a bounded or semi-infinite medium containing a dilute suspension of reactive, spherical particles under steady-state or transient conditions. The influence of the boundary was given explicit, detailed consideration and the results were compared with a mean-field treatment. Physical motivation is provided by the process of ash vaporization during pulverized coal combustion. The analysis was subsequently extended to study the decay of an initially uniform distribution of reactant which allows comparison with other theoretical approaches. The result suggests that the present method reproduces the solution to this well-known problem by a seemingly simpler, more physical approach. The configurational averaging technique was employed in a study of heterogeneous reaction in a porous material under diffusion-controlled conditions. The porous solid is assumed to have a bimodal pore structure with a random, isotropic distribution of cylindrical macropores. The results are relevant to the pulverized combustion of char from softening coals. In the diffusion-controlled limit, the results coincide with a simpler, single pore model.

A simplified model of char combustion has been developed which treats pore diffusion and growth coupled to gas-phase heat and mass transport. An efficient model-based algorithm was developed for the determination of oxidation rates from combustion data. These models were applied in two studies involving well-defined laboratory combustion experiments.

TABLE OF CONTENTS

LIST OF TABLES

LIST OF FIGURES

CHAPTER 1

Introduction

Introduction

1 Problem Statement

Relating the macroscopic properties of a material to its microstructure is a problem pervading much of modern engineering science. In most situations, the microstructure refers to the molecular scale, however, under some circumstances, there exists an intermediate scale, much smaller than the system dimension, yet sufficiently large to allow application of the continuum hypothesis on the molecular scale. Under these circumstances, the microstructure refers to the structure of this intermediate scale. Traditionally, the continuum hypothesis has been applied to the intermediate scale as well. This approach ignores the effect of the detailed microstructure which, in some problems, is small thereby permitting such an approach. In some problems, however, the detailed microstructure has a significant, macroscopically observable, manifestation thus rendering a continuum treatment useless. Frequently, such problems arise in the field of heterogeneous reaction and diffusion but only recently have serious attempts been made to gain a fundamental understanding through the proper analysis.

This thesis constitutes a theoretical investigation of heterogeneous reaction and diffusion in microstructured materials. The physical processes of char combustion and ash vaporization were used as vehicles for the study. These processes provide excellent examples of the interaction between microstructure and macroscopic processes. The relevant microstructure in the problem of char combustion is the pore structure of the char while the distribution of mineral matter defines the microstructure for the ash vaporization problem. In both cases, the microstructure is disordered and, to some extent, random. Under some conditions, the microstructure of

each problem can be effectively treated as a continuum whereas in some, practically important, situations, the detailed structure can have a significant, macroscopic impact.

The primary contribution of this work is the development of a configurational averaging approach which allows explicit consideration of the detailed microstructure. Three problems are studied: (1) the flux of reactant into a bounded medium containing reactive centers, (2) reaction and diffusion in a random, porous material, and (3) the decay of an initially uniform distribution of reactant in an unbounded medium. The first two problems, relevant to ash vaporization and char combustion, have heretofore been analyzed primarily through application of the continuum hypothesis to the microstructure of the material. Comparison with previous results permits an assessment of the significance of the detailed microstructure. Previous theoretical results which address the detailed microstructure relevant to the third problem are available which allow a useful comparison.

Secondary contributions of the work contained in this thesis include computer simulations of char oxidation under conditions which allow a continuum description of the char matrix. A simplified model of char oxidation was developed which addresses the issues of pore diffusion and growth coupled to gas-phase heat and mass transport and an efficient, model-based algorithm was constructed for the prediction of kinetic parameters from particle combustion data. These models were subsequently applied to studies involving well-defined laboratory combustion experiments.

2 Physical Background

Although, the majority of the work presented in this thesis is theoretical in nature and somewhat independent of specific physical phenomena, the following general discussion of the particular problems which motivated this work is useful and adds concreteness. The aforementioned processes of char combustion and ash vaporization are relevant to the industrially important problem of pulverized coal combustion. Pulverized coal combustion has been a subject of numerous theoretical and experimental investigations because of its obvious importance in the operation of coal combustion systems. It has been well established that the burning of pulverized coal particles occurs in two stages: rapid pyrolysis and evolution of volatiles followed by the comparatively slow heterogeneous oxidation of the residue (char) (Mulcahy and Smith 1969, Timothy *et al.* 1982). The initial pyrolysis process has been given a comprehensive treatment by Gavalas (1982) while reviews on the field of char combustion are available from several authors including Smith (1982a). The initial thermal decomposition stage profoundly affects the structure and reactivity of the residual char which consists of a porous carbon structure and small quantities of hydrogen, oxygen, nitrogen, sulfur depending on the rank of the parent coal. Additionally, the char contains any (inert) mineral matter contained in its coal precursor.

The mineral content of coal can exhibit a variety of effects on the char combustion process. The coalescence of mineral matter during combustion can result in pore blockage thus hindering intraparticle mass transport. The accumulation of ash on the particle surface can inhibit external oxygen transport by occlusion of the particle surface (Senior 1984). Particularly significant, is the catalytic effect of various metals on the heterogeneous oxidation process which was reviewed by

Walker *et al.* (1968).

The fate of the mineral matter in coal has received much attention because of its detrimental contribution to the particulate pollutants produced during pulverized coal combustion. Studies have shown that the distribution of mineral matter resulting from combustion is bimodally distributed with respect to particle size. The smaller particles result largely from the vaporization and subsequent condensation of mineral matter initially contained within the coal. A review of work in this field was recently conducted by Flagan and Seinfeld (1988).

During char oxidation, the interior of the particle is subjected to a high-temperature, carbon monoxide environment. Under these conditions, micron size inclusions of refractory metal oxides (*e.g.*, SiO_2, MgO, CaO, etc.) undergo rapid reduction to a more volatile sub-oxide which diffuses through the char matrix and escapes into the oxidizing atmosphere which surrounds the particle (Quann and Sarofim 1982). In the oxidizing environment, the sub-oxide species is oxidized and subsequently condenses forming submicron size particles of the metal oxide. This chemically augmented vaporization process accounts for only a small fraction of the particulate matter produced during combustion but it is an important problem because the submicron particles produced are very difficult to capture by particulate control devices.

3 Theoretical Background

In this section, various theoretical approaches relevant to the analysis of the foregoing problems are reviewed. In the first subsection, the more traditional continuum hypothesis approach is discussed in the context of char combustion where it is often a viable technique. The second subsection contains an overview of theoretical work in

the area of diffusion-controlled reactions which is pertinent to the ash vaporization process. The final subsection is devoted to a review of averaging techniques which are useful for a variety of problems including char combustion and ash vaporization in situations where a continuum description of the material fails.

3.1 The Continuum Description

Modern char combustion modelling typically relies on a continuum description of the char involving differential equations to treat intraparticle transport (Sotirchos and Amundson 1984a, 1984b). Such equations require local values for transport coefficients and structure properties such as void volume and pore surface area. These quantities are often obtained through the use of a random pore model in conjunction with measured physical data (Bhatia and Perlmutter 1980, 1981; Gavalas 1980). This approach yields local transport and structure properties as functions of the local burnoff with proper account given to pore overlap. However, a tacit assumption in this approach is the disparity of the characteristic length scales of the particle pore structure and oxygen concentration gradients. Often the length scale of the pore structure is orders of magnitude less than that for changes in oxygen concentration thus justifying a continuum treatment of the char structure.

Cenospheres provide an important counter-example where a continuum description of the char is inappropriate. In practice, these hollow, spherical char particles are often produced during the combustion of softening coals or heavy fuel oils and have a bubbly pore structure which tends to exhibit a bimodal pore size distribution (Northrop 1988). Under the typical high-temperature conditions used in practice, the oxygen penetration length is often the same order of magnitude as the size of the large pores (Chapter 2). In this case, the detailed pore structure must be included in any rational analysis aimed at understanding the combustion behavior of these

particles.

3.2 Diffusion-Controlled Reactions

Diffusion-controlled reaction is a field with relevance to a variety of important engineering problems which typically reduce to the consideration of a diffusing chemical species in a medium with concentration sinks. Examples include spray evaporation or condensation, suspension polymerization, fluorescence quenching, and the production of metabolic products in immobilized cell systems. Smoluchowski (1916) did the pioneering work in this field by developing the mean-field approximation in the context of a study on the coagulation of colloidal sized particles. According to the mean-field approximation, a macroscopic equation describes the material as a continuum with a homogeneous reaction rate constant determined by considering an isolated sink in the ambient concentration field.

Recently, significant advances been made in this field by several workers whose general approach has been to determine a rate constant which characterizes the bulk properties of the material and accounts for the details of the microstructure. Felderhof and Deutch (1976) examined the effect of two sphere interactions and obtained results valid for a dilute volume fraction of sinks using a superposition approximation. Subsequently, Muthukumar and Cukier (1981) extended their results to an arbitrary volume fraction of monopole sinks. The volume fraction dependence of the diffusion coefficient was investigated by Muthukumar (1982) and, most recently, Mattern and Felderhof (1986, 1987) applied a cluster expansion approach to the problem and discussed the discrepancies among previous results.

The time-dependent problem has received comparatively less attention but the approach has been essentially the same, however, in this case, the desired rate constant is allowed to vary with time. Felderhof (1977) considered the effect of pair-wise

interactions under dilute conditions and non-local effects relevant to this problem were considered by Tokuyama and Cukier (1982). The techniques of multiple scattering were applied by Bixon and Zwanzig (1981) and later modified by Felderhof *et al.* (1982).

The ash vaporization problem is a diffusion controlled process in which the metal oxide inclusions behave as sinks of carbon monoxide. Thus, the foregoing results have pertinence to this problem. Quann and Sarofim (1982) have performed an experimental investigation of this problem and modelled their results using the mean-field theory of Smoluchowski.

3.3 Averaging Techniques

In the final category of the review of theoretical methods, several averaging techniques are discussed which address the detailed microstructure. These methods have been developed over the past few decades for use in various situations where the details of the relevant microstructure may be important. Equation averaging has proven to be a useful approach for a variety of problems in which detailed treatment of the microstructure is required.

3.3.1 Volume Averaging

In general, an ensemble average is the correct average for random, microstructured materials (Hashin 1964), however, in problems with statistical homogeneity (macroscopic quantities constant on a volume large enough to properly sample the microstructure), a volume average is equivalent to an ensemble average (Batchelor 1970). The application of volume averaging to random, microstructured materials is the basis of Darcy's law (1856) for the permeability of a material. A rigorous foun-

dation for this approach has been established through the work of Slattery (1967, 1970) in his investigations of viscoelastic and two-phase flows through porous media, and the independent work of Anderson and Jackson (1967) and Whitaker (1967). The essence of their work is the development of a spatial averaging theorem based on an appropriate volume average of the microstructure in the material. The recent work of Whitaker (1985) clarifies the earlier result.

Many problems exhibit the required statistical homogeneity and are amenable to a volume averaging analysis which addresses their detailed microstructure. Such problems include the determination of sedimentation velocity in a suspension of particles under gravity and the bulk stress in a suspension of force-free particles each of which was first considered in the dilute limit (no particle interactions) by Smoluchowski (1912) and Einstein (1906). Batchelor (1972a, 1972b) improved upon these early results by retaining the effects of pair-wise particle interactions in both problems through the development of a volume averaging technique which involved a renormalization procedure to eliminate divergences which commonly arise from this long-range interaction. This approach was borrowed by Jeffery (1973) to improve upon the dilute limit result obtained by Maxwell (1873) for the effective conductivity of a solid suspension of spherical particles.

3.3.2 Difficulties with Volume Averaging

However, the volume averaging approach cannot be applied to a few types of important problems. In certain problems, the particles which comprise the microstructure exhibit especially strong interactions (Batchelor 1974). A classical example is the problem is fluid flow through a (dilute) array of fixed particles which was first studied by Brinkman (1947). He suggested that the governing equations must be modified to include a volumetric force which results from the "screening" influence

of the fixed particles. His results were later supported by Childress (1972), Lundgren (1972) and Howells (1973) who retained the effect of pair-wise interactions in the solution to this problem. Screening is also an essential feature of problems involving diffusion-controlled reactions. The screening interaction results in a much stronger influence of the microstructure than in the sedimentation and effective viscosity/conductivity problems.

A second important situation in which a volume average is inappropriate is in the vicinity of a macroscopic boundary. In this case, statistical homogeneity is destroyed and thus the equivalence of ensemble and volumetric averages. This situation is relevant to problems including steady heat conduction in a bounded, microstructured material and ash vaporization during pulverized coal combustion. In the former problem, the boundary induces local, microscale order which is manifest as a macroscopic temperature offset far from the boundary when a bulk gradient is applied to the material (Chang and Acrivos 1987). In the latter problem, the mass flux of metal oxide on the particle surface is sought which depends on the details of the local concentration field in the neighborhood of the boundary. However, detailed treatment of macroscopic boundaries seems to have escaped attention in the context of diffusion-controlled reactions. A tacit assumption seems to have been that boundaries, when present, would be accommodated through application of the customary boundary conditions to the averaged equations which were obtained in the absence of macroscopic boundaries.

3.3.3 Configurational Averaging

According to a configurational averaging approach, the governing equations of a problem are averaged over all allowable realizations of the microstructure. Bulk equations are thus produced which contain a term in which the averaging is per-

formed with one particle fixed. This term is obtained from the solution to a conditionally averaged equation which is obtained by averaging the original equations over all configurations in which the specified particle is fixed. However, the resulting equation relates to a doubly conditional averaged equation which is similarly obtained. According to this approach, an infinite hierarchy of coupled, configurationally averaged equations are produced with an additional particle fixed at each higher level. The hierarchy is truncated under the condition that the microstructure is dilute or sparse. Using this approach, Hinch was able to reproduce, and therefore support, Batchelor's results for sedimentation and bulk viscosity which were obtained by volume averaging (Hinch 1977). Furthermore, he demonstrated that this approach could be successfully applied to determine the permeability of a fixed array of particles, a problem intractable by volume averaging.

3.3.4 Concentrated Systems

A rather severe restriction to the results obtained by either of the foregoing averaging procedures is the restriction to dilute volume fractions. Many problems of practical interest arise in concentrated systems where alternate methods are required. Recently developed approaches include computer simulations (*e.g.*, Durlofsky, Brady and Bossis 1987), the development tight, rigorous upper and lower bounds (*e.g.*, Torquato 1985) and the effective continuum approach developed by Acrivos and Chang (1986). The topic of microstructures in concentrated systems is reviewed further in the context of future research.

4 Outline of Thesis

In this thesis, a theoretical investigation of heterogeneous reaction and diffusion in microstructured materials is presented with emphasis on the proper treatment of the microstructure. Motivation for the study is provided by the physical processes of char oxidation and ash vaporization, under conditions relevant to pulverized coal combustion. The primary contribution of this work is contained in the second portion of the thesis which consists of Chapters 5-8 which contain the derivation and implementation of a configurational averaging approach which properly treats the detailed microstructure pertinent to the diffusion-controlled reaction problems considered therein. The first portion of the thesis, consisting of Chapters 2-4, is more specifically focused on the problem of char oxidation but serves, in part, to motivate the work contained in the latter portion.

4.1 Char Combustion

In Chapter 2, cenosphere structure and combustion behavior is studied. Particles were collected and their structure characterized. Their combustion behavior was modelled omitting pore diffusion but retaining the effects of pore growth and gas-phase heat and mass transport. The film transport equations were reduced by quadrature to a set of nonlinear algebraic equations by an approach similar to that of Libby and Blake (1979). The numerical results indicate that oxygen penetration is on the same order of magnitude as the size of the largest voids. A continuum description of the char is inappropriate.

In Chapter 3, a continuum-based treatment of the intraparticle transport for a spherical particle is coupled to the gas-phase treatment developed in Chapter 2. A highly simplified intraparticle transport model valid for high Thiele modulus as well

as a traditional model which involved a tessellation of the particle were examined. Numerical solutions are presented under a variety of practical conditions in which both gas-phase and intraparticle resistances were significant.

In Chapter 4, an efficient algorithm is developed for the estimation of kinetic parameters from combustion experiments and is applied to data gathered from several well-characterized chars (Levendis and Flagan). This procedure was used in conjunction with the computer simulation developed in Chapters 2 and 3 to model the combustion behavior of these chars. The results were compared with experiment (Levendis *et al.*). Appendix 1 describes an investigation of the catalytic effects of calcium during the char oxidation process. Three procedures are described for inducing calcium content in synthetic char particles and combustion experiments with the calcium-enriched particles were performed. The catalytic effects of this mineral were subsequently quantified by application of the algorithm for estimating kinetic parameters.

4.2 Configurational Averaging Approach

In Chapter 5, the configurational averaging approach is developed. The technique is applied to the problem of determining the steady-state reactant flux on the boundary of a finite or semi-infinite material containing a dilute suspension of reactive particles. The governing equations are explicitly averaged producing an infinite set of coupled equations which is subsequently truncated using the physical considerations of diluteness and screening. The macroscopic boundary is given detailed consideration. The interaction between reactive centers and the boundary is treated and shown to significantly affect the macroscopic flux and dominate pair-wise interactions which are complicated by the presence of the boundary and excluded from the analysis. Numerical solutions are presented for the flux into spherical and

semi-infinite domains. The problem has direct application to the ash vaporization process and the results are compared with the previous theoretical study of Quann and Sarofim (1982). The result of the comparison demonstrates the significance of sphere-boundary interactions in this problem.

In Chapter 6, the foregoing averaging approach developed in a steady-state context is extended to consider the transient problem. The time-dependent reactant flux into a bounded or semi-infinite domain is determined and numerical results presented for spherical and semi-infinite domains. The results are compared with those of a mean-field analysis The decay of an initially uniform distribution of reactant in an infinite medium of spherical sinks is studied in Chapter 7. In this, statistically homogeneous situation, two-sphere interactions are included in the analysis. Following the approach of previous workers, a time-dependent rate coefficient is determined which is compared with the theoretical results of Smoluchowski (1916), Felderhof (1977), and Bixon and Zwanzig (1981). It is demonstrated that such an approach cannot be applied unless the domain is unbounded; the presence of macroscopic boundaries affects the bulk equations. Numerical results are presented which demonstrate the impact of detailed interactions upon the time-dependent, bulk concentration.

In Chapter 8, a configurational averaging approach, similar to that presented Chapter 5, is developed for the study of heterogeneous reaction and diffusion in a porous material. The pore structure was assumed to consist of a bimodal pore size distribution with a random, isotropic distribution of cylindrical macropores. The hierarchy of coupled equations was truncated under the assumption that the void volume attributable to the macropores was low. The resulting set of differential equations were analytically solved to determine the overall reaction rate for a variety of geometries and the solution contrasted with the results of a continuum approach.

The conditions of interest correspond to the regime of diffusion control in which the details of the macropore network become important. The analysis is shown to be valid in this regime and thus compliments the continuum treatment. The differential equation governing the bulk concentration field has a modified form relative to the local reaction-diffusion equation, thus a bulk rate coefficent cannot be defined. The approach may have important implication to the analysis of cenosphere combustion (Chapter 2) where a continuum treatment fails.

5 References

1. Anderson, T.B. and Jackson, R. (1967) A fluid mechanical description of fluidized beds. *Ind. Eng. Chem. Fundam.* **6** (4) 527-539.

2. Batchelor, G.K. (1970) The stress system in a suspension of force-free particles. *J. Fluid Mech.* **41**, 545.

3. Batchelor, G.K. (1972a) Sedimentation in a dilute suspension of spheres. *J. Fluid Mech.* **52**, 245.

4. Batchelor, G.K. and Green, J.T. (1972b) The determination of the bulk stress in a suspension of spherical particles to order c^2. *J. Fluid Mech.* **56**, 401.

5. Batchelor, G.K. (1974) Transport properties of two-phase materials with random structure. *Ann. Rev. Fluid Mech.* 227.

6. Bhatia, S.K., and Perlmutter, D.D. (1980). A random pore model for fluid solid reactions: I. Isothermal, kinetic control. *A.I.Ch.E.Jl.***26**, 379.

7. Bhatia, S.K., and Perlmutter, D.D. (1981). A random pore model for fluid solid reactions: II. Diffusion and transport effects. *A.I.Ch.E.Jl.***27**, 247.

8. Bixon, M. and Zwanzig, R. (1981) Diffusion in a medium with static traps. *J. Chem. Phys.* **75** (5), 2354.

9. Brinkman, H. C. (1947) A calculation of the viscous force exerted by a flowing fluid on a dense swarm of particles. *Appl. Sci. Res. A* **1**, 27.

10. Chang, E.Y., Yendler, B.S. and Acrivos, A. (1986) A model for estimating the effective thermal conductivity of a random suspension of spheres. *Proceedings of the SIAM Workshop on Multiphase Flow.*

11. Chang, E.Y. and Acrivos, A. (1987) The conduction of heat from a planar wall with uniform surface temperature to a monodisperse suspension of spheres. *J. Appl. Phys.* **62**, (3), 771-776.

12. Childress, S. (1972) Viscous flow past a random array of spheres. *J. Chem. Phys.* **56** (6), 2527-2539.

13. Darcy, H. (1856) Les Fontaines Publiques de la Ville de Dijon. Paris: Victor Dalmont.

14. Durlofsky, L., Brady, J.F. and Bossis, G. (1987) Dynamic simulation of hydrodynamically interacting particles. *J. Fluid Mech.* **180**, 21.

15. Einstein, A. (1906) Eine neue Bestimmung der Moleküldimension. *Annln. Phys.* **19**, 289 (and **34**, 591).

16. Felderhof, B.U. and Deutch, J.M. (1976) Concentration dependence of the rate of diffusion-controlled reactions. *J. Chem. Phys.* **64**, (11), 4551-4558.

17. Felderhof, B.U. (1977) Frequency-dependent rate coefficient in diffusion-controlled reactions. *J. Chem. Phys.* **66** (10), 4385.

18. Felderhof, B.U., Deutch, J.M. and Titulaer, U.M. (1982) Diffusion and absorption in a medium with spherical sinks. *J. Chem. Phys.* **76** (8), 4178.

19. Flagan, R.C. and Seinfeld, J.H. (1988) *Fundamentals of Air Pollution Engineering.* Inglewood Cliffs: Prentice Hall. p.362.

20. Gavalas, G.R. (1980) A random capillary model with application to char gasification at chemically controlled rates. *A.I.Ch.E.Jl.***26**, 577.

21. Gavalas, G.R. (1981) Analysis of char combustion including the effect of pore enlargement. *Comb. Sci. Tech.*, **24**,197.

22. Gavalas, G.R. (1982) *Coal Pyrolysis.* New York: Elsevier Scientific Co.

23. Hashin, Z. and Shtrikman, S. (1962) A variational approach to the theory of the effective magnetic permeability of multiphase materials. *J. Appl. Phys.* **33**, 10, 3125.

24. Hashin, Z. (1964) Theory of mechanical behavior of heterogeneous media. *Appl. Mech. Rev.* **17**, 1.

25. Hinch, E.J. (1977) An averaged-equation approach to particle interactions in a fluid suspension. *J. Fluid Mech.***83**, 695-720.

26. Howes, F.A. and Whitaker, S. (1985) The spatial averaging theorem revisited. *Chem. Eng. Sci.* **40** (8), 1387-1391.

27. Howells, I.D. (1973) Drag due to the motion of a Newtonian fluid through a sparse array of small fixed rigid objects. *J. Fluid Mech.* **64**, 449-475.

28. Jeffrey, D. J. (1973) Conduction through a random suspension of spheres. *Proc. R. Lond. A* **335**, 355-367.

29. Libby, P.A., and Blake, T.R. (1979) Theoretical study of burning carbon particles. *Comb. Flame*,**36**,139.

30. Levendis, Y.A. and Flagan, R.C. Synthesis, formation and characterization of glassy spheres of variable properties. submitted to *Carbon.*

31. Levendis, Y.A., Flagan, R.C. and Gavalas, G.R. Oxidation kinetics of monodisperse spherical, carbonaceous particles of variable properties. *Comb. & Flame* In Press.

32. Lundgren, T.S. (1972) Slow flow through stationary random beds and suspensions of spheres. *J. Fluid Mech.* **51**, 273-299.

33. Mattern, K. and Felderhof, B.U. (1986) Rate of diffusion-controlled reactions in a random array of monopole sinks. *Physica* **135A**, 505-518.

34. Mattern, K. and Felderhof, B.U. (1987) Rate of diffusion-controlled reactions in a random array of spherical sinks. *Physica* **147A**, 1-20.

35. Maxwell, J.C. (1873) *Electricity and Magnetism* (1st ed.). Clarendon Press.

36. Mulcahy, M. F. R. and Smith I. W. (1969) Kinetics of combustion of pulverized fuel: A review of theory and experiment. *Reviews of Pure and Applied Chemistry* **19**, 81.

37. Muthukumar, M. and Cukier, R.I. (1981) Concentration dependence of diffusion-controlled processes among stationary reactive sinks. *J. Stat. Phys.* **26**, 453-469.

38. Muthukumar, M. (1982) Concentration dependence of diffusion-controlled processes among static traps. *J. Chem. Phys.* **76**, (5), 2667-2671.

39. Northrop, P.S. (1988) A fundamental study in char combustion: changes in particle morphology during combustion. Ph.d. thesis.

40. Quann, R.J. and Sarofim, F., 1982, Vaporization of refractory oxides during pulverized coal combustion. *19^{th} Symposium (International) on Combustion, The Combustion Institute*, 1429-1440.

41. Senior, C. L. (1984) Submicron aerosol formation during combustion of pulverized coal. Ph.D. Thesis.

42. Slattery, J.C. (1967) Flow of viscoelastic fluids through porous media. *A.I.Ch.E. Jl.* **13** (6), 1067-1071.

43. Slattery, J.C. (1970) Two-phase flow through porous media. *A.I.Ch.E. Jl.* **16** (3), 345-352.

44. Smith, I.W. (1982a) The combustion rates of coal chars: A review. *19th Symposium (international) on Combustion, The Combustion Institute*, 1045.

45. Smith, I.W. (1982b) The combustion rates of coal chars: a review. *Nineteenth Symposium (International) on Combustion*, The Combustion Institute, 1045.

46. Smoluchowski, M.V. (1912) On the practical applicability of Stokes' law. *Proc. 5th Intern. Cong. Math.* vol. 2, 192.

47. Smoluchowski, M.V. (1916) Drei Vortrage uber Diffusion Brownische Bewegung und Koagulation von Kolloidteilchen. *Phys. Z.* **17**, 557-585.

48. Sotirchos, S.V., and Amundson, N.R. (1984a). Dynamic behavior of a porous char particle burning in an oxygen-containing environment. 1. Constant radius particle. *A.I.Ch.E.Jl.***30**, 537.

49. Sotirchos, S.V., and Amundson, N.R. (1984b). Dynamic behavior of a porous char particle burning in an oxygen-containing environment. 2. Transient analysis of a shrinking particle. *A.I.Ch.E.Jl.***30**, 549.

50. Timothy, L. D., Sarofim, A. F. and Béer, J. M. (1982). Characteristics of Single Particle Coal Combustion. *Nineteenth Symposium (International) on Combustion*, The Combustion Institute, 1123.

51. Tokuyama, M. and Cukier, R.I. (1982) *J. Chem. Phys.* **76** (12), 6202.

52. Torquato, S. (1985) Effective electrical conductivity of two-phase disordered composite media. *J. Appl. Phys.* **58** (10), 3790.

53. Walker, P.L., Shelef, M. and Anderson, R.A. (1968). *Chemistry and physics of carbon* (edited by P.L. Walker), Vol. 4, p. 287. Edward Arnold, London.

54. Whitaker, S. (1967) Diffusion and dispersion in porous media. *A.I.Ch.E. J.* **13** (3), 420-427.

PART I.

CHAR COMBUSTION

CHAPTER 2

Structure and Combustion of Cenosphere Particles

Structure and Combustion of Cenosphere Particles

G.R. Gavalas* and M. Loewenberg*

J. Bellan** and R.M. Clayton**

* Department of Chemical Engineering 206-41

** Jet Propulsion Laboratory

California Institute of Technology

Pasadena, California 91125

Abstract

Carbonaceous cenosphere particles from an oil furnace are characterized by scanning electron microscopy, mercury intrusion and nitrogen porosimetry. The porosimetry data are used to construct a random pore model describing the evolution of surface area and pore volume distribution. The pore model is combined with gas-phase transport to formulate the equations for transient particle combustion and some numerical solutions are presented.

1 Introduction

The analysis of particle combustion is a subject of long standing largely in connection with the modelling of coal combustion. Earlier treatments of particle combustion assumed that the reaction is located on the external particle surface, and is coupled with the surrounding gas by suitable heat and mass transfer coefficients. Recently analyses have included a more accurate description of external transport (Caram and Amundson 1977, Mon and Amundson 1978, Libby and Blake 1979, Sundaresan and Amundson 1980, Sotirchos and Amundson 1984a, 1984b) and have taken into account the effects of pore diffusion and pore enlargement (Gavalas 1981, Sotirchos and Amundson 1984b). These and other recent analyses indicate that the effect of pore structure is significant except when the overall rate is determined solely by film transport.

The porous structure of carbonaceous particles is frequently established during devolatilization of the precursor fuel upon injection in the combustion furnace. The most common instance is the formation of coal char devolatilization of the parent coal. Most bituminous coals melt as they are heated above 350−400°C. With further increase of the temperature, bubbles of volatile material nucleate, grow, coalesce and escape leaving behind the solid char residue. In combustion of pulverized coal, the rate of heating exceeds 10^4°C/s, and devolatilization proceeds very rapidly resulting in highly spongy or bubbly char particles. Sometimes the particles contain a large bubble surrounded by a porous carbonaceous shell, whence the name "cenospheres." Cenosphere particles are also produced during the combustion of atomized heavy fuel oil with high asphaltene content. Because of the short residence time in the oil furnaces, cenosphere particles may not burn completely and thus end up in the exhaust gas.

The porous structure of cenospheres from high volatile coals or oil has a feature that sets it apart from other chars or cokes: the size of the largest voids is on the same order of magnitude as the thickness of the cenosphere shell, hence diffusion in the cenosphere cannot be described in terms of the customary effective diffusion coefficient. The description of pore diffusion and reaction in cenosphere combustion must take into account the peculiarities of cenosphere structure.

The purpose of this paper is to report some results on the characterization and modelling of cenosphere combustion. Characterization is illustrated by means of some experimental measurements obtained from oil-derived cenosphere particles. The modelling addresses the problem of film transport, and the problem of evolution of the pore structure under conditions of fast pore diffusion. The analysis of the more general case when pore diffusion is also a determinant of the rate is currently in progress.

2 Structure of Cenosphere Particles

2.1 Experimental

Cenosphere particles were provided by KVB Corporation. They had been collected from the exhaust of an oil-fired (#6 oil) utility boiler, hence, they were partially oxidized. Because of substantial impurities present in the samples, it was not possible to determine the degree of burnoff from elemental composition data. The particles were characterized by scanning electron microscopy (SEM), optical microscopy, mercury intrusion porosimetry, nitrogen adsorption porosimetry, and helium pycnometry. Figure 1a shows an SEM micrograph of a collection of cenosphere particles at 500X magnification. The particles show spongy structure with poremouths 1 to

8μm in size. The extent of burnout seems to vary from particle to particle. Figure 1b is a 2000X micrograph of a single particle showing pores 0.5 to 10μm in size. Poremouths of 0.5 to 3μm diameter punctuate the external surface as well as the the surface of the large voids. The spheroid shape of the voids reflects their generation from the nucleation, growth, coalescence, and bursting of bubbles during the period of fuel droplet devolatilization.

A few cenosphere particles were imbedded in resin and cured under vacuum. After hardening, the resin surface was ground and polished, exposing various particles cross sections. Photomicrographs of typical cenosphere cross sections are shown in Figures 1c,d at 1100X magnification. These and other photographs show that the cenospheres contain a large central bubble surrounded by a carbonaceous shell appearing as light-colored material. The shell itself contains bubbles of various sizes as observed in Figures 1a,b. Some of the bubbles are doublets generated by coalescence. Some bubbles have broken through the outside surface while others seem to be completely surrounded by the carbonaceous phase. The central bubble is often connected to the outside by openings known as "blowholes."

Mercury intrusion porosimetry measurements were conducted by Micromeritics, Inc. The results are displayed in Figure 2. The pressure range corresponds to pore diameters between 0.017 and 127μm based on the conventional assumption of cylindrical pores. In reality and given size refers to the diameter of the opening and not to the maximum diameter of the void, which can be considerably larger. Void openings above 11μm correspond largely to the space between particles and are irrelevant to the subsequent discussion. Void openings between 1 and 11μm correspond to the central bubbles and large bubbles in the shell. Openings below 1μm correspond to smaller bubbles in the shell. As shown in Figure 2, only a small fraction of the pore volume belongs to voids with openings below 1μm. However,

these voids possess the largest fraction of the surface area.

Nitrogen adsorption equilibria were also measured by Micromeritics, Inc. to determine total surface area by the BET equation and pore volume distribution in the range $15 - 300$Åby the Kelvin equation, assuming cylindrical voids. The pore volume distribution presented in Figure 3 is fairly even over the size range 15 to 300Å. Additional data include $\rho_{He} = 2.41\text{g/cm}^3$, $\rho_{Hg} = 0.232\text{g/cm}^3$, $S_{BET} = 16.8\text{m}^2/\text{g}$. The density ρ_{Hg} is the apparent density of the particles measured by displacement in mercury at 0.097 atm.

2.2 Geometric Modelling

Analysis of particle combustion requires a geometric model of the porous structure. In view of the lack of detailed knowledge about the geometry of the pores and in the interest of simplifying the description of the intraparticle diffusion and reaction, the pore structure will be represented by three groups of voids as defined below. As an illustration, we will define the three groups of voids based on the porosimetry data presented previously.

The first group of voids accessible through openings of diameter 1 to 11μm. The total volume, V_1, of these voids is obtained from mercury intrusion data (Figure 2). To estimate the surface area, we assume that the voids are spherical and that the opening diameter is 1/3 of the sphere diameter. On the basis of this assumption, we calculate the surface area, S_1. We represent these voids by uniform spheres of diameter, $D_1 = 6V_1/S_1$, preserving the volume to surface ratio.

The second group consists of voids accessible through openings of diameter 0.018 to 1μm and total volume V_2 determined from mercury intrusion data. Making the same geometrical assumptions as for the previous group, we can calculate the surface area, S_2, and the average diameter, $D_2 = 6V_2/S_2$.

The third group consists of voids with openings between 180Åand 15Å. These are not accessible to mercury at the highest pressure applied in the intrusion experiment but are accessible to nitrogen during the adsorption measurements (Figure 3). We could assume again that these voids are spheres with diameters three times the size of their opening. However, in preliminary low-temperature (450° – 500°) thermogravimetric oxidation runs, the reaction rate was found to decline monotonically with conversion. This behavior suggests that the smaller voids, which possess most of the surface area (as illustrated below), have lenticular rather than spherical shape. They can be represented as flat discs, in which the relevant dimension for Kelvin's equation is the disc thickness. The volume of these voids will be denoted by V_3. The surface area, S_3, of these voids is approximately given by, $S_3 = S_{BET} - S_1 - S_2$. An average void for this class can be defined as a disc with diameter, D_3', and thickness δ ($D_3' >> \delta$). To define D_3' and δ from V_3 and S_3, it is necessary to specify D_3'/δ. However, in the limit of large D_3'/δ, δ tends to V_3/S_3.

There is another volume, V_μ, not considered yet. This is the volume penetrated by helium but not by nitrogen during the adsorption isotherm measurement:

$$V_\mu = \left(\frac{1}{\rho_{Hg}} - V_{T,Hg}\right) - V_3 - \frac{1}{\rho_{He}} \qquad (1)$$

where $V_{T,Hg}$ is the volume penetrated by Hg at the highest pressure of intrusion, and ρ_{Hg} and ρ_{He} were defined previously. The quantity in the parentheses is the total volume of the cenosphere shell not accessible to mercury but accessible to nitrogen, and $1/\rho_{He}$ is the the volume of the dense carbonaceous phase, inaccessible to helium. The openings to these voids are probably smaller than 10Å, although the void size could be considerably larger. It will be seen below that for the material under consideration, $V_\mu >> V_3$, hence these voids could contribute substantially to the reaction rate once they became accessible during combustion.

It remains to be specify the overall size of the cenosphere. For this purpose it is assumed that the cenosphere consists of a central bubble of radius b surrounded by a shell of outer radius a. The radii a and b can be estimated from microscopic observations. Mercury intrusion data (Figure 2) provide directly the quantities: $V_0, V_i + V_1, V_2, \rho_{Hg}$ and $V_{T,Hg}$. Nitrogen adsorption provides V_3, while helium pycnometry provides ρ_{He}. The various volumes are related as follows:

$$V_0 + V_i + V_{SH} = \frac{1}{\rho_{Hg}} \tag{2}$$

$$V_{SH} = V_1 + V_2 + V_3 + V_\mu + V_c = \frac{1}{\rho_{Hg}} - V_{T,Hg} + V_1 + V_2 \tag{3}$$

$$\frac{V_i}{V_{SH} + V_i} = \left(\frac{b}{a}\right)^3 \tag{4}$$

Hence by specifying the ratio b/a on the basis of microscopic observations, we can determine the remaining quantities: V_i, V_1 and V_{SH}. As an example, the data reported in Figures 2 and 3 and Table 1 provide $V_0 = 1.98, V_1 + V_i = 1.48, V_2 = 1.50, V_{T,Hg} = 0.711$. Assuming b/a = 0.75, we obtain: $V_i = 0.987, V_1 = 0.492$, and $V_{SH} = 1.35$. We also have $V_3 = 0.016, V_\mu = 0.28$, and $V_c = \rho_{He}^{-1}$. All volumes are given in cm^3/g.

3 Combustion of Cenospheres

The first subsection treats the evolution of the porous structure using a random pore model. The second subsection presents an analysis of film heat and mass transfer and the third subsection formulates and solves the particle combustion equations for the special case of fast pore diffusion.

3.1 Random pore model for structure evolution

The description of the evolution of porous structure is an essential feature in the modelling of high temperature combustion (Gavalas 1980, 1981; Bhatia and Perlmutter 1980, 1981; Sotirchos and Amundson 1984b). It is also directly applicable to the interpretation of low temperature oxidation experiments designed to probe the role of the char's porous structure. The basic requirement is to describe the surface area and pore volume distribution as functions of conversion or burnoff.

Following the discussion of the previous section, we assume that the pore space of the cenosphere shell consists of three groups of voids, each group containing voids of identical shape and size. The first group consists of spheres of initial radius $a_{10} = D_1/2$ and number density λ_1 (sphere centers per unit volume). the second group consists of spheres of initial radius $a_{20} = D_2/2$ and number density λ_2. The third group consists of flat discs of initial diameter D_3', initial thickness δ_0 and number density λ_3. It is assumed that the voids are completely randomly located. This means that the centers of each group follow a three dimensional Poisson density with parameters λ_1, λ_2 and λ_3. Furthermore, the axis of each disc has random direction. Being randomly located, the voids partially overlap.

The assumption is usually made that every element of the pore surface remains parallel to itself while it receds during reaction. For a spatial region, exposed to uniform temperature and gas composition, we have:

$$a_i = a_{i0} + q(t) \tag{5}$$

$$\delta = \delta_0 + q(t) \tag{6}$$

The reaction length, $q(t)$, increases in proportion to the reaction rate:

$$\frac{dq}{dt} = \frac{1}{\rho_c} R_{in}(c, T) \tag{7}$$

where ρ_c is the density of the carbonaceous phase and R_{in} is the intrinsic rate.

A number of useful relationships can be derived for the pore volume distribution and surface area at any conversion. If v_i is the volume of a single void of type i and $\mathrm{W}_i = \lambda_i v_i$, then the volume fractions (volume per unit volume of cenosphere shell)

$$\epsilon_1 = 1 - \exp(-\mathrm{W}_1) \tag{8}$$

$$\epsilon_2 = \exp(-\mathrm{W}_1) - \exp(-\mathrm{W}_1 - \mathrm{W}_2) \tag{9}$$

$$\epsilon_3 = \exp(-\mathrm{W}_1 - \mathrm{W}_2) - \exp(-\mathrm{W}_1 - \mathrm{W}_2 - \mathrm{W}_3) \tag{10}$$

$$\epsilon = \epsilon_1 + \epsilon_2 + \epsilon_3 = 1 - \exp(-\mathrm{W}_1 - \mathrm{W}_2 - \mathrm{W}_3) \tag{11}$$

have the following interpretation: ϵ_1 is the volume fraction of voids 1, including their overlap with voids 2 and 3; ϵ_2 is the volume fraction of voids 2 excluding their overlap with 1 but including their overlap with voids 3; ϵ_3 is the volume fraction of voids 3 excluding their overlap with voids 1 and 2. Finally, ϵ is the total pore volume fraction. The conversion X and surface area S are given by:

$$X = \frac{\epsilon - \epsilon_0}{1 - \epsilon_0} \tag{12}$$

$$S = \frac{d\epsilon}{dq} = (1 - \epsilon)\left(\lambda_1 \frac{dv_1}{dq} + \lambda_2 \frac{dv_2}{dq} + \lambda_3 \frac{dv_3}{dq}\right) \tag{13}$$

The volumes v_i are functions of a_i, hence functions of q. Thus, ϵ_i, ϵ, S and X are functions of the initial parameters and q.

In the previous section, we discussed the specification of the size parameters a_{10}, a_{20}, D_{30} and h_0 from porosimetry data. The specification of the density parameters λ_i is made using the same data by setting

$$\epsilon_{i0} = \frac{\mathrm{V}_i}{\mathrm{V}_{SH}} \tag{14}$$

where ϵ_{i0} are given are given by Eqs. (7)-(10) and W_i are evaluated using the initial void sizes.

The above expressions developed for three groups of pores can be generalized in an obvious way to any number of pore groups. In the previous section, we identified a fourth group of pores inaccessible to nitrogen at $-195.8°C$ but accessible to helium at room temperatures. These pores, of volume V_μ, could contribute substantially to combustion either immediately or after an induction time required for the enlargement of their pore mouths. Measurement of the surface area and reaction rate at various extents of conversion during oxidation at temperatures below 500°C can be used to probe the contribution of this group of pores. For short induction times, the fourth group of pores can be treated as immediately accessible, and can be combined with group 3.

3.2 Analysis of Film Heat Transfer and Diffusion

The rate of particle combustion is generally controlled by reaction, pore diffusion and film heat transfer and diffusion. Reaction and pore diffusion are intimately coupled throughout the cenosphere shell, and their combined process in series with heat transfer and diffusion in the surrounding film. Depending on temperature and particle size, the overall rate may be controlled by reaction alone, reaction and pore diffusion and film transport, and at sufficiently high temperatures, film transport alone. This section we analyze the film transport equations in the framework of the overall dynamic equations describing particle combustion. This problem has been treated by Libby and Blake (1979) who assumed that heat capacities and certain transport parameters were independent of temperature to reduce the external pseudosteady-state boundary value problem to a transcendental equation. The solution of this equation could be inserted into the differential equation describing the evolution of particle temperature. Sotirchos and Amundson (1984a,b) made a general and thorough analysis of particle combustion including film transport as well as

intraparticle diffusion and reaction. The model equations were solved numerically. In this section, we follow the approach of Libby and Blake (1979) but remove the assumption of constant heat capacities and transport parameters.

The gas-phase surrounding the burning particle is composed of O_2, CO, and N_2 indicated as components 1, 2, and 3. Carbon dioxide and other minor constituents are combined with nitrogen. Combustion is represented by the reaction

$$C + \frac{1}{2}O_2 \rightleftharpoons CO \tag{15}$$

The reaction of carbon dioxide with carbon and the oxidation of CO in the gas-phase are neglected. Letting Y_i and F_i be the mass fraction and mass flux of the i^{th} component we can write the pseudosteady component balances as:

$$r^2 F_i = a_p^2 F_{ip} \tag{16}$$

The fluxes, F_i are related by the Stefan-Maxwell equations:

$$\nabla Y_i = \sum_j \frac{1}{\rho_g(T)\mathcal{D}_{ij}}(Y_i F_j - Y_j F_i) \tag{17}$$

where the contributions of pressure and temperature gradients have been neglected. Following the previous investigators, we assume: $\mathcal{D}_{12} = \mathcal{D}_{13} = \mathcal{D}_{23} = \mathcal{D}$ which allows (17) to be written in the simpler form:

$$F_i = -\rho_g(T)\mathcal{D}\frac{dY_i}{dr} + FY_i \tag{18}$$

where

$$F = \sum_i F_i$$

is the total mass flux satisfying:

$$r^2 F = a_p^2 F_p \tag{19}$$

The stoichiometry of reaction (15) provides the relationships:

$$F_{3p} = 0, \quad F_{1p} = -\frac{4}{3}F_p, \quad F_{2p} = \frac{7}{3}F_p \tag{20}$$

Introducing (19) and (20) into (18) we obtain by suitable linear combination

$$\rho \mathcal{D} r^2 \frac{dZ}{dr} = a_p^2 F_p Z \tag{21}$$

where

$$Z = \frac{Y_1}{4} + \frac{Y_2}{7} \tag{22}$$

Equation (18) for component 3 (N_2) reads:

$$\rho \mathcal{D} r^2 \frac{dY_3}{dr} = a_p^2 F_p Y_3 \tag{23}$$

Dividing (21) by (23) we obtain

$$\frac{dZ}{dY_3} = \frac{Z}{Y_3}$$

with the condition at the free stream

$$Y_3 = Y_{3b} : Z = Z_b = \frac{Y_{1b}}{4} + \frac{Y_{2b}}{7}$$

It follows that

$$Z = \frac{Y_1}{4} + \frac{Y_2}{7} = \frac{Z_b}{Y_{3b}} Y_3 \tag{24}$$

This equation is solved along with

$$Y_1 + Y_2 + Y_3 = 1 \tag{25}$$

to express Y_2 and Y_3 in terms of Y_1:

$$Y_2 = \frac{7A}{7A+1} - \frac{7(4A+1)}{4(7A+1)} Y_1 \tag{26}$$

$$Y_3 = \frac{1}{7A+1} + \frac{3}{4(7A+1)} Y_1 \tag{27}$$

where

$$A = \frac{1}{Y_{3b}} \left(\frac{Y_{1b}}{4} + \frac{Y_{2b}}{7} \right) \tag{28}$$

The pseudosteady energy equation for a gas that does not absorb or emit radiation can be written as

$$r^2 \left[-\lambda \frac{dT}{dr} + \sum_i F_i \bar{H}_i \right] = a_p^2 e_p \tag{29}$$

where

$$e_p = \left[-\lambda \frac{dT}{dr} + \sum_i F_i \bar{H}_i \right]_{r=a_p} \tag{30}$$

using Equations (16) and (20) we rewrite Eq. (29) as

$$r^2 \lambda(T) \frac{dT}{dr} = a_p^2 \left[h(T) F_p - e_p \right] \tag{31}$$

$$r = a_p \ : \ T = T_p; \ r \to \infty : T \to T_b$$

where

$$h(T) = \frac{1}{3} \left[7\bar{H}_2(T) - 4\bar{H}_1(T) \right] \tag{32}$$

along with (31) we consider the balance for component 1,

$$r^2 \rho \mathcal{D} \frac{dY_1}{dr} = a_p^2 F_p \left(Y_1 + \frac{4}{3} \right) \tag{33}$$

Dividing (33) by (31) we obtain

$$\frac{\rho \mathcal{D}}{\lambda} \frac{dY_1}{dT} = \frac{\frac{4}{3} + Y_1}{h(T) - \gamma_p} \tag{34}$$

$$T = T_b \ : \ Y_{1b}$$

where

$$\gamma_p = \frac{e_p}{F_p} \tag{35}$$

Integrating (31) we obtain

$$\int_{T_b}^{T_p} \frac{\lambda(T)dT}{\gamma_p - h(T)} = a_p F_p \tag{36}$$

Likewise, integrating (34) we obtain

$$\ln\left(\frac{Y_{1b} + \frac{4}{3}}{Y_{1p} + \frac{4}{3}}\right) = \int_{T_b}^{T_p} \frac{\lambda(T)}{\rho \mathcal{D}} \frac{dT}{\gamma_p - h(T)} \tag{37}$$

In the case of uniform conditions within the particle, the mass flux is related to the reaction rate $R_{in}(c,T)$ as follows

$$4\pi a_p^2 F_p = \frac{4\pi}{3} a_p^3 S(q) R_{in}(c_{1p}, T_p) \tag{38}$$

where $S(q)$, the pore surface area per unit volume is given by Eq. (13). Using the ideal gas equation of state and Eqs. (26) and (27) we write c_{1p} as a function of Y_{1p}:

$$c_{1p} = \frac{p}{RT_p} \frac{7Y_{1b}}{4 + 3Y_{1b}} \tag{39}$$

such that (38) can be expressed as follows

$$F_p = \frac{1}{3} a_p S(q) R_{in}(Y_{1p}, T_p) \tag{40}$$

Equations (36), (37) and (40) define implicitly the quantities F_p, e_p and Y_{1p} as functions of particle temperature T_p and conversion, q:

$$F_p = f_1(T_p, q) \tag{41}$$

$$e_p = f_2(T_p, q) \tag{42}$$

$$Y_{1p} = f_3(T_p, q) \tag{43}$$

These functions must now be introduced into the differential equations describing the evolution of particle temperature and conversion.

3.3 The Dynamic Equations

The equations will be derived for the limiting case of fast pore diffusion, such that the overall rate is controlled by chemical reaction and film transport. Under these conditions, the particle radius a_p is constant and temperature, gas composition and solid conversion are uniform throughout the particle. The particle energy balance then becomes

$$\frac{d}{dt}(m_p\bar{U}) = -4\pi a_p^2(e_p + e_R) \tag{44}$$

where

$$e_R = \sigma(k_p T_p{}^4 - k_b T_b{}^4) \tag{45}$$

is the radiative flux. Now,

$$\begin{aligned} \frac{dm_p}{dt} &= 4\pi a_p^2 F_p \\ \frac{dU}{dt} &\simeq \frac{d\bar{H}_c}{dt} = c_p \frac{dT}{dt} \end{aligned}$$

so that (44) can be written as

$$\rho_p c_p \frac{dT_p}{dt} = \frac{3}{a_p}\left[F_p \bar{H}_c(T_p) - e_p - e_R\right] \tag{46}$$

To carry out actual calculations we need to specify the reference state for enthalpies. By defining: $\bar{H}_1(T_b) = 0$, $\bar{H}_c(T_b) = 0$ we have $\bar{H}_2(T) = \frac{1}{28}\Delta H(T_b)$, where ΔH is the heat of reaction (15). With this convention

$$\bar{H}_c(T_p) = \int_{T_b}^{T_p} c_p dT \tag{47}$$

$$h(T) = \frac{1}{12}\left[\Delta H(T_b) + \int_{T_b}^{T_p} (\tilde{c}_{p_2} - \frac{1}{2}\tilde{c}_{p_1})dT\right] \tag{48}$$

We also have

$$\rho_p = \rho_{p0}\,(1 - X(q)) \tag{49}$$

where the conversion $X(q)$ is given as a function of q by Eqs. (11) and (12). The particle temperature equation then becomes

$$\frac{dT_p}{dt} = \frac{1}{1-X(q)} \frac{3}{a_p c_p \rho_{p0}} \left[F_p \int_{T_b}^{T_p} c_p dT - e_p - e_R \right] \tag{50}$$

where F_p and e_p are functions of T_p and q. We finally have Eq. (7) for in the form

$$\frac{dq}{dt} = \frac{1}{\rho_c} R_{in} \left(f_3(T_p, q), T_p \right) \tag{51}$$

Equations (50) and (51) with suitable initial values $T_p(0)$ and $q(0) = 0$ describe the transient combustion.

Equations (50) and (51) were integrated with

$$Y_{1b} = 0.233 \ , \quad T_b = 1500K \ , \quad T_p(0) = 300K$$

$$\mathrm{V}_1 = 0.492 \mathrm{cm}^3/\mathrm{g} \ , \quad D_1 = 4.3 \mu\mathrm{m}$$

$$\mathrm{V}_2 = 0.15 \mathrm{cm}^3/\mathrm{g} \ , \quad D_2 = 0.51 \mu\mathrm{m}$$

$$\mathrm{V}_3 + \mathrm{V}_\mu = 0.296 \mathrm{cm}^3/\mathrm{g} \ , \quad D_3 = 270 \mathring{A} \ , \quad h = 27 \mathring{A}$$

The intrinsic rate was taken as

$$R_{in} = A \exp(-E/RT) y_{1p} \qquad (\mathrm{g/cm^2 s})$$

following the correlation presented by Smith (1982) with $E = 42.8$ kcal/gmol and A in the range $200 - 1000 \mathrm{g/cm^2 s}$ to cover the range of reactivities of petroleum cokes lisited in the same reference.

The results of the numerical calculations are presented in Figures 4 and 5. Figure 4 shows particle temperature and oxygen mass fraction versus time for three sets of parameters. Combustion can be divided into three periods. During the first period, the particle is heated by conduction and radiation form the surrounding gas

and solid walls while reaction is negligible. The end of this period is marked by particle ignition. During the second period, reaction becomes significant, as shown by the rapidly decreasing oxygen concentration at the particle surface. The particle is initially heated by reaction and heat transfer. When the particle temperature exceeds the surrounding temperature, heat transfer becomes negative but is still smaller than the heat of reaction. The two terms eventually reach a rough balance marking the end of the second period. During this second period, the oxygen concentration at the particle surface becomes very small and the combustion rate is controlled by external diffusion. The third and last period is characterized by approximate balance of the heat of reaction with the heat transfer. During this period, the reaction rate is determined by external diffusion and the end of the period is marked by a slight drop in temperature due to the essential depletion of carbonaceous matter. Curves a and b differ only in the preexponential factor A which is lower by a factor of 5 in curve b. The two curves are quite similar save for a modest time delay for curve b. The parameters for curve c are the same as for a except for the particle size is lower by a factor of 2. The smaller particles have earlier ignition and shorter burnout time although the pseudosteady particle temperature is the same.

In Figure 5, particle temperature and oxygen fraction are plotted versus conversion. The reaction beyond conversion 0.1 takes place under external diffusion control. However, the temperature does not reach its pseudosteady state until conversion 0.4. The temperature curves for the three sets of parameters essentially coincide, a result that can be explained by the prevalence of control by external mass trasfer.

4 Acknowledgement

This work was funded by the U.S. Department of Energy under contract: DE-AIO1-81CS66001.

5 Notation

Roman Symbols

A	preexponential factor of intrinsic rate
a	external cenosphere radius
a_i	radius of the ith group of spherical voids
b	radius of central bubble
c_p	heat capacity of carbon
$\tilde{c}_{p_i}$	molar heat capacity of component i
D_1, D_2	diameter of spherical voids
D_3'	diameter of disc-shaped voids
E	activation energy pf intrinsic rate
e_p	energy flux (other than radiative) at the particle surface
e_R	radiative energy flux
F_i	mass flux of i^{th} component
F_p	mass flux at the particle surface
$\bar{H}_i$	enthalpy per unit mass of the i^{th} component
h	enthalpy function defined by Eq. (32)
k_p, k_b	emissivities of particle and surroundings
m_p	mass of particle
q	reaction distance
R_{in}	intrinsic rate
r	radial position
S	pore surface area per unit volume
T	temperature
t	time

$\bar{U}$ internal energy per unit mass of solid

V volume

V_i volume of the i^{th} void

W_i defined by $W_i = \lambda_i V_i$

X conversion

Y_i mass fraction of component i^{th}

Z defined by Eq. (22)

Greek Symbols

γ_p defined by Equation (35)

δ thickness of disc-shaped voids

ϵ pore volume fraction of i^{th} group of voids

ϵ total pore volume fraction

λ thermal conductivity

λ_i number density of i^{th} group of voids

ρ_p apparent density of particle

ρ_c density of carbonaceous phase

σ Boltzmann constant

subscripts

1 oxygen

2 carbon monoxide

3 nitrogen

b conditions of free stream

c carbon

p property at particle surface

SH refers to cenosphere shell

6 References

1. Bhatia, S.K., and Perlmutter, D.D. (1980). A random pore model for fluid-solid reactions: I. Isothermal, kinetic control. *A.I.Ch.E.Jl.***26**, 379.

2. Bhatia, S.K., and Perlmutter, D.D. (1981). A random pore model for fluid-solid reactions: II. Diffusion and transport effects. *A.I.Ch.E.Jl.***27**, 247.

3. Caram, H.S., and Amundson, N.R. (1977). Diffusion and reaction in a stagnant boundary layer about a carbon particle. *Ind. Eng. Chem. Fundamentals*, **16**, 171.

4. Gavalas, G.R. (1980). A random capillary model with application to char gasification at chemically controlled rates. *A.I.Ch.E.Jl.***26**, 577.

5. Gavalas, G.R. (1981). Analysis of char combustion including the effect of pore enlargement. *Comb. Sci. Tech.*, **24**,197.

6. Libby, P.A., and Blake, T.R. (1979). Theoretical study of burning carbon particles. *Comb. Flame*,**36**,139.

7. Mon, E., and Amundson, N. R. (1978). Diffusion and reaction in a stagnant boundary layer about a carbon particle 2. An Extension. *Ind. Eng. Chem. Fundamentals*, **17**,313.

8. Smith, I.W. (1982). The combustion rates of coal chars: A review. *19^{th} Symposium (international) on Combustion, The Combustion Institute*, 1045.

9. Sotirchos, S.V., and Amundson, N.R. (1984a). Dynamic behavior of a porous char particle burning in an oxygen-containing environment. 1. Constant radius particle. *A.I.Ch.E.Jl.***30**, 537.

10. Sotirchos, S.V., and Amundson, N.R. (1984b). Dynamic behavior of a porous char particle burning in an oxygen-containing environment. 2. Transient analysis of a shrinking particle. *A.I.Ch.E.Jl.***30**, 549.

11. Sundaresan, S. and Amundson, N.R. (1980). Diffusion and reaction in a stagnant boundary layer about a carbon particle 5. Pseudosteady state structure and parameter sensitivity. *Ind. Eng. Chem. Fund.*,**19**,344.

a

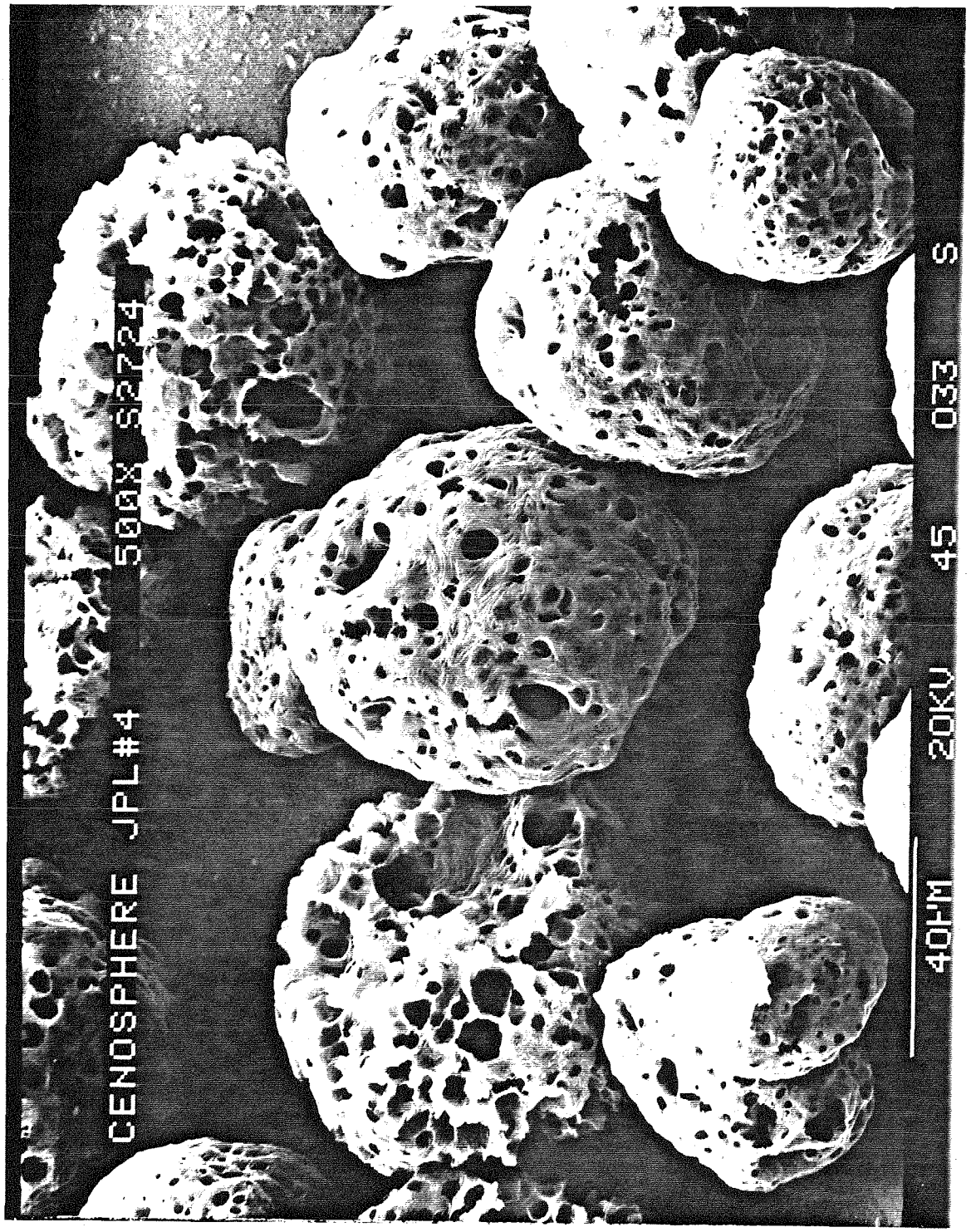

Figure 1: (a,b) SEM micrographs of cenospheres.

(c,d) optical micrographs of cross-sectioned cenospheres.

b

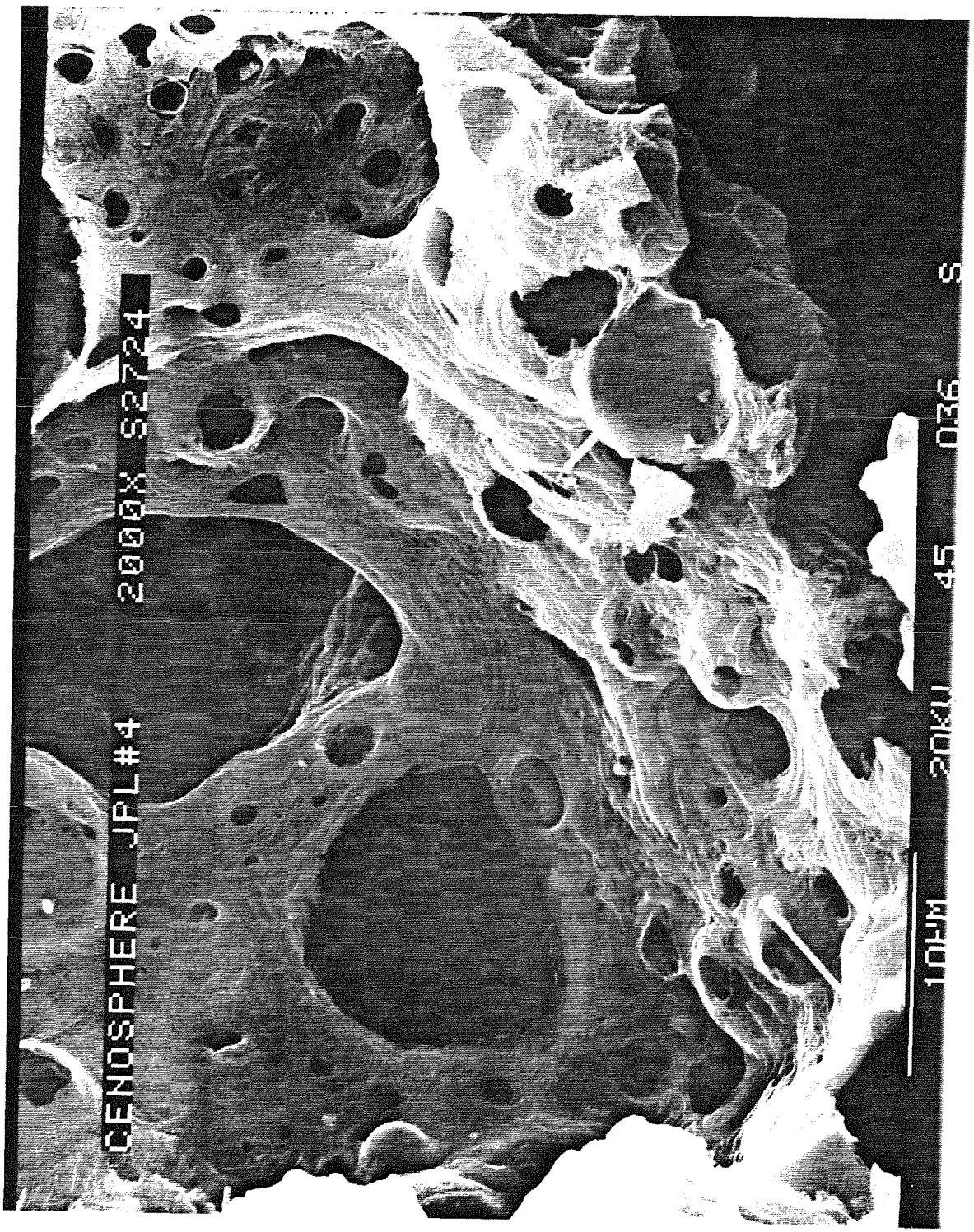

C

d

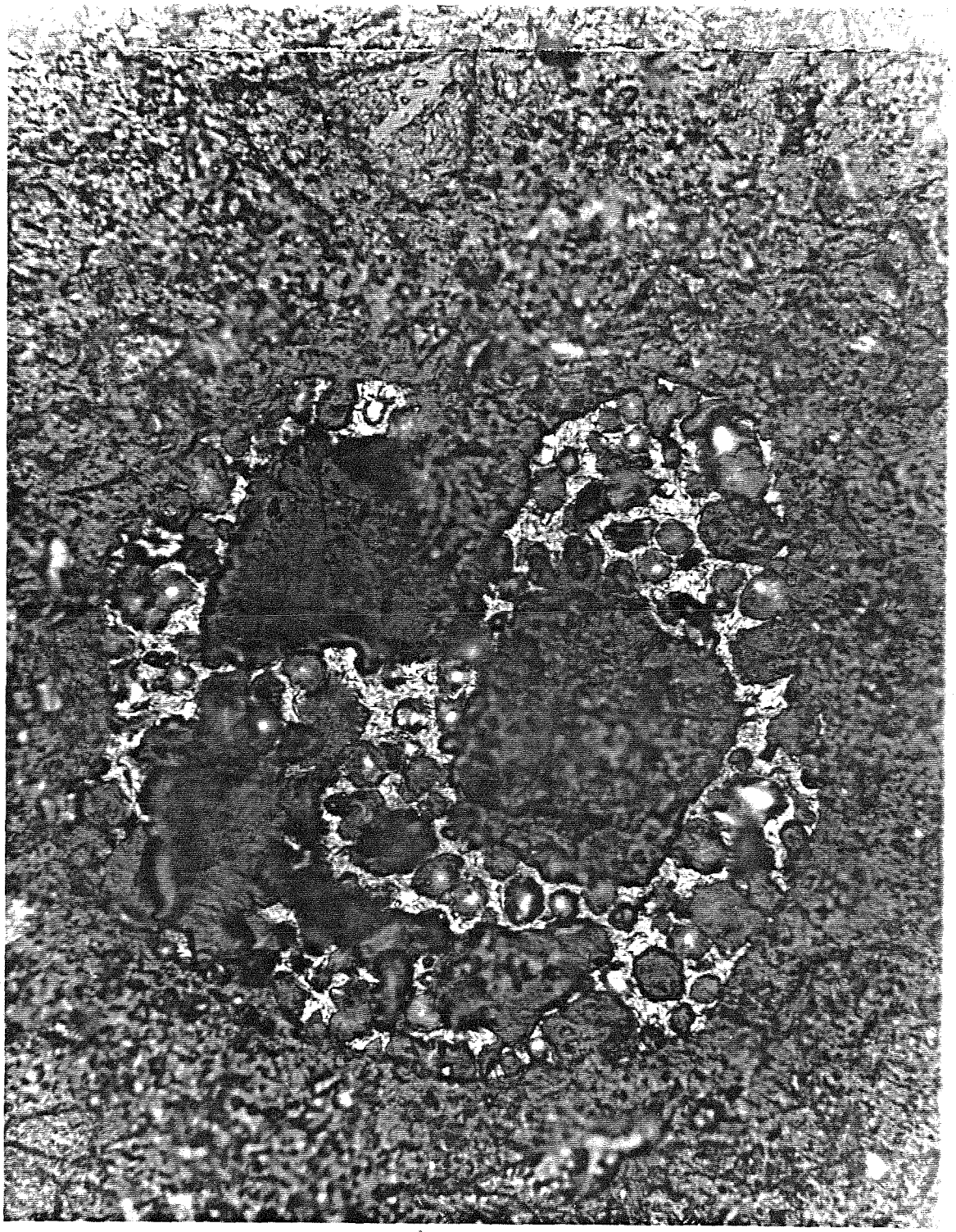

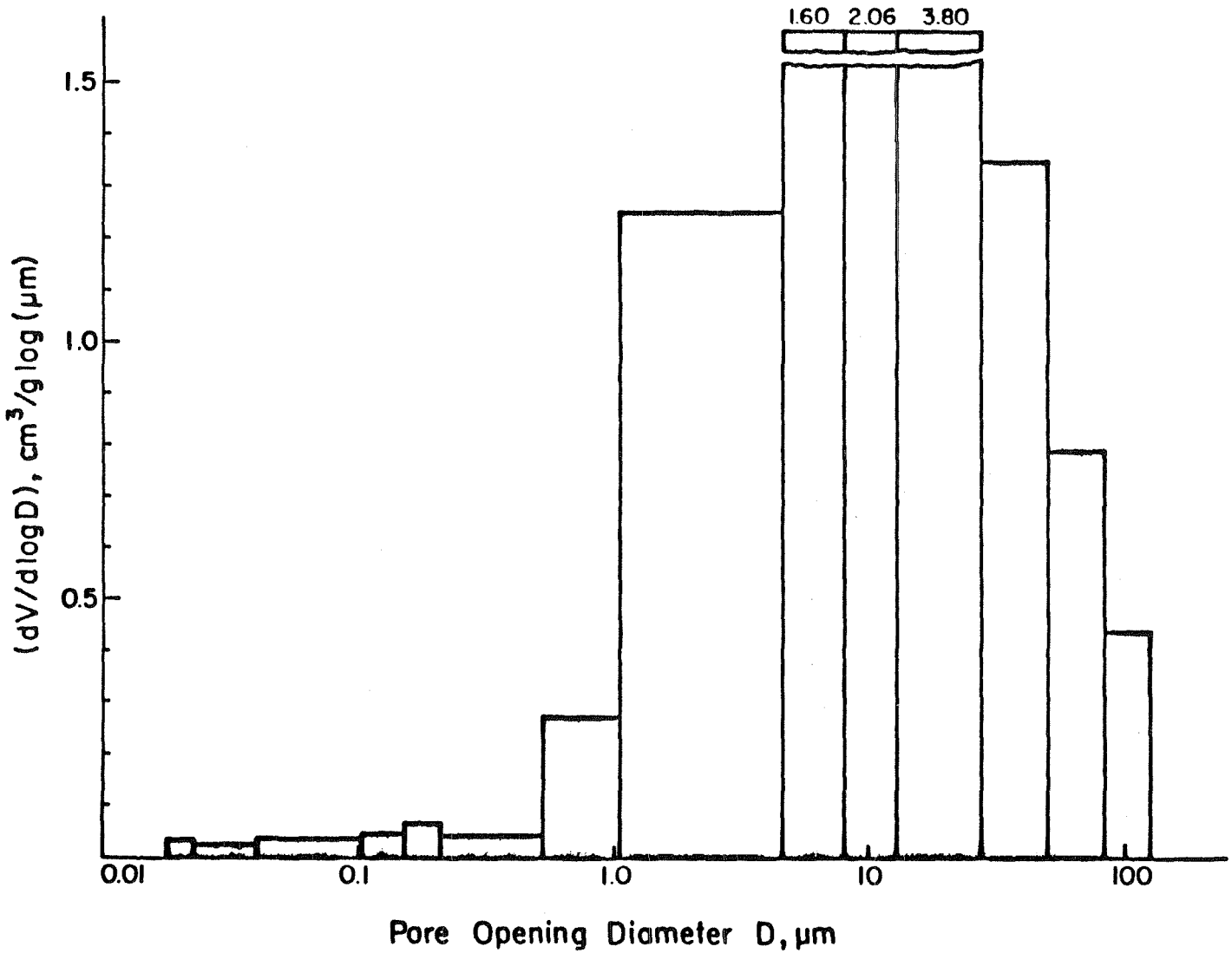

Figure 2: Pore size distribution of cenospheres by mercury intrusion.

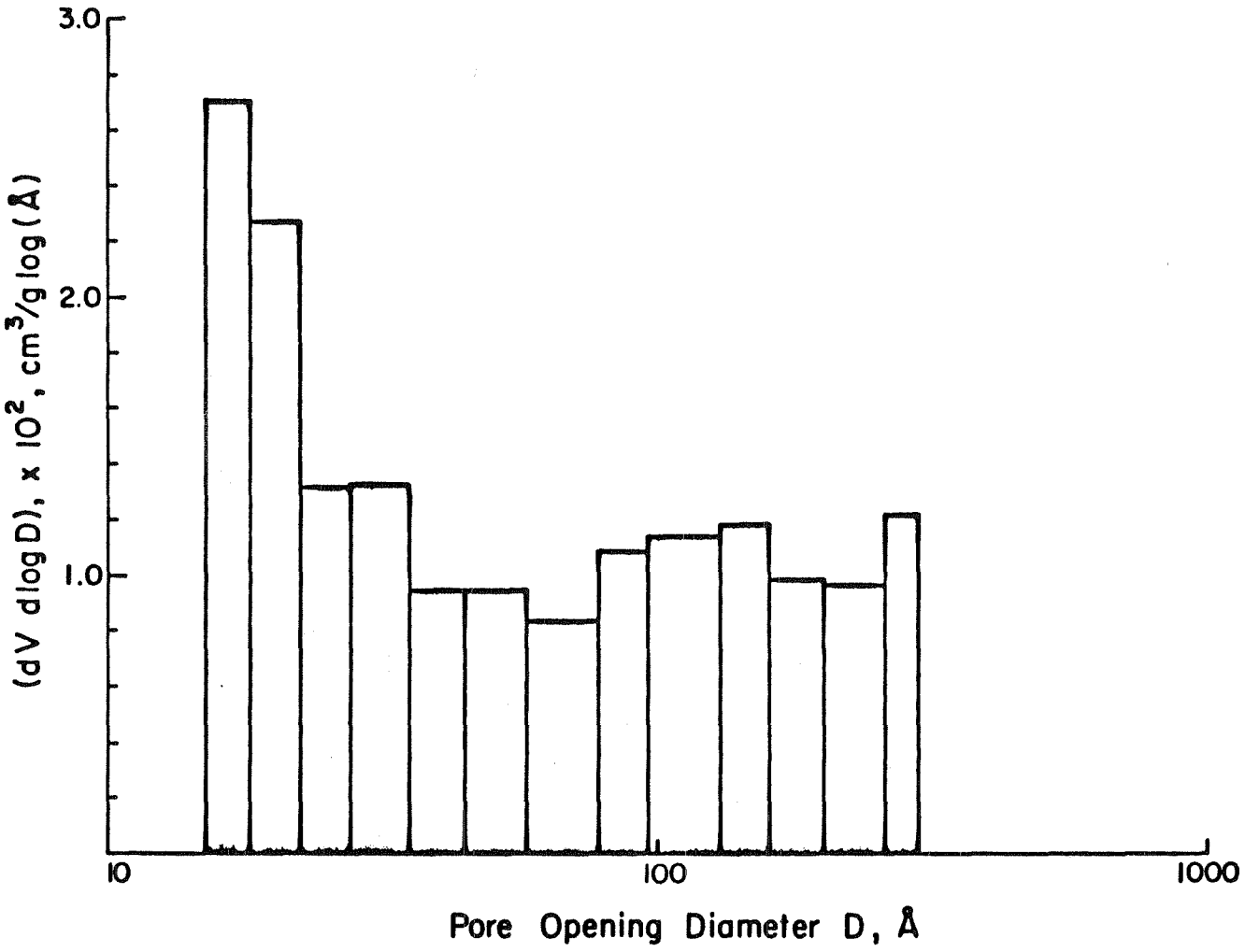

Figure 3: Pore size distribution of cenospheres by nitrogen adsorption.

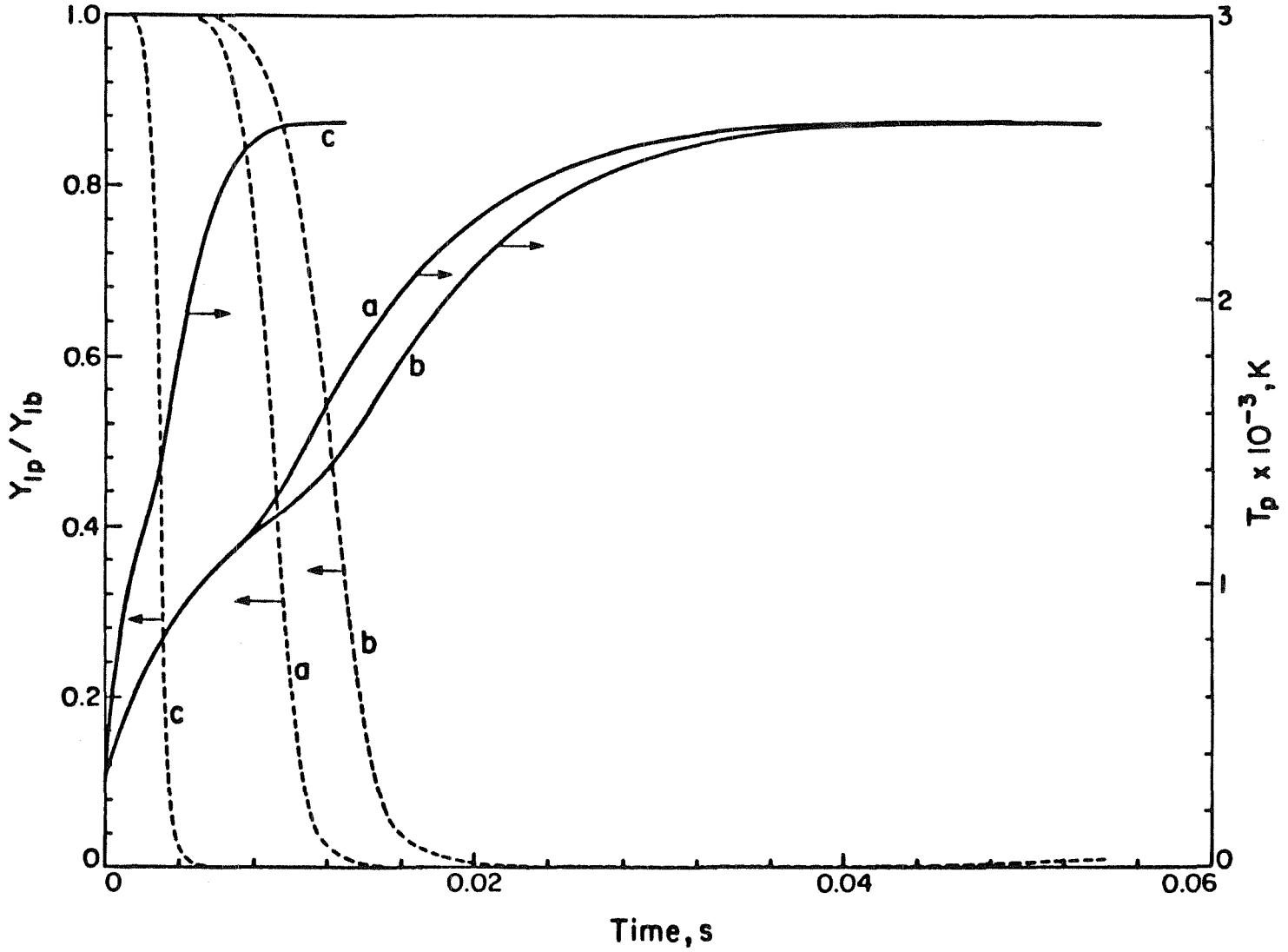

Figure 4: Particle temperature and oxygen fraction versus time.

(a) A=1000g/cm^{2}s, a=50μm (b) A=200, a=50 (c) A=1000, a=25

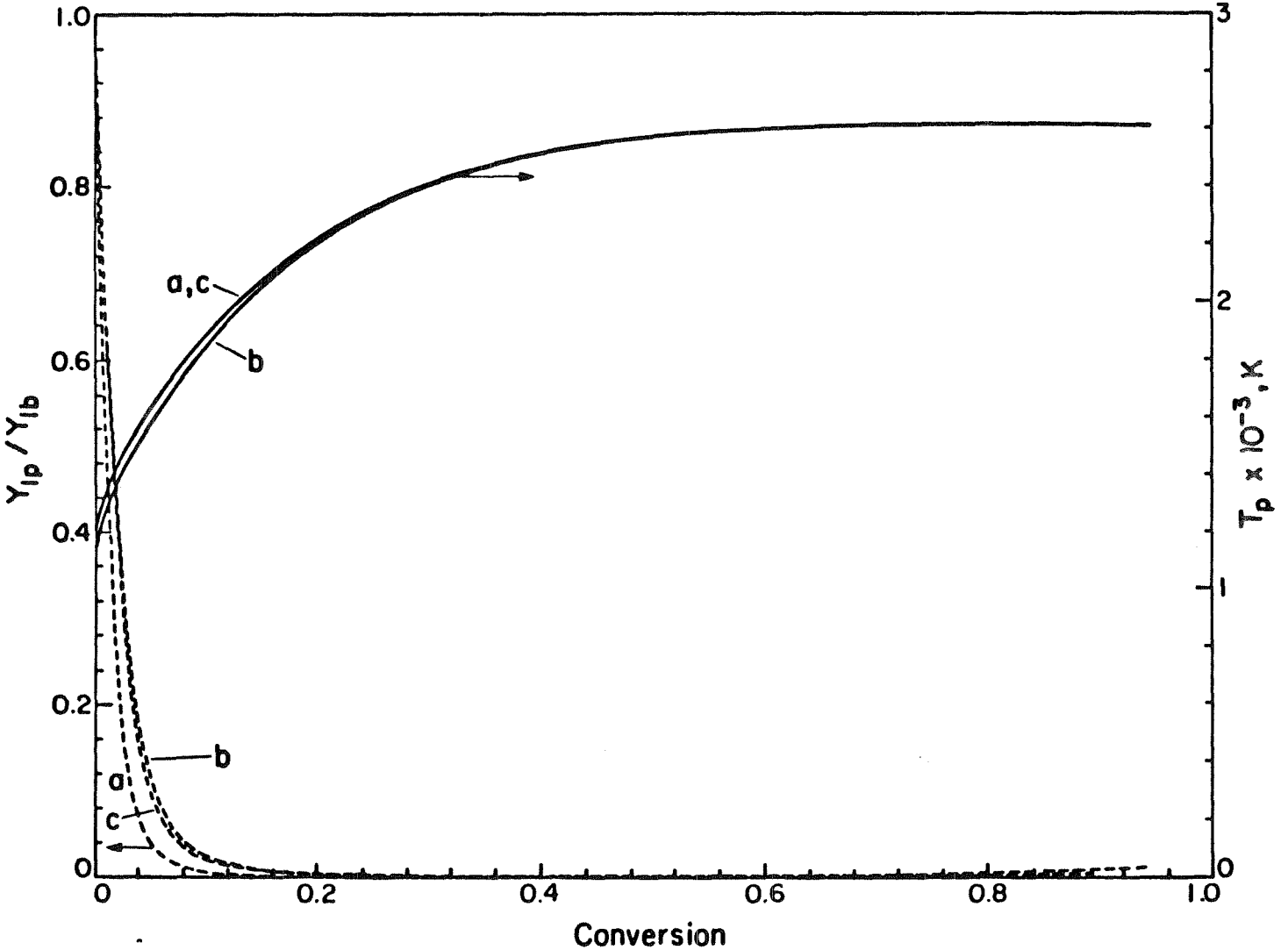

Figure 5: Particle temperature and oxygen fraction versus conversion.

(a) A=1000g/cm^{2}s, a=50μm (b) A=200, a=50 (c) A=1000, a=25

CHAPTER 3

A Simplified Description of Char Combustion

A Simplified Description of Char Combustion

M. Loewenberg*, J. Bellan** and G. R. Gavalas*

* Department of Chemical Engineering 206-41

** Jet Propulsion Laboratory

California Institute of Technology

Pasadena, California 91125

Abstract

A simplified analysis of carbonaceous particle combustion is presented that includes the effects of pore diffusion and growth as well as gas-phase heat and mass transfer. The combustion dynamics are described by time-dependent equations for particle temperature,radius and a number of intraparticle conversion variables. These are coupled to pseudosteady equations for gas-phase transport and internal reaction and diffusion. The differential equations for gas-phase transport are reduced by quadrature to a nonlinear boundary condition to the intraparticle boundary value problem. Numerical calculations are performed for conditions pertaining to pulverized coal combustion. An analytical solution of the intraparticle problem pertinent to the regime of strong diffusional limitations reduces the intraparticle solution into a set of two quadratures which drastically simplifies the numerical calculations. The simplified intraparticle solution is in excellent agreement with the full solution at 1800K free stream temperature and fair agreement at 1500K.

Introduction

The analysis of particle combustion (coal,coke,etc.)is a subject of long standing. Early analyses of particle combustion lumped the reaction on the external particle surface and treated the gas-phase transport problem by heat and mass transfer coefficients. Two significant advances were made in the late 70's and early 80's. Gas-phase transport was described by differential equations rather than overall transfer coefficients and intraparticle pore growth was first considered simultaneously with diffusion and heterogeneous reaction.

Amundson and his collaborators were instrumental in these developments. In a series of comprehensive and subtle analyses, they documented the rich complexities of this nonlinear problem and discovered some rather unexpected phenomena. Caram and Amundson (1977), Mon and Amundson (1978) and Sundaresan and Amundson (1980) tackled the nonlinear complications of gas-phase transport coupled with reaction at the external particle surface, while Sotirchos and Amundson (1984 a,b) extended the analysis to include the complications of intraparticle reaction, diffusion and pore growth. These papers provide a valuable resource for the detailed analysis of char combustion and gasification.

The purpose of this paper is to provide a simplified formulation and numerical treatment of particle combustion which addresses the coupled processes of heterogeneous reaction, pore diffusion, pore growth and external film transport. We will consider combustion in a regime where all rate processes are important. The analysis presented yields a straight forward solution procedure: The pseudosteady film transport equations are reduced to a nonlinear boundary condition to the intraparticle oxygen balance equation. The pseudosteady solution of this equation is then inserted into a system of ordinary differential equations describing the dynamical

quantities: particle temperature, radius and intraparticle conversion variables.

The solution approach outlined above can be simplified drastically by exploiting a closed-form solution of the intraparticle problem that was developed for the regime of strong pore diffusion resistance. This approach eliminates the intraparticle conversion variables reducing the dynamical equations from fifty or one hundred to two: for the particle temperature and radius. It provides a good approximation to the more complete solution when the ambient temperature is higher than 1500K. Such simplified solutions to the particle problem are very useful in the interpretation of experimental data and as components in coal flame models.

Analysis of Intraparticle Transport

As in a previous paper (Gavalas, 1981), we define local conversion in terms of a reaction distance $q(r,t)$ which is the length that the pore surface at a location r has receded during the time interval $[0,t]$. Throughout our analysis of the intraparticle problem, we shall make the following assumptions:

(i) The only heterogeneous reaction taking place is the direct oxidation of carbon to form carbon monoxide

$$C + \frac{1}{2}O_2 = CO \tag{1}$$

(ii) The oxygen profile is at steady-state with respect changes in particle temperature, radius, and the intraparticle conversion variables

(iii) The particle temperature,T_p, is uniform throughout the particle although temporal dependence is retained.

(iv) The intrinsic rate $R_{in}(c,T_p)$ expressed in terms of mass of carbon per unit surface area and time is independent of the local conversion

(v) The porous char can be treated as a continuum using a local effective diffusion coefficient $\delta_e(q)$ and local surface area (per unit volume) $S(q)$.

Assumption (ii) constitutes the pseudosteady treatment of the intraparticle problem. For large char particles and low values of thermal diffusivity, assumption (iii) may be questionable (Sotirchos and Amundson, 1984 c,d and Sotirchos and Burganos, 1986). The structure functions, $S(q)$ and $\delta_e(q)$ may be measured, in principle, by low-temperature (400-500°C) oxidation experiments, or can be obtained from the initial pore surface area and pore size distribution by means of a suitable geometric pore model. Gavalas (1980,1981), Bhatia and Perlmutter (1980,1981) and Su and Permutter (1985) employed a random capillary model for this purpose; Gavalas *et al.* (1985) used randomly distributed spherical voids for the same purpose. In this paper, we shall also use spherical voids. The sphere centers are spatially uncorrelated and thus located by a three-dimensional Poisson density. Consideration of pore overlap between voids of all sizes in the distribution is an implicit feature of the model.

The conservation equations for the oxygen concentration, c, can be written as:

$$\frac{1}{r^2}\frac{\partial}{\partial r}\left(r^2\delta_e(q)\frac{\partial c}{\partial r}\right) = bR_{in}(c,T_p)S(q) \tag{2}$$

$$\frac{\partial q}{\partial t} = \frac{1}{\rho_c}R_{in}(c,T_p) \tag{3}$$

$$t = 0 \quad : \quad q = 0 \tag{4}$$

$$r = 0 \quad : \quad \frac{\partial c}{\partial r} = 0, \quad \frac{\partial q}{\partial r} = 0 \tag{5}$$

$$r = r^*(t) \quad : \quad c = c_s \tag{6}$$

$$r = r^*(t) \quad : \quad r^*(t) = r_0, \quad q < q^* \tag{7a}$$

$$r = r^*(t) \quad : \quad \frac{dr^*}{dt} = -\left(\frac{\partial q/\partial t}{\partial q/\partial r}\right)_{r=r^*} \tag{7b}$$

where $r^*(t)$ is the instantaneous particle radius and q^* is the value of the local conversion variable at the onset of fragmentation (Gavalas, 1981). The intrinsic rate is given in terms of grams of carbon and the conservation equations are for moles of oxygen, thus we introduce the stoichiometric factor,$b = 1/24$. Solution of the above equations allows us to calculate the total mass flux, F_p^T, at the particle surface:

$$F_p^T = F_p + F_p^* \tag{8}$$

where F_p is the mass flux at the particle surface resulting from chemical reaction within the particle and is given by:

$$F_p = b\delta_e \left.\frac{\partial c}{\partial r}\right|_{r=r^*} \tag{9}$$

F_p^* is the mass flux (at the particle surface) due to fragmentation. We can write:

$$F_p^* = -\frac{dr^*}{dt}\rho^* \tag{10}$$

where ρ^* is the density of the carbon matrix at the particle surface.

Equations (2) - (10) need some further comments. Equations (7a,b) result from the observation that, initially, a particle burns with constant size until the surface porosity reaches a critical value, ϵ^*, which causes fragmentation of the local carbonaceous matrix. At that instant, the boundary starts receding with a velocity dr^*/dt given by Equation (7b). The value q^* is defined by:

$$\epsilon_T(q^*) = \epsilon^*$$

Limited data by Dutta *et al.* (1977) suggest ϵ^* is approximately equal to 0.8. for the char they analyzed. Kerstein and Niksa (1984) showed using percolation theory that ϵ^* is 0.68 for a random network of cylindrical voids and 0.96 for a random network of spherical voids. They also measured critical porosities between 0.5 and

0.85 for various carbonaceous materials. Gavalas (1981) found that his calculations were quite insensitive to the precise value chosen for ϵ^* in the range 0.7 to 0.9. We chose ϵ^* equal to 0.8.

Boundary condition (6) and Equation (9) couple the intraparticle equations to the gas-phase equations. The above distinction between total mass flux, F_p^T, and mass flux due to chemical reaction, F_p, is important to the coupling between the intraparticle and film transport problems. It can be readily shown that the velocity of the gas-phase is directed radially outward with a magnitude given by:

$$v(r) = \frac{1}{\rho_g} F = \frac{1}{\rho_g} \frac{r^{*2}}{r^2} F_p \tag{11}$$

For parameters pertaining to pulverized combustion, this velocity is on the order of 1 m/s causing detached fragments to move out of the particle's sphere of influence in a fraction of a millisecond and, hence, without further substantial reaction. These fragments burn in the free stream and have little influence upon the film transport.

An important special case within the framework of Equations (2) - (7) is the high Thiele modulus limit where the particle burns with nearly constant density and decreasing radius. Gavalas (1981) considered the pseudosteady situation in which the surface velocity, dr^*/dt has reached a constant value. Equations (2) - (7) simplify considerably in this case yielding the following solution:

$$\frac{dr^*}{dt} = \frac{1}{b^{1/2}\rho_c} \frac{I^{1/2}}{J^{1/2}} \tag{12}$$

where $I^{1/2}$ and $J^{1/2}$ are simple quadratures which describe kinetic and physical parameters respectively:

$$I = \int_0^{c_s} R_{in}(c, T_p) dc \tag{13}$$

$$J = \int_0^{q^*} \frac{\epsilon_T(q) - \epsilon_{T_0}}{\delta_e(q)} dq \tag{14}$$

The total mass flux is simply the product of surface velocity and the (initial) particle density; Equation (8) becomes:

$$F_p^T = -\rho_0 \frac{dr^*}{dt} \tag{15}$$

The mass flux which results from fragment shedding, F_p^*, is given by Equation (10); therefore, the mass flux given by chemical reaction within the particle becomes:

$$F_p = -(\rho_0 - \rho^*)\frac{dr^*}{dt} \tag{16}$$

The above analytical solution remains coupled to the gas-phase equations through c_s in the upper limit of integration in Equation (13). We shall compare the results of the above analytical solution with the results from full numerical solution of Equations (2) - (7).

Analysis of Gas-Phase Transport

This section is concerned with heat and mass transport from the particle surface to the free stream. In the first part of the section, we derive algebraic expressions for the pseudosteady mass and energy fluxes evaluated at the particle surface which serve as a nonlinear boundary condition of the intraparticle problem. In the second part, we derive the equation describing the particle temperature. The approach used is an extension of the approach of Libby and Blake (1979) to account for temperature dependent diffusivity, thermal conductivity, and heat capacities. Throughout the gas-phase analysis, we shall employ the following assumptions:

(i) The temperature and concentration profiles are at steady-state with respect to the dynamical quantities T_p, r^* and $q(r,t)$.

(ii) The gas-phase oxidation of CO to CO_2 takes place in the free stream and therefore does not appear in the species balances.

(iii) The fluxes induced by thermal and pressure gradients are insignificant

(iv) Mass transfer is described by ternary diffusion involving O_2, CO and "inert", the latter including N_2 and CO_2. The three binary diffusion coefficients are equal but not constant.

(v) The gas-phase is transparent to radiation, neither absorbing nor emitting radiation.

Denoting by Y_i and F_i the mass fraction and mass flux of the i^{th} component (O_2:i=1, CO:i=2, inert : i=3), we can write the pseudosteady component balances as:

$$r^2 F_i = r^*(t)^2 F_{ip} \tag{17}$$

where F_{ip} denotes the mass flux of the i^{th} component at the particle surface. The fluxes, F_i are related by the Stefan-Maxwell equations:

$$\nabla Y_i = \sum_j \frac{1}{\rho_g(T)\mathcal{D}_{ij}(T)}(Y_i F_j - Y_j F_i) \tag{18}$$

where the contributions of pressure and temperature gradients have been neglected according to assumption (iii). Using assumption (iv) above: $\mathcal{D}_{12} = \mathcal{D}_{13} = \mathcal{D}_{23} = \mathcal{D}$ simplifies this equation to :

$$F_i = -\rho_g(T)\mathcal{D}(T)\frac{dY_i}{dr} + FY_i \tag{19}$$

where $F = \sum_i F_i$ is the total mass flux satisfying:

$$r^2 F = r^*(t)^2 F_p \tag{20}$$

The stoichiometry of the reaction given by Equation (1) yields the relationships:

$$F_{3p} = 0, \quad F_{1p} = -\frac{4}{3}F_p, \quad F_{2p} = \frac{7}{3}F_p \tag{21}$$

Introducing (20) and (21) into (19) we obtain by suitable linear combination:

$$\rho_g(T)\mathcal{D}(T)r^2 \frac{dZ}{dr} = r^*(t)^2 F_p Z \tag{22}$$

where

$$Z = \frac{Y_1}{4} + \frac{Y_2}{7} \tag{23}$$

Equation (19) for component 3 (N_2) reads:

$$\rho_g(T)\mathcal{D}(T)r^2 \frac{dY_3}{dr} = r^*(t)^2 F_p Y_3 \tag{24}$$

We divide Equation (22) by (24) and obtain

$$\frac{dZ}{dY_3} = \frac{Z}{Y_3}$$

with the free stream boundary conditions:

$$Y_3 = Y_{3\infty} : Z = Z_\infty = \frac{Y_{1\infty}}{4} + \frac{Y_{2\infty}}{7}$$

It follows:

$$Z = \frac{Y_1}{4} + \frac{Y_2}{7} = \frac{Z_\infty}{Y_{3\infty}} Y_3 \tag{25}$$

This equation is solved along with $\sum_i Y_i = 1$ to express Y_2 and Y_3 in terms of Y_1:

$$Y_2 = \frac{7A}{7A+1} - \frac{7(4A+1)}{4(7A+1)} Y_1 \tag{26}$$

$$Y_3 = \frac{1}{7A+1} + \frac{3}{4(7A+1)} Y_1 \tag{27}$$

where A is given by:

$$A = \frac{1}{Y_{3\infty}} \left(\frac{Y_{1\infty}}{4} + \frac{Y_{2\infty}}{7} \right) \tag{28}$$

The pseudosteady energy equation for a gas transparent to radiation is:

$$r^2\left[-\lambda(T)\frac{dT}{dr}+\sum_i F_i\bar{H}_i\right]=r^*(t)^2e_p \tag{29}$$

where

$$e_p=\left[-\lambda(T)\frac{dT}{dr}+\sum_i F_i\bar{H}_i\right]\Bigg|_{r=r^*(t)} \tag{30}$$

By using Equations (17) and (21), we rewrite (29) as:

$$r^2\lambda(T)\frac{dT}{dr}=r^*(t)^2\left[h(T)F_p-e_p\right] \tag{31}$$

with boundary conditions:

$$r=r^*(t):T=T_p;r\to\infty:T\to T_\infty$$

where h(T) is given by:

$$h(T)=\frac{1}{3}\left[7\bar{H}_2(T)-4\bar{H}_1(T)\right] \tag{32}$$

Using Equations (17),(19),(20) and (21) the balance for component 1 (oxygen) becomes:

$$r^2\rho_g(T)\mathcal{D}(T)\ \frac{dY_1}{dr}=r^*(t)^2F_p\left(Y_1+\frac{4}{3}\right) \tag{33}$$

We divide Equation (33) by Equation (31) to obtain:

$$\frac{\rho_g(T)\mathcal{D}(T)}{\lambda(T)}\ \frac{dY_1}{dT}=\frac{\frac{4}{3}+Y_1}{h(T)-\gamma_p} \tag{34}$$

$$T=T_\infty:Y_{1\infty}$$

where γ_p is the ratio of energy flux to mass flux:

$$\gamma_p=\frac{e_p}{F_p} \tag{35}$$

Integrating Equation (31) and invoking (35) we obtain:

$$\int_{T_\infty}^{T_p} \frac{\lambda(T)dT}{\gamma_p - h(T)} = r^*(t)F_p \tag{36}$$

Similarly, Equation (34) yields by integration:

$$\ln\left(\frac{Y_{1\infty} + \frac{4}{3}}{Y_{1p} + \frac{4}{3}}\right) = \int_{T_\infty}^{T_p} \frac{\lambda(T)}{\rho_g(T)\mathcal{D}(T)} \frac{dT}{\gamma_p - h(T)} \tag{37}$$

Equations (36) and (37) are the algebraic expressions for the mass and energy fluxes at the particle surface. The oxygen concentration at the particle surface,c_s, can be expressed in terms of species mass fractions at the particle surface.

$$c_s = \frac{1}{R_g T_p} \frac{Y_{1p}/32}{Y_{1p}/32 + Y_{2p}/28 + Y_{3p}/28} \tag{38}$$

Equations (26) - (28) then allow c_s to be expressed solely in terms of the mass fraction of oxygen at the particle at the particle surface, Y_{1p}. Equations (36), (37) and (38) couple to Equations (6) and (9) from the intraparticle problem via the quantities c_s and F_p.

The particle energy balance can be written as:

$$\frac{d}{dt}\int_{V_p} \rho \bar{U} dV_p = -4\pi r^*(t)^2(e_p + e_R) \tag{39}$$

where

$$e_R = \sigma(\varepsilon_p {T_p}^4 - \varepsilon_\infty {T_\infty}^4) \tag{40}$$

is the radiative flux. In view of the assumed uniform intraparticle temperature profile, we can rewrite (39) as:

$$m_p c_{p_c} \frac{dT_p}{dt} = 4\pi r^*(t)^2 \left[F_p \bar{H}_c(T_p) - F_p \gamma_p - e_R\right] \tag{41}$$

having made the additional approximation: $c_{v_c} \simeq c_{p_c}$.

The reference states for the enthalpies are chosen as: $\bar{H}_1(T_\infty) = 0, \bar{H}_c(T_\infty) = 0$ which imply

$$\bar{H}_2(T) = \frac{1}{28}\Delta H(T_\infty)$$

where ΔH is the heat of reaction (1). Thus the quantity $h(T)$ defined by Equation (32) is given by :

$$h(T) = \frac{1}{12}\left[\Delta H(T_\infty) + \int_{T_\infty}^{T_p}(\tilde{c}_{p_2} - \frac{1}{2}\tilde{c}_{p_1})dT\right] \tag{42}$$

Equation (41) becomes:

$$m_p c_{p_c}\frac{dT_p}{dt} = 4\pi r^*(t)^2 \left[F_p\int_{T_\infty}^{T_p} c_{p_c}dT - F_p\gamma_p - e_R\right] \tag{43}$$

Solution Procedure

In the present section, we shall list the values of the parameters used to describe the combustion of hypothetical char particles and outline the solution procedure with special attention to the coupling of the intraparticle and gas-phase equations. We consider a spherical particle of initial radius $r_0 = 25\mu m$. Its porous structure consists of randomly located spherical voids of initial radii: 0.5 μm,0.05 μm and 0.005 μm with initial pore volume fraction 0.1 for each group. These parameters fully define the porous structure and the functions $S(q)$ and $\delta_e(q)$ (Gavalas, 1981). The intrinsic rate is chosen as:

$$R_{in} = 150\ R_g T_p exp(\frac{-42,800}{R_g T_p})c \qquad g(C)/cm^2 s \tag{44}$$

taken in the range suggested by Smith (1978). The free stream is air at one atmosphere and temperature, T_∞=1500 or 1800K. In either case, the initial particle temperature is taken equal to the free stream temperature.

Having chosen first order kinetics, Equation (44), we can easily solve the boundary value problem defined by Equations (2) and (5) and express the total mass flux,F_p^T, the mass flux due to chemical reaction,F_p, and the mass flux due to fragmentation, F_p^* as:

$$F_p^T = G_p^T c_s \tag{45a}$$

$$F_p = G_p c_s \tag{45b}$$

$$F_p^* = G_p^* c_s \tag{45c}$$

where G_p^T, G_p and G_p^* are calculated for fixed values of the dynamical quantities: T_p,r^*, $q(r,t)$. Equation (36) becomes:

$$\int_{T_\infty}^{T_p} \frac{\lambda(T)dT}{\gamma_p - h(T)} = r^*(t) G_p c_s \tag{46}$$

Equations (38) in combination with Equations (26) - (28) yield c_s as a function of Y_{1p}. Then Equation (37) expresses Y_{1p} in terms of γ_p which ultimately yields c_s in terms of γ_p. The result is inserted into Equation (46) yielding a single algebraic equation for γ_p which is efficiently solved using a Newton-Raphson scheme. Equation (37) then yields Y_{1p} directly and c_s is found by Equations (38) and (26) - (28) which provides a boundary condition for the intraparticle problem (Equation (6)) and the mass fluxes are found via Equations (45a,b,c). Thus, the film-transport equations have been reduced to a nonlinear boundary condition for the intraparticle problem.

The dynamical equations consist of Equations (3),(7a,b) and (43) for $q(r,t)$, r^* and T_p respectively. Equation (3) is solved at a discrete set of points chosen to describe an *a priori* estimated radial profile of $q(r,t)$. In the present calculations, we used a set of 100 grid points. The corresponding dynamical equations coupled with the equations for particle radius and temperature were solved by Gear's method.

Numerical Results

Two runs were made with free stream temperatures T_∞ = 1500 and 1800K. In both cases, combustion was followed to 90% conversion. Using the full numerical solution, the time required to reach 90% conversion was 147 milliseconds for T_∞=1500K and 46 milliseconds for T_∞= 1800K. The approximate solution, employing Equation (12), predicted 143 milliseconds to reach 90% conversion for T_∞=1500K and agreed perfectly with the full intraparticle problem for T_∞=1800K also predicting 46 milliseconds. Figures 1 - 4 show the results from the model and are discussed below. The solid curves result from the full intraparticle equations (Equations (2) - (7)) and the dashed curves refer to the approximate solution employing Equation (12). The approximate solution shows excellent agreement to the full solution for T_∞ = 1800K and fair agreement for T_∞ = 1500K. The two solutions are further compared below.

Figures 1 and 2 show the particle temperature histories during combustion. For both choices of free stream temperature, the particle temperature goes through a maximum; this is most pronounced for the the lower free stream temperature. At the higher free stream temperature the particle temperature displays a less pronounced temperature maximum. Also shown in Figures 1 and 2 is the oxygen concentration at the particle surface normalized by the free stream concentration (air). Film diffusion is important but not rate-controlling. At T_∞ = 1800K, film diffusion resistance has an approximately equal effect upon the overall rate as the intraparticle resistance. In both cases, the surface oxygen concentration goes through a gentle minimum and in both cases, the minimum oxygen concentration occurs prior to the maximum in particle temperature.

Figures 3 and 4 show conversion, dimensionless radius, r^*/r_0, and average dimen-

sionless particle density ($\bar{\rho}/\rho_0$) as functions of time for each run. Figure 3 indicates that for $T_\infty = 1500$K, the particle burns with decreasing density and constant radius until about 18% conversion; in an 1800K free stream, the same is true only until about 7% conversion. After shedding begins, in an 1800K free stream, the particle burns with nearly constant density and approximately linearly decreasing radius until complete (90%) conversion. The foregoing holds for $T_\infty = 1500$K but only until approximately 65% conversion at which point the average particle density resumes a gradual decline until 90% conversion is attained.

For both choices of ambient temperature the average density of the particle actually *increases* slightly following start of particle shedding. This phenomenon can be explained by the observation that the particle temperature is continually increasing in the neighborhood of the point where shedding begins; the lower temperatures prior to particle shedding allow more oxygen penetration causing the local density near the particle surface to decrease during combustion prior to particle shedding. As particle shedding begins, the particle temperature continues to increase allowing less oxygen penetration thus retarding further density decrease. The shedding removes the less-dense layer of char near the particle surface thereby increasing the *average* particle density.

A tacit assumption in the foregoing analysis is that when the char reaches a prescribed local void volume, ϵ^* *exactly* equal to 0.8, shedding of fragments from the particle surface ensues causing a discontinuity in dr^*/dt. This discontinuity is propagated to the total mass flux,F_p^T, as implied by Equation (8) which causes the conversion rate to exhibit a discontinuity at the point at which fragmentation starts. Figures 3 and 4 indicate that for both free stream temperatures, the conversion increases smoothly with time with the exception of a slight discontinuity in slope at the onset of fragmentation.

Figures 1 - 4 compare the results calculated using the analytical solution with the results of the full intraparticle solution given by Equations (2) - (7). For an 1800K ambient, the results are in excellent agreement, but even for T_∞ = 1500K, the approximate solution is adequate. The discrepancy between the approximate and the full solution is a consequence of the fact that the former assumes that particle fragmentation begins immediately thereby predicting smaller particle size and higher initial conversion rate as indicated in Figures 3 and 4. Lighter particles are heated faster and reach their maximum temperature earlier as indicated by Figures 1 and 2. The foregoing discrepancies are more pronounced for T_∞=1500K. The success of the approximate solution is consistent with estimates of the Thiele modulus based upon initial structure and average particle temperature. These estimates were 10 and 40 for T_∞ = 1500 and 1800K respectively.

Conclusions

An efficient, simplified analysis of single-particle char combustion has been presented taking into account pore diffusion and growth coupled with gas-phase transport. Assuming frozen, homogeneous reaction and equal diffusivities while maintaining the temperature dependence of various properties allows integration of the gas-phase equations into a sequentially-solved set of algebraic equations. These equations serve as a nonlinear boundary condition to the intraparticle diffusion problem.

Numerical calculations performed for parameter values representative of pulverized combustion show that film diffusion and pore diffusion are both important in determining the rate of particle combustion. In an 1800K free stream, the particle burns essentially in a shrinking core fashion. An analytical solution derived

for the regime of strong limitations by pore diffusion gave excellent agreement to the complete numerical solution for a free stream at 1800K and fair agreement at 1500K. The analytical intraparticle solution greatly simplifies the overall numerical problem.

Acknowledgement

This work was supported by DOE Office of Energy Utilization Research, ECUT Program.

Nomenclature

Roman Symbols

A defined by Equation (28)

b stoiciometric coefficient ($= 1/24$)

c oxygen concentration (gmoles/cm^3)

c_s oxygen concentration at particle surface (gmoles/cm^3)

c_{p_i} specific heat capacity of i^{th} species (cal/g K)

$\tilde{c}_{p_i}$ molar heat capacity of i^{th} species (cal/mol K)

$\mathcal{D}$ gas-phase diffusion coefficient (cm^2/s)

e total energy flux (cal/cm^{2}s)

e_R radiative energy flux

F^T total mass flux (g/cm^{2}s)

F total mass flux due to chemical reaction(g/cm^{2}s)

F_i mass flux of i^{th} species(g/cm^{2}s) see Equation (17)

F^* mass flux due to particle fragmentation (g/cm^{2}s)

G^T defined by Equation (45a)

G_p defined by Equation (45b)

G^* defined by Equation (45c)

h defined by Equation (32)

H_i enthalpy of i^{th} species

ΔH heat of reaction (Equation(1))

I defined by Equation (13)

J defined by Equation (14)

m_p particle mass (g)

q local conversion variable (cm)

q^* value of q at critical porosity, ϵ^*

r radial position (cm)

r_0 initial particle radius (cm)

r^* instantaneous particle radius (cm)

R_{in} intrinsic rate per unit pore surface area(g/cm^2s)

R_g gas constant

T temperature (K)

t time (s)

$\bar{U}$ specific internal energy of carbon (cal/g)

X overall conversion

Y_i mass fraction of i^{th} species

Z defined by Equation (23)

Greek Symbols

γ_p defined by Equation (35)

δ_e effective diffusion coefficient (cm^2/s)

ϵ_T total porosity

ϵ_{T0} total initial porosity

ϵ^* critical porosity

ε emissivity

ρ_g density of gas-phase (g/cm^3)

ρ local value of particle density (g/cm^3)

ρ_0 initial particle density (g/cm^3)

$\bar{\rho}$ average particle density (g/cm^3)

ρ^* local particle density at critical porosity(g/cm^3)

ρ_c true carbonaceous density(g/cm^3)

σ Stefan-Boltzmann constant

subscripts

1 oxygen

2 carbon monoxide

3 nitrogen

c carbon

p at particle surface

∞ at ambient conditions

References

1. Bhatia, S.K., and Perlmutter, D.D. (1980). A random pore model for fluid solid reactions: I. Isothermal, kinetic control. *A.I.Ch.E.Jl.***26**, 379.

2. Bhatia, S.K., and Perlmutter, D.D. (1981). A random pore model for fluid solid reactions: II. Diffusion and transport effects. *A.I.Ch.E.Jl.***27**, 247.

3. Caram, H.S., and Amundson, N.R. (1977). Diffusion and reaction in a stagnant boundary layer about a carbon particle. *Ind. Eng. Chem. Fundamentals*, **16**, 171.

4. Dutta, S.,Wen, C.Y., and Belt, R.J. (1977). Reactivity of coal and char 1. in carbon dioxide atmosphere. *Ind. Eng. Chem., Process Des. Dev.*, **16**,20.

5. Gavalas, G.R. (1980). A random capillary model with application to char gasification at chemically controlled rates. *A.I.Ch.E.Jl.***26**, 577.

6. Gavalas, G.R. (1981). Analysis of char combustion including the effect of pore enlargement. *Comb. Sci. Tech.*, **24**,197.

7. Gavalas, G.R., Loewenberg, M.,Bellan, and J.,Clayton, M. (1985). Structure and combustion of cenosphere particles. Paper presented at the annual A.I.Ch.E. meeting, Chicago, November 10-15.

8. Kerstein, A.R., and Niksa, S. (1984). Fragmentation during carbon conversion: predictions and measurements. *20^{th} Symposium (international) on Combustion, The Combustion Institute*, 941.

9. Libby, P.A., and Blake, T.R. (1979). Theoretical study of burning carbon particles. *Comb. Flame*,**36**,139.

10. Mon, E., and Amundson, N. R. (1978). Diffusion and reaction in a stagnant boundary layer about a carbon particle 2. An Extension. *Ind. Eng. Chem. Fundamentals*, **17**,313.

11. Smith, I.W. (1982). The combustion rates of coal chars: A review. *19th Symposium (international) on Combustion, The Combustion Institute*, 1045.

12. Sotirchos, S.V., and Amundson, N.R. (1984a). Diffusion and reaction in a porous char particle and in the surrounding gas phase. Two limiting model. *Ind. Eng. Chem. Fundamentals*,**23**, 180.

13. Sotirchos, S.V., and Amundson, N.R. (1984b). Diffusion and reaction in a porous char particle and in the surrounding gas phase. A continuous model. *Ind. Eng. Chem. Fundamentals*,**23**, 191.

14. Sotirchos, S.V., and Amundson, N.R. (1984c). Dynamic behavior of a porous char particle burning in an oxygen- containing environment. 1. Constant radius particle. *A.I.Ch.E.Jl.***30**, 537.

15. Sotirchos, S.V., and Amundson, N.R. (1984d). Dynamic behavior of a porous char particle burning in an oxygen- containing environment. 2. Transient analysis of a shrinking particle. *A.I.Ch.E.Jl.***30**, 549.

16. Sotirchos, S.V., and Burganos, V.N. (1986). Intraparticle diffusion and char combustion. *Chem. Eng. Sci.*,**41**, 1599.

17. Su, J.L., and Perlmutter, D.D. (1985). Effect of pore structure on char oxidation kinetics. *A.I.Ch.E.Jl.* **31**, 973.

18. Sundaresan, S. and Amundson, N.R. (1980). Diffusion and reaction in a stagnant boundary layer about a carbon particle 5. Pseudosteady state structure and parameter sensitivity. *Ind. Eng. Chem. Fund.*,**19**,344.

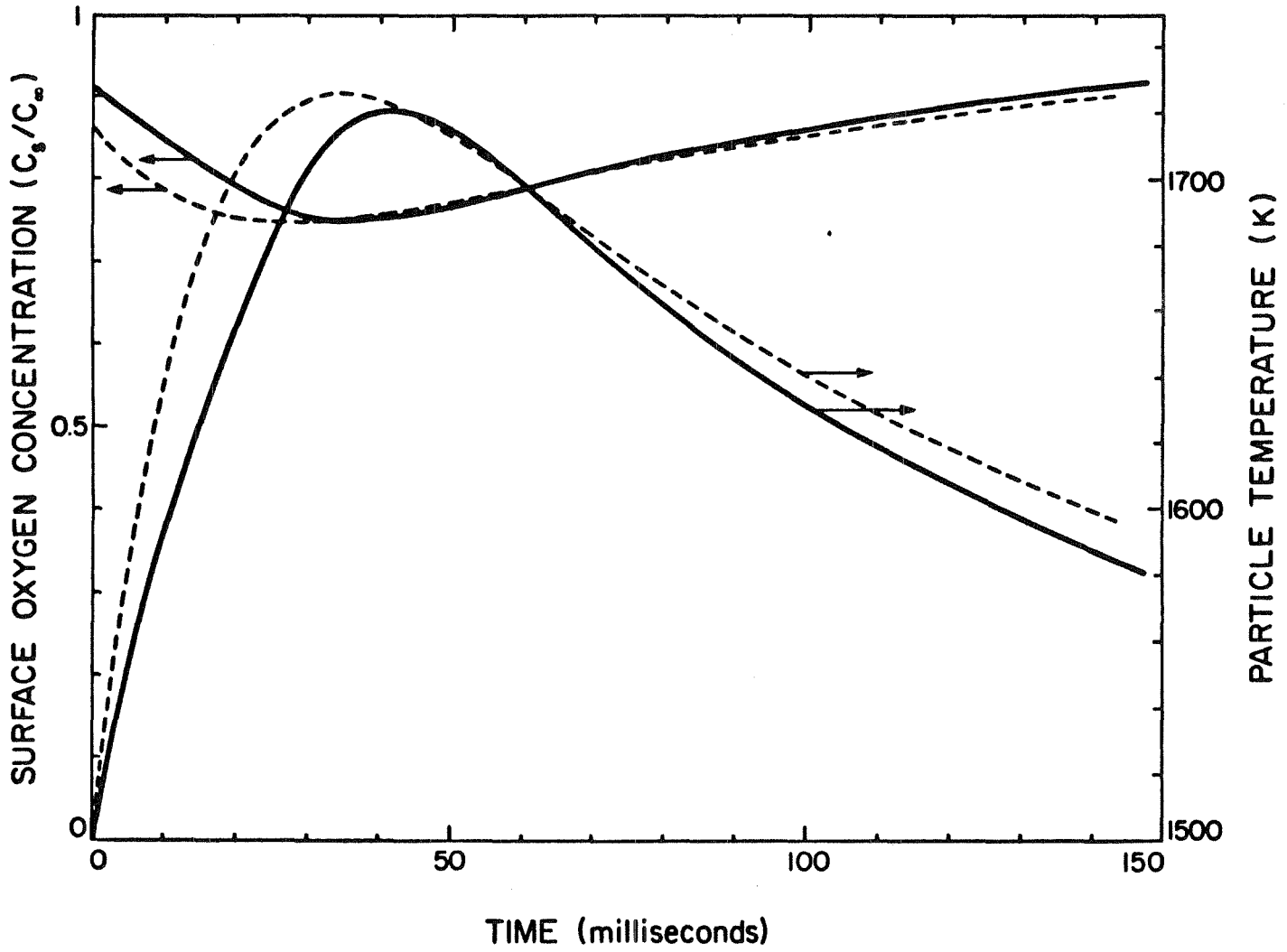

Figure 1: Histories of particle temperature and surface oxygen concentration during combustion in air with $T_\infty = 1500K$

(——): complete numerical solution; (- - - -): approximate solution.

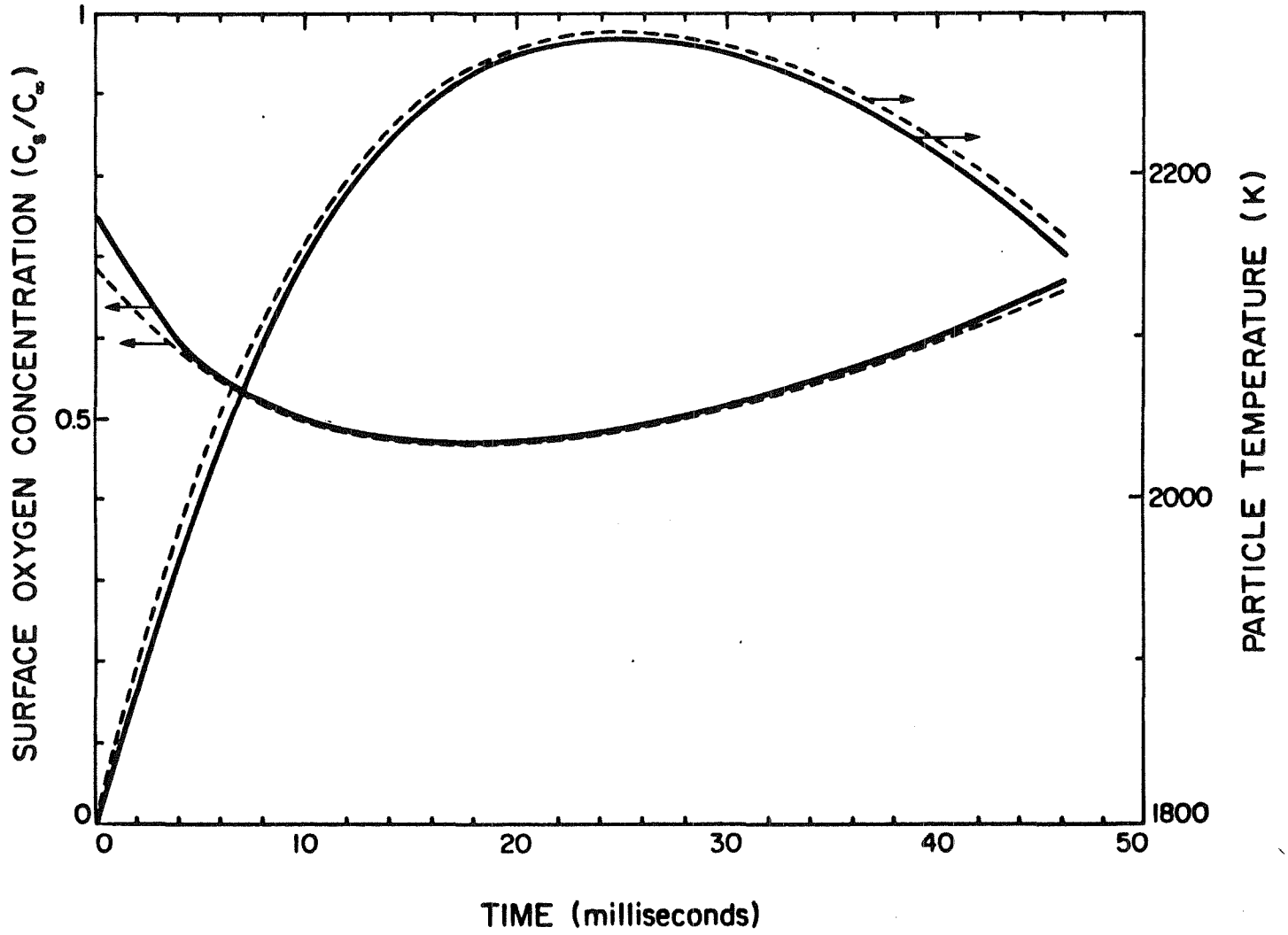

Figure 2: Histories of particle temperature and surface oxygen concentration during combustion in air with $T_\infty = 1800K$

(——): complete numerical solution; (- - - -): approximate solution.

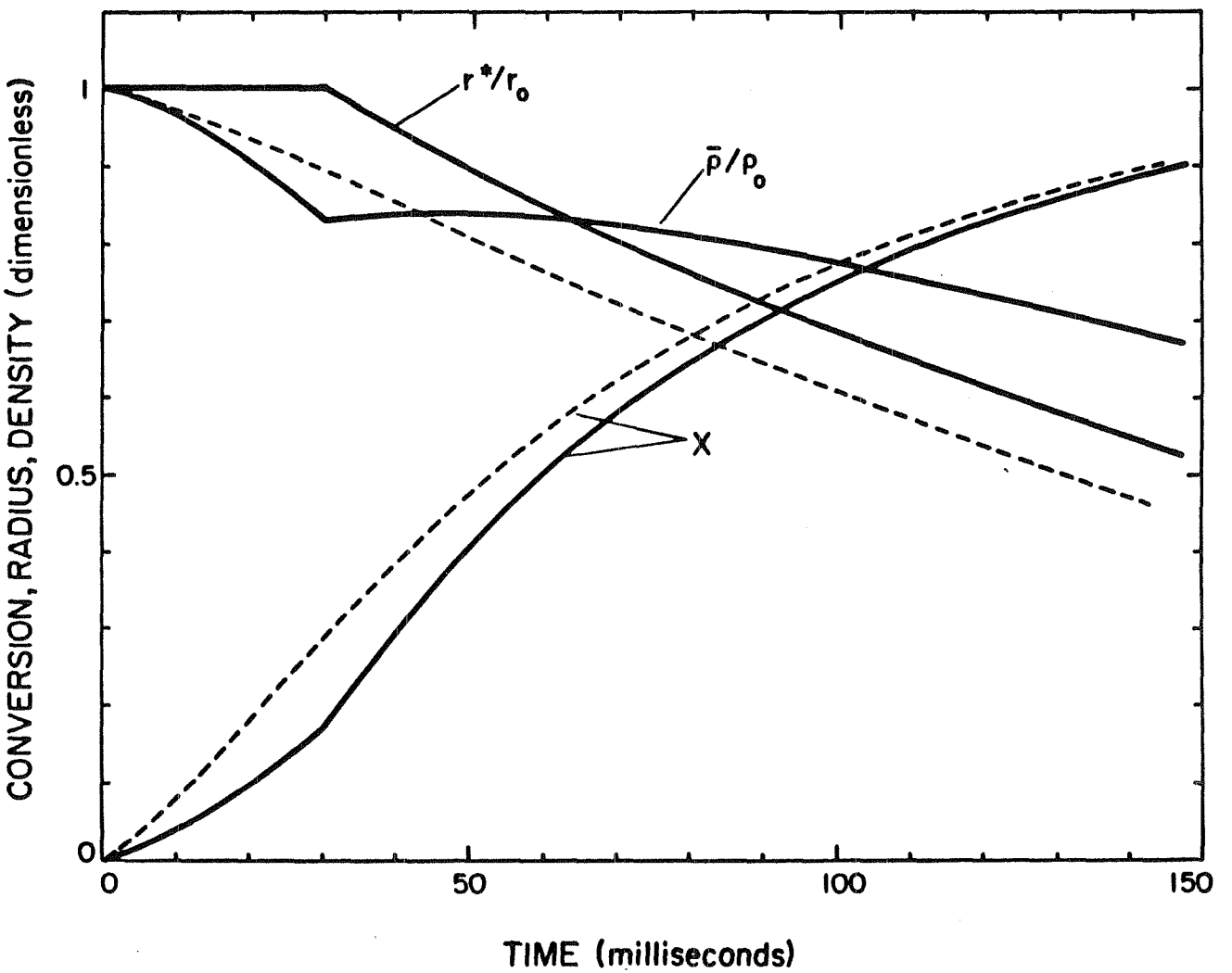

Figure 3: Particle radius, average density, and conversion versus time during combustion in air with $T_\infty = 1500K$

(——): complete numerical solution; (- - - -): approximate solution.

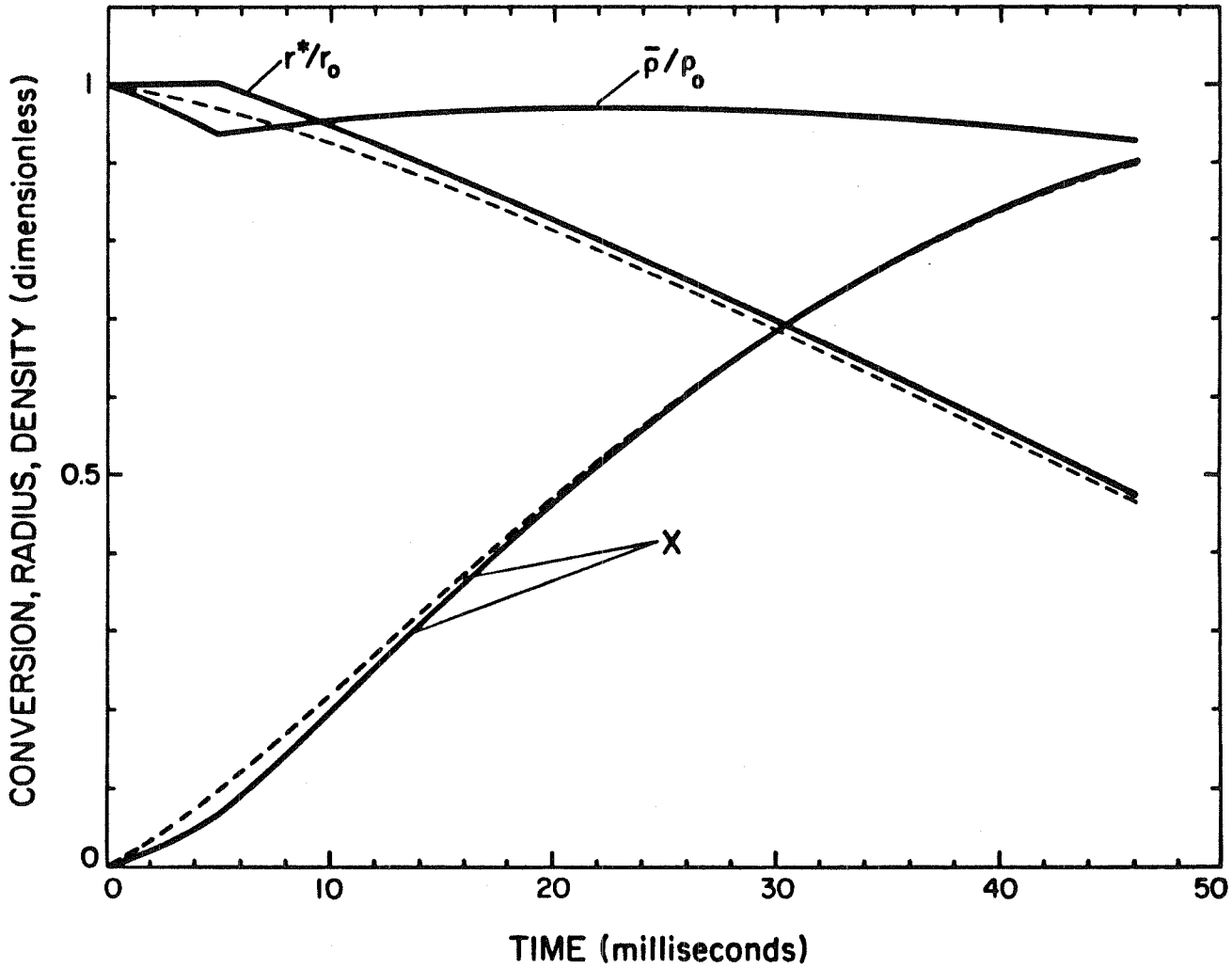

Figure 4: Particle radius, average density, and conversion versus time during combustion in air with $T_\infty = 1800K$

(——): complete numerical solution; (- - - -): approximate solution.

CHAPTER 4

Combustion Behavior and Kinetics of Synthetic and Coal-derived Chars: Comparison of Theory and Experiment

Combustion Behavior and Kinetics of Synthetic and Coal-derived Chars: Comparison of Theory and Experiment

M. Loewenberg* and Y. A. Levendis**

* Department of Chemical Engineering 206-41

** Department of Environmental Engineering Science 138-78

California Institute of Technology

Pasadena, California 91125

Abstract

A theoretical model describing the combustion of carbonaceous particles at intermediate and high temperatures has been developed and compared with experimental results. The analysis includes the effects of pore diffusion and growth, inert mineral matter, gas-phase heat and mass transfer, and treats solid spherical and cenospheric char particles. The combustion dynamics are described by time-dependent equations for particle temperature, radius, ash layer thickness and a number of intraparticle conversion variables. These are coupled to pseudosteady equations for gas-phase transport and internal reaction and diffusion. Model predictions were contrasted with combustion measurements obtained for several synthetic chars and two coal-derived chars. The synthetic chars were glassy carbons produced in the form of solid monodisperse

spheres. Cenospheric synthetic chars were also produced. All synthetic chars were mineral free. The coal-derived chars contained mineral matter and were considered spherical. In each case, apparent and intrinsic rate parameters were deduced by direct application of the combustion model to experimental data gathered under conditions of moderate to large Thiele modulus. The estimated kinetic parameters were subsequently used to generate temperature-time profiles of single burning particles. The results obtained are in good agreement with the experimentally observed behavior of the synthetic and coal-derived chars. The validity of the intrinsic rate calculation was tested by simulating the combustion behavior of particles burning in the kinetically limited (low Thiele modulus) regime.

1 Introduction

The combustion of char particles has been the subject of numerous experimental and theoretical investigations because of its obvious importance in the operation of coal combustion systems. During the last ten years experimental capabilities have been greatly expanded by the introduction of powerful optical techniques for direct measurements of temperature, size, and velocity of individual particles[1-5]. During the same period, theoretical description of particle combustion has become increasingly more sophisticated by including multicomponent diffusion and heat transfer in the gas phase and diffusion with simultaneous pore growth phenomena within the particle[6-11].

While experimental technique and theoretical analysis have both undergone significant advance, they have evolved along somewhat independent paths. To appreciate the difficulties encountered in bringing together theory and experiment we consider the determination of intrinsic rate parameters from combustion experiments. These typically include temperature, conversion, and perhaps porosimetry measurements at a few locations along a drop tube furnace. The analysis of such data by means of a particle combustion model requires treating all particles as spherical and uniform in size and properties, and using a pore model consistent with the available porosimetry data. However, the porosimetry data will not, in general, provide adequate information to determine independently the evolution of pore structure with conversion at high temperatures. Moreover, the distributions of sizes, shapes and properties of the char particles versus the identical spherical particles postulated in the analysis introduces an uncertainty that has not been evaluated as yet. In view of these difficulties and uncertainties, it is not surprising that the analysis of experimental data has not progressed rapidly since the original

work of Field and Smith (*eg.* [12,13]).

This paper describes an attempt to bring closer experiment and theory by eliminating certain experimental uncertainties and comparing with calculations that include diffusion and pore growth as well as external transport processes. The experiments include combustion tests using synthetic chars and coal chars. The use of synthetic chars consisting of monodisperse spherical particles removes the uncertainty caused by the irregular shape and variable size and properties of individual particles. The present work supplements previous work [14] through the use of a more detailed treatment of gas-phase and intraparticle transport involved in the estimation of kinetic rate parameters. Moreover, new particle types were introduced (cenospheres) and smaller size particles were investigated. Finally, the model was applied to the combustion of coal-derived char particles. The analysis consists of three steps. In the first step the apparent rate parameters are estimated from the time-averaged combustion rate by solving the heat and mass transfer equations in the gas film surrounding the particle. In the second step intrinsic parameters are estimated from the apparent parameters using a random pore model and measured physical properties. The third step consists of simulations with the complete model and a limiting form of the model appropriate to large values of the Thiele modulus. The calculated temperature-time histories are compared to the experimental histories for a broad range of particle temperatures.

2 Theory

In this section, we develop the equations describing energy and mass transport following the approach of Loewenberg *et al.*[11] Accordingly, the temperature and concentration profiles are assumed to be at steady state with respect to the dy-

namical quantities: particle conversion, temperature and radius. The temperature within the particle is assumed to be uniform. The only reaction considered is the direct oxidation of carbon to form carbon monoxide:

$$C + \frac{1}{2}O_2 = CO \tag{1}$$

The gas-phase oxidation of CO to CO_2 is assumed to occur in the free stream and therefore does not enter in the energy and material balance equations for the film. The char is treated as a continuum with a local diffusion coefficient $\delta_e(q)$ and surface area (per unit volume) $S(q)$, where $q(r,t)$ is the length by which the local surface has receded by oxidation. The structure functions, $S(q)$ and $\delta_e(q)$, are determined from given initial pore surface area and pore size distribution by means of a random pore model. The pores may be modelled as cylindrical voids[12] and/or spherical voids[11]. Pore overlap between voids of all sizes in the distribution is an implicit feature of this model.

At any given time, the state of the particle is fully defined by its temperature, T_p, radius, r_p, and radial distribution of the structural variable, $q(r)$ $(0 \leq r \leq r_p)$. The radial oxygen profile within the particle is described by the pseudosteady equation:

$$0 \leq r \leq r_p(t) \quad : \quad \frac{1}{r^2}\frac{\partial}{\partial r}\left(r^2 \delta_e(q)\frac{\partial C}{\partial r}\right) = bR_{in}(C,T_p)S(q), \tag{2}$$

subject to the boundary conditions:

$$r = r_p(t) \quad : \quad C = C_s, \qquad r = 0 \quad : \quad \frac{\partial C}{\partial r} = 0 \tag{3}$$

where the intrinsic rate $R_{in}(C,T_p)$ is independent of local conversion and is expressed as mass of carbon per unit surface area and time, thus, the stoichiometric factor, $b = 1/24$. Solution of the boundary value problem, (2) and (3) yields a relation for the mass flux at the particle surface caused by chemical reaction, F_p, which can be

expressed succinctly as:

$$F_p = G_1(C_s; T_p, r_p, q(r)) \tag{4}$$

In general, G_1 must be evaluated numerically.

The radial profiles of temperature and oxygen concentration outside the particle are governed by energy and material balances[11] pseudosteady in particle temperature and radius. The solution of these equations is simplified by assuming ternary mass transfer involving O_2, CO and "inert," the latter including N_2, and CO_2. The three binary diffusion coefficients are assumed equal but temperature dependent, as are the thermal conductivity and density of the gas-phase. Fluxes induced by thermal and pressure gradients are neglected and the gas-phase is assumed to be transparent to radiation. These assumptions permit the solution of the film equations which is presented in the appendix. In symbolic form, the pseudosteady expressions for the surface oxygen concentration and energy flux are:

$$C_s = G_2(F_p, e_p, T_p, r_p) \tag{5}$$

$$e_p = G_3(F_p, T_p, r_p) \tag{6}$$

where e_p is the energy flux resulting from conduction and enthalpy flux at the particle surface and the functions G_2 and G_3 are defined by Eqs. (A.12) and (A.13).

Eqs. (4)-(6) yield the mass and energy fluxes, and the oxygen concentration at the particle surface for given values of the time-dependent quantities: T_p, r_p, $q(r)$; it remains to derive their dynamical equations. The local structure variable satisfies[12]:

$$\frac{\partial q}{\partial t} = \frac{1}{\rho_T} R_{in}(C, T_p) \tag{7}$$

with the initial condition:

$$t = 0 \quad : \quad q = 0 \tag{8}$$

which is solved on a suitable discrete set of grid points simultaneously with the equations for r_p and T_p. The pseudosteady oxygen concentration at each grid point is given by the solution of Eqs. (2) and (3). The particle radius decreases by combustion on the pore surfaces according to equations[10]:

$$r_p(t) = r_{p0}, \quad q < q^* \tag{9}$$

$$\frac{dr_p}{dt} = -\left(\frac{\partial q/\partial t}{\partial q/\partial r}\right)_{r=r_p}, \quad q = q^* \tag{10}$$

where q^* is the value of the local structure variable at the onset of fragmentation[13,15] and is defined by: $\epsilon(q^*) = \epsilon^*$. The apparent rate (total mass flux), F_p^T, is equal to the sum of the mass flux generated by chemical reaction, F_p, and the flux of fragmented particles which is given by:

$$F_p^* = -\rho^* \frac{dr_p}{dt} \tag{11}$$

where ρ^* is the local density at the onset of fragmentation. The detached char fragments are assumed to burn in the free stream thereby not affecting the heat and mass balances.[11] We chose ϵ^* equal to 0.8 although the combustion rate is not very sensitive to the precise value.[10] If fragmentation does not occur or if char fragments are retained, *e.g.*, by an ash layer, $\epsilon^* = 1$. The fragmentation process is not sufficiently understood to be described in greater detail. The differential equation for the particle temperature derived in the appendix is:

$$m_p c_p \frac{dT_p}{dt} = 4\pi r_p(t)^2 \left[F_p \int_{T_\infty}^{T_p} c_p dT - e_p - e_R\right] \tag{12}$$

where e_R is the radiative heat transfer which is given by the Stefan-Boltzmann law.

Mineral matter is assumed to be inert and finely distributed throughout the carbonaceous matrix and forms an ash layer as combustion progresses.[16-18] The additional diffusional resistance of this layer is neglected[18,19]. A volume balance

on the mineral matter contained within the char relates the radius of the ash layer to the radius of the carbonaceous particle:

$$r_a^3 = \frac{v_a}{1-\epsilon_a}\left(r_{p0}^3 - r_p^3\right) + r_p^3 \tag{13}$$

where $1-\epsilon_a$ is the solid volume fraction within the ash layer and v_a is the volume fraction of ash within the carbonaceous phase and is given by:

$$v_a = \frac{x_{a0}\bar{\rho}_0}{\rho_a} \tag{14}$$

where x_{a0} is the measured initial mass fraction of ash, ρ_a is the density of the mineral matter, and $\bar{\rho}_0$ is the initial apparent density of the char (including ash). Although the volume fraction of ash within the particle increases with conversion, v_a is constant.

The combustion of a cenosphere that contains one or more large voids within a thin, porous shell was also modelled. Such particles are often produced by rapid devolatilization of softening coals or heavy oil droplets. In the present work, cenospheres that have a single central void can be described by the modifications of the above equations as described below. Two limiting cases were considered:

(I) Oxygen diffuses into the char solely through the external surface of the cenosphere shell; the central void is not directly accessible.

(II) The interior of the cenosphere shell "communicates" directly with the external surface through several large "blow-holes" in the cenosphere shell[20]. Oxygen penetrates the central void.

For cenospheric char, boundary condition (3) at $r = 0$ is replaced with the appropriate boundary condition at the inner cenosphere surface, $r = r_i$. In case (I), r_i is constant, but in case (II), r_i is described by equations similar to (9) and (10).

The physical and chemical properties of the char and the ambient conditions are required for modelling. An assortment of independent experimental techniques, described below, were used to determine the particle size, density, pore structure and mineral content. The composition of the gas phase is specified by the mole (volume) fraction of oxygen; the remainder is assumed inert. The ambient conditions also include the gas and wall temperatures. The initial particle temperature, T_{p0}, is taken equal to the ambient gas temperature.

The solution procedure consists of integrating the dynamical Equations (7)-(10) and (12) for the local structural variable, particle radius and particle temperature. Evaluation of the dynamical equations requires the quantities C_s, e_p and F_p, given by simultaneous solution of Eqs. (4)-(6)[11]. An important simplification results by the choice of an intrinsic rate linear in oxygen concentration. In this case, Eq. (4) is separable and becomes:

$$F_p = C_s \, \tilde{G}_1(T_p, r_p, q(r)) \tag{15}$$

In the limiting case of high Thiele modulus, the solution can be simplified drastically by exploiting a closed-form solution of the intraparticle problem[10] which eliminates the local structural variable and the corresponding dynamical equation at each grid point. The limiting solution is[10]:

$$\frac{dr_p}{dt} = -\frac{1}{b^{1/2}\rho_T}\frac{I^{1/2}}{J^{1/2}} \tag{16}$$

where $I^{1/2}$ and $J^{1/2}$ are simple quadratures which describe kinetic and physical parameters respectively:

$$I = \int_0^{C_s} R_{in}(C, T_p)dC \tag{17}$$

$$J = \int_0^{q^*} \frac{\epsilon(q) - \epsilon_0}{\delta_e(q)}dq \tag{18}$$

Then according to Eq. (11), F_p and the apparent rate, F_p^T, become:

$$F_p = \frac{\rho_0 - \rho^*}{b^{1/2}\rho_T}\frac{I^{1/2}}{J^{1/2}} \qquad \text{and} \qquad F_p^T = \frac{\rho_0}{b^{1/2}\rho_T}\frac{I^{1/2}}{J^{1/2}} \tag{19}$$

which reflects the assumption that detached char fragments burn in the free stream. According to this procedure, Eq. (5), (6) and (19) are solved for C_s, e_p and F_p and the dynamical equations are reduced to two: Eq. (16) and (12) for the particle radius and temperature.

The results of the above semi-analytical solution have been compared with those of the full numerical solution and found in fair agreement for Thiele moduli larger than 3 and excellent agreement for Thiele moduli larger than 15 [11] (based upon characteristic length, $r_p/3$). Thus, the simplified intraparticle solution procedure can be successfully employed in the regime of strong pore diffusion resistance. This will be shown again herein by comparison with the results of the full solution of Equations (4)-(10) and (12).

3 Experimental

3.1 *Experimental Methods*

The foregoing model has been used to simulate the combustion of both synthetic (glassy carbon) and coal-derived chars. Spherical glassy carbon particles of equal size have been produced, from polyfurfuryl alcohol (PFA) and pore forming agents[21]. The pore formers used in conjunction with the present study were *tannic acid, glycerol, polyethylene glycol (PEG), Triton X-100* and solid *carbon black* spheres. The particles were generated by atomization of the PFA-pore former mixtures in a thermal reactor (650 K, 4s). Different particle sizes were produced ranging from 8-100 μm in diameter. The solidified particles were subsequently carbonized at 800 K for

1 hr. The two coal chars were derived by pyrolyzing a bituminus coal (PSOC-176 HVBA) at 1200 and 1600 K, respectively in N_2 for 2 seconds.

Combustion studies were conducted in an externally heated laminar flow furnace. The wall temperatures were monitored by both a thermocouple and a brightness pyrometer, the gas temperature by a suction pyrometer and the particle temperature by a near-infrared, two-color pyrometer (800 and 1000 nm)[14]. Particle temperatures were calculated from the ratio of the signals of the two channels, applying Planck's law. Partial combustion experiments were also conducted under conditions where the particle temperatures were low. The extent of burnout in those experiments was monitored by measuring the change in the mass, size and density of the particles.

Char characterization included determination of particle size, morphology, density and pore structure as well as density and mass of mineral matter. The parameters required for the intrinsic rate were empirically determined, but the form of the intrinsic rate was chosen *a priori.*

3.2 *Experimental Results*

The various synthetic and coal-derived chars have widely different porosities and pore structures. While all synthetic chars contained micropores, only the chars containing carbon black had transitional pores. The coal-derived chars contained a broad distribution of pore sizes. The pore size distribution of the transitional- and macropores was obtained by high-pressure mercury intrusion, and the results were analyzed by means of the Washburn equation[22]. The resulting distribution was verified by application of Kelvin's equation to gas adsorption measurements. SEM microscopy was used to observe the surface morphology and the structure of the interior of the particles, by examining ground and polished sections. Plain polymer

particles and particles containing 25% carbon black are shown in Fig. 1 a,b and a cenospheric particle is shown in Fig. 2a. In Fig. 2b, a section of a partially burned particle is shown. The particle appears dense, and no porosity can be detected with the SEM. The average size of the micropores in the unoxidized chars, deduced by small-angle x-ray scattering (SAXS), was around 10Å. Corresponding BET sorption experiments indicate that most of this porosity is closed and impermeable to the outside gases. High temperature heat treatment increases pore size because of the densification of the carbon matrix. Parallel oxidation further increases pore size and removes constrictions at the pore entrances. The size of the micropores for the partially oxidized chars was determined from the BET area in conjunction with the pore volume measurements, using the random capillary model. The agreement with the SAXS results was good. The enhanced pore sizes (20-30 Å) are reported in Table I. As a result of the opening and enlarging of the pores, the N_2 BET area, measured at 77 K, increases dramatically from a few square meters per gram, for the unoxidized materials, to a few hundred square meters per gram for the partially burned materials.

Apparent densities, $\bar{\rho}$, and helium densities, ρ_T, for the synthetic chars, measured by mercury porosimetry and helium pycnometry are given in Table I. The apparent density of the synthetic chars remained almost constant (decreased slightly) in the course of combustion at mid-range temperatures (1200-1600 K), meanwhile the helium density increased substantially (by up to 50%). The fact that the carbon matrix becomes denser in the course of high-temperature combustion has also been verified by wide and small-angle scattering. Porosity values for particular intervals in the transitional and macropore region can be deduced from the mercury porosimetry data, the remaining void volume being due to micropores.

In air, the synthetic char particles burned slowly, at temperatures close to that

of the combustion chamber walls. Temperatures of clouds of particles burning under this condition were measured by both the two color and the brightness pyrometer, for the latter assuming a carbon emissivity of 0.8. At higher oxygen partial pressures, the particles ignited and burned with luminous flashes. At the 0.5 and 1.0 atm oxygen partial pressures selected for the present study all particles ignited and burned at high temperature.

To account for the opening of the pore restrictions at the early stages of combustion, the initial total area, true (helium) density, and pore sizes were taken as those of the partially burned chars at about 25% conversion. This procedure is justified for combustion under conditions of strong pore diffusion resistance in which the particle burns with nearly constant apparent density.

A coal char particle is shown in Fig. 3; the particle is irregular in shape and mineral matter inclusions are obvious. The mass fraction and composition of mineral matter (for the coal-derived chars) were obtained from ashing experiments and from elemental analysis of the ash constituents. The mass fraction of ash was found to be 8.5% and 10% for the chars obtained by pyrolysis at 1200 K and 1600 K, respectively. The composition of the ash allows calculation of its heat capacity and density. The coal chars analyzed in the present study contained mineral matter with the approximate composition: SiO_2, 46%; Fe_2O_3, 20%; Al_2O_3, 30%; CaO, 4%, which yields an ash density, $\rho_a = 3.59$ gm/cm[3].

4 Estimation of Kinetic Parameters

The form of the apparent and intrinsic rates were assumed *a priori*. Particle temperatures and apparent densities were assumed constant, as observed. The instan-

taneous rate of mass loss is given by the elementary relation:

$$\frac{dm_p}{dt} = -4\pi r_p^2 F_p^T \tag{20}$$

The apparent rate is assumed to have the separable form:

$$F_p^T = k_a(T_p) C_s^n \tag{21}$$

which is inserted into Eq. (20) and integrated under the assumption of constant apparent particle density to yield:

$$k_a(T_p) = \frac{\rho_0}{t_b} \int_{r_{p0}(1-X)^{1/3}}^{r_{p0}} \frac{dr_p}{C_s^n} \tag{22}$$

where t_b and X are the experimentally observed burnout time and conversion. Eq. (19) yields:

$$F_p = \frac{\rho_0 - \rho^*}{\rho_0} F_p^T \tag{23}$$

Under the assumption of constant particle temperature, Eq. (12) becomes:

$$\left(\frac{\rho_0 - \rho^*}{\rho_0}\right) k_a(T_p) C_s^n \int_{T_\infty}^{T_p} c_p dT - e_p - e_R = 0 \tag{24}$$

Eqs. (5) and (6) may be combined to yield the surface oxygen concentration as a function of the apparent rate constant and the instantaneous values of particle radius and temperature:

$$C_s = G_4(k_a, r_p, T_p) \tag{25}$$

Inserting this result and (6) into Eq. (24) yields the particle temperature in terms of the apparent rate constant and instantaneous particle radius:

$$T_p = G_5(k_a, r_p) \tag{26}$$

Inserting (25) and (26) into (22) yields the desired result:

$$k_a(T_p) = G_6(t_b, X, r_{p0}) \tag{27}$$

where the particle temperature, assumed constant, is taken as the arithmetic mean value within the integrand of (22). Thus, according to this approach, each particle temperature history yields a pair: (k_a, T_p) in terms of the burnout time, conversion and initial particle radius. An Arrhenius-type plot of the pairs, (k_a, T_p), yields estimates of the observed apparent activation energy, E_a, and pre-exponential factor, A_a. The apparent reaction order, n, can be determined, in principle, from rate measurements at constant particle temperature and different ambient oxygen concentrations. However, first-order kinetics were assumed throughout.

The assumption of constant apparent particle density allows the use of the simplified model defined by Eqs. (16)-(19). For an intrinsic rate given by a power law model[23] $R_{in} = k_{in}(T_p)C^m$ Eq. (19) yields:

$$F_p^T = \frac{\rho_0}{b^{1/2}\rho_T J^{1/2}} \sqrt{\frac{k_{in}(T_p)C_s^{m+1}}{m+1}} \tag{28}$$

where J is depends only physical parameters. Comparing (28) with (21) yields relations for the intrinsic rate parameters in terms of the apparent parameters:

$$E_{in} = 2E_a \tag{29}$$

$$m = 2n - 1 \tag{30}$$

$$A_{in} = 2nbJ \left(\frac{\rho_T A_a}{\rho_0} \right)^2 \tag{31}$$

The foregoing approach is valid only in the case where small variations in particle temperature are observed. In cases where the particle temperature varies significantly during combustion, the approach of obtaining a pair: (k_a, T_p) from each particle temperature history should not be applied. In such cases, a trial and error procedure must be performed to determine $k_a(T_p)$ such that error between predicted and observed particle temperature histories is globally minimized on a large set of combustion data. The present approach, when valid, is more direct and greatly

simplifies the computations required to determine the estimated rate parameters.

5 Results and Discussion

Arrhenius plots of the apparent and the intrinsic rates, calculated as outlined above, are shown in Figs. 4 and 5, respectively, for selected synthetic chars and the two coal-derived chars. The apparent rates calculated by the present method are in good agreement (within a factor of two) with rates estimated elsewhere[14] for some of the materials examined herein. The approach used in that work does not account for the temperature dependence of transport coefficients and thermodynamic properties of the gas-phase.

Intrinsic activation energies are in the range of 32 to 37 kcal/mol for the synthetic chars, and about 47 kcal/mol for the coal-derived chars. The solid line in Fig. 5 corresponds to Smith's best-fit line for a variety of coal chars[24]. The intrinsic reaction constants calculated in this study fall below Smith's curve which can be attributed to a combination of two factors: lower reactivity of the present materials and, the inherent differences between the two methods. To address the latter issue, a comparison was made between intrinsic rates estimated by both methods for the same materials. This comparison revealed that the intrinsic rates estimated by the present method are 2-3 times lower than those predicted by Smith's method at low temperatures, and 4-5 times lower at higher temperatures. The prediction of lower intrinsic rates using a random pore model has been explained as a consequence of pore enlargement which produces a larger pore surface area and diffusion coefficient in the "reaction zone."[10] A comparison between the apparent and the intrinsic rates reveals that the coal-chars, although apparently more reactive because of their enhanced macropore network, seem to be intrinsically less reactive.

Using the intrinsic rate constants of Fig. 5 and properties listed in Table I, temperature-time profiles for chars oxidized under various conditions were obtained. At the high particle temperatures encountered under most conditions investigated, estimates of the Thiele modulus (based upon average pore structure and particle temperature) were high (100-130 for synthetic chars and 15-20 for coal-derived chars). Thus, application of the simplified intraparticle model (Eq. 19) was justified. At these high values of the Thiele modulus particle combustion occurs with constant apparent density and monotonically decreasing radius.

To reproduce the observed initial sharp increase in particle temperature exhibited by the synthetic chars under oxygen-rich conditions, it was necessary to take into account the combustion of residual volatile matter in these chars. Pyrolysis at 1600 K resulted in mass loss up to 10% [14] on an estimated time scale of 1 ms. Further evidence for the existence of volatile material is given by high heating values (calorimetry) in comparison to pure carbon, and the existence of H_2 and O_2 (elemental analysis). At high oxygen concentrations, the volatiles may burn near the particle surface and cause significant influence upon particle ignition by inducing rapid heatup. At lower O_2 concentrations, the residual volatile matter did not ignite. The coal chars were assumed volatile-free because of their previous high-temperature pyrolysis.

Figures 6a and 7a show the experimental (dotted) and the theoretical (solid) temperature histories for PFA particles and particles formed from 50% Tannic acid and 50% PFA, respectively. Figures 6b and 7b show the conversion and normalized values for surface oxygen concentration and particle radius versus time. The particles had a diameter of 45 μm and were burned in pure oxygen at a wall temperature, T_W, of 1500 K and a free-stream gas temperature, T_∞, of 1400 K.

The steep rise in particle temperature and decrease in surface oxygen concen-

tration within the first 1-2 milliseconds predicted by the model reflects the assumed combustion of volatiles at the particle surface and is consistent with the observed behavior. After the initial heatup period, the theoretical temperature and surface oxygen profiles are relatively flat. Film diffusion is important but not rate-controlling. Figures 6b and 7b indicate that experimental extinction occurs at about 85% theoretical conversion when the normalized particle radius is 53% of its initial value. Extinction may be caused by the increased convective heat losses accompanying the decrease in particle size.

Figures 8a and b show the combustion of 45 μm glassy carbon particles containing 25% carbon black (O_2, T_W = 1450 K, T_∞=1350 K). These particles burn more quickly and at higher temperatures, and exhibit a sharper initial temperature rise than those described above because of their lower density and the presence of transitional pores which facilitate intraparticle diffusion. The calculated and measured extinction times nearly coincide in this case.

Model predictions and experimental traces for synthetic char cenospheres are shown in Figs. 9a and b (O_2, T_W=1500 K, T_∞=1400 K). The particles have an outer diameter of $\approx$ 114 μm and wall thickness of $3 - 5\mu$m. The same kinetic parameter values as obtained for the solid particles of the same composition were used to simulate combustion of the cenospheres. The solid line in Fig. 9a corresponds to case (I), explained earlier, where oxygen diffuses into the char through the external surface only, and the dashed line corresponds to case (II) where oxygen diffuses into the char through both shell surfaces. The experimental curves clearly favor case (I), suggesting that depletion by the oxidation reaction effectively shields the central void from oxygen penetration under the particular experimental conditions.

Figure 9b displays particle conversion, as well as normalized values for surface concentration and shell thickness $(r_p - r_i)/(r_{p0} - r_{i0})$; these quantities are presented

only for case (I). Particle size is essentially constant during the combustion process, hence, neither convective heat losses nor film diffusion are appreciably enhanced with burnoff thereby explaining the plateaus in particle temperature and surface oxygen concentration. This reasoning suggests that the cenospheres burn in a luminous mode throughout their history thus explaining the coincidence of experimental extinction and theoretical burnout.

The combustion of the coal chars PSOC-176 pyrolyzed at 1600 and 1200 K are shown in Figs. 10 and 11 (50% O_2, T_W=1500 K, T_∞=1400 K). The calculated curves were obtained by treating the particles as spherical, with 50 μm diameter. Considerable variability is observed among the measured traces as expected from variations in size, shape and properties of individual particles. The calculated curve lies within the range of the measured traces in terms of temperature and burnout time. Figures 10b and 11b include and additional curve showing the ratio of ash layer thickness to particle radius, $(r_a - r_p)/r_p$.

Synthetic chars (solid spheres) burning in air exhibit particle temperatures between the gas and wall temperatures yielding estimates for the Thiele modulus in the range 3-6 thus allowing deeper oxygen penetration than under the conditions investigated above. Therefore, decreasing particle density is expected to accompany combustion. To describe combustion behavior under these conditions and to justify the earlier use of the simplified intraparticle model, the full intraparticle solution (Eq. (5)) is implemented (solid curves) and compared with the approximate solution (dashed curves) in Figures 12 and 13. In both cases, the surface oxygen concentration was predicted to be within 1% of the ambient value and, thence, is not shown. Film diffusion is fast.

Figures 12 and 13 depict the behavior of a synthetic char particle burning in air with T_∞=1450 K, T_W=1500 K; and T_∞=1350 K, T_W=1400 K, respectively. The

simplified solution necessarily predicts constant density and monotonically decreasing radius while the full solution predicts decreasing density with constant radius initially followed by shrinking-core combustion. The discrepancy between the two solutions is most pronounced at lower temperatures (Fig. 13) but both correctly predict the observed particle temperatures and conversion after 2 s, the residence time in the combustor. These results support the application of the simplified intraparticle model to simulations at higher particle temperatures. The kinks in the particle radius and density profiles (Figs. 12 and 13) reflect the tacit assumption in the full intraparticle model that the char fragments upon reaching a prescribed local void volume, ϵ^* exactly equal to 0.8[11].

The combustion behavior of all chars described in Table I, burning at various combustor (wall) temperatures (1300 K - 1600 K) and different ambient oxygen concentrations (air, 50%, 100%), were simulated by the model with qualitatively similar results, although only selected cases have been shown for the sake of brevity.

The general fidelity with which temperature profiles were reproduced in the foregoing examples demonstrates some degree of accuracy in the determination of apparent reaction rates but not intrinsic parameters. This point is illustrated by application of the model (case (I)) to cenosphere combustion behavior. In this case, intrinsic rate parameters were determined from solid particles of the same material; however, both particles (solid and hollow) have similar pore structure and burn under conditions of high Thiele modulus. Therefore, this test cannot be used to access the method by which intrinsic rate parameters are estimated but it does provide support for the apparent rate determinations.

Comparison between experimental results and model predictions under a variety of conditions which affect intraparticle transport is required to test the estimated intrinsic kinetic parameters. This would demonstrate that indeed the intrinsic pa-

rameters are a chemical property of the material and, thus, are independent of pore structure and evolution. Such a test was achieved by using the intrinsic activation energy and pre-exponential factor previously determined for a particle burning under conditions of high Thiele modulus to describe the combustion of a particle with identical material and pore structure under conditions of low diffusional resistance.

Combustion parameters for 8 μm diameter PFA particles are depicted in Fig. 14 The particles burned slowly in air at particle temperatures approximately equal to the gas (T_W = 1400 K, T_∞ = 1350 K; and T_W = 1300 K, T_∞ = 1250 K). To obtain the profiles of these parameters, the intrinsic rate previously derived from the 45 μm particles was employed. The model satisfactorily predicted the experimentally observed conversion (at the end of the 2 s. residence time in the furnace). The average Thiele modulus during combustion was small (less than unity) consistent with the model predictions of continuously decreasing apparent density and nearly constant size. The foregoing example supports the present model of intraparticle transport which was used to infer intrinsic rate parameters from apparent rate data.

6 Conclusions

The intrinsic and apparent kinetic parameters of several synthetic chars and two coal chars were deduced by a simple analysis of time-temperature traces of individual particles, measured by two-color pyrometry. Estimated intrinsic parameters were then used in a detailed particle combustion model to calculate complete temperature-time histories of burning particles. Measured and calculated temperature profiles were found in good agreement for the the synthetic char particles. The experimental temperatures of the coal char particles exhibited considerable particle-to-particle variation and could only be described approximately by the calculated

temperatures corresponding to nominal particle properties.

Under most conditions employed in the experiments, the Thiele modulus was in the range of 50-200 and a limiting form of the combustion model represented the data very well. Even at values of the Thiele modulus as low as 10, the limiting calculations were in good agreement with the complete calculations and the experimental results. It is concluded that the limiting form of the model is sufficient under most conditions. At temperatures above 2000 K, the intrinsic rates of all chars examined varied by less than a factor of two. The kinetic parameters determined from experiments conducted at moderate to high Thiele modulus conditions were applied to simulate the combustion behavior of particles burning under kinetic control. The results support the procedure by which intrinsic rate parameters were deduced.

7 Acknowledgements

This work was supported by DOE Office of Energy Utilization Research, ECUT Program and by the DOE University Coal Programs Grant Number DE-FG22-84PC70775. The authors are indebted to G. R. Gavalas and R. C. Flagan for valuable comments and discussions in all aspects of this work.

8 Notation

SYMBOL	DESCRIPTION	UNITS
A_a	apparent pre-exponential factor	g/cm^2 s (atm)^n
A_{in}	intrinsic pre-exponential factor	g/cm^2 s (atm)^m
b	stoichiometric coefficient	(=1/24)
C	oxygen concentration	atm
C_s	oxygen concentration at particle surface	atm
c_p	average specific heat capacity of particle	cal/g K
$\tilde{c}_p$	molar heat capacity of particle	cal/mole K
D	gas phase diffusion coefficient	cm^2/s
e_p	energy flux by conduction and enthalpy flow	cal/cm^2 s
e_R	radiative energy flux	cal/cm^{2}s
E_a	apparent activation energy	kcal/g
E_{in}	intrinsic activation energy	kcal/g
f	total molar flux	moles/cm^2 s
f_i	molar flux of ith component	moles/cm^2 s
F_p^T	total mass flux; apparent rate	g/cm^2 s
F_p	mass flux due to reaction at particle surface	g/cm^2 s
F_p^*	fragmentation flux at particle surface	g/cm^2 s
$\tilde{H}_i$	molar enthalpy of ith species	cal/mole
$\Delta\tilde{H}$	molar heat of reaction	cal/mole
k_a	apparent rate coefficient	g/cm^2 s (atm)^n
k_{in}	intrinsic rate coefficient	g/cm^2 s (atm)^m
m	intrinsic reaction order	
m_p	particle mass	g

n	apparent reaction order	
q	local structural variable	cm
q^*	value of q at critical porosity, ϵ^*	
r	radial position	cm
r_a	instantaneous ash radius	cm
r_i	instantaneous inner shell radius (cenosphere)	cm
r_p	instantaneous particle radius	cm
R_{in}	intrinsic reaction rate	gm/cm^2 s (atm)^m
S	pore surface area per volume	cm^{-1}
T_p	particle temperature	K
T_W	wall temperature	K
t	time	s
t_b	burnout time	s
$\bar{U}$	specific internal energy of carbon	cal/mole
v_a	volume fraction of ash in carbon matrix	
V_p	particle volume	cm^3
X	conversion	
x_a	mass fraction of minerals	
y_i	mole fraction of ith	
δ_e	effective intraparticle diffusion coefficient	cm^2/s
ϵ	total porosity	
ϵ_a	volume fraction of ash in carbon matrix	
ϵ^*	critical porosity	
ρ	particle density	g/cm^3
$\bar{\rho}$	average particle density	g/cm^3
ρ_a	density of ash	g/cm^3

ρ^*	particle density at critical porosity	g/cm^3
ρ_T	true carbonaceous density	g/cm^3

SYMBOL	DESCRIPTION
SUBSCRIPTS	
p	at particle surface
0	initial value
∞	at ambient conditions

9 References

1. McLean, W. J., Hardesty, R. D. and Pohl, J. H. *Eighteen Symp. (Int.) on Combustion,* The Combustion Institute, Pittsburgh, PA. p.1239 (1981).

2. Mitchell, R. E., McLean, W. J. Nineteenth Symposium (International) on Combustion. The Combustion Institute, Pittsburgh, PA. p.1113 (1982).

3. Timothy, L. D., Sarofim, A. F. and Beér, J. M. *Nineteenth Symp. (Int.) on Combustion.* The Combustion Institute, Pittsburgh, PA. p.1123 (1982).

4. Jorgensen, F. R. A. and Zuiderwyk, M. J. *J. Phys. E: Sci. Instrum.* 18:486 (1985).

5. Levendis Y. A. and Flagan R. C. *Comb. Sci. Tech.* 53:117 (1987).

6. Libby, P.A., and Blake, T.R. *Comb. Flame* 36:139 (1979).

7. Sundaresan, S. and Amundson, N.R. *Ind. Eng. Chem. Fund.* 19:344 (1980).

8. Sotirchos, S.V., and Amundson, N.R. *Ind. Eng. Chem. Fund.* 23:191 (1984b).

9. Sotirchos, S.V., and Amundson, N.R. *A.I.Ch.E.Jl.* 30:549 (1984d).

10. Gavalas, G.R. *Comb. Sci. Tech.* 24:197 (1981).

11. Loewenberg, M., Bellan, J. and Gavalas, G. R. *Chem. Eng. Comm.* 58:89 (1987).

12. Gavalas, G.R. *A.I.Ch.E.Jl.* 26:577 (1980).

13. Dutta, S.,Wen, C.Y., and Belt, R.J. *Ind. Eng. Chem., Process Des. Dev.* 16:20 (1977).

14. Levendis Y. A., Flagan R. C. and Gavalas G. R. submitted to Comb. and Flame.

15. Kerstein, A.R., and Niksa, S. *Twentieth Symp. (Int.) on Combustion.* The Combustion Institute, Pittsburgh, PA. p.941 (1984).

16. Sarofim. A. F., Howard, J. B., and Padia, A. S. *Comb. Sci. Tech.* 60:187 (1977).

17. Hamblen, D. G., Solomon, P. R., Hobbs, R. H.: *Physical and Chemical Characterization of Coal*, EPA Report No. EPA-600/7-80-106, 1980.

18. Northrop P.S.: (1987), personal communication.

19. Senior, C. Y. "Submicron Aerosol Formation During Combustion of Pulverized Coal." Ph.D. Thesis, Caltech, 1984.

20. Gavalas, G.R., Loewenberg, M.,Bellan, J. and Clayton, M. Paper presented at the annual A.I.Ch.E. meeting, Chicago, November 10-15, 1985.

21. Levendis Y. A. and Flagan R. C. Submitted to Carbon.

22. Scholten, J. J.: From Porous Carbon Solids (R. L. Bond, Ed.), Academic Press, p.225, 1967.

23. Smith, I. W., and Tyler, R. J. *Comb. Sci. Tech.* 9:87 (1974).

24. Smith, I.W. *Nineteenth Symp. (Int.) on Combustion.* The Combustion Institute, Pittsburgh, PA. p.1045, 1982.

10 Appendix

Analysis of Gas-Phase Transport

In this appendix, we develop the pseudo-steady equations describing gas-phase transport and in particular, we derive Eqs. (5), (6) and (12). Although this material may be found elsewhere[11], a self-contained development is useful. In the first subsection, we derive algebraic expressions for the pseudosteady mass and energy fluxes evaluated at the particle surface (Eqs. 5 and 6 in section 2). In the second subsection, we derive the energy equation (Eq. 12 in section 2). The previous derivation[11] is considerably simplified through the use of gas-phase concentrations expressed in mole fractions rather than mass fractions.

10.1 *Pseudosteady Mass and Energy Fluxes*

Denoting by y_i and f_i the mole fraction and molar flux of the i$^{\text{th}}$ component (O_2:i=1, CO:i=2, inert:i=3), we can write the pseudosteady component balances as:

$$r^2 f_i = r_p^2 f_{ip} \tag{A.1}$$

where f_{ip} denotes the molar flux of the i^{th} component at the particle surface. The fluxes, f_i are related by the Stefan-Maxwell equations, which under the assumptions made earlier, simplify to:

$$f_i = -\rho(T) D(T) \frac{dy_i}{dr} + f y_i \tag{A.2}$$

where $f = \sum_{i=1}^{3} f_i$. The stoichiometry of Eq. (1) yields:

$$f_{3p} = 0, \quad f_{1p} = -f_p, \quad f_{2p} = 2f_p \tag{A.3}$$

which are related to the mass fluxes:

$$F_i = M_i f_i, \qquad F = 24 f \tag{A.4}$$

where F_i is the mass flux of the ith-species of molecular weight M_i and $F = \sum_{i=1}^{3} F_i$. Combining (A.1)-(A.3) yields the balance for oxygen (i = 1):

$$r^2 \rho(T) D(T) \frac{dy_1}{dr} = r_p^2 f_p (y_1 + 1) \tag{A.5}$$

The pseudosteady energy equation for a gas transparent to radiation is:

$$r^2 \left[-\lambda(T) \frac{dT}{dr} + \sum_i f_i \tilde{H}_i(T) \right] = r_p^2 e_p \tag{A.6}$$

$$e_p = \left[-\lambda(T) \frac{dT}{dr} + \sum_i f_i \tilde{H}_i(T) \right]_{r=r(t)} \tag{A.7}$$

By using Eqs. (A.1) and (A.3), we rewrite (A.6) as:

$$r^2 \lambda(T) \frac{dT}{dr} = r_p^2 \left[h(T) f_p - e_p \right] \tag{A.8}$$

with boundary conditions:

$$r = r_p \ : \ T = T_p; \qquad r \to \infty \ : \ T \to T_\infty$$

where h(T) is given by:

$$h(T) = \left[2\tilde{H}_2(T) - \tilde{H}_1(T) \right] \tag{A.9}$$

We divide Eq. (A.4) by Eq. (A.8) to obtain:

$$\frac{\rho(T) D(T)}{\lambda(T)} \frac{dy_1}{dT} = \frac{y_1 + 1}{h(T) - \gamma_p} \tag{A.10}$$

$$T = T_\infty \ : \ y_{1\infty}$$

where γ_p is the ratio of energy flux to mass flux:

$$\gamma_p = \frac{e_p}{f_p} \tag{A.11}$$

Integrating Eqs. (A.8) and (A.10) yields, respectively:

$$\int_{T_\infty}^{T_p} \frac{\lambda(T) dT}{\gamma_p - h(T)} = r_p f_p \tag{A.12}$$

$$\ln\left(\frac{y_{1\infty}+1}{y_{1p}+1}\right)=\int_{T_\infty}^{T_p}\frac{\lambda(T)}{\rho(T)D(T)}\,\frac{dT}{\gamma_p-h(T)} \qquad (A.13)$$

Eqs. (A.12) and (A.13) are the algebraic expressions for the mass and energy fluxes at the particle surface.

10.2 *Energy Equation*

The particle energy balance can be written as:

$$\frac{d}{dt}\int_{V_p}\rho\bar{U}\,dV_p=-4\pi r_p^2(e_p+e_R) \qquad (A.14)$$

where $e_R=\sigma(\varepsilon_p {T_p}^4-\varepsilon_\infty {T_\infty}^4)$ is the radiative flux. In view of the assumed uniform intraparticle temperature profile:

$$m_p\tilde{c}_p\frac{dT_p}{dt}=4\pi r_p^2\left[f_p\tilde{H}_c(T_p)-f_p\gamma_p-e_R\right] \qquad (A.15)$$

having made the additional approximation: $c_v\simeq c_p$. The reference states for the enthalpies are chosen as:

$$\tilde{H}_1(T_\infty)=0, \qquad \tilde{H}_c(T_\infty)=0$$

which implies:

$$\tilde{H}_2(T)=\Delta\tilde{H}(T_\infty)$$

where $\Delta\tilde{H}$ is the heat of reaction (1). Thus, the quantity $h(T)$ defined by Eq. (A.9) is given by :

$$h(T)=\left[\Delta\tilde{H}(T_\infty)+\int_{T_\infty}^{T_p}(\tilde{c}_{p_2}-\frac{1}{2}\tilde{c}_{p_1})dT\right] \qquad (A.16)$$

and the energy equation (A.15) becomes:

$$m_p\tilde{c}_p\frac{dT_p}{dt}=4\pi r_p^2\left[f_p\int_{T_\infty}^{T_p}\tilde{c}_p dT-f_p\gamma_p-e_R\right] \qquad (A.17)$$

11 List of Figures

9. Combustion parameters for 114 μm cenospheric particles formed from 50% tannic acid and 50% PFA burning in O_2 at a T_W of 1500 K. (a) temperature-time profile, model: case (I) solid line, case(II) dashed line; experiments: dotted line. (b) burnout, relative surface oxygen concentration and relative radius vs. time.

10. Combustion parameters for 50 μm PSOC-176 coal-char particles (1600 K pyrolysis) burning in O_2 at a T_W of 1500 K. (a) temperature-time profile, model: solid line, experiments: dotted line. (b) burnout, relative surface oxygen concentration, relative particle radius and relative ash layer thickness vs. time.

11. Combustion parameters for 50 μm PSOC-176 coal-char particles (1200 K pyrolysis) burning in O_2 at a T_W of 1500 K. (a) temperature-time profile, model: solid line, experiments: dotted line. (b) burnout, relative surface oxygen concentration, relative particle radius and relative ash layer thickness vs. time.

12. Combustion parameters for 45 μm solid particles formed from 50% tannic acid - 50% PFA burning in air at a T_W of 1500 K Temperature-time profile, burnout, surface oxygen concentration, relative radius and apparent density vs. time; complete model: solid line, simplified model: dotted line.

13. Combustion parameters for 45 μm solid particles formed from 50% tannic acid - 50% PFA burning in air at a T_W of 1400 K. Temperature-time profile, burnout, surface oxygen concentration, relative radius and apparent density vs. time; complete model: solid line, simplified model: dotted line.

14. Combustion parameters for 8 μm solid PFA particles burning in air at a T_W of (a) 1400 K and (b) 1300 K. Temperature-time profile, burnout, surface oxygen concentration, relative radius and apparent density vs. time. (Temperature increments are 100 K.)

TABLE I

Physical Properties of Synthetic Chars

CHAR	Apparent Density g/cm^3	Helium Density g/cm^3	Porosity Mic-Trans-Mac %	BET area m^2	Pore Radius Mic-Trans-Mac Å	Heating Value cal/g
Plain Polymer	1.25	1.69	26 - 1 - 1	400	11-100-1000	8160
Plain Polymer + 18% Tan.Acid	1.33	1.85	26 - 1 - 1	420	12-100-1000	7706
Plain Polymer + 50% Tan.Acid	1.37	1.96	28 - 1 - 1	320	13-100-1000	7655
Plain Polymer + 18% PEG	1.17	1.80	30 - 1 - 1	430	18-100-1000	8184
Plain Polymer + 35% Glycerol + 7% Triton	1.26	1.80	33 - 1 - 1	620	14-100-1000	8534
Plain Polymer + 25% CarbonBlack	0.88	1.70	22 - 25 - 1	360	11-75-1000	7900
Plain Polymer + 50% Tan.Acid 'Cenospheres'	0.65	2.0	26 -.5 -.5	300	12-100-1000	7690
PSOC-176 1600 K char	0.76	1.85	30 - 12 - 20	350	10-250-1000	7250 Ash free
PSOD-176 1400 K char	0.65	1.80	28 - 1 - 27	450	10-100-1000	7800 Ash free

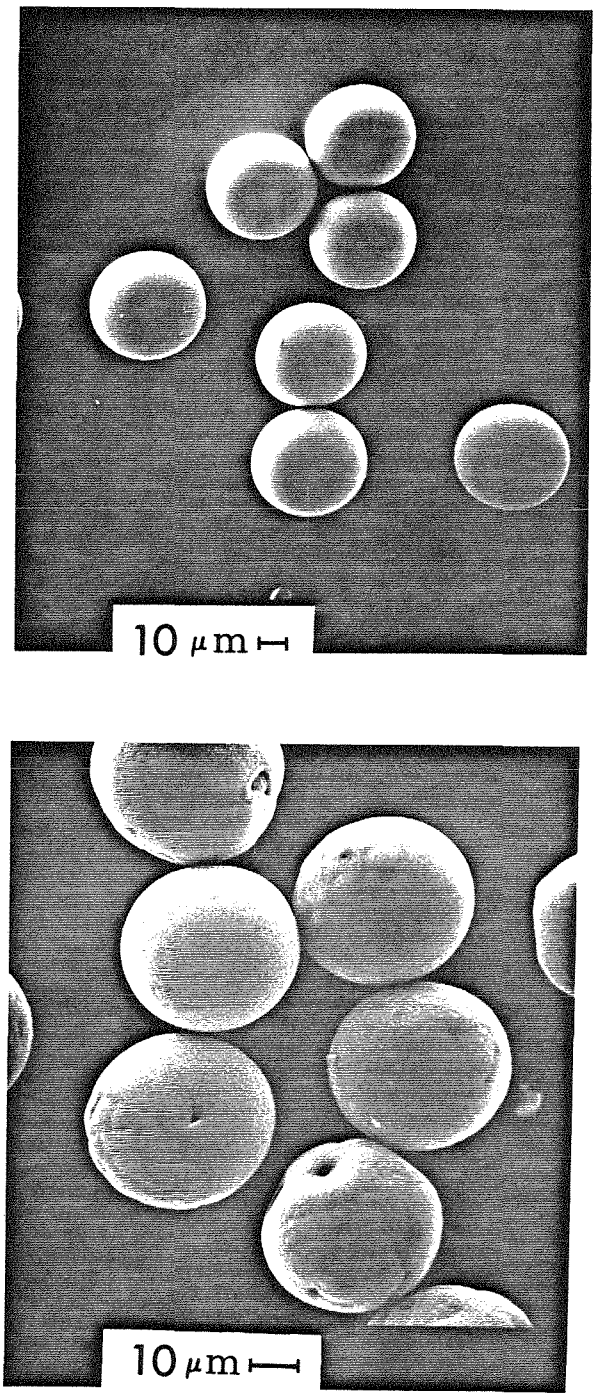

Figure 1: SEM micrographs of solid synthetic particles: (a) plain polymer (PFA) (b) PFA with 25% carbon black.

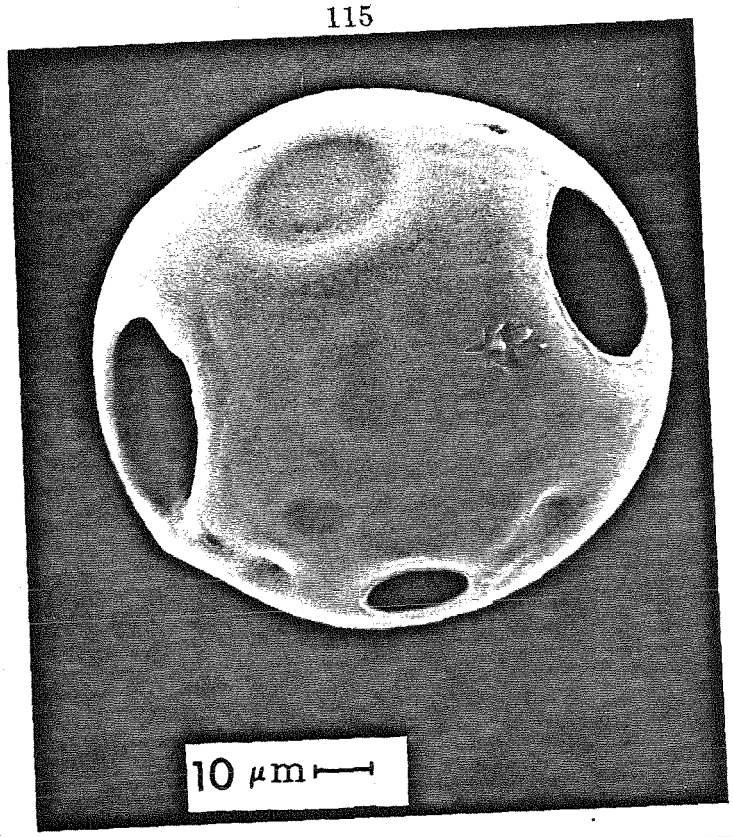

a

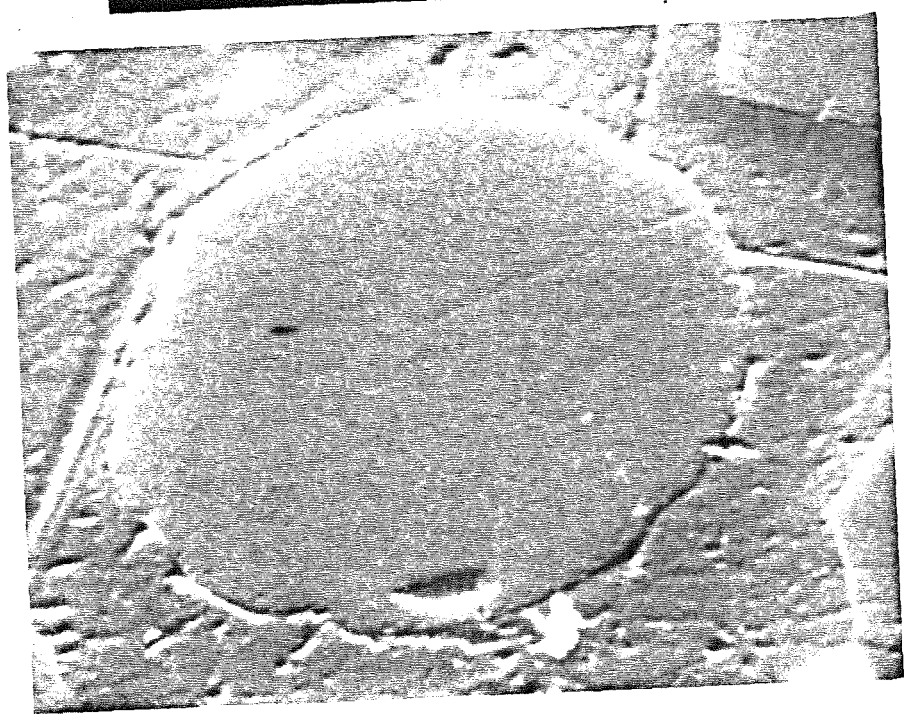

b

Figure 2: SEM micrographs of: (a) a cenospheric particle
(b) a section through a partially burned PFA particle.

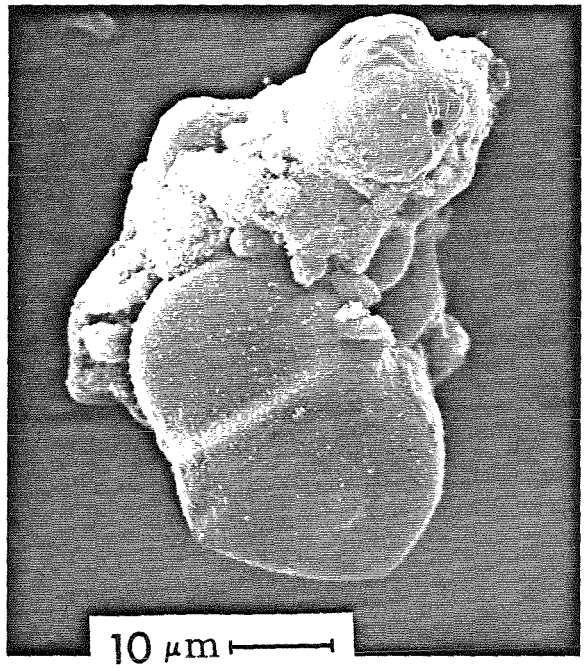

Figure 3: SEM micrograph of PSOC-176 coal-char particle pyrolyzed at 1600 K.

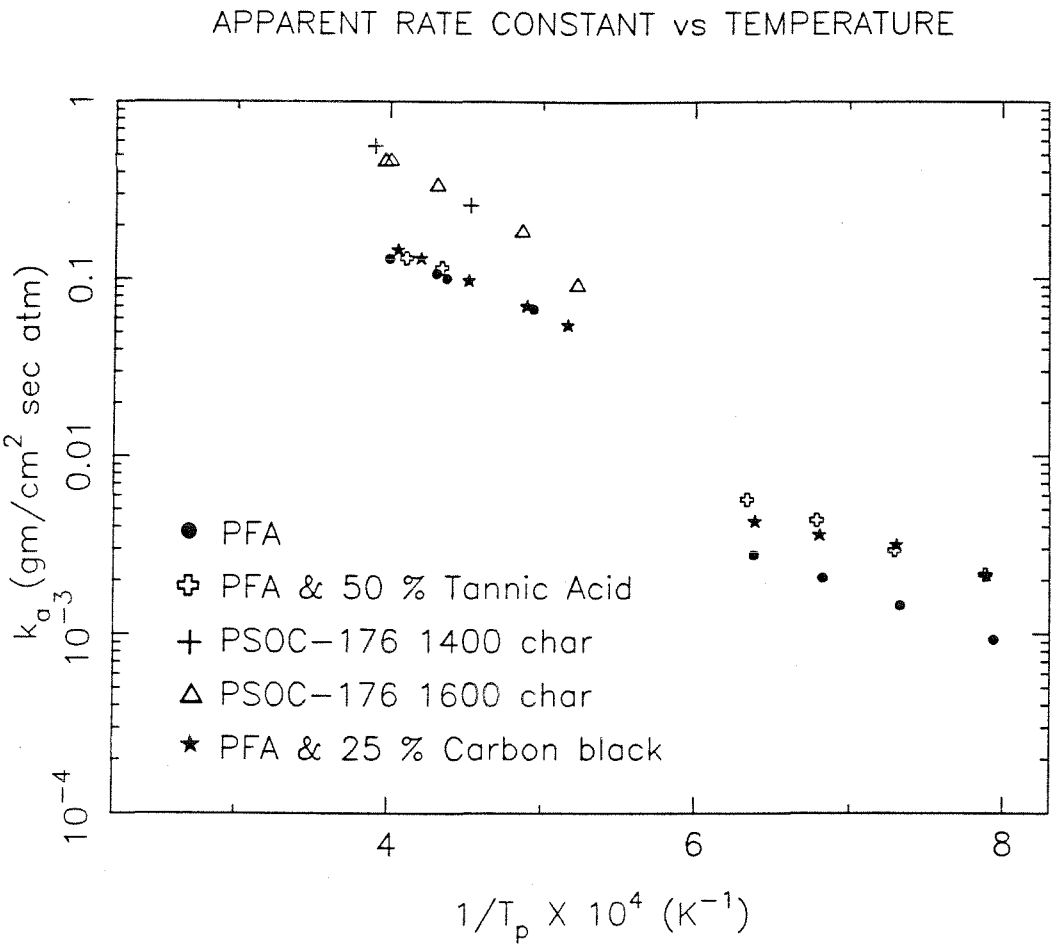

Figure 4: Arrhenius-type plot of the apparent reaction rate coefficient vs. the inverse of particle temperature.

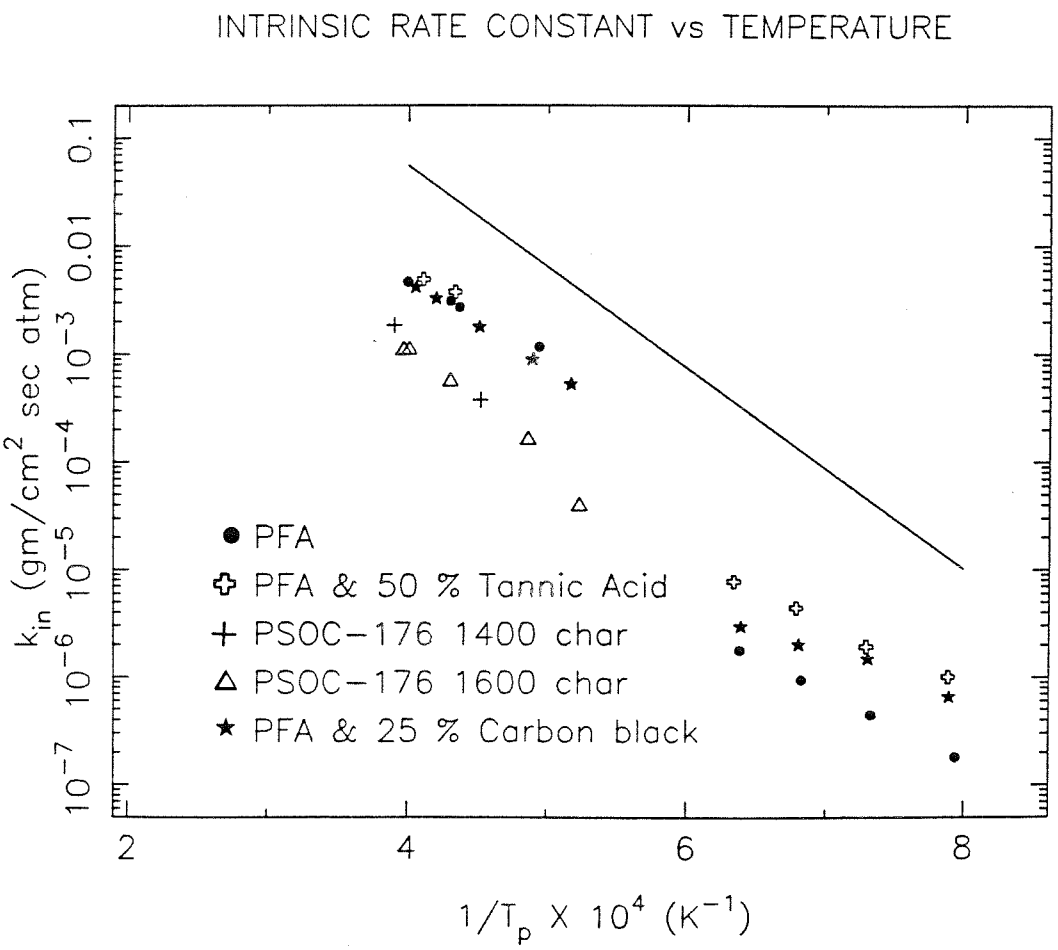

Figure 5: Arrhenius-type plot of the intrinsic reaction rate coefficient vs. the inverse of particle temperature.

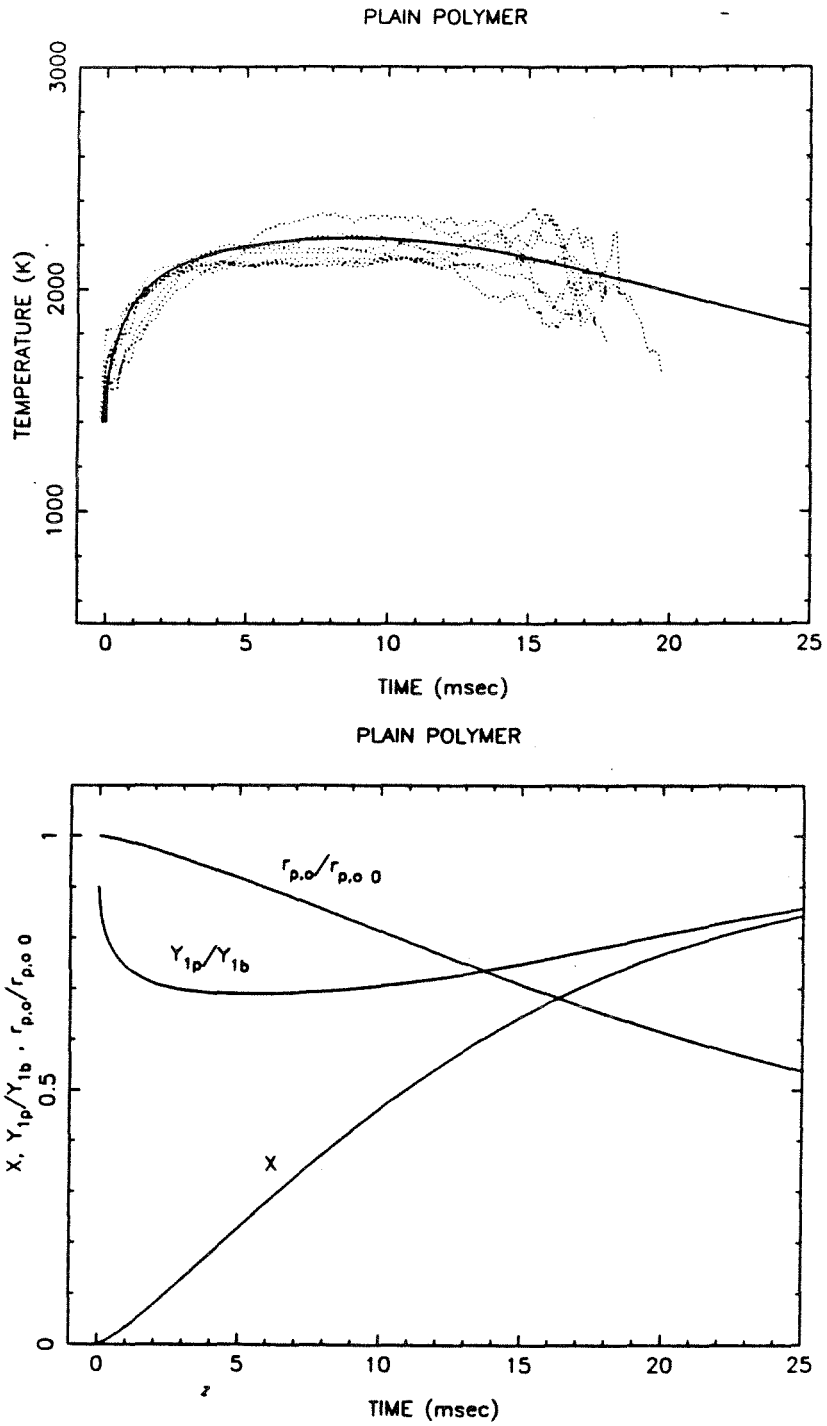

Figure 6: Combustion parameters for 45 μm solid PFA particles burning in O_2 at a T_W of 1500 K. (a) temperature-time profile, model: solid line, experiments: dotted line. (b) burnout, relative surface oxygen concentration and relative radius vs time.

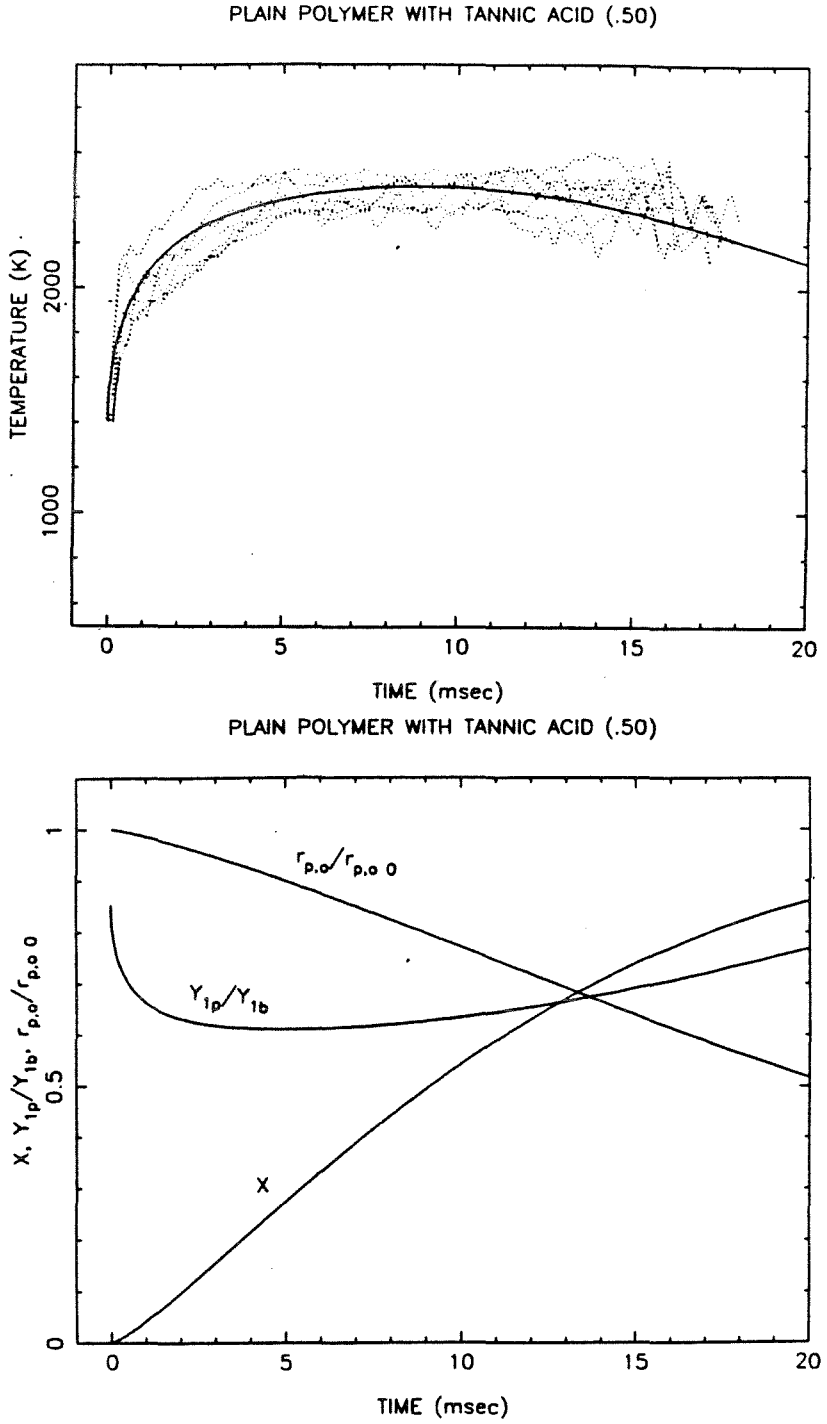

Figure 7: Combustion parameters for 45 μm solid particles formed from 50% tannic acid - 50% PFA burning in O_2 at a T_W of 1500 K. (a) temperature-time profile, model: solid line, experiments: dotted line. (b) burnout, relative surface oxygen concentration and relative radius vs time.

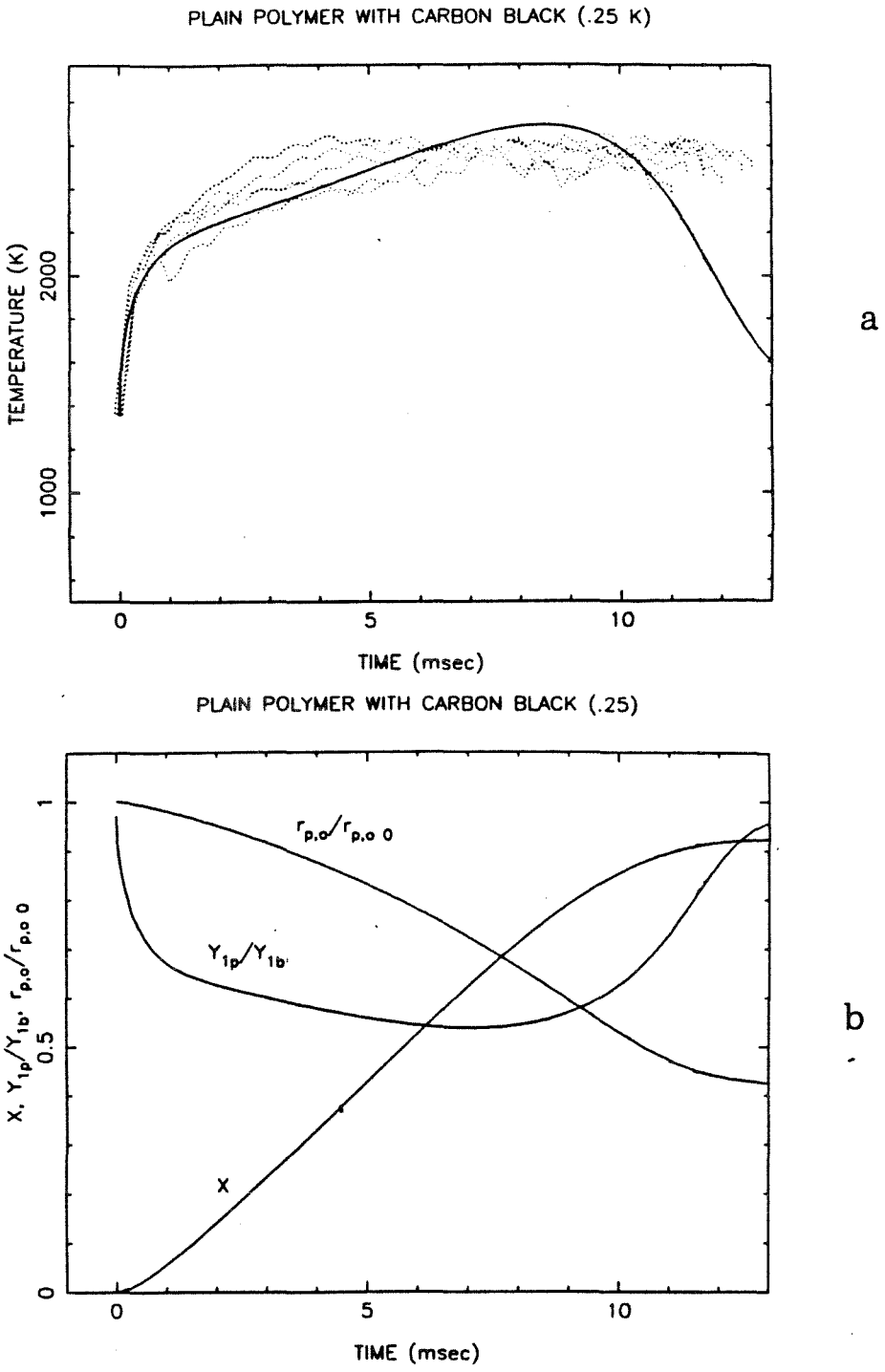

Figure 8: Combustion parameters for 45 μm solid PFA particles containing 25% carbon black burning in O_2 at a T_W of 1450 K (a) temperature-time profile, model: solid line, experiments: dotted line. (b) burnout, relative surface oxygen concentration and relative radius vs. time.

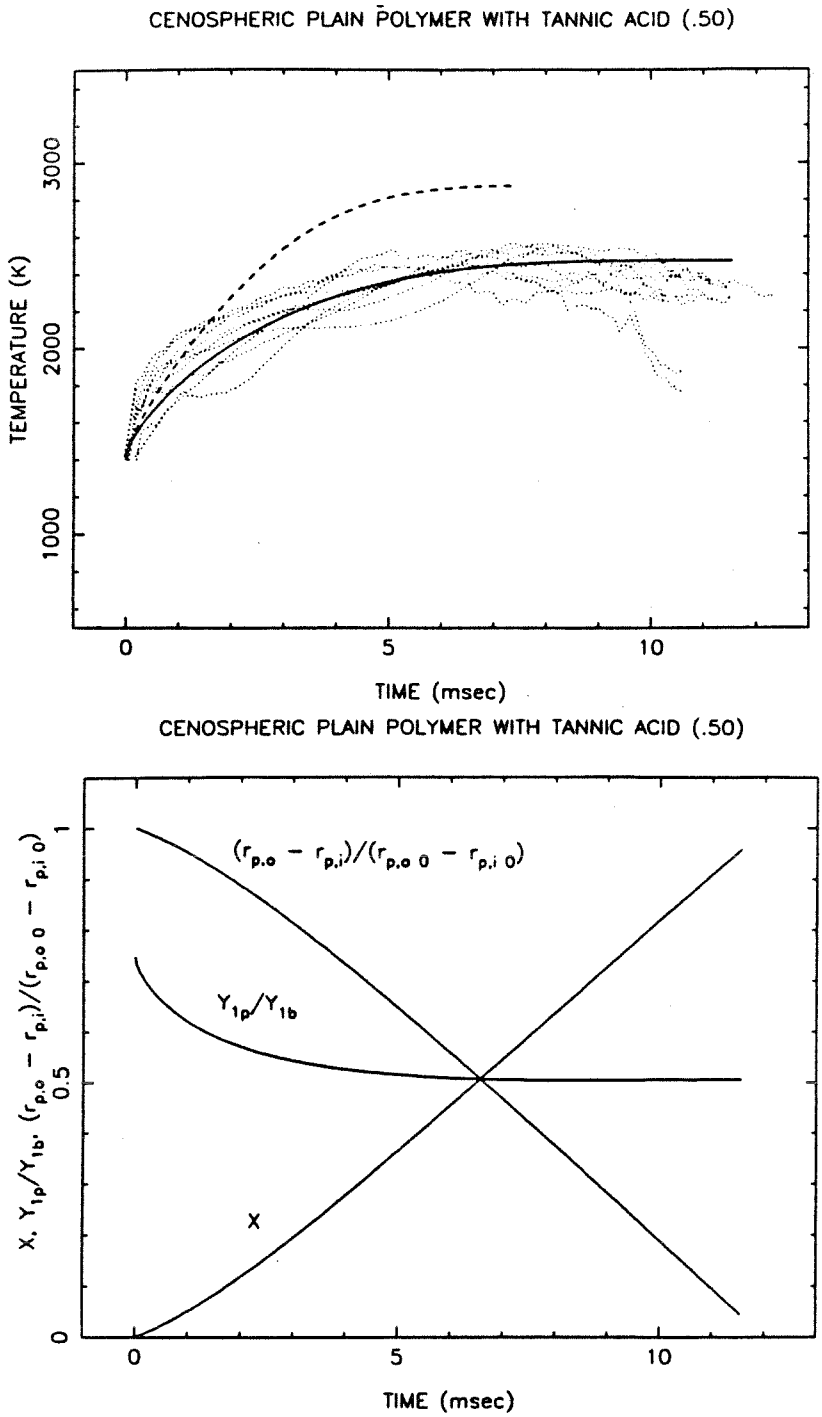

Figure 9: Combustion parameters for 45 μm and 114 μm cenospheric particles formed from 50% tannic acid and 50% PFA burning in O_2 at a T_W of 1500 K. (a) temperature-time profile, model: case (I) solid line, case(II) dashed line; experiments: dotted line. (b) burnout, relative surface oxygen concentration and relative radius vs. time.

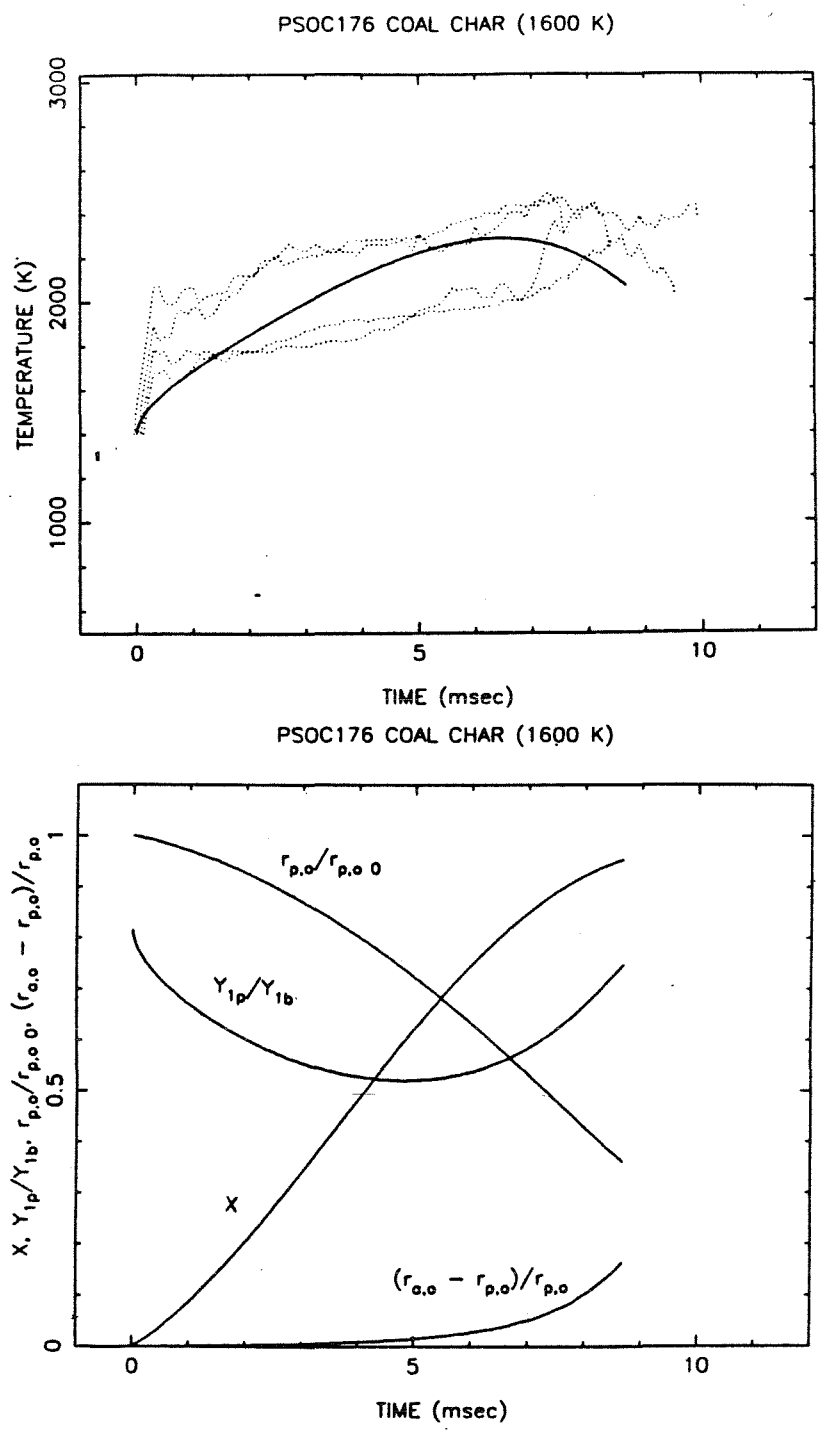

Figure 10: Combustion parameters for 50 μm PSOC-176 coal-char particles (1600 K pyrolysis) burning in O_2 at a T_W of 1500 K. (a) temperature-time profile, model: solid line, experiments: dotted line. (b) burnout, relative surface oxygen concentration, relative particle radius and relative ash layer thickness vs. time.

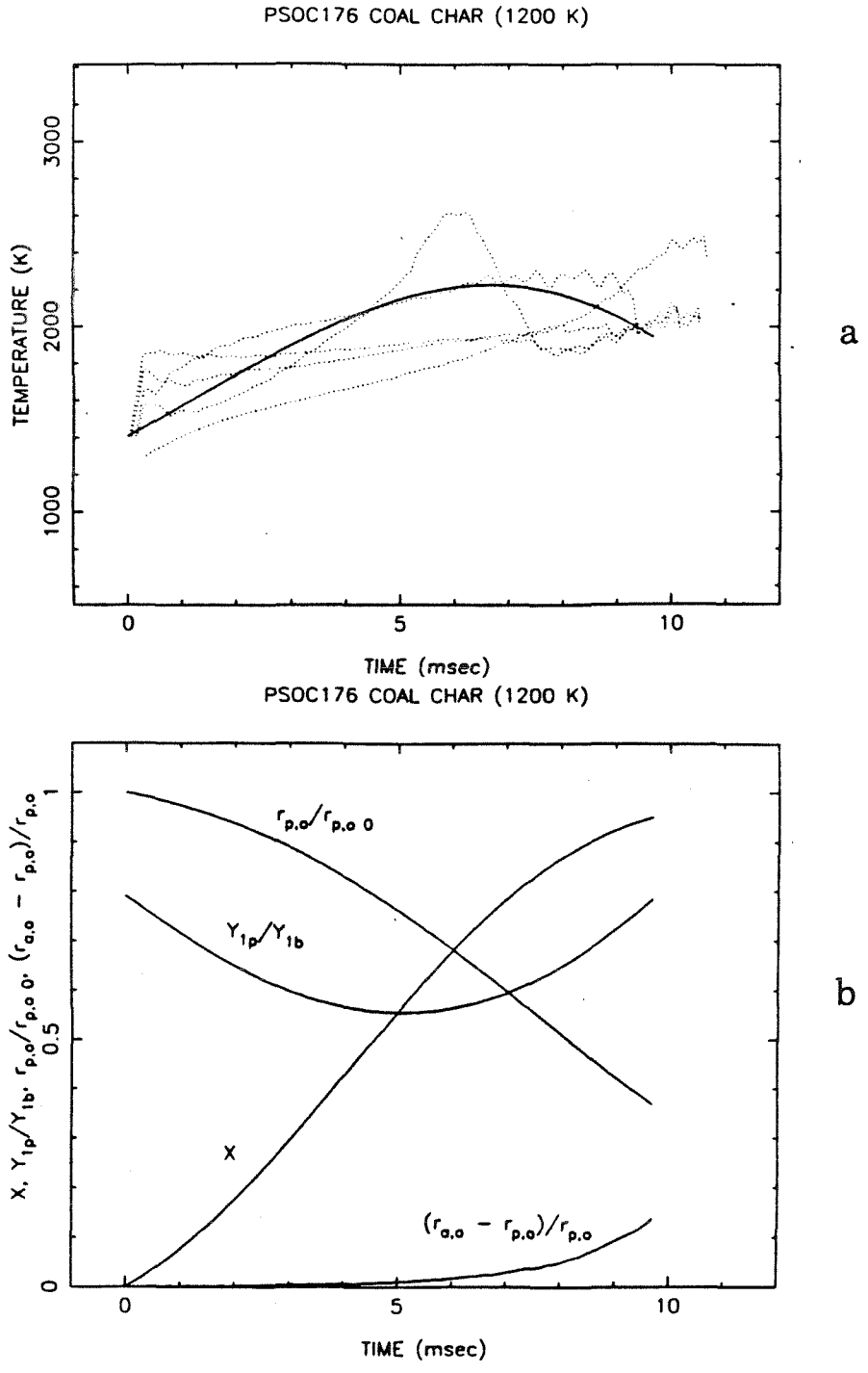

Figure 11: Combustion parameters for 50 μm PSOC-176 coal-char particles (1200 K pyrolysis) burning in O_2 at a T_W of 1500 K. (a) temperature-time profile, model: solid line, experiments: dotted line. (b) burnout, relative surface oxygen concentration, relative particle radius and relative ash layer thickness vs. time.

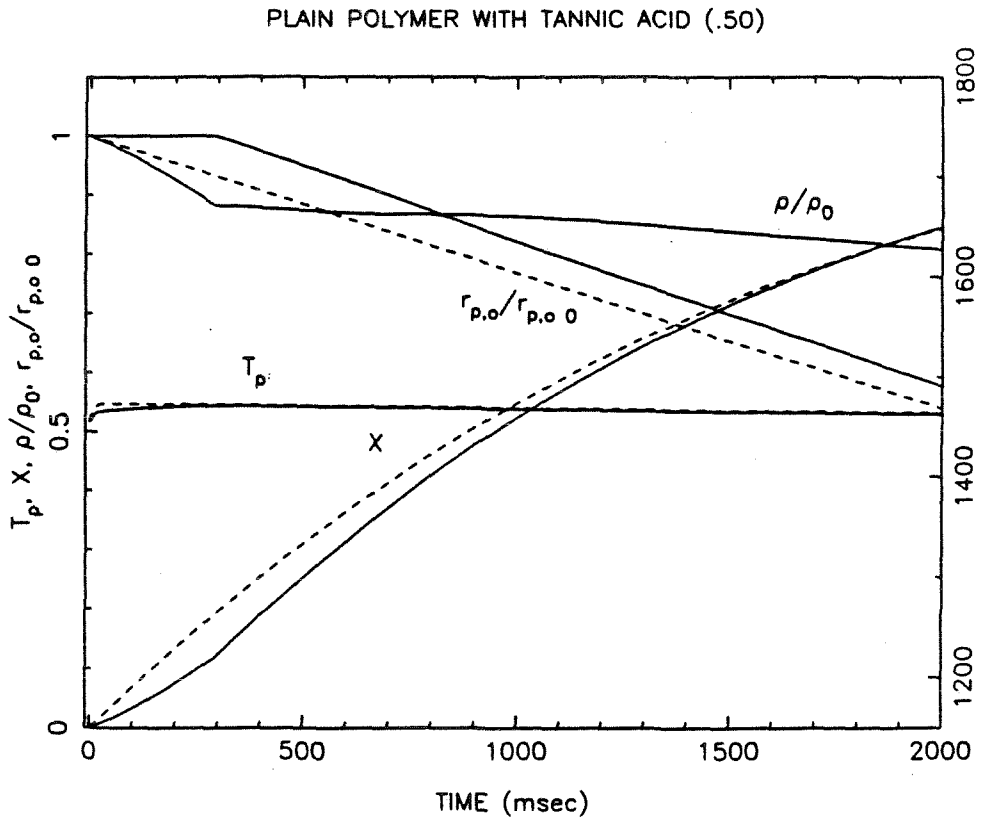

Figure 12: Combustion parameters for 45 μm solid particles formed from 50% tannic acid - 50% PFA burning in air at a T_W of 1500 K. Temperature-time profile, burnout, surface oxygen concentration, relative radius and apparent density vs. time; complete model: solid line, simplified model: dotted line.

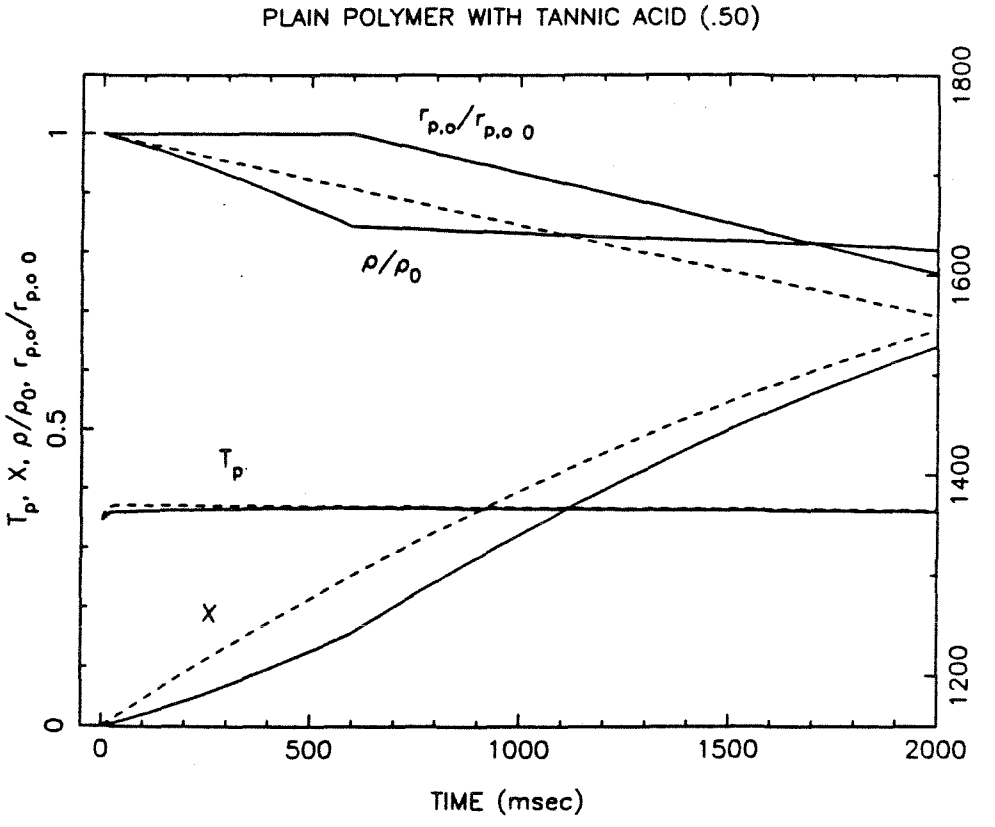

Figure 13: Combustion parameters for 45 μm solid particles formed from 50% tannic acid - 50% PFA burning in air at a T_W of 1400 K. Temperature-time profile, burnout, surface oxygen concentration, relative radius and apparent density vs. time; complete model: solid line, simplified model: dotted line.

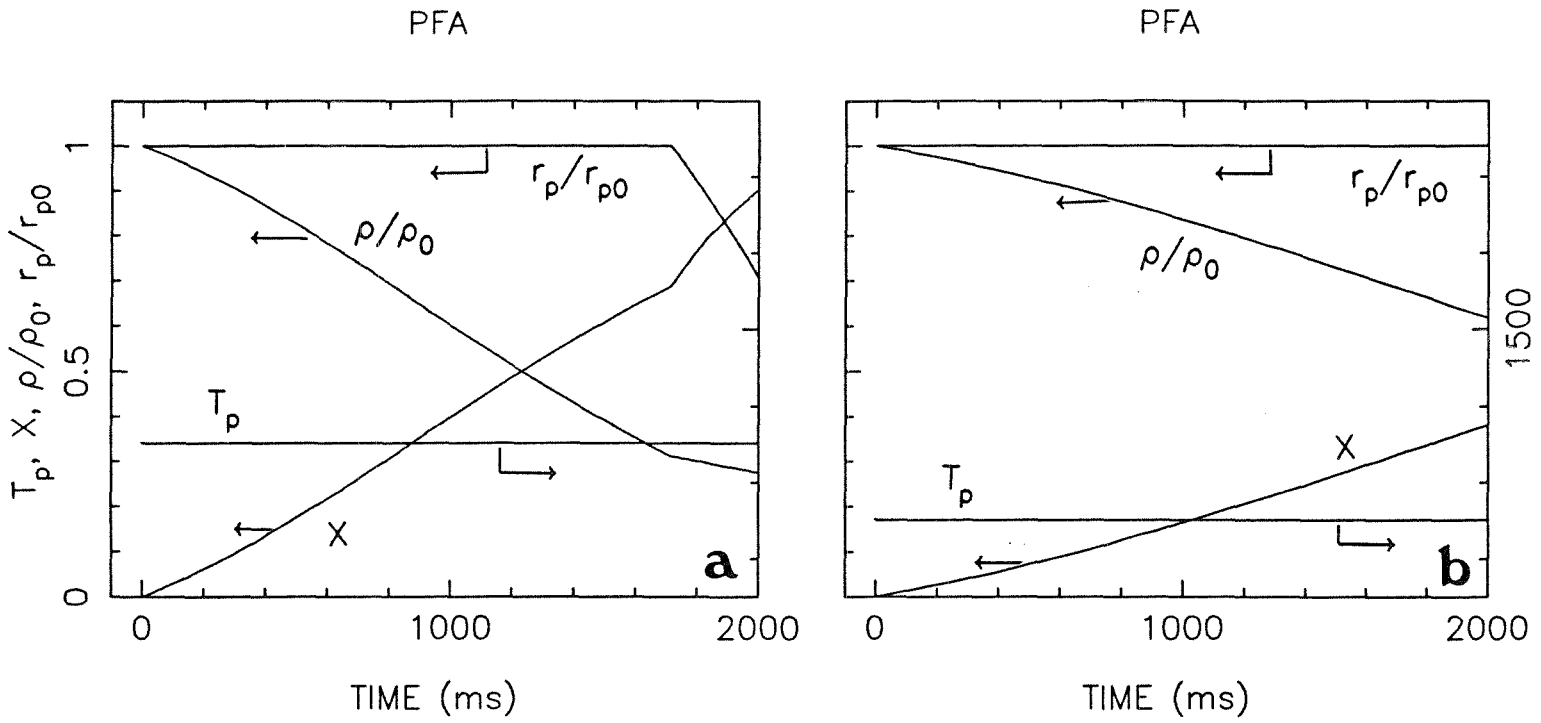

Figure 14: Combustion parameters for 8 μm solid PFA particles burning in air at a T_W of (a) 1400 K and (b) 1300 K. Temperature-time profile, burnout, surface oxygen concentration, relative radius and apparent density vs. time (Temperature increments are 100 K.)

PART II.

CONFIGURATIONAL AVERAGING

CHAPTER 5

Steady-State Reactant Flux into a Medium Containing Spherical Sinks

Steady-State Reactant Flux into a Medium Containing Spherical Sinks

M. Loewenberg and G. R. Gavalas
Department of Chemical Engineering 206-41
California Institute of Technology
Pasadena, California 91125

Abstract

A detailed analysis is presented for determining the reactant flux into a composite material containing randomly-located, reactive spherical centers. The governing equations are configurationally averaged assuming the spheres are distributed according to a hard-sphere potential. The resulting infinite hierarchy of coupled equations is truncated using physical considerations of screening and diluteness of the particulate phase. A general asymptotic solution is obtained valid to order c for all bounded and semi-infinite domains. The solution reproduces the mean-field result and includes the previously-neglected effects of sphere-boundary interactions. These interactions dominate the effect of two-sphere interactions which affect the solution at order $c^{3/2} \ln c$. Explicit consideration is given to the case in which the domain is spherical or semi-infinite and a solution obtained for each. The solutions obtained generally predict an enhanced reactant flux relative to the mean-field result. The solution is illustrated by application to the problem of coal ash vaporization.

1 Introduction

The customary analysis of reaction and diffusion in heterogeneous catalysis is predicated upon an atomic scale dispersion of the reaction sites. In some systems of practical importance, the reaction sites are small but macroscopic particles imbedded in a matrix which permits diffusion but is otherwise inert. Examples of such discrete reaction-diffusion problems can be drawn from biotechnology and coal combustion. An example from the former area is that of immobilized cell systems where the cells are fixed within an inert matrix permitting the diffusion of nutrients and metabolic products (Chibata and Wingard (1983)). An important example from coal combustion is the reaction of discrete mineral inclusions within the char particles leading to the formation and vaporization of volatile inorganic species (Quann and Sarofim (1982)).

The diffusive transport through an infinite medium containing spherical particles with instantaneous reaction on the particle surfaces was considered by several authors starting with by Smoluchowski (1916). Felderhof and Deutch (1976) employed an electrostatic analogy to develop a governing differential equation for the reactant concentration field at steady-state. Their results apply to dilute volume fractions of spherical sinks and depend upon a superposition approximation. More recently, Muthukumar and Cukier (1981) used a multiple scattering approach to extend the work of Felderhof and Deutch to an arbitrary volume fraction of monopole sinks. A self-consistent scheme was used by Muthukumar (1982) to obtain the simultaneous volume fraction dependence of the effective rate and diffusion coefficients. Mattern and Felderhof (1986, 1987) determined the rate coefficient on the basis of a cluster expansion and discussed differences with previous results.

The general approach followed in these papers is the formulation of a differential

equation that describes, approximately, the average concentration. This equation is derived by some form of averaging procedure assuming a spatially homogeneous medium. The boundaries, if any, are taken into account by imposing the customary boundary conditions. However, in some problems, external boundaries play a more pervasive role and must be considered in the formulation of the approximating differential equations. This feature is especially important for determining the concentration flux into the medium which depends upon the details of the local field near the boundary.

Related to the discrete reaction-diffusion problem is the problem of heat conduction through a material consisting of spherical particles imbedded in a matrix of different conductivity. This problem has been treated by Jeffrey (1973) via a renormalization technique, by Hinch (1977) using a truncation of a hierarchy of configurationally averaged equations, and by Chang and Acrivos (1986) using a modified effective medium approximation. These methods are not readily applicable to finite media which do not possess translational symmetry. However, Chang and Acrivos (1987) have recently treated the problem of heat conduction into a composite medium adjacent to a plane wall.

The purpose of this paper is to determine the flux of reactant on the boundary of a finite or semi-infinte region containing a dilute suspension of reactive spheres. Our approach utilizes a hierarchy of configurationally averaged equations as introduced by Hinch (1977). We explicitly include the interaction of a sphere with the boundary which significantly affects the reactant flux and dominates the effect of all multi-sphere interactions. Direct two- sphere interactions are confounded by the loss of translational symmetry and are thus not included in our analysis. A screening modulus determines the transition from a power series dependence on sink concentration to a more complicated non-analytic behavior. Explicit solutions

are obtained for spherical and semi-infinite domains and the solution is illustrated by application to the problem of coal ash vaporization.

2 Problem Formulation

The object of this paper is to seek the reactant flux, at steady-state, on the boundary, $\partial\Omega$, of a domain, Ω, containing a dilute, solid suspension of reactive spheres in an inert matrix material. The analysis is restricted to all domains which are either bounded or semi-infinite. We will assume that the reactant diffuses within the inert phase with a constant diffusivity, D. We will also assume that the spheres are identical with radius, a, although the present analysis can easily be extended to a distribution of sphere radii as demonstrated by Jeffrey (1973). The spheres can be distributed according to any specified distribution function. A popular choice of practical interest is the hard-sphere distribution and is the one adopted throughout: spheres are not allowed intersection with either each other or with the boundary of the domain but are otherwise randomly located. We can define a sphere number density, n, which is related to the volume fraction of the spherical phase, c.

$$c = \frac{4\pi}{3} a^3 n \tag{2.1}$$

The *total* number of spheres in Ω is approximately given by:

$$N \approx nV \tag{2.2}$$

where V is the volume of the material. We shall be interested in the case $N >> 1$. Diluteness of the spherical phase implies $c << 1$.

At steady-state, the reactant concentration field, $y(\mathbf{x})$, obeys Laplace's equation

$$\nabla^2 y(\mathbf{x}) = 0 \tag{2.3}$$

for all points $\mathbf{x}$ which lie in the inert phase of the domain. We shall assume that chemical reaction on the spherical surfaces is essentially instantaneous relative to interparticle diffusion which implies:

$$y(\mathbf{x}) = y_e \quad \text{when } \mathbf{x} \text{ lies on any sphere surface} \tag{2.4}$$

where y_e is the equilibrium concentration which is assumed constant. We will assume that reactant concentration is constant over the domain boundary, $\partial\Omega$:

$$y(\mathbf{x}) = y_0 \quad \mathbf{x} \in \partial\Omega \tag{2.5}$$

Using the dimensionless variables:

$$\mathbf{x} = \frac{\mathbf{x}'}{a}, \qquad u(\mathbf{x}) = \frac{y(\mathbf{x}) - y_e}{y_0 - y_e} \tag{2.6}$$

we obtain the equations:

$$\nabla^2 u(\mathbf{x}) = 0 \tag{2.7}$$

$$u(\mathbf{x}) = 0 \quad \text{when } \mathbf{x} \text{ lies on any sphere surface} \tag{2.8}$$

$$u(\mathbf{x}) = 1 \qquad \mathbf{x} \in \partial\Omega \tag{2.9}$$

The dimensionless reactant flux into the domain at a point $\mathbf{x}$ on the boundary will be denoted:

$$\mathbf{F}(\mathbf{x}) = -\frac{\partial u(\mathbf{x})}{\partial n} \qquad \mathbf{x} \in \partial\Omega \tag{2.10}$$

The *average* flux on the boundary is given by:

$$\mathbf{F} = \frac{1}{S}\int_{\partial\Omega} \mathbf{F}(\mathbf{x})d\mathbf{x} \tag{2.11}$$

where S is the surface area of $\partial\Omega$. In general, $\mathbf{F}$ will depend on the sphere volume fraction, c, and is specific to the particular domain.

3 Configurational Averaging

In this section, we average the governing equations over all allowable configurations of the spheres in the domain. The results of the averaging procedure are presented below and follow from the derivation in Appendix A.

Before averaging over all allowable configurations of spheres, Equation (2.7) and boundary condition (2.8) are replaced by the following equation:

$$\nabla^2 u(\mathbf{x}|\mathbf{x}_1,\cdots,\mathbf{x}_N) = \sum_{i=1}^{N} \frac{\partial}{\partial n} u(\mathbf{x}|\mathbf{x}_1,\cdots,\mathbf{x}_N)\delta(\|\mathbf{x}-\mathbf{x}_i\|-1) \tag{3.1}$$

which is valid over the whole region, the spherical phase as well as the inert matrix according to the derivation given in Appendix A. This equation is valid for all $\mathbf{x}$ in Ω and is subject only to boundary condition (2.9) on $\partial\Omega$. Excepting the sphere surfaces where it is singular, the sink term on the right vanishes everywhere in the domain. The set of position vectors, $\{\mathbf{x}_1,\cdots,\mathbf{x}_N\}$, locate the N indistinguishable sphere centers and define a particular configuration of the spheres. Equation (3.1) provides the starting point for configurational averaging.

According to the derivation in Appendix A, the configurational average of Equation (3.1) is:

$$\nabla^2\langle u(\mathbf{x})\rangle = \frac{3c}{4\pi}\int_{\{\|\mathbf{x}-\mathbf{x}_1\|=1\}\cap\bar{\Omega}} \frac{\partial}{\partial n}\langle u(\mathbf{x}|\mathbf{x}_1)\rangle d\mathbf{x}_1 \tag{3.2}$$

where $\bar{\Omega}$ is the allowed portion of the domain for sphere centers consisting of the domain Ω less the region within one dimensionless hard-sphere radius of the boundary, $\partial\Omega$. The solution of Equation (3.2) must satisfy the normalized boundary condition (2.9) on $\partial\Omega$.

Equation (3.2) couples the unconditionally averaged field to the conditionally averaged field with one sphere fixed at $\mathbf{x}_1$. Averaging Equation (3.1) over configurations which have a sphere fixed at $\mathbf{x}_1$ yields the first conditionally averaged field

equation:

$$\nabla^2\langle u(\mathbf{x}|\mathbf{x}_1)\rangle = \frac{3c}{4\pi}\int_{\{\|\mathbf{x}-\mathbf{x}_2\|=1\}\cap\bar{\Omega}_1}\frac{\partial}{\partial n}\langle u(\mathbf{x}|\mathbf{x}_1,\mathbf{x}_2)\rangle d\mathbf{x}_2 \qquad \|\mathbf{x}-\mathbf{x}_1\|>1 \quad (3.3)$$

where Ω_1 is defined by the intersection: $\bar{\Omega}\cap\{\|\mathbf{x}_1-\mathbf{x}_2\|\geq 2\}$ and, according to the hard-sphere distribution, is the allowed portion of the domain for a second sphere center given one center is at $\mathbf{x}_1$. The solution of Equation (3.3) must, in addition to satisfying boundary condition (2.9) on $\partial\Omega$, also satisfy (2.8) on the surface of the sphere centered at $\mathbf{x}_1$.

The first conditionally averaged field equation, (3.3), is coupled to the second conditionally averaged field in the same manner as (3.2) is coupled to (3.3). Thus, the same averaging process used to obtain the first conditionally averaged field equation is repeated to obtain the second. The result is:

$$\nabla^2\langle u\rangle(\mathbf{x}|\mathbf{x}_1,\mathbf{x}_2) =$$

$$\frac{3c}{4\pi}\int_{\{\|\mathbf{x}-\mathbf{x}_3\|=1\}\cap\bar{\Omega}_2}\frac{\partial}{\partial n}\langle u\rangle(\mathbf{x}|\mathbf{x}_1,\mathbf{x}_2,\mathbf{x}_3)d\mathbf{x}_3 \qquad \|\mathbf{x}-\mathbf{x}_1\|>1, \quad \|\mathbf{x}-\mathbf{x}_2\|>1 \quad (3.4)$$

where Ω_2 is defined by the intersection: $\bar{\Omega}\cap\{\|\mathbf{x}_3-\mathbf{x}_1\|\geq 2\}\cap\{\|\mathbf{x}_3-\mathbf{x}_2\|\geq 2\}$ and is the allowed portion of the domain for a third sphere center given centers at $\mathbf{x}_1$ and $\mathbf{x}_2$. The solution of Equation (3.4) must satisfy boundary condition (2.9) on $\partial\Omega$ and (2.8) on the surface of both fixed spheres and is analogously coupled to the conditionally averaged field with three spheres fixed.

As may now be apparent, the foregoing procedure may be repeated indefinitely producing an infinite hierarchy of coupled, conditionally averaged equations with an additional sphere fixed at each level. The hierarchy is truncated by exploiting the diluteness condition, $c << 1$, and employing the physics of screening as described below. The truncated hierarchy is solved in reverse order: the equation with the most spheres fixed is solved first because it is decoupled from the others; its solution

provides the forcing term for the next equation. The procedure is continued until the unconditionally averaged field is found. The truncation procedure follows.

4 Truncation of Hierarchy

The hierarchy is truncated by exploiting the diluteness condition, $c << 1$, and employing the physics of screening: far from a fixed sphere, the influence of the sphere is "screened" by the presence of the intervening sinks in the material (Brinkman (1947)). Thus, the field at a point $\mathbf{x}$ is relatively unaffected by the presence of a sphere fixed at $\mathbf{x}_1$ for large separation, $\|\mathbf{x} - \mathbf{x}_1\| >> L_s$:

$$\langle u(\mathbf{x}|\mathbf{x}_1)\rangle \sim \langle u(\mathbf{x})\rangle \tag{4.1}$$

This result is exploited in Appendix B to truncate the foregoing hierarchy. L_s is the "screening length" defined by:

$$L_s = \frac{a}{\sqrt{3c}} \tag{4.2}$$

which is the characteristic length for the decay of reactant concentration away from the boundary and, in general, is the characteristic decay length for all disturbances in the field as shown below. The diluteness condition implies: $L_s >> a$. We define a "screening modulus":

$$\phi = \frac{L_c}{L_s} \equiv \left(\frac{L_c}{a}\right)\sqrt{3c} \tag{4.3}$$

where L_c is a characteristic length for Ω (e.g., $L_c = V^{1/3}$). The screening modulus, ϕ, determines the extent of reactant penetration into the domain and thus the extent by which the influence of boundary is screened by the sinks in the material. $\phi << 1$ implies that all the spheres in the domain are immersed in a constant concentration

field equal to unity according to boundary condition (2.9). $\phi >> 1$ indicates significant "boundary screening": only spheres relatively near the boundary are exposed to significant reactant concentration.

Combining Equations (4.1) and (3.2) according to the procedure in Appendix B, yields the lowest-order truncation:

$$\nabla^2\langle u(\mathbf{x})\rangle = 3c\langle u(\mathbf{x})\rangle \tag{4.4}$$

which constitutes the "mean-field" approximation. The solution must satisfy boundary condition (2.9) and determines the reactant flux into the domain via Equation (2.10). Rescaling Equation (4.4) by the screening length, L_s, balances the diffusive and dissipative terms supporting the claim that L_s is the characteristic concentration decay length.

The mean-field approximation neglects all sphere-sphere and sphere-boundary interactions; only the collective screening effect of the spheres in the material is retained through the dissipative term in the equation. The results obtained in this paper indicate that the effect of sphere-boundary interactions is order c for $\phi << 1$ and order $c \ln c$ for $\phi >> 1$. Sphere-sphere interactions produce a higher-order effect.

Combining the two-sphere analog of Equation (4.1) with (3.3) yields the analog of Equation (4.4) by the procedure shown in Appendix B:

$$\nabla^2\langle u(\mathbf{x}|\mathbf{x}_1)\rangle = 3c\langle u(\mathbf{x}|\mathbf{x}_1)\rangle \tag{4.5}$$

where $\langle u(\mathbf{x}|\mathbf{x}_1)\rangle$ must satisfy boundary condition (2.8) on the fixed sphere surface and boundary condition (2.9) on the domain boundary. The solution determines the sink term in the unconditionally averaged equation according to Equation (3.2). Equation (4.5) is analogous to Equation (4.4) and is the mean-field approximation of the first conditionally averaged equation.

Following this program retains the primary screening effect previously treated by the mean-field approximation as well as the effect of sphere-boundary interactions neglected by the mean-field approximation. Sphere-sphere interactions remain unaccounted; only the second-order screening effect upon the sphere fixed at $\mathbf{x}_1$ is retained through the dissipative term in Equation (4.5). The above truncation allows general solution of the reactant flux to order c for all domains analyzed herein. According to Appendix B, the error commited by neglecting sphere-sphere interactions is order c^2 for $\phi << 1$ and order $c^{3/2} \ln c$ for $\phi >> 1$.

5 Mean-Field Solution

In the present section, we shall obtain the mean-field solution for a spherical and semi-infinite domain. If Ω is a semi-infinite domain, the characteristic length of the domain becomes infinite thus ϕ defined by (4.3) is infinite. The solution of (4.4) with boundary condition (2.9) yields:

$$u_{mf}(\mathbf{x}) = e^{-\sqrt{3c}x} \tag{5.1}$$

where x is the distance from the plane boundary. The subscript, mf, replaces the angled brackets indicating that the result depends upon the mean-field approximation given by Equation (4.4). The dimensionless reactant flux is:

$$\mathbf{F}_{mf}(c) = \sqrt{3c} \tag{5.2}$$

where $\mathbf{F}_{mf}(c)$ is the mean-field result defined by Equation (2.10) (or (2.11)) for a semi-infinite domain. $\mathbf{F}_{mf}(c)$ depends explicitly upon the sphere volume fraction, c, but is independent of position on the boundary, $\partial\Omega$.

If Ω is a spherical domain with normalized radius, R, the characteristic length

of the domain is aR and the screening modulus is given by:

$$\phi = R\sqrt{3c} \tag{5.3}$$

Equations (4.4) and (2.9) yield the mean-field result:

$$u_{mf}(\mathbf{x}) = \frac{R\ \sinh(\sqrt{3c}r)}{r\ \sinh(\phi)} \tag{5.4}$$

where r is the radial coordinate and is the distance from the center of the domain. The reactant flux is:

$$\mathbf{F}_{mf}(c,R) = \frac{1}{R}\left[\phi\coth\phi - 1\right] \tag{5.5}$$

$\mathbf{F}_{mf}(c,R)$ is the mean-field reactant flux and depends upon c and R but is independent of position on the boundary, $\partial\Omega$.

If $L_c << L_s$ ($\phi << 1$), all spheres in the domain are immersed in a uniform ambient concentration field equal to unity and the total reactant flux is proportional to the total number of spheres in the domain, N, and is therefore order c. The general result is illustrated by considering Equation (5.5) in the limit $\phi << 1$:

$$\lim_{\phi\to 0}\mathbf{F}_{mf}(c,R) = cR \tag{5.6}$$

In the limit $L_c >> L_s$ (for constant c) the number of spheres in the domain diverges yet the reactant flux remains finite. This fact is a consequence of boundary-screening: spheres far from the boundary are immersed in a sharply depleted ambient concentration; the flux into a test sphere far from the boundary approaches zero. The presence of boundary-screening yields a finite reactant flux independent of the characteristic length of the domain, L_c, for $\phi >> 1$. This result is exemplified by reconsidering Equation (5.5) which in the limit $\phi >> 1$ recovers the semi-infinite domain result:

$$\lim_{\phi\to\infty}\mathbf{F}_{mf}(c,R) = \sqrt{3c} = \mathbf{F}_{mf}(c) \tag{5.7}$$

which is a general limiting result for all domains in the limit $\phi >> 1$.

The leading order correction to the mean-field solution results from the interaction of the spheres with the boundary. In the following, we will truncate the hierarchy at the next level and thereby retain this effect which permits an order c solution for all domains within the scope of this paper.

6 General Solution to Order c

In the following, we determine a general solution valid to order c. The resulting error is bounded by order $c^{3/2} \ln c$ for all domains within the scope of this paper. Applying a steady-state material balance on the domain for a particular configuration of the spheres, yields the following expression for the total reactant flux into the domain:

$$\int_{\partial\Omega} \mathbf{F}(\mathbf{x}|\mathbf{x}_1,\cdots,\mathbf{x}_N)d\mathbf{x} = \sum_{i=1}^{N} \int_{\|\mathbf{x}-\mathbf{x}_i\|=1} \frac{\partial}{\partial n} u(\mathbf{x}|\mathbf{x}_1,\cdots,\mathbf{x}_N)d\mathbf{x} \tag{6.1}$$

where $\mathbf{F}(\mathbf{x}|\mathbf{x}_1,\cdots,\mathbf{x}_N)$ is defined by (2.10) for a given configuration of the sphere centers, $\{\mathbf{x}_1,\cdots,\mathbf{x}_N\}$. Similarly, we can express the *average* reactant flux on the boundary:

$$\mathbf{F}(\mathbf{x}_1,\cdots,\mathbf{x}_N) = \frac{1}{S} \sum_{i=1}^{N} \int_{\|\mathbf{x}-\mathbf{x}_i\|=1} \frac{\partial}{\partial n} u(\mathbf{x}|\mathbf{x}_1,\cdots,\mathbf{x}_N)d\mathbf{x} \tag{6.2}$$

where $\mathbf{F}(\mathbf{x}_1,\cdots,\mathbf{x}_N)$ is defined by (2.11). According to the derivation in Appendix C, the configurational average of (6.2) yields:

$$\langle \mathbf{F} \rangle = \frac{3c}{S} \int_{\bar{\Omega}} \left[\frac{1}{4\pi} \int_{\|\mathbf{x}-\mathbf{x}_1\|=1} \frac{\partial}{\partial n} \langle u(\mathbf{x}|\mathbf{x}_1) \rangle d\mathbf{x} \right] d\mathbf{x}_1 \tag{6.3}$$

Equation (6.3) expresses the average flux into the domain in terms of the average flux into a single sphere which, in general, requires the solution of Equation (3.3) from the complete, coupled hierarchy. According to Appendix C, the above result is exact to order c^2, however, it cannot be evaluated without truncating the hierarchy.

To obtain the reactant flux to order c, we shall truncate the hierarchy with Equation (4.5), the first conditional mean-field equation, which induces an order $c^{3/2}\ln c$ error in the solution according to Appendix B. The solution of (4.5) is inserted into (6.3) to yield the reactant flux directly without solving for the unconditionally averaged field, $\langle u(\mathbf{x})\rangle$.

The solution procedure is facilitated by defining a function $v(\mathbf{x}|\mathbf{x}_1)$:

$$v(\mathbf{x}|\mathbf{x}_1) = u_{mf}(\mathbf{x}) - \langle u(\mathbf{x}|\mathbf{x}_1)\rangle \tag{6.4}$$

where $u_{mf}(\mathbf{x})$ and $\langle u(\mathbf{x}|\mathbf{x}_1)\rangle$ satisfy the mean-field equations (4.4) and (4.5) respectively. By linearity, $v(\mathbf{x}|\mathbf{x}_1)$ is also a solution of Equation (4.5) satisfying boundary conditions:

$$v(\mathbf{x}|\mathbf{x}_1) = 0 \qquad \mathbf{x} \in \partial\Omega \tag{6.5}$$

and

$$v(\mathbf{x}|\mathbf{x}_1) = u_{mf}(\mathbf{x}_1) \qquad \|\mathbf{x} - \mathbf{x}_1\| = 1 \tag{6.6}$$

where we have neglected local gradients of $u_{mf}(\mathbf{x})$ at $\mathbf{x}_1$ which are bounded by order $c^{1/2}$ as shown in Appendix B. The approximation introduced by Equation (6.6) affects the solution at order $c^{3/2}$ as shown below. Expressing Equation (6.3) in terms of $v(\mathbf{x}|\mathbf{x}_1)$ yields:

$$\langle \mathbf{F}\rangle = 3c\mathbf{B}(c) \tag{6.7}$$

where $\mathbf{B}(c)$ is defined by:

$$\mathbf{B}(c) = \frac{1}{S}\int_{\bar{\Omega}} u_{mf}(\mathbf{x}_1)\mathbf{H}(\mathbf{x}_1;c)d\mathbf{x}_1 \tag{6.8}$$

and $\mathbf{H}(\mathbf{x}_1;c)$ is defined as:

$$\mathbf{H}(\mathbf{x}_1;c) = \frac{1}{4\pi u_{mf}(\mathbf{x}_1)}\int_{\|\mathbf{x}-\mathbf{x}_1\|=1}\frac{\partial}{\partial n}v(\mathbf{x}|\mathbf{x}_1)d\mathbf{x} \tag{6.9}$$

Equation (6.7) indicates that the flux can be calculated to order c if $\mathbf{B}(c)$ is determined to order unity.

The order $c^{1/2}$ gradients in $u_{mf}(\mathbf{x})$ at $\mathbf{x}_1$ which are neglected according to boundary condition (6.6) induce a dipole of the same order at $\mathbf{x}_1$. The first reflection disturbance of a dipole is integrable on all domains considered in this paper. Therefore, upon integration in Equation (6.8), the first reflection disturbance due to an order $c^{1/2}$ dipole affects $\mathbf{B}(c)$ also at order $c^{1/2}$. Then, according to Equation (6.7), the approximation embodied in boundary condition (6.6) introduces only an order $c^{3/2}$ error to the predicted reactant flux as claimed.

In Appendix D, we develop the general approximation:

$$\mathbf{B}(c) = \frac{1}{S}\int_{\bar{\Omega}}\Big[u_{mf}(\mathbf{x}_1)\left[(1+\sqrt{3c}) + \mathbf{H}^{(1)}(\mathbf{x}_1;c)\right] + \mathbf{J}(\mathbf{x}_1)\Big]d\mathbf{x}_1 \qquad (6.10)$$

which introduces an order $c^{3/2}\ln c$ error consistent with the error induced by the truncation as shown in the Appendix D. The quantities: $(1+\sqrt{3c})$ and $\mathbf{H}^{(1)}(\mathbf{x}_1;c)$ are, respectively, the exact contributions to $\mathbf{H}(\mathbf{x}_1;c)$ resulting from the incident field and first reflection disturbance induced by the boundary. $\mathbf{J}(\mathbf{x}_1)$ is the approximate contribution from the second and all higher-order reflections with the boundary as obtained by solution of Laplace's equation. Inserting (6.10) into (6.7) yields the expression:

$$\mathbf{F} = \frac{3c}{S}\int_{\bar{\Omega}}\Big[u_{mf}(\mathbf{x}_1)\left[(1+\sqrt{3c}) + \mathbf{H}^{(1)}(\mathbf{x}_1;c)\right] + \mathbf{J}(\mathbf{x}_1)\ \Big]d\mathbf{x}_1 + O(c^{3/2}\ln c) \qquad (6.11)$$

where we have dropped the angled brackets on $\langle\mathbf{F}\rangle$; the configurationally averaged reactant flux is heretofore implied.

It proves useful to consider the above solution as the sum of three distinct contributions:

$$\mathbf{F} = \mathbf{F}_0 + \mathbf{F}_1 + \mathbf{F}_2 + O(c^{3/2}\ln c) \qquad (6.12)$$

where $\mathbf{F}_0$, $\mathbf{F}_1$ and $\mathbf{F}_2$ are the approximate contributions to the reactant flux from the incident field, the first reflection disturbance, and all higher-order reflections with the boundary. Explicitly, these contributions are:

$$\mathbf{F}_0 = (1 + \sqrt{3c})\mathbf{F}_{mf} - 3c + O(c^{3/2}) \tag{6.13}$$

$$\mathbf{F}_1 = \frac{3c}{S}\int_{\bar{\Omega}} u_{mf}(\mathbf{x}_1)\mathbf{H}^{(1)}(\mathbf{x}_1, c)d\mathbf{x}_1 \tag{6.14}$$

$$\mathbf{F}_2 = \frac{3c}{S}\int_{\bar{\Omega}} \mathbf{J}(\mathbf{x}_1)d\mathbf{x}_1 + O(c^{3/2}\ln c) \tag{6.15}$$

Equation (6.13) is derived as follows. According to (6.11), $\mathbf{F}_0$ is defined by:

$$\mathbf{F}_0 = \frac{3c}{S}\int_{\bar{\Omega}} u_{mf}(\mathbf{x}_1)(1 + \sqrt{3c})d\mathbf{x}_1 \tag{6.16}$$

We can write:

$$\int_{\bar{\Omega}} u_{mf}(\mathbf{x}_1)d\mathbf{x}_1 = \int_{\Omega} u_{mf}(\mathbf{x}_1)d\mathbf{x}_1 - \int_{\Omega-\bar{\Omega}} u_{mf}(\mathbf{x}_1)d\mathbf{x}_1 \tag{6.17}$$

The first integral on the right side ultimately reproduces the mean-field solution and the second is a consequence of the hard-sphere distribution: sphere centers are excluded from the volume within one sphere radius of the boundary. We can insert (4.4) into the first integral and apply the divergence theorem to obtain:

$$\int_{\Omega} u_{mf}(\mathbf{x}_1)d\mathbf{x}_1 = \frac{1}{3c}\int_{\Omega} \nabla^2 u_{mf}(\mathbf{x}_1)d\mathbf{x}_1 = \frac{1}{3c}\int_{\partial\Omega} \mathbf{F}_{mf}(\mathbf{x})d\mathbf{x}_1 \tag{6.18}$$

The term, $u_{mf}(\mathbf{x}_1)$, in the second integrand can be approximated by the boundary value given by Equation (2.9):

$$\int_{\Omega-\bar{\Omega}} u_{mf}(\mathbf{x}_1)d\mathbf{x}_1 = \int_{\partial\Omega} d\mathbf{x}_1 + O(c^{1/2}) \tag{6.19}$$

which is justified because gradients of $u_{mf}(\mathbf{x}_1)$ are bounded by $O(c^{1/2})$ as shown in Appendix B. Inserting (6.18) and (6.19) into (6.17) and the result into (6.16) yields:

$$\mathbf{F}_0 = \frac{(1 + \sqrt{3c})}{S}\int_{\partial\Omega}[\mathbf{F}_{mf}(\mathbf{x}) - 3c]d\mathbf{x} + O(c^{3/2}) \tag{6.20}$$

which is equivalent to (6.13).

As indicated, $\mathbf{F}_0$ reproduces the mean-field result. Subtraction of the quantity $3c$ reflects the excluded hard-sphere volume. The leading reactant flux is order $c^{1/2}$ for $\phi >> 1$ therefore this consequence of the hard-sphere distribution is a higher-order effect but it affects the solution at leading order in the case $\phi = O(1)$. The multiplicative factor, $(1 + \sqrt{3c})$, reflects the second-order screening effect of the spheres in the material upon the fixed sphere. This effect clearly yields a higher-order enhancement of the mean-field solution for all ϕ.

The terms $\mathbf{F}_1$ and $\mathbf{F}_2$ result from the sphere-boundary interaction. $\mathbf{F}_1$ is the additional reactant flux induced by the first reflection disturbance of the boundary and $\mathbf{F}_2$ is the additional flux induced by the second and all higher-order reflections. Both contributions are necessarily positive for all domains; the sphere-boundary interaction enhances the predicted reactant flux relative to the mean-field solution. The excluded hard-sphere volume reduces the influence of the sphere-boundary interaction by restricting the range of integration in Equations (6.14) and (6.15). $\mathbf{F}_1$ is order c for $\phi = O(1)$ but yields a stronger, order $c \ln c$ contribution for $\phi >> 1$ as illustrated below. By construction, $\mathbf{F}_2$ is order c for all ϕ.

The foregoing corrections to mean-field solution have opposing effects upon the predicted reactant flux. The enhancing effects of second-order screening and the sphere-boundary interaction are countered by the reducing effect of the excluded hard-sphere volume. We shall define, Δ, the relative correction to the mean-field:

$$\Delta = \frac{\langle \mathbf{F} \rangle - \mathbf{F}_{mf}(c,R)}{\mathbf{F}_{mf}(c,R)} = \frac{\sqrt{3c}\mathbf{F}_{mf} + \mathbf{F}_1 + \mathbf{F}_2 - 3c}{\mathbf{F}_{mf}} \tag{6.21}$$

where we have employed Equations (6.12) and (6.13). For a semi-infinite domain, we can insert Equation (5.2) into (6.13) to obtain the interesting result:

$$\mathbf{F}_0(c) = \sqrt{3c} = \mathbf{F}_{mf} \tag{6.22}$$

which states that the effects of second-order screening and the excluded hard-sphere volume just cancel each other in this case. The remaining contribution to Δ from the sphere-boundary interaction is positive for all c as is, therefore, the net correction to the mean-field solution. Thus, the present results show an enhancement to the mean-field solution in the case $\phi >> 1$ for all dilute c for which the analysis is valid. We shall examine Δ quantitativly for more general ϕ below.

According to Appendix B, the truncation given by Equation (4.5) induces an order $c^{3/2} \ln c$ error, and the approximation for $\mathbf{B}(c)$ given by Equation (6.10) and derived in Appendix D induces an error of the same order of magnitude. Approximations (6.3) and (6.6) are exact to higher order. Therefore, we conclude that the above procedure yields a solution valid to order c with an error bounded by order $c^{3/2} \ln c$ for all bounded and semi-infinite domains. We summarize the general procedure for determining the flux of reactant into an arbitrary domain, Ω:

(i) Equation (4.4) is solved with boundary condition (2.9) yielding $u_{mf}(\mathrm{x})$.

(ii) The first reflection disturbance field is determined for Equation (4.5) with boundary conditions (6.5) and (6.6) yielding $\mathbf{H}^{(1)}(\mathrm{x}_1, c)$ Laplace's equation is solved exactly with the same boundary conditions yielding $\mathbf{J}(\ bfx_1)$.

(iii) The flux of reactant is given by the sum of (6.13)-(6.15).

7 Spherical and Semi-Infinite Domains

In the present section, the foregoing procedure is applied to determine the reactant flux into a spherical and a semi-infinite domains to order c. For the spherical domain, we will consider $1 < R < \infty$ and obtain a solution *uniformly* valid in the normalized domain radius R. The screening modulus is given by (5.3). As demonstrated by

Equation (5.7) for the mean-field solutions, the flux into a semi-infinite domain is the limiting case of that for a spherical domain for $\phi \to \infty$ (or, equivalently, $R \to \infty$ for fixed volume fraction, c). We can obtain an analytical result for the semi-infinite domain and, therefore, will analyze the case R finite and $R \to \infty$ separately.

For a semi-infinite domain, $u_{mf}(\mathbf{x})$ is given by (5.1). $\mathbf{F}_0(c)$ was previously determined and is displayed in Equation (6.22). The first reflection disturbance, $\mathbf{H}^{(1)}(\mathbf{x}_1, c)$, is determined according to Equation (4.5) with boundary conditions (6.5) and (6.6). Application of the "method of images" (Jackson, (1962)) facilitates determination of the reflection disturbances induced by the boundary. Accordingly, the plane boundary is replaced by an appropriate image sphere. The first reflection disturbance is found by the method of reflections and the result inserted into (6.14) to yield:

$$\mathbf{F}_1(c) = 3c \int_1^\infty \frac{e^{-3\sqrt{3c}\ x}}{2x} dx \tag{7.1}$$

where integration parallel to the boundary has canceled the factor S in Equation (6.14) and the remaining integration is in the normal direction to the boundary. The exponential integral above can be analytically evaluated to order c, yielding:

$$\mathbf{F}_1(c) = -\frac{3}{4} c \ln c - 3c \left(\frac{3}{4} \ln 3 + \frac{1}{2} \gamma \right) + O\left(c^{3/2}\right) \tag{7.2}$$

where $\gamma = 0.57722\cdots$ is Euler's constant. We obtain the exact solution to Laplace's equation in bi-spherical co-ordinates (Jeffery (1912)) yielding $\mathbf{L}(\mathbf{x}_1)$ defined by (D.1). The first reflection disturbance for Laplace's equation is determined by the method of images and inserted together with $\mathbf{L}(\mathbf{x}_1)$ into (D.6) and the result into Equation (6.15) to obtain:

$$\mathbf{F}_2(c) = 3c \int_1^\infty \mathbf{J}(x) dx \tag{7.3}$$

where the integration is normal to the boundary and S has been cancelled as in

Equation (7.1). Equation (7.3) is numerically evaluated yielding:

$$\mathbf{F}_2(c) = 3c(0.47472\cdots) \tag{7.4}$$

with numerical accuracy as shown. Equations (6.22), (7.2) and (7.4) are summed according to (6.12) to yield the reactant flux into a semi-infinite domain to order c with an order $c^{3/2}\ln c$ error:

$$\mathbf{F}(c) = \sqrt{3c} - \frac{3}{4}c\ln c - 3c\left(\frac{3}{4}\ln 3 + \frac{1}{2}\gamma - 0.47472\right) + O\left(c^{3/2}\ln c\right) \tag{7.5}$$

The mean-field result, given by Equation (5.2), is reproduced by the first term. The first reflection with the boundary affects the solution at order $c\ln c$ and is the strongest correction to the mean-field solution. This observation supports the foregoing assertion that neglecting the sphere-boundary interaction introduces an order $c\ln c$ error for $\phi >> 1$. Higher-order reflections with the boundary produce an order c effect. The neglected two-sphere interactions produce an error of order $c^{3/2}\ln c$ as shown in Appendix B. The above result demonstrates that the interaction of the spheres with the boundary is the leading order correction to the mean-field, dominating two-sphere interactions.

Next we analyze the more general case of a spherical domain with dimensionless radius R. In this case, the spherical symmetry implies that the quantities: $u_{mf}(\mathbf{x}_1)$, $\mathbf{J}(\mathbf{x}_1)$ and $\mathbf{H}(\mathbf{x}_1, c)$ (for fixed c) depend only on r, the radial distance from the center of the domain. Therefore the angular integration yields 4π, and the surface area, S, is $4\pi R^2$ thus, the net effect is $1/R^2$.

In this case, $u_{mf}(\mathbf{x})$ is given by (5.4) and $\mathbf{F}_{mf}$ by (5.5). According to Equation (6.13), we obtain:

$$\mathbf{F}_0(c, R) = (1 + \sqrt{3c})\left[\frac{1}{R}(\phi\coth\phi - 1)\right] - 3c \tag{7.6}$$

The method of images can be used again to determine the first reflection disturbance and Equation (6.14) yields:

$$\mathbf{F}_1(c,R) = \frac{3c}{\sinh(\phi)} \int_0^{R-1} \frac{\sinh(\sqrt{3c}r)}{R^2-r^2} \exp\left(-\sqrt{3c}\,\frac{R^2-r^2}{r}\right) r\,dr \qquad (7.7)$$

The exact solution to Laplace's equation is again available in bi-spherical coordinates and is inserted into (D.6) with the first reflection disturbance for Laplace's equation. Inserting the result into Equation (6.15) yields:

$$\mathbf{F}_2(c,R) = \frac{3c}{R^2} \int_0^{R-1} \mathbf{J}(r) r^2\,dr \qquad (7.8)$$

Equations (7.7) and (7.8) are readily evaluated numerically and the three contributions summed according to (6.12) to yield the reactant flux into a spherical domain to order c with an error of order $c^{3/2}\ln c$. By construction, the solution is uniformly valid in R.

The mean-field result, given by Equation (5.5), is recovered in the first term which is order c for $\phi = O(1)$ as asserted by (5.6). The second and third contributions resulting from the sphere-boundary interaction also affect the solution at order c for $\phi = O(1)$. The contribution from the first reflection, $\mathbf{F}_1(c,R)$, rises to order $c\ln c$ as $R \to \infty$ while higher order reflections affect the solution at order c for all R. Neglected two-sphere interactions produce, at most, an order $c^{3/2}\ln c$ error according to Appendix B. In general, each of the above contributions to the reactant flux becomes equal to the corresponding term in the semi-infinite solution for $R \to \infty$.

The above solution demonstrates that, in general, the interaction of the spheres with the boundary must be included in the analysis even at leading order. This effect dominates two-sphere interactions uniformly for all R.

8 Numerical Solution

We will now investigate the dependence of the above solutions on the parameters c and R in a range of practical importance. In compliance with the diluteness assumption, we restrict our attention to $c \leq 0.01$. For practical application, we are usually interested in the case where the number of spherical sinks in the domain is large. $N >> 1$ implies $R >> c^{-1/3}$ thus, for $c = 0.01$, we shall consider R in the range $5 << R < \infty$ and for $c = 0.0001$, in the range $22 << R < \infty$. The semi-infinite and spherical domains were considered separately above; however, for purpose of examining parametric dependence, the flux into a semi-infinite domain is considered as the limiting result for that into a spherical domain as $R \to \infty$.

Figure (1) shows the reactant flux into the domain as a function of c for several values of R including $R \to \infty$ (semi-infinite domain). For fixed c, the flux increases with R and approaches the semi-infinite domain flux as $R \to \infty$. For small values of c and R, the logarithm of reactant flux depends approximately linearly upon $\log_{10} c$ with unit slope suggesting order c overall dependence, but changes to slope $1/2$ indicating $c^{1/2}$ behavior for larger values.

Figure (2) shows the approach of $\mathbf{F}(c, R)$ to $\mathbf{F}(c)$ as a function of ϕ (defined by (5.3)) for a few fixed volume fractions. The figure indicates that $\mathbf{F}(c, R)$ is a monotonically increasing with ϕ and bounded above by $\mathbf{F}(c)$ which corresponds to $\phi \to \infty$. $\mathbf{F}(c, R)/\mathbf{F}(c)$ is well described by the single parameter, ϕ, over the range shown and becomes essentially independent of ϕ for $\phi > 30$. The figure indicates that for $\phi = 10$, the flux into a spherical domain is about 90% of that into a semi-infinite domain and increases to within about 1% for $\phi = 100$. Thus, $\phi \geq 100$ can be used as an approximate criterion for application of Equation (7.5). The qualitative features of Figure (2) hold for all bounded domains with ϕ defined, more generally,

by Equation (4.3).

Finally, we are interested in the relative correction to the mean-field solutions displayed in Equations (5.2) and (5.5). We define $\Delta(c,R)$ according to Equation (6.21) for a spherical domain and, similarly, $\Delta(c)$ for a semi-infinite domain. Figure (3) shows $\Delta(c,R)$ as a function of R for several fixed values of c. The dashed lines give $\Delta(c)$ as the large R asymptote for each fixed volume fraction. The relative correction to the mean-field solutions is significant. The correction is positive for all R which satisfy: $R >> c^{-1/3}$ as required for $N >> 1$. $\Delta(c,R)$ changes sign for very small values of R corresponding to $N = O(1)$ but this range is of little practical significance. Both $\Delta(c)$ and $\Delta(c,R)$ increase monotonically with volume fraction over the range of R shown. For $c = 0.01$ and 0.001, $\Delta(c,R)$ increases monotonically with R and is bounded above by $\Delta(c)$. However, for $c = 0.0001$, $\Delta(c,R)$ exceeds $\Delta(c)$ for $R > 15$ and exhibits a well-defined maximum at $R \approx 33$. In general, we found that $\Delta(c,R)$ exceeds $\Delta(c)$ for a finite range of R and exhibits a maximum for all c below approximately 0.0007. The maximum becomes more pronounced with increased dilution but its location is approximately constant.

9 Ash Vaporization in Coal; A Practical Application

The vaporization of refractory oxides during pulverized coal combustion is an important physical process relevant to the study of particulate emissions. Studies have shown that fly-ash produced during pulverized coal combustion is bimodally distributed by particle size. The smaller size group results from the vaporization and subsequent condensation of a small fraction of the mineral matter initially contained in the coal. These smaller particles which are difficult to remove by particulate con-

trol devices pose a health hazard and reduce visibility. Inasmuch as mineral matter is distributed in particulate form within the char particles, vaporization of mineral components via reaction on the mineral particle surface and diffusion through the char particle can be analyzed by the methods of this paper.

Quann and Sarofim (1982) performed a number of combustion experiments and measured the vaporization of silicon, magnesium and calcium. They analyzed their results assuming spherical char particles containing a random, monodisperse distribution of spherical mineral inclusions. During combustion, the mineral material is exposed to a reducing environment resulting from the carbon monoxide atmosphere within the burning char. The mineral matter is reduced to a volatile suboxide or metal on the surface of the inclusions via the heterogeneous reduction reaction:

$$MO_n(s) + CO \rightleftharpoons MO_{n-1}(g) + CO_2 \tag{9.1}$$

where MO_n refers to the refractory oxide (SiO_2, CaO, MgO) and MO_{n-1} to the corresponding volatile suboxide (SiO) or metal (Ca, Mg) vapor. Each mineral inclusion acts as a source of the metal suboxide with strength given by the local equilibrium vapor pressure,

$$y_e = \sqrt{K_e P_{CO}} \tag{9.2}$$

where K_e is the equilibrium constant for the reaction displayed in (9.1). The partial pressure of carbon monoxide, P_{CO}, is uniform throughout the char and is obtained by assuming that oxygen is completely consumed at the char surface and CO is the only product. Thus, according to Equation (9.2), y_e is a constant value on all inclusion surfaces therefore, boundary condition (2.4) is satisfied. The vapor pressure at the char surface satisfies boundary condition (2.5).

Quann and Sarofim calculated the flux of the vaporized mineral component using the mean-field solution, Equation (5.5). We now evaluate the importance

of the higher-order correction for the range of parameter values relevant to their problem. The volume fraction of spherical inclusions, c, was fixed at 0.01 and the screening modulus was considered in the range: $5 \leq \phi \leq 20$. Then, according to Equation (5.3), the normalized particle radius is in the range: $29 \leq R \leq 115$. Figure (3) indicates that for this choice of parameters the enhancement to the mean-field solution is about 10 % for $R = 29$ and about 12 % for $R = 115$.

10 Conclusions

A detailed analysis was presented for determining the reactant flux into a composite material containing reactive, randomly-located, spherical particles. The governing equations were configurationally averaged yielding an infinite hierarchy of coupled equations. The hierarchy was truncated using physical considerations of screening and diluteness of the spherical phase. A general asymptotic solution was obtained valid to order c for all bounded and semi-infinite domains. The solution reproduces the mean-field result and includes the effects of three previously neglected interactions. These are the sphere-boundary reflections, the hard-sphere interaction between the spheres and the boundary, and the screening effect of spheres in the domain upon a fixed test sphere (second-order screening). Each of these interactions dominate the effect of two-sphere interactions which affect the solution at order $c^{3/2} \ln c$.

Explicit consideration was given to the case in which the domain is spherical or semi-infinite and a solution was obtained for each. The latter solution has a particularly simple form and exhibits non-analytic dependence on c. The solution for a spherical domain exhibits analytic dependence on c and depends in a non-trivial manner upon R for $\phi << 1$. The transition to the semi-infinite solution behavior

is well characterized by a screening modulus, ϕ. The corrections to the mean-field generally enhance the predicted reactant flux. In an application to the problem of ash vaporization in coal during pulverized coal combustion, the correction to the mean-field solution was on the order of 10 %.

Acknowledgement

The authors wish to acknowledge useful discussions with Professor A. Acrivos.

Nomenclature

Roman Symbols

a	sphere radius
$\mathbf{B}$	defined by Equation (6.8)
c	volume fraction of particulate phase
D	diffusivity of supporting matrix
$\mathbf{F}$	total dimensionless reactant flux
$\mathbf{F}_0$	flux from incident field (Equation (6.13))
$\mathbf{F}_1$	flux from first reflection disturbance (Equation (6.14))
$\mathbf{F}_2$	flux from higher-order reflections (Equation (6.15))
$\mathbf{H}$	defined by Equation (6.9)
$\mathbf{H}^{(1)}$	defined by Equation (D.4)
$\mathbf{J}$	defined by Equation (D.6)
$\mathbf{L}$	defined by Equation (D.1)
L_c	characteristic dimension of domain
L_s	characteristic screening length
mf	mean-field result
R	domain radius normalized by sphere radius, a
S	surface area of domain boundary

Greek Symbols

Δ	relative correction to mean-field (Equation (6.21)
Ω	domain
$\bar{\Omega}$	restricted domain (Equation (3.21))
$\partial\Omega$	domain boundary
ϕ	screening modulus (Equation (4.3))

References

1. Brinkman, H. C., 1947, A calculation of the viscous force exerted by a flowing fluid on a dense swarm of particles. *Appl. Sci. Res. A* **1**, 27.

2. Chang, E.Y., Yendler, B.S. and Acrivos, A., 1986, A model for estimating the effective thermal conductivity of a random suspension of spheres. *Proceedings of the SIAM Workshop on Multiphase Flow.*

3. Chang, E.Y. and Acrivos, A., 1987, The conduction of heat from a planar wall with uniform surface temperature to a monodisperse suspension of spheres. *J. Appl. Phys.* **62**, (3), 771-776.

4. Chibata, I. and Wingard, L.B., 1983, *Applied Biochemistry and Biotechnology*, vol. 4: *Immobilized Microbial Cells.* New York: Academic Press.

5. Felderhof, B.U. and Deutch, J.M., 1976, Concentration dependence of the rate of diffusion-controlled reactions. *J. Chem. Phys.* **64**, (11), 4551-4558.

6. Happel, J. and Brenner, H., 1965, *Low Reynolds Number Hydrodynamics.* New York: Prentice Hall.

7. Hinch, E.J., 1977, An averaged-equation approach to particle interactions in a fluid suspension. *J. Fluid Mech.***83**, 695-720.

8. Jackson, J.D., 1962, *Classical Electrodynamics.* New York: John Wiley & Sons, Inc.

9. Jeffery, G. B., 1912, On the form of the solution of Laplace's equation suitable for problems relating two spheres. *Proc. R. Lond. A* **87**, 109-120.

10. Jeffrey, D. J., 1973, Conduction through a random suspension of spheres. *Proc. R. Lond. A* **335**, 355-367.

11. Mattern, K. and Felderhof, B.U., 1986, Rate of diffusion-controlled reactions in a random array of monopole sinks. *Physica* **135A**, 505-518.

12. Mattern, K. and Felderhof, B.U., 1987, Rate of diffusion-controlled reactions in a random array of spherical sinks. *Physica* **147A**, 1-20.

13. Muthukumar, M. and Cukier, R.I., 1981, Concentration dependence of diffusion-controlled processes among stationary reactive sinks. *J. Stat. Phys.* **26**, 453-469.

14. Muthukumar, M., 1982, Concentration dependence of diffusion-controlled processes among static traps. *J. Chem. Phys.* **76**, (5), 2667-2671.

15. Reed, T.M. and Gubbins, K.E., 1973, *Applied Statistical Mechanics.* New York: Mcgraw-Hill.

16. Smoluchowski, M. V., 1916, Drei Vortrage uber Diffusion Brownische Bewegung und Koagulation von Kolloidteilchen. *Phys. Z.* **17**, 557-585.

17. Quann, R.J. and Sarofim, F., 1982, Vaporization of refractory oxides during pulverized coal combustion. *19^{th} Symposium (International) on Combustion, The Combustion Institute*, 1429-1440.

18. Ziman, J.M., 1979, *Models of Disorder.* Cambridge: Cambridge University Press.

Appendix A:

Configurational Averaged Equations

In this appendix, we present a detailed derivation of the configurationally averaged equations (3.1) - (3.4). Although the technique has been employed by others (e.g., Hinch (1977)), a self-contained derivation is useful. The starting point is replacing boundary condition (2.8) on the sphere surfaces by a sink term consisting of a distribution of singularities on the sphere surfaces with strength given by the normal field derivative at each point. Laplace's equation then becomes:

$$\nabla^2 u(\mathbf{x}|\mathbf{x}_1,\cdots,\mathbf{x}_N) = \sum_{i=1}^{N} \int_{\|\xi-\mathbf{x}_i\|=1} \frac{\partial}{\partial n} u(\xi|\mathbf{x}_1,\cdots,\mathbf{x}_N)\delta(\xi-\mathbf{x})d\xi \qquad (A.1)$$

which is valid for all $\mathbf{x}$ in Ω and the solution of which must satisfy boundary condition (2.9) on $\partial\Omega$. Excepting the sphere surfaces where it is singular, the sink term vanishes everywhere in the domain. The set of position vectors, $\{\mathbf{x}_1,\cdots,\mathbf{x}_N\}$, locate the N indistinguishable sphere centers contained in Ω and constitutes a configuration of the spheres. The sink term in Equation (A.1) can be simplified by decomposing the 3-dimensional Dirac delta function into a product of three one-dimensional delta functions and performing the angular integration on each sphere surface eliminating all but a single one-dimensional delta function. Inserting the result into (A.1) yields:

$$\nabla^2 u(\mathbf{x}|\mathbf{x}_1,\cdots,\mathbf{x}_N) = \sum_{i=1}^{N} \frac{\partial}{\partial n} u(\mathbf{x}|\mathbf{x}_1,\cdots,\mathbf{x}_N)\delta(\|\mathbf{x}-\mathbf{x}_i\|-1) \qquad (A.2)$$

which provides the starting point for configurational averaging.

The configurational average of Equation (A.2) can be written formally as:

$$\langle\nabla^2 u(\mathbf{x}|\mathbf{x}_1,\cdots,\mathbf{x}_N)\rangle = \nabla^2\langle u(\mathbf{x})\rangle = \langle\sum_{i=1}^{N} \frac{\partial}{\partial n} u(\mathbf{x}|\mathbf{x}_1,\cdots,\mathbf{x}_N)\delta(\|\mathbf{x}-\mathbf{x}_i\|-1)\rangle \quad (A.3)$$

where we have used the fact that the configurational averaging operation commutes with any linear operator. The configurational average is given explicitly by an N-fold volume integration over the sphere positions weighted by a configurational probability. Thus, we can rewrite the averaged sink term as:

$$\langle \sum_{i=1}^{N} \frac{\partial}{\partial n} u(\mathbf{x}|\mathbf{x}_1, \cdots, \mathbf{x}_N) \delta(\|\mathbf{x} - \mathbf{x}_i\| - 1) \rangle =$$

$$\frac{1}{N!} \sum_{i=1}^{N} \int_{\Omega^N} \frac{\partial}{\partial n} u(\mathbf{x}|\mathbf{x}_1, \cdots, \mathbf{x}_N) \delta(\|\mathbf{x} - \mathbf{x}_i\| - 1) P(\mathbf{x}_1, \cdots, \mathbf{x}_N) d\mathbf{x}_1 \cdots d\mathbf{x}_N \qquad (A.4)$$

The function, $P(\mathbf{x}_1, \cdots, \mathbf{x}_N)$, is the distribution function for the configuration $\{\mathbf{x}_1, \cdots, \mathbf{x}_N\}$, and is normalized by (Reed and Gubbins (1973)):

$$\int_{\Omega^N} P(\mathbf{x}_1, \cdots, \mathbf{x}_N) d\mathbf{x}_1 \cdots d\mathbf{x}_N = N! \qquad (A.5)$$

We define a conditional distribution function for the configuration, $\{\mathbf{x}_1, \cdots, \mathbf{x}_N\}$, given that a sphere center is fixed at $\mathbf{x}_i$:

$$P(\mathbf{x}_1, \cdots, \mathbf{x}_N|\mathbf{x}_i) = \frac{P(\mathbf{x}_1, \cdots, \mathbf{x}_N)}{P(\mathbf{x}_i)} \qquad (A.6)$$

which is normalized by:

$$\int_{\Omega^{N-1}} P(\mathbf{x}_1, \cdots, \mathbf{x}_N|\mathbf{x}_i) d\mathbf{x}_1 \cdots d\mathbf{x}_N = (N-1)! \qquad (A.7)$$

Using the conditional distribution function, Equation (A.4) becomes:

$$\langle \sum_{i=1}^{N} \frac{\partial}{\partial n} u(\mathbf{x}|\mathbf{x}_1, \cdots, \mathbf{x}_N) \delta(\|\mathbf{x} - \mathbf{x}_i\| - 1) \rangle =$$

$$\frac{1}{N!} \sum_{i=1}^{N} \int_{\Omega^N} \frac{\partial}{\partial n} u(\mathbf{x}|\mathbf{x}_1, \cdots, \mathbf{x}_N) \delta(\|\mathbf{x} - \mathbf{x}_i\| - 1) P(\mathbf{x}_i) P(\mathbf{x}_1, \cdots, \mathbf{x}_N|\mathbf{x}_i) d\mathbf{x}_1 \cdots d\mathbf{x}_N \qquad (A.8)$$

Then, performing all but the i^{th} volume integration on each term in the sum yields, by definition, the conditional average of each with the i^{th} sphere center fixed:

$$\langle \sum_{i=1}^{N} \frac{\partial}{\partial n} u(\mathbf{x}|\mathbf{x}_1, \cdots, \mathbf{x}_N) \delta(\|\mathbf{x} - \mathbf{x}_i\| - 1) \rangle = \frac{1}{N} \sum_{i=1}^{N} \int_{\Omega} \frac{\partial}{\partial n} \langle u(\mathbf{x}|\mathbf{x}_i) \rangle \delta(\|\mathbf{x} - \mathbf{x}_i\| - 1) P(\mathbf{x}_i) d\mathbf{x}_i \qquad (A.9)$$

Since the spheres are indistinguishable, all terms in the sum are equal, hence:

$$\langle \sum_{i=1}^{N} \frac{\partial}{\partial n} u(\mathbf{x}|\mathbf{x}_1, \cdots, \mathbf{x}_N) \delta(\|\mathbf{x} - \mathbf{x}_i\| - 1) \rangle = \int_{\Omega} \frac{\partial}{\partial n} \langle u(\mathbf{x}|\mathbf{x}_1) \rangle \delta(\|\mathbf{x} - \mathbf{x}_1\| - 1) P(\mathbf{x}_1) d\mathbf{x}_1 \tag{A.10}$$

$P(\mathbf{x}_1)$ is the dimensionless number density of spheres given by:

$$P(\mathbf{x}_1) = a^3 n = \frac{3c}{4\pi} \quad \text{for all} \quad \mathbf{x}_1 \in \bar{\Omega}$$

$$P(\mathbf{x}_1) = 0 \quad \text{for all} \quad \mathbf{x}_1 \in \Omega - \bar{\Omega} \tag{A.11}$$

where n is the dimensional number density defined by (2.1) and $\bar{\Omega}$ is the domain Ω less the region within one dimensionless sphere radius of the boundary, $\partial\Omega$. In general, the boundary induces local structure into the material producing an order c relative deviation from the assumed uniform distribution in $\bar{\Omega}$ in the vicinity of the boundary (Ziman (1979)). This higher-order effect is neglected by the diluteness assumption.

Inserting (A.11) into Equation (A.10), performing the integration to eliminate the delta function and inserting the result into Equation (A.3) yields:

$$\nabla^2 \langle u(\mathbf{x}) \rangle = \frac{3c}{4\pi} \int_{\{\|\mathbf{x}-\mathbf{x}_1\|=1\} \cap \bar{\Omega}} \frac{\partial}{\partial n} \langle u(\mathbf{x}|\mathbf{x}_1) \rangle d\mathbf{x}_1 \tag{A.12}$$

which is the desired unconditionally averaged field equation.

Equation (A.12) couples the unconditionally averaged field to the conditionally averaged field with one sphere fixed at $\mathbf{x}_1$. The foregoing averaging procedure can be repeated to yield an equation for the conditionally averaged field with a sphere fixed at $\mathbf{x}_1$. We proceed as above, but only average Equation (A.2) over configurations which have a sphere fixed at $\mathbf{x}_1$:

$$\nabla^2 \langle u(\mathbf{x}|\mathbf{x}_1) \rangle = \langle \sum_{i=1}^{N} \frac{\partial}{\partial n} u(\mathbf{x}|\mathbf{x}_1, \cdots, \mathbf{x}_N) \delta(\|\mathbf{x} - \mathbf{x}_i\| - 1) \rangle_1 \tag{A.13}$$

where the subscript 1 on the angled brackets denotes the restriction to configurations with a sphere centered at $\mathbf{x}_1$. The conditionally averaged sink term is given explicitly by:

$$\langle \sum_{i=1}^{N} \frac{\partial}{\partial n} u(\mathbf{x}|\mathbf{x}_1, \cdots, \mathbf{x}_N) \delta(\|\mathbf{x} - \mathbf{x}_i\| - 1) \rangle_1 =$$

$$\frac{1}{(N-1)!} \sum_{i=1}^{N} \int_{\Omega^{N-1}} \frac{\partial}{\partial n} u(\mathbf{x}|\mathbf{x}_1, \cdots, \mathbf{x}_N) \delta(\|\mathbf{x} - \mathbf{x}_i\| - 1) P(\mathbf{x}_1, \cdots, \mathbf{x}_N|\mathbf{x}_1) d\mathbf{x}_2 \cdots d\mathbf{x}_N \tag{A.14}$$

By analogy with the foregoing procedure, we define a doubly conditional probability:

$$P(\mathbf{x}_1, \cdots, \mathbf{x}_N|\mathbf{x}_1, \mathbf{x}_i) = \frac{P(\mathbf{x}_1, \cdots, \mathbf{x}_N|\mathbf{x}_1)}{P(\mathbf{x}_i|\mathbf{x}_1)} \tag{A.15}$$

which is the distribution function of a configuration with spheres fixed at $\mathbf{x}_1$ and $\mathbf{x}_i$. $P(\mathbf{x}_1, \cdots, \mathbf{x}_N|\mathbf{x}_1, \mathbf{x}_i)$ is normalized by analogy to Equation (A.7):

$$\int_{\Omega^{N-2}} P(\mathbf{x}_1, \cdots, \mathbf{x}_N|\mathbf{x}_1, \mathbf{x}_i) d\mathbf{x}_2 \cdots d\mathbf{x}_N = (N-2)! \tag{A.16}$$

In terms of a doubly conditional probability, Equation (A.14) becomes:

$$\langle \sum_{i=1}^{N} \frac{\partial}{\partial n} u(\mathbf{x}|\mathbf{x}_1, \cdots, \mathbf{x}_N) \delta(\|\mathbf{x} - \mathbf{x}_i\| - 1) \rangle_1 =$$

$$\frac{1}{(N-1)!} \sum_{i=1}^{N} \int_{\Omega^{N-1}} \frac{\partial}{\partial n} u(\mathbf{x}|\mathbf{x}_1, \cdots, \mathbf{x}_N) \delta(\|\mathbf{x} - \mathbf{x}_i\| - 1) P(\mathbf{x}_i|\mathbf{x}_1) P(\mathbf{x}_1, \cdots, \mathbf{x}_N|\mathbf{x}_1, \mathbf{x}_i) d\mathbf{x}_2 \cdots d\mathbf{x}_N \tag{A.17}$$

Using the obvious relationships: $P(\mathbf{x}_1|\mathbf{x}_1) = 1$ and $P(\mathbf{x}_1, \cdots, \mathbf{x}_N|\mathbf{x}_1, \mathbf{x}_1) = P(\mathbf{x}_1, \cdots, \mathbf{x}_N|\mathbf{x}_1)$ and the normalization given by Equation (A.7), we can evaluate the first term in the summation:

$$\frac{1}{(N-1)!} \int_{\Omega^{N-1}} \frac{\partial}{\partial n} u(\mathbf{x}|\mathbf{x}_1, \cdots, \mathbf{x}_N) \delta(\|\mathbf{x} - \mathbf{x}_1\| - 1) P(\mathbf{x}_1|\mathbf{x}_1) P(\mathbf{x}_1, \cdots, \mathbf{x}_N|\mathbf{x}_1, \mathbf{x}_1) d\mathbf{x}_2 \cdots d\mathbf{x}_N$$

$$= \frac{\partial}{\partial n} \langle u(\mathbf{x}|\mathbf{x}_1) \rangle \delta(\|\mathbf{x} - \mathbf{x}_1\| - 1) \tag{A.18}$$

Inserting this result into Equation (A.17) then yields:

$$\langle\sum_{i=1}^{N}\frac{\partial}{\partial n}u(\mathbf{x}|\mathbf{x}_1,\cdots,\mathbf{x}_N)\delta(\|\mathbf{x}-\mathbf{x}_i\|-1)\rangle_1=\frac{\partial}{\partial n}\langle u(\mathbf{x}|\mathbf{x}_1)\rangle\delta(\|\mathbf{x}-\mathbf{x}_1\|-1)+$$

$$\frac{1}{(N-1)!}\sum_{i=2}^{N}\int_{\Omega^{N-1}}\frac{\partial}{\partial n}u(\mathbf{x}|\mathbf{x}_1,\cdots,\mathbf{x}_N)\delta(\|\mathbf{x}-\mathbf{x}_i\|-1)P(\mathbf{x}_i|\mathbf{x}_1)P(\mathbf{x}_1,\cdots,\mathbf{x}_N|\mathbf{x}_1,\mathbf{x}_i)d\mathbf{x}_2\cdots d\mathbf{x}_N \tag{A.19}$$

Then, proceeding as before, performing all but the i^{th} integration on each term in the sum yields the following expression for the conditionally averaged sink term:

$$\langle\sum_{i=1}^{N}\frac{\partial}{\partial n}u(\mathbf{x}|\mathbf{x}_1,\cdots,\mathbf{x}_N)\delta(\|\mathbf{x}-\mathbf{x}_i\|-1)\rangle_1=\frac{\partial}{\partial n}\langle u(\mathbf{x}|\mathbf{x}_1)\rangle\delta(\|\mathbf{x}-\mathbf{x}_1\|-1)+$$

$$\frac{1}{N-1}\sum_{i=2}^{N}\int_{\Omega}\frac{\partial}{\partial n}\langle u(\mathbf{x}|\mathbf{x}_1,\mathbf{x}_i)\rangle\delta(\|\mathbf{x}-\mathbf{x}_i\|-1)P(\mathbf{x}_i|\mathbf{x}_1)d\mathbf{x}_i \tag{A.20}$$

As before, each term in the sum is identical thus allowing the summation:

$$\langle\sum_{i=1}^{N}\frac{\partial}{\partial n}u(\mathbf{x}|\mathbf{x}_1,\cdots,\mathbf{x}_N)\delta(\|\mathbf{x}-\mathbf{x}_i\|-1)\rangle_1=\frac{\partial}{\partial n}\langle u(\mathbf{x}|\mathbf{x}_1)\rangle\delta(\|\mathbf{x}-\mathbf{x}_1\|-1)+$$

$$\int_{\Omega}\frac{\partial}{\partial n}\langle u(\mathbf{x}|\mathbf{x}_1,\mathbf{x}_2)\rangle\delta(\|\mathbf{x}-\mathbf{x}_2\|-1)P(\mathbf{x}_2|\mathbf{x}_1)d\mathbf{x}_2 \tag{A.21}$$

where we have arbitrarily labeled the second fixed center $\mathbf{x}_2$ thereby distinguishing it from $\mathbf{x}_1$ and the remaining $N-2$ sphere centers $P(\mathbf{x}_2|\mathbf{x}_1)$ is the conditional number density function given a sphere center at $\mathbf{x}_1$. This is related to the hard-sphere radial distribution function $g(\mathbf{x}_2|\mathbf{x}_1)$ (Ziman (1979)):

$$P(\mathbf{x}_2|\mathbf{x}_1)=P(\mathbf{x}_2)g((\mathbf{x}_2|\mathbf{x}_1)) \tag{A.22}$$

The radial distribution function contains the local structure induced by the sphere at $\mathbf{x}_1$. However, this local structure can be neglected by the diluteness assumption, therefore:

$$P(\mathbf{x}_2|\mathbf{x}_1)=P(\mathbf{x}_2)\qquad\|\mathbf{x}_1-\mathbf{x}_2\|\geq 2$$

$$P(\mathbf{x}_2|\mathbf{x}_1) = 0 \qquad \|\mathbf{x}_1 - \mathbf{x}_2\| < 2 \tag{A.23}$$

where $P(\mathbf{x}_2)$ is the single sphere distribution function defined by Equation (A.11).

Inserting (A.23) into (A.21) yields:

$$\langle \sum_{i=1}^{N} \frac{\partial}{\partial n} u(\mathbf{x}|\mathbf{x}_1, \cdots, \mathbf{x}_N) \delta(\|\mathbf{x} - \mathbf{x}_i\| - 1) \rangle_1 =$$

$$\frac{\partial}{\partial n} \langle u(\mathbf{x}|\mathbf{x}_1) \rangle \delta(\|\mathbf{x} - \mathbf{x}_1\| - 1) + \frac{3c}{4\pi} \int_{\{\|\mathbf{x}-\mathbf{x}_2\|=1\} \cap \bar{\Omega}_1} \frac{\partial}{\partial n} \langle u(\mathbf{x}|\mathbf{x}_1, \mathbf{x}_2) \rangle d\mathbf{x}_2 \tag{A.24}$$

where $\bar{\Omega}_1$ is defined by the intersection: $\bar{\Omega} \cap \{\|\mathbf{x}_1 - \mathbf{x}_2\| \geq 2\}$ and is the allowed portion of the domain for a second sphere center distinct from the center at $\mathbf{x}_1$. Then, inserting the above into Equation (A.13) and replacing the first term on the right side of (A.24) by the boundary condition on the sphere at $\mathbf{x}_1$ yields the first conditionally averaged field equation:

$$\nabla^2 \langle u(\mathbf{x}|\mathbf{x}_1) \rangle = \frac{3c}{4\pi} \int_{\{\|\mathbf{x}-\mathbf{x}_2\|=1\} \cap \bar{\Omega}_1} \frac{\partial}{\partial n} \langle u(\mathbf{x}|\mathbf{x}_1, \mathbf{x}_2) \rangle d\mathbf{x}_2 \qquad \|\mathbf{x} - \mathbf{x}_1\| > 1 \tag{A.25}$$

which, in addition to satisfying boundary condition (2.9) on $\partial\Omega$, must also satisfy (2.8) on the sphere surface fixed at $\mathbf{x}_1$.

The first conditionally averaged field equation, (A.25), is coupled to the second conditionally averaged field in the same manner as (A.12) is coupled to (A.25). Thus, the foregoing averaging process used to obtain the first conditionally averaged field equation is repeated to obtain the second. The result is:

$$\nabla^2 \langle u \rangle (\mathbf{x}|\mathbf{x}_1, \mathbf{x}_2) =$$

$$\frac{3c}{4\pi} \int_{\{\|\mathbf{x}-\mathbf{x}_3\|=1\} \cap \bar{\Omega}_2} \frac{\partial}{\partial n} \langle u \rangle (\mathbf{x}|\mathbf{x}_1, \mathbf{x}_2, \mathbf{x}_3) d\mathbf{x}_3 \qquad \|\mathbf{x} - \mathbf{x}_1\| > 1, \quad \|\mathbf{x} - \mathbf{x}_2\| > 1 \tag{A.26}$$

where $\bar{\Omega}_2$ is defined by the intersection: $\bar{\Omega} \cap \{\|\mathbf{x}_3 - \mathbf{x}_1\| \geq 2\} \cap \{\|\mathbf{x}_3 - \mathbf{x}_2\| \geq 2\}$ and is the allowed portion of the domain for a third sphere center distinct from the centers

at $\mathbf{x}_1$ and $\mathbf{x}_2$. The solution of Equation (A.26) must satisfy boundary condition (2.9) on $\partial\Omega$ and (2.8) on the surface of both fixed spheres and is analogously coupled to the conditionally averaged field with three spheres fixed.

As may now be apparent, the foregoing procedure may be repeated indefinitely producing an infinite hierarchy of coupled, conditionally averaged equations with an additional sphere fixed at each level.

Appendix B:

Truncation of Hierarchy

The hierarchy is truncated by exploiting the diluteness condition, $c << 1$, and employing Equation (4.1) which follows from the physics of screening: far from a fixed sphere, the influence of the sphere is "screened" by the presence of the intervening sinks in the material (Brinkman (1947)). The following derivation yields the closure Equations (4.4) and (4.5) which, when used in place of (3.2) *or* (3.3) respectively, transform the infinite hierarchy into a closed set of equations.

We commence the truncation procedure by observing that Equation (4.1) implies that the flux into a sphere fixed at $\mathbf{x}_2$ is relatively unaffected by the presence a sphere fixed at $\mathbf{x}_1$ for large separation, $\|\mathbf{x}_1 - \mathbf{x}_2\| >> L_s$:

$$\int_{\{\|\mathbf{x}-\mathbf{x}_2\|=1\}\cap\bar{\Omega}_1} \frac{\partial}{\partial n}\langle u(\mathbf{x}|\mathbf{x}_1,\mathbf{x}_2)\rangle d\mathbf{x}_2 \approx \int_{\{\|\mathbf{x}-\mathbf{x}_2\|=1\}\cap\bar{\Omega}} \frac{\partial}{\partial n}\langle u(\mathbf{x}|\mathbf{x}_2)\rangle d\mathbf{x}_2 \qquad (B.1)$$

where L_s is the "screening length" defined by Equation (4.2).

We introduce the function, $v(\mathbf{x}|\mathbf{x}_1)$:

$$v(\mathbf{x}|\mathbf{x}_1) = \langle u(\mathbf{x})\rangle - \langle u(\mathbf{x}|\mathbf{x}_1)\rangle \qquad (B.2)$$

Subtracting Equation (3.3) from Equation (3.2) and invoking the approximation (B.1), yields Laplace's equation:

$$\nabla^2 v(\mathbf{x}|\mathbf{x}_1) = 0 \qquad \|\mathbf{x} - \mathbf{x}_1\| > 1 \qquad (B.3)$$

with the boundary conditions:

$$v(\mathbf{x}|\mathbf{x}_1) = 0 \qquad \|\mathbf{x} - \mathbf{x}_1\| \to \infty \qquad (B.4)$$

$$v(\mathbf{x}|\mathbf{x}_1) = \langle u(\mathbf{x}_1)\rangle \qquad \|\mathbf{x} - \mathbf{x}_1\| = 1 \qquad (B.5)$$

(B.4) incorporates Equation (4.1) and is tantamount to neglecting the effect of sphere-boundary interactions. The validity of the approximation requires that most spheres are much further from the boundary than L_s or, equivalently, $\phi >> 1$ according to (4.3). (B.5) is obtained by neglecting local variations of $\langle u(\mathbf{x})\rangle$ on the surface of the sphere at $\mathbf{x}_1$ which are order $c^{1/2}$ as shown below.

The right-hand-side of Equation (3.2) expressed in terms of $v(\mathbf{x}|\mathbf{x}_1)$ is given by:

$$\frac{3c}{4\pi}\int_{\{\|\mathbf{x}-\mathbf{x}_1\|=1\}\cap\bar{\Omega}} \frac{\partial}{\partial n}\langle u(\mathbf{x}|\mathbf{x}_1)\rangle d\mathbf{x}_1 =$$

$$\subset ps\int_{\|\mathbf{x}-\mathbf{x}_1\|=1} \frac{\partial}{\partial n}\langle u(\mathbf{x})\rangle d\mathbf{x}_1 - \frac{3c}{4\pi}\int_{\|\mathbf{x}-\mathbf{x}_1\|=1} \frac{\partial}{\partial n} v(\mathbf{x}|\mathbf{x}_1) d\mathbf{x}_1 \qquad (B.6)$$

The first integral on the right side vanishes identically by symmetry and the second is determined by solution of Equation (B.3) with boundary conditions (B.4) and (B.5). The spherical symmetry of the boundary conditions yield a solution which is only a function of $\|\mathbf{x}-\mathbf{x}_1\|$ and is therefore symmetric with respect to $\mathbf{x}$ and $\mathbf{x}_1$. We can therefore write:

$$\int_{\|\mathbf{x}-\mathbf{x}_1\|=1} \frac{\partial}{\partial n} v(\mathbf{x}|\mathbf{x}_1) d\mathbf{x}_1 = \int_{\|\mathbf{x}-\mathbf{x}_1\|=1} \frac{\partial}{\partial n} v(\mathbf{x}_1|\mathbf{x}) d\mathbf{x}_1 \qquad (B.7)$$

which is immediately computed from the solution of (B.3) - (B.5):

$$-\frac{1}{4\pi}\int_{\|\mathbf{x}-\mathbf{x}_1\|=1} \frac{\partial}{\partial n} v(\mathbf{x}_1|\mathbf{x}) d\mathbf{x}_1 = \langle u(\mathbf{x})\rangle \qquad (B.8)$$

Combining Equations (B.6), (B.7) and (B.8) and inserting into Equation (3.2) yields the lowest order truncation:

$$\nabla^2\langle u(\mathbf{x})\rangle = 3c\langle u(\mathbf{x})\rangle \qquad (B.9)$$

which constitutes the "mean-field" approximation. The solution must satisfy boundary condition (2.9) and determines the reactant flux into the domain via Equation (2.10).

$\nabla\langle u(\mathbf{x})\rangle$ satisfies Equation (B.9) which is elliptic, therefore, by an appropriate maximum principle, each component of $\nabla\langle u(\mathbf{x})\rangle$ attains a maximum on $\partial\Omega$. According to the discussion following Equation (5.7), the component of $\nabla\langle u(\mathbf{x})\rangle$ normal to the boundary is bounded by order $c^{1/2}$. Boundary condition (2.9) implies that the tangential components of $\nabla\langle u(\mathbf{x})\rangle$ are zero on the boundary. Therefore, each component of $\nabla\langle u(\mathbf{x})\rangle$ is bounded by order $c^{1/2}$ which justifies the approximation embodied by Equation (B.5). This result is also employed to bound the error of the approximations (6.6) and (6.19).

The mean-field approximation neglects all sphere-sphere and sphere-boundary interactions of the spheres; only the collective screening effect of the spheres in the material is retained through the dissipative term in the equation. The leading order correction to the mean-field solution results from the interaction of the spheres with the boundary. In the following, we will truncate the hierarchy at the next level and thereby retain this effect which permits an order c solution for all domains within the scope of this paper.

A truncation analogous to that performed to obtain Equation (B.9) can be applied to the first conditionally averaged equation. By analogy to the argument used to obtain Equation (4.1), the field at $\mathbf{x}$ is relatively unaffected by the presence a sphere fixed at $\mathbf{x}_2$ for large separation, $\|\mathbf{x}-\mathbf{x}_2\| >> L_s$:

$$\langle u(\mathbf{x}|\mathbf{x}_1,\mathbf{x}_2)\rangle \sim \langle u(\mathbf{x}|\mathbf{x}_1)\rangle \qquad (B.10)$$

which, by analogy to (B.1), implies the flux into a sphere fixed at $\mathbf{x}_3$ is relatively unaffected by the presence a sphere fixed at $\mathbf{x}_2$ for large separation, $\|\mathbf{x}_2-\mathbf{x}_3\| >> L_s$:

$$\int_{\{\|\mathbf{x}-\mathbf{x}_3\|=1\}\cap\bar{\Omega}_2} \frac{\partial}{\partial n}\langle u\rangle(\mathbf{x}|\mathbf{x}_1,\mathbf{x}_2,\mathbf{x}_3)d\mathbf{x}_3 \sim \int_{\{\|\mathbf{x}-\mathbf{x}_3\|=1\}\cap\bar{\Omega}_1} \frac{\partial}{\partial n}\langle u(\mathbf{x}|\mathbf{x}_1,\mathbf{x}_3)\rangle d\mathbf{x}_3 \quad (B.11)$$

Invoking (B.11), we proceed as above and define the deviation function $v(\mathbf{x}|\mathbf{x}_1,\mathbf{x}_2) =$

$\langle u(\mathbf{x}|\mathbf{x}_1)\rangle - \langle u(\mathbf{x}|\mathbf{x}_1,\mathbf{x}_2)\rangle$ which satisfies Laplace's equation with the boundary conditions:

$$v(\mathbf{x}|\mathbf{x}_1,\mathbf{x}_2) = 0 \qquad \|\mathbf{x}-\mathbf{x}_2\| \to \infty \tag{B.12}$$

$$v(\mathbf{x}|\mathbf{x}_1,\mathbf{x}_2) = \langle u(\mathbf{x}_2|\mathbf{x}_1)\rangle \qquad \|\mathbf{x}-\mathbf{x}_2\| = 1 \tag{B.13}$$

where, by analogy to Equation (B.4), we have incorporated Equation (B.10) to obtain (B.12) thereby neglecting two-sphere interactions. An analysis of two-sphere interactions must include their coupled interaction with the domain boundary thus requiring treatment of a complex three-body interaction. Local (order $c^{1/2}$) variations of $\langle u(\mathbf{x}|\mathbf{x}_1)\rangle$ on the surface of the sphere at $\mathbf{x}_2$ have been neglected as in Equation (B.5).

Following the procedure given by Equations (B.6) - (B.8), yields the next higher-order truncation:

$$\nabla^2\langle u(\mathbf{x}|\mathbf{x}_1)\rangle = 3c\langle u(\mathbf{x}|\mathbf{x}_1)\rangle \tag{B.14}$$

where $\langle u(\mathbf{x}|\mathbf{x}_1)\rangle$ must satisfy boundary condition (2.8) on the fixed sphere surface and boundary condition (2.9) on the domain boundary. The solution determines the sink term for the unconditionally averaged equation according to Equation (3.2). Equation (B.14) is analogous to Equation (B.9) and is the mean-field approximation of the first conditionally averaged equation.

Truncation of the hierarchy with Equation (B.14) implies that the present analysis necessarily neglects two-sphere interactions which are confounded by the domain boundary as discussed above. For $\phi << 1$, the induced error is order c^2 as suggested by the heuristic argument below. We initially assert that the error introduced by neglecting two-sphere interactions is largest for $\phi >> 1$ and, accordingly, consider the solution error for a semi-infinite domain. Felderhof and Deutch (1976) showed that, neglecting solid boundaries, the effect of two-sphere interactions upon

$\mathbf{H}(\mathbf{x}_1; c)$, the normalized flux from a sphere, is order $c \ln c$. Inserting their result and the mean-field solution, $u_{mf}(\mathbf{x})$, for a semi-infinite domain (Equation (5.1)) into Equation (6.8) and the result into Equation (6.7) indicates that two-sphere interactions influence the reactant flux at order $c^{3/2} \ln c$ for a semi-infinite domain. The presence of solid boundaries reduces the effect of two-sphere interactions on $\mathbf{H}(\mathbf{x}_1; c)$ because the range of integration is restricted; however, we assume that for $\phi >> 1$, two-sphere interactions have the same order effect as the above result.

For the case $\phi << 1$, the overall effect of two-sphere interactions upon the reactant flux is order c^2 according to the following argument. A second sphere in an order one neighborhood of a test sphere affects the reactant flux into the test sphere at order one. The probability of a second sphere being located in such a neighborhood of a test sphere is c. Therefore, two-sphere interactions affect $\mathbf{H}(\mathbf{x}_1; c)$, the averaged dimensionless flux into a test sphere, at order c. For the case $\phi << 1$, $u_{mf}(\mathbf{x})$, is uniform and equal to unity as asserted by Equation (D.2). Inserting these results into Equation (6.8) and the result into (6.7) indicates that two-sphere interactions affect the solution at order c^2 for $\phi << 1$ as claimed above. Therefore, we conclude that the error introduced by the truncation is bounded by order $c^{3/2} \ln c$ for all domains considered in this paper.

The truncation procedure may, in principle, be performed at any level of the hierarchy thereby retaining the effect of an additional sphere with each higher level. Induction of the foregoing procedure to the second conditionally averaged equation yields the mean-field approximation of the second conditionally averaged equation:

$$\nabla^2 \langle u \rangle (\mathbf{x}|\mathbf{x}_1, \mathbf{x}_2) = 3c \langle u(\mathbf{x}|\mathbf{x}_1, \mathbf{x}_2) \rangle \qquad (B.15)$$

where $\langle u(\mathbf{x}|\mathbf{x}_1, \mathbf{x}_2) \rangle$ must satisfy boundary conditions on both fixed spheres and the domain boundary. The truncated hierarchy is then solved in reverse order as de-

scribed above. However, solution of Equation (B.15) is prohibitive thus confounding any attempt to adhere to such a program. In this paper, we employ the mean-field and first conditional mean-field approximations (Equations (4.4) and (4.5)) and abandon all higher-order truncations.

Appendix C:

Configurationally Averaged Reactant Flux

In the following, we apply the averaging techniques used in Appendix A to derive Equation (6.3), the configurationally averaged reactant flux on the boundary of the domain. The derivation begins with Equation (6.2) which is obtained via a steady-state material balance on the domain for a particular configuration of the spheres, $\{\mathbf{x}_1, \cdots, \mathbf{x}_N\}$. Following the procedure in Appendix A, the configurational average of (6.2) yields:

$$\langle \mathbf{F} \rangle = \frac{1}{S}\frac{1}{N!}\sum_{i=1}^{N}\int_{\Omega^N}\left[\int_{\|\mathbf{x}-\mathbf{x}_i\|=1}\frac{\partial}{\partial n}u(\mathbf{x}|\mathbf{x}_1,\cdots,\mathbf{x}_N)d\mathbf{x}\right]P(\mathbf{x}_i)P(\mathbf{x}_1,\cdots,\mathbf{x}_N|\mathbf{x}_i)d\mathbf{x}_2\cdots d\mathbf{x}_N \tag{C.1}$$

where we have expressed the configurational probability in terms of a conditional probability defined by Equation (A.6). Then following the procedure in Appendix A, we perform all but the i^{th} integration on each term in the sum yielding the conditional average of each with the i^{th} sphere center fixed. Equation (C.1) becomes:

$$\langle \mathbf{F} \rangle = \frac{1}{S}\frac{1}{N}\sum_{i=1}^{N}\int_{\Omega}\left[\int_{\|\mathbf{x}-\mathbf{x}_i\|=1}\frac{\partial}{\partial n}\langle u(\mathbf{x}|\mathbf{x}_i)\rangle d\mathbf{x}\right]P(\mathbf{x}_i)d\mathbf{x}_i \tag{C.2}$$

Each term in the sum is identical so that:

$$\langle \mathbf{F} \rangle = \frac{1}{S}\int_{\Omega}\left[\int_{\|\mathbf{x}-\mathbf{x}_1\|=1}\frac{\partial}{\partial n}\langle u(\mathbf{x}|\mathbf{x}_1)\rangle d\mathbf{x}\right]P(\mathbf{x}_1)d\mathbf{x}_1 \tag{C.3}$$

where we have arbitrarily labeled the fixed sphere center $\mathbf{x}_1$. Insering the approximate one-sphere distribution function defined by Equation (A.11) yields:

$$\langle \mathbf{F} \rangle = \frac{3c}{S}\int_{\bar{\Omega}}\left[\frac{1}{4\pi}\int_{\|\mathbf{x}-\mathbf{x}_1\|=1}\frac{\partial}{\partial n}\langle u(\mathbf{x}|\mathbf{x}_1)\rangle d\mathbf{x}\right]d\mathbf{x}_1 \tag{C.4}$$

which is the desired result expressing the average flux into the domain in terms of the average flux into a single sphere. Excepting the diluteness approximation embodied in the distribution function, (A.11), the above result is exact, albeit irreducible.

The approximate distribution function, $P(\mathbf{x}_1)$, given by Equation (A.11) neglects the local, order c relative deviations from the uniform probability. Deviations from the uniform value are only significant in a layer of (dimensionless) thickness one. Therefore, these deviations from a uniform distribution are integrable on the domain. Inspection of Equations (C.3) and (C.4) then imply that the solution error induced by neglecting the local structure in the material is order c^2. The same argument shows that the approximation made by employing the uniform distribution function given by Equation (A.23) induces an additional error of order c^3.

Appendix D:

Approximation of $\mathbf{B}(c)$

In the following, we derive an order one approximation for $\mathbf{B}(c)$ which, according to Equation (6.7), is sufficient to determine the reactant flux to order c. The derivation follows from a heuristic argument; a proof is not available. $\mathbf{B}(c)$ is given by (6.8) which requires $\mathbf{H}(\mathbf{x}_1; c)$ defined by Equation (6.9).

The mean-field equation (4.5) reduces to Laplace's equation in the dilute limit. We shall define $\mathbf{L}(\mathbf{x}_1)$ by Equation (6.9) for the case where $v(\mathbf{x}|\mathbf{x}_1)$ satisfies Laplace's equation. This definition implies:

$$\lim_{c\to 0} \mathbf{H}(\mathbf{x}_1; c) = \mathbf{L}(\mathbf{x}_1) \qquad (D.1)$$

which is uniformly valid on any bounded domain. Similalry Equation, (4.4), reduces to Laplace's equation in the limit $c \to 0$ implying that $u_{mf}(\mathbf{x}_1)$ is harmonic and satisfies boundary condition (2.9) in the dilute limit. Then, according to Equation (2.9):

$$\lim_{c\to 0} u_{mf}(\mathbf{x}_1) = 1 \qquad (D.2)$$

which is also uniformly valid on any bounded domain. Combining Equations (D.1) and (D.2), suggests the following approximation of (6.8) for $\mathbf{B}(c)$:

$$\mathbf{B}(c) \simeq \lim_{c\to 0} \frac{1}{S}\, int_{\bar{\Omega}} u_{mf}(\mathbf{x}_1)\mathbf{H}(\mathbf{x}_1; c)d\mathbf{x}_1 = \frac{1}{S}\int_{\bar{\Omega}} \mathbf{L}(\mathbf{x}_1) \qquad (D.3)$$

which requires that the above limit exist.

We claim that the above is valid for $\phi << 1$. Intuitively, we expect the screening terms of the mean-field equations equations (4.4) and (4.5) are relatively unimportant in the case $L_c << L_s$ ($\phi << 1$). According to this argument, Equation (4.4)

and (4.5) could be approximated by Laplace's equation which implies the validity of Equation (D.3). For the case $\phi << 1$, the reactant flux is order c which, according to Equation (6.7), implies that $\mathbf{B}(c)$ is order one thereby further supporting the existence of the required limit in (D.3). However, as shown above, for $\phi >> 1$ the leading order reactant flux is order $c^{1/2}$ Then, according to Equation (6.7), $\mathbf{B}(c)$ is order $c^{-1/2}$ which diverges as $c \to 0$. Therefore, the assumed limit in Equation (D.3) cannot exist for $\phi >> 1$.

The above approximation is remedied by subtracting the portion of the integrand which causes divergence in the limit $c \to 0$ and calculating its contribution to $\mathbf{B}(c)$ *exactly*. The contribution from the remaining, convergent portion of the integrand can be found to order one via (D.3). We assume the existence of a regular perturbation solution for $\mathbf{H}(\mathbf{x}_1; c)$ obtained by reflections with the boundary (Happel and Brenner (1965)):

$$\mathbf{H}(\mathbf{x}_1; c) = \sum_{k=0}^{\infty} \mathbf{H}^{(k)}(\mathbf{x}_1; c) \qquad (D.4)$$

where $\mathbf{H}^{(k)}(\mathbf{x}_1; c)$ is the contribution to $\mathbf{H}(\mathbf{x}_1; c)$ from the k^{th} reflection with the boundary. The existence of an analogous solution for $\mathbf{L}(\mathbf{x}_1)$ is also assumed with $\mathbf{L}^{(k)}(\mathbf{x}_1)$ defined by analogy to $\mathbf{H}^{(k)}(\mathbf{x}_1; c)$. We assert that the diverging portion of the integrand, $u_{mf}(\mathbf{x}_1)\mathbf{H}(\mathbf{x}_1; c)$, results from from the incident field contribution, $\mathbf{H}^{(0)}(\mathbf{x}_1; c)$, and, $\mathbf{H}^{(1)}(\mathbf{x}_1; c)$, the first reflection disturbance.

The foregoing suggests the revised approximation:

$$\mathbf{B}(c) \simeq \frac{1}{S} \int_{\bar{\Omega}} \left[u_{mf}(\mathbf{x}_1) \left[(1 + \sqrt{3c}) + \mathbf{H}^{(1)}(\mathbf{x}_1; c) \right] + \mathbf{J}(\mathbf{x}_1) \right] d\mathbf{x}_1 \qquad (D.5)$$

which we claim is valid to order one for all domains considered. The quantity $(1 + \sqrt{3c})$ is the contribution from the incident field and is boundary-independent; $\mathbf{H}^{(1)}(\mathbf{x}_1; c)$ is boundary-specific. $\mathbf{J}(\mathbf{x}_1)$ is the $c = 0$ approximation for the remaining

portion of the integrand in Equation (6.8) obtained according to (D.3):

$$\mathbf{J}(\mathbf{x}_1) = \sum_{k=2}^{\infty} \mathbf{L}^{(k)}(\mathbf{x}_1) = \mathbf{L}(\mathbf{x}_1) - \left[1 + \mathbf{L}^{(1)}(\mathbf{x}_1)\right] \qquad (D.6)$$

The contribution from the incident field, $\mathbf{L}^{(0)}(\mathbf{x}_1)$ is boundary-independent and equal to unity while $\mathbf{L}^{(1)}(\mathbf{x}_1)$ is boundary-specific.

The naive approximation given by Equation (D.3) is valid for $\phi << 1$ but diverges for $\phi >> 1$. This approximation was revised to accomodate the screening effect for dilute, non-zero c into the contributions to $\mathbf{H}(\mathbf{x}_1; c)$ resulting from the incident field and the first reflection disturbance. We now assert that the error induced by Equation (D.5) is largest for the case $\phi >> 1$. Thus, we shall consider the solution error induced by this approximation for a semi-infinite domain which is the limit $\phi \to \infty$. In this case, we can determine the error introduced to $\mathbf{B}(c)$ by substituting $\mathbf{L}^{(2)}(\mathbf{x}_1)$ for $\mathbf{H}^{(2)}(\mathbf{x}_1; c)$ is order $c^{1/2} \ln c$ and $\mathbf{L}^{(k)}(\mathbf{x}_1)$ for $\mathbf{H}^{(k)}(\mathbf{x}_1; c)$ for $k > 2$ is order $c^{1/2}$. The resulting error in the reactant flux is order $c^{3/2} \ln c$ and $c^{3/2}$ respectively as implied by (6.7). Then, according to the assumption that the largest error is induced for a semi-infinite domain, the solution error induced by approximation (D.5) is bounded by order $c^{3/2} \ln c$.

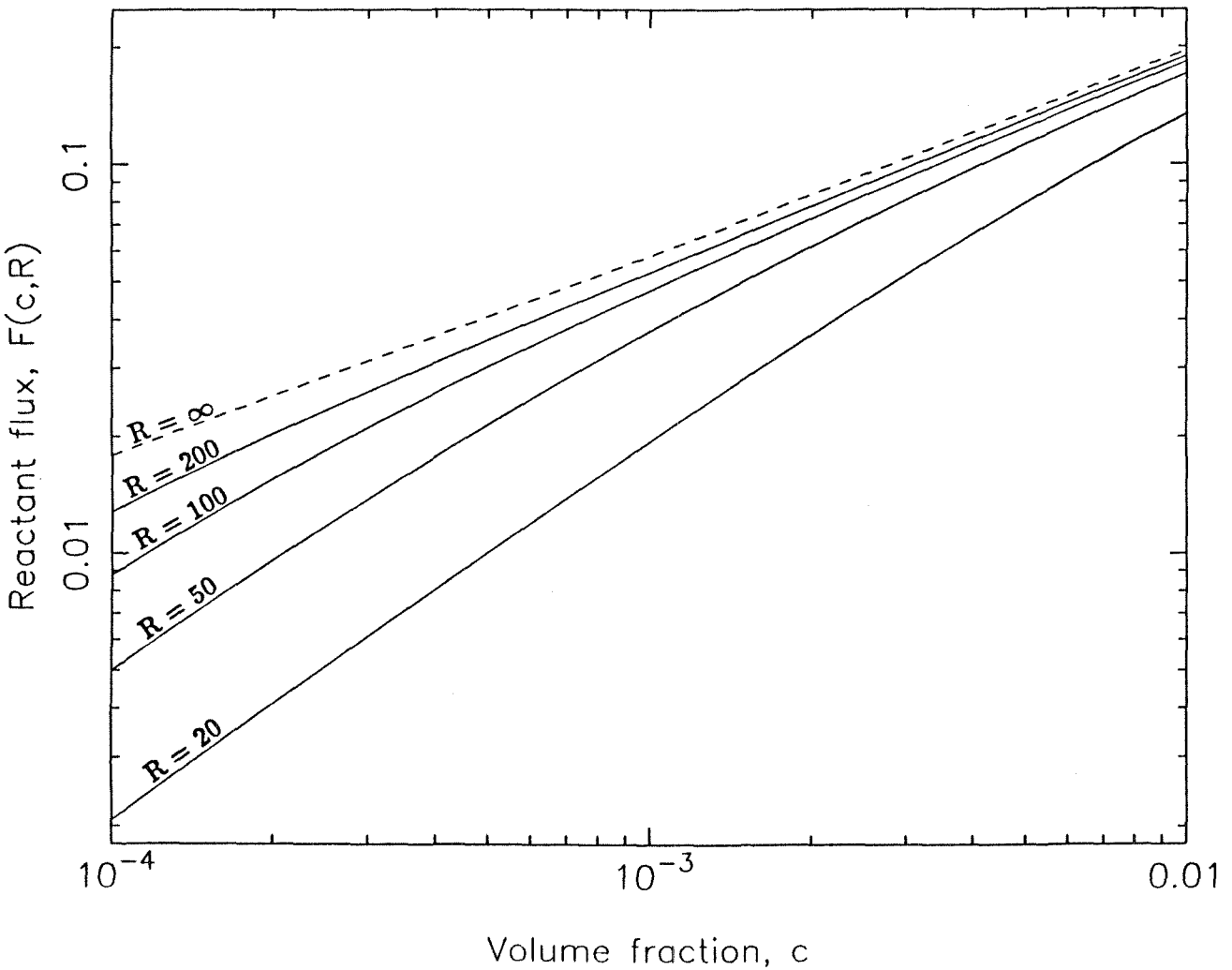

Figure 1: Reactant flux versus volume fraction of spheres.

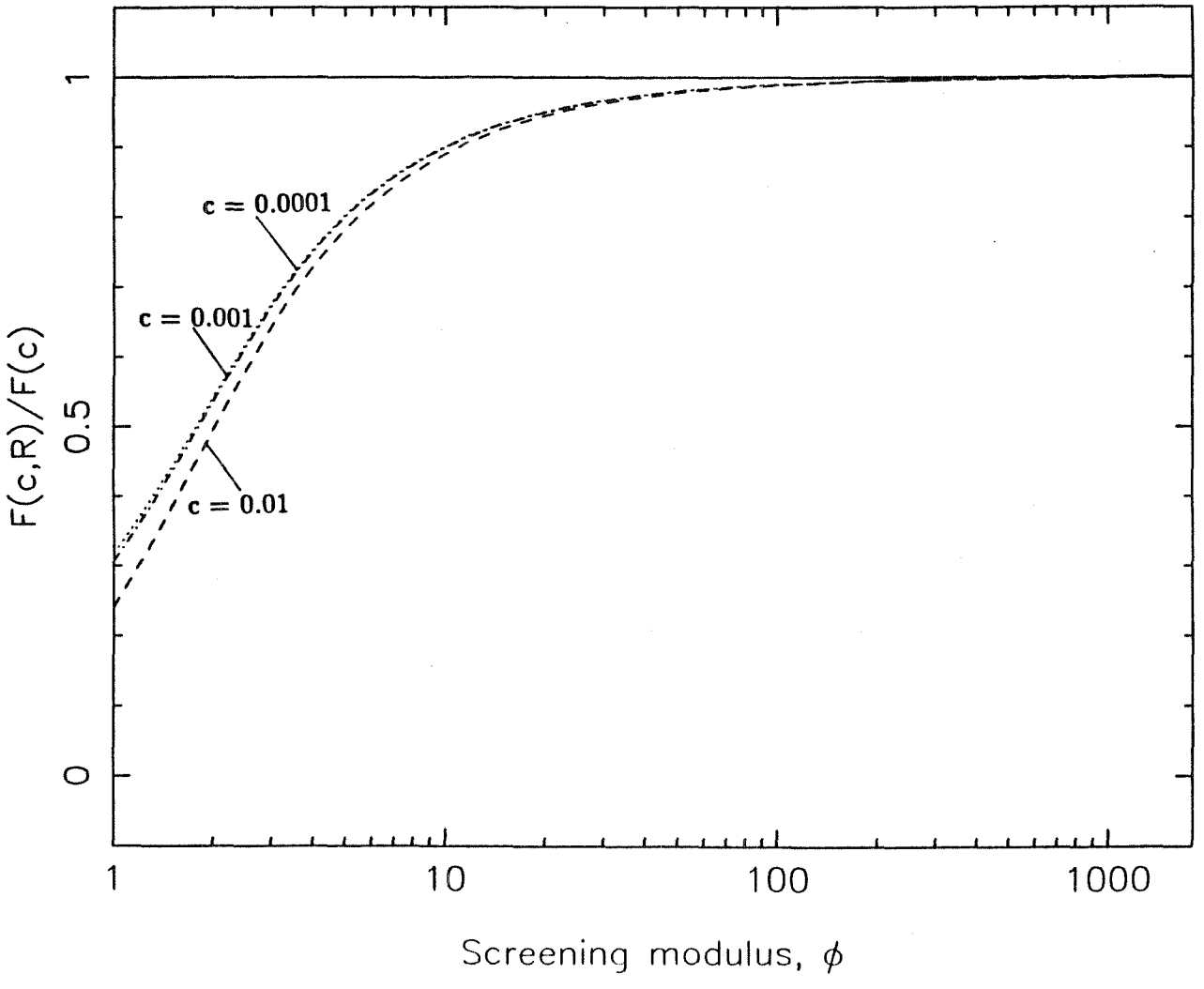

Figure 2: Approach to semi-infinite domain solution versus.

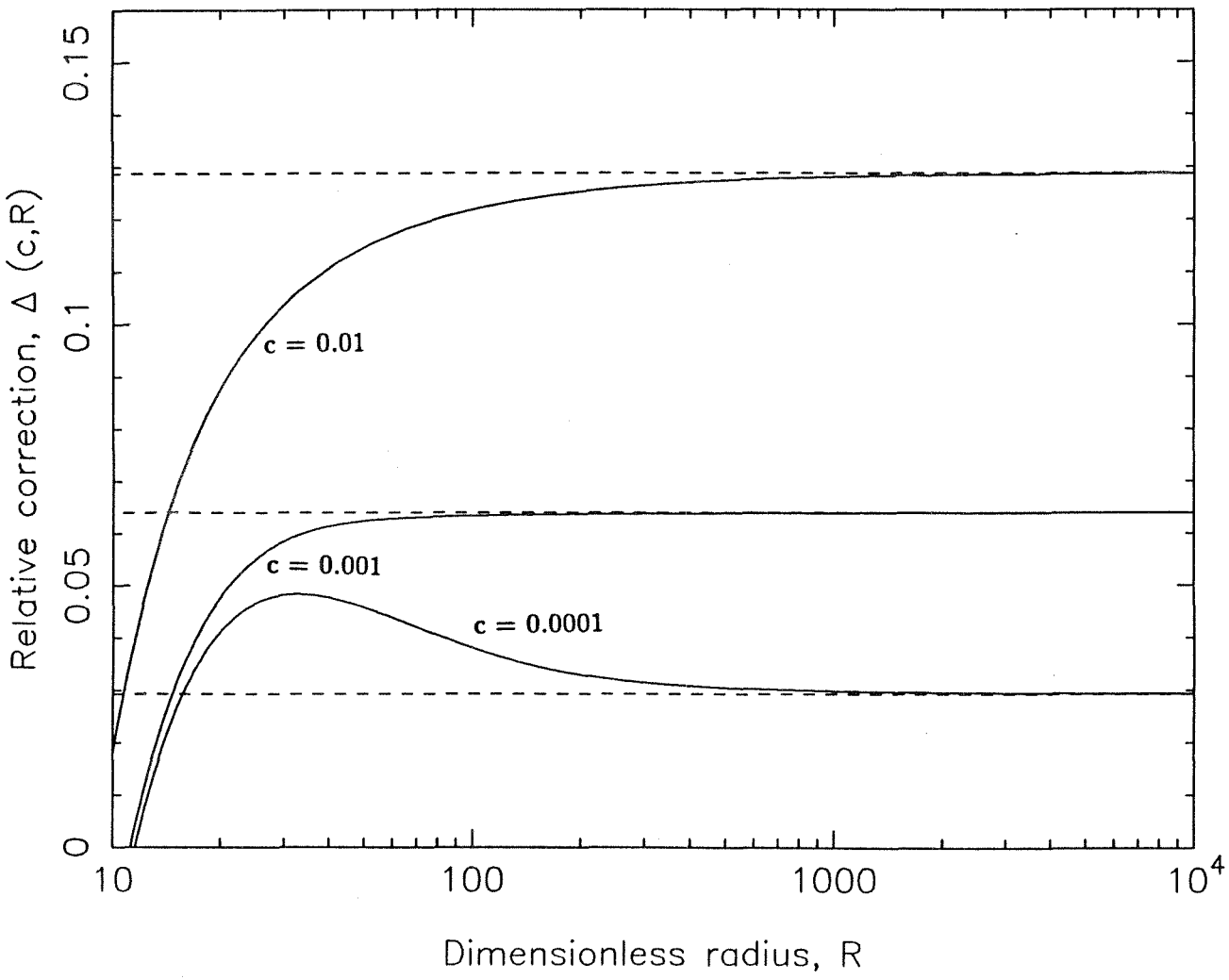

Figure 3: Correction to mean-field solution versus radius.

CHAPTER 6

Reactant Flux into a Medium Containing Spherical Sinks: The Time-Dependent Problem

Reactant Flux into a Medium Containing Spherical Sinks: The Time-Dependent Problem

M. Loewenberg and G. R. Gavalas
Department of Chemical Engineering 206-41
California Institute of Technology
Pasadena, California 91125

Abstract

A previous analysis is extended to determine the transient reactant flux into a material containing a random suspension of reactive, hard spheres. A configurational averaging approach is employed resulting in an infinite hierarchy of coupled equations which is truncated using physical considerations of screening and diluteness of the particulate phase. A uniformly valid, asymptotic solution is obtained for bounded and semi-infinite domains to order c with $O(c^{3/2} \ln c)$ error for long times. Numerical results are presented for a step change in concentration on the boundary of a spherical and semi-infinite domain. The solution exhibits algebraic decay initially and tends to the previously-obtained steady-state solution at long times.

1 Introduction

An important class of problems involves a distribution of discrete, reactive centers. Examples may be drawn from a variety of fields and include such diverse processes as ash vaporization during pulverized coal combustion, spray evaporation, suspension polymerization, fluorescence quenching and metabolic reactions in immobilized cell systems.

The theory of diffusion-controlled reactions was established by Smoluchowski (1916) who developed the mean-field approximation in an investigation on the growth of colloidal-sized particles. Most of the recent work in the area of diffusion-controlled reactions has focused on the steady-state problem (*e.g.*, Felderhof and Deutch 1976, Muthukumar 1982, Mattern and Felderhof 1986, 1987). The unsteady problem has been studied by Felderhof (1977) who determined a frequency-dependent rate coefficient which improved upon the early results of Smoluchowski by treating pair-wise interactions between reactive centers. His results are valid for long times and dilute volume fractions of the reactive particles. Bixon and Zwanzig (1981) exploited the techniques of multiple scattering to derive a configurationally averaged Green's function for the problem to first order in sink density. This approach was later refined by Felderhof, Deutch and Titulaer (1982) to account for the absence of concentration within the sinks. Tokuyama and Cukier (1982) studied non-local effects and used a scaling expansion approach to derive a local damping equation to describe the time-dependent concentration field.

The general approach followed in these papers is the formulation of an effective (time-dependent) reaction rate which characterizes the the bulk process. The implicit assumption is that macroscopic boundaries would be treated by application of the customary boundary conditions to the averaged governing equation involving an

effective rate constant. However, the boundary condition is ignored in the derivation of the rate constant. Such an approach neglects the details of the interaction between the macroscopic boundary and the reactive centers. Recently, Loewenberg and Gavalas developed a configurational averaging approach for the steady-state analysis of diffusion-controlled reactions in finite domains. Explicit consideration was given to the detailed effect to the macroscopic boundary and the reactant flux on the boundary was specifically evaluated for semi-infinite and spherical domains.

The purpose of this paper is to generalize the steady-state results of Loewenberg and Gavalas, henceforth (I), by determining the transient reactant flux on the boundary, $\partial\Omega$, of a finite or semi-infinite region, Ω, containing a suspension of reactive spheres. The approach involves configurational averaging of the governing conservation equations, a concept introduced by Hinch (1977). The boundary-sink interaction is explicitly considered but two-sphere interactions are complicated by the presence of the boundary and are excluded from the analysis. We shall obtain simple numerical solutions for the case where the domain is spherical or semi-infinite.

2 Problem Formulation

We will assume that the reactant diffuses within the inert phase with a constant diffusivity, D. The spheres are equisized with radius, a, and distributed according to a hard-sphere potential Accordingly, we define a sphere number density, n:

$$n = \frac{N}{V} \tag{1}$$

where N is the total number of spheres and V is the volume of the material. The volume fraction of the spherical phase, c, is given by:

$$c = \frac{4\pi}{3} a^3 n \tag{2}$$

The case of interest is $N >> 1$, and the present analysis is restricted to dilute volume fractions, $c << 1$.

The process is assumed to be diffusion-controlled; the reactant concentration of the sphere surfaces is zero (or some equilibrium value). The initial concentration is prescribed by a steady-state profile, $y_0(\mathbf{x}')$. For $t > 0$, the boundary condition is given by $f(t)$ which is independent of position but may vary with time. The governing equations are normalized by:

$$\mathbf{x} = \frac{\mathbf{x}'}{a}, \qquad t = \frac{Dt'}{a^2}, \qquad u(\mathbf{x},t) = \left[y(\mathbf{x},t) - y_0(\mathbf{x})\right]/y_c \tag{3}$$

where y_c is some characteristic concentration. The Laplace transformed, dimensionless conservation equations are:

$$\nabla^2\hat{u}(\mathbf{x}) - s\hat{u}(\mathbf{x}) = 0 \qquad \text{(inert phase)} \tag{4}$$

$$\hat{u}(\mathbf{x}) = 0 \qquad \text{(spherical phase)} \tag{5}$$

$$\hat{u}(\mathbf{x},0) = 0 \qquad \text{(initial condition)} \tag{6}$$

$$\hat{u}(\mathbf{x}) = \hat{f} \qquad \mathbf{x} \in \partial\Omega \tag{7}$$

where s is the (dimensionless) frequency variable. The transformed dimensionless reactant flux into the boundary is defined by:

$$\hat{\mathbf{F}} = -\frac{\partial}{\partial n}\hat{u}(\mathbf{x}) \qquad \mathbf{x} \in \partial\Omega \tag{8}$$

which, in general, depends upon c, the geometry of the domain and position on the domain boundary. Heretofore, we restrict our our attention to symmetric domains for which $\hat{\mathbf{F}}$ is spatially invariant.

3 Configurational Averaging

In this section, we present the configurational average of equations (4)-(6). The results follow easily from the derivation presented in (I) thus, a separate derivation is not given. According to (I), we obtain the averaged equations:

$$\nabla^2\langle\hat{u}(\mathbf{x})\rangle - s\langle\hat{u}(\mathbf{x})\rangle = \frac{3c}{4\pi}\int_{\{\|\mathbf{x}-\mathbf{x}_1\|=1\}\cap\bar{\Omega}} \frac{\partial}{\partial n}\langle\hat{u}(\mathbf{x}|\mathbf{x}_1)\rangle d\mathbf{x}_1 \tag{9}$$

$$\nabla^2\langle\hat{u}(\mathbf{x}|\mathbf{x}_1)\rangle - s\langle\hat{u}(\mathbf{x}|\mathbf{x}_1)\rangle = \frac{3c}{4\pi}\int_{\{\|\mathbf{x}-\mathbf{x}_2\|=1\}\cap\bar{\Omega}_1} \frac{\partial}{\partial n}\langle\hat{u}(\mathbf{x}|\mathbf{x}_1,\mathbf{x}_2)\rangle d\mathbf{x}_2 \tag{10}$$

$$\|\mathbf{x}-\mathbf{x}_1\| > 1$$

$$\nabla^2\langle\hat{u}\rangle(\mathbf{x}|\mathbf{x}_1,\mathbf{x}_2) - s\langle\hat{u}(\mathbf{x}|\mathbf{x}_1,\mathbf{x}_2)\rangle = \frac{3c}{4\pi}\int_{\{\|\mathbf{x}-\mathbf{x}_3\|=1\}\cap\bar{\Omega}_2} \frac{\partial}{\partial n}\langle\hat{u}\rangle(\mathbf{x}|\mathbf{x}_1,\mathbf{x}_2,\mathbf{x}_3) d\mathbf{x}_3 \tag{11}$$

$$\|\mathbf{x}-\mathbf{x}_1\| > 1, \quad \|\mathbf{x}-\mathbf{x}_2\| > 1$$

$$\vdots$$

where (9), the (unconditionally) averaged field equation, is coupled to (10), the conditionally averaged equation with a sphere fixed at $\mathbf{x}_1$. Similarly, (10) is coupled to (11), the second conditionally averaged equation with spheres fixed at $\mathbf{x}_1$ and $\mathbf{x}_2$. As is apparent, this coupling ultimately produces an infinite hierarchy of coupled equations with an additional sphere fixed at each level. All averaged equations are subject to boundary condition (7) on $\partial\Omega$ and the conditionally averaged equations must satisfy (6) on all fixed sphere surfaces.

The region $\bar{\Omega}$ in Equation (9) is the allowed portion of the domain for sphere centers consisting of the domain Ω less the excluded volume within one dimensionless hard-sphere radius of the boundary, $\partial\Omega$. Similarly, Ω_1 in is defined by the intersection: $\bar{\Omega}\cap\{\|\mathbf{x}_1-\mathbf{x}_2\|\geq 2\}$ and, according to the hard-sphere distribution, is the allowed portion of the domain for a second sphere center given one center is at $\mathbf{x}_1$. Ω_2 is the allowed portion of the domain for a third sphere center given centers at $\mathbf{x}_1$ and $\mathbf{x}_2$. A tacit assumption in the foregoing is a uniform distribution

of sphere centers except in the excluded hard-sphere volume near the boundary and surrounding any fixed spheres. In actuality, a hard-sphere distribution exhibits local, order c, variations in the neighborhood of a boundary (or fixed sphere) which, as shown previously (I) affect the solution higher order.

The hierarchy must be truncated to permit solution of the unconditionally averaged field. The truncated hierarchy is solved in reverse order: the equation with the most spheres fixed is solved first because it is decoupled from the others; its solution provides the forcing term for the next equation. The procedure is continued until the unconditionally averaged field is found. The truncation procedure follows.

4 Truncation of Hierarchy

The hierarchy is truncated by exploiting the diluteness condition, $c << 1$, and employing the physics of screening: far from a fixed sphere, the influence of the sphere is "screened" by the presence of the intervening sinks in the material (Brinkman 1947). The screening of the spheres in the material implies that the concentration field at a point $\mathbf{x}$ is relatively unaffected by the presence of a sphere fixed at $\mathbf{x}_1$ for large separation, $\|\mathbf{x} - \mathbf{x}_1\| >> L_s$:

$$\langle \hat{u}(\mathbf{x}|\mathbf{x}_1) \rangle \sim \langle \hat{u}(\mathbf{x}) \rangle \tag{12}$$

where L_s is the "screening length" and is defined below. By diluteness, the right side of Equation (10) is neglected yielding:

$$\nabla^2 \hat{u}(\mathbf{x}|\mathbf{x}_1) - s\hat{u}(\mathbf{x}|\mathbf{x}_1) \approx 0 \tag{13}$$

which is solved subject to boundary conditions (6) and (12) yielding:

$$\frac{1}{4\pi} \int_{\|\mathbf{x}-\mathbf{x}_1\|=1} \frac{\partial}{\partial n} \langle \hat{u}(\mathbf{x}|\mathbf{x}_1) \rangle d\mathbf{x}_1 \approx \hat{u}(\mathbf{x}) \tag{14}$$

where boundary condition (7) has been neglected in favor of (12). The $\sqrt{s}$ term omitted above is significant only on the time scale, $t = O(1)$ and is consistently omitted throughout (Felderhof 1977). Inserting the result into (9) yields the lowest order truncation:

$$\nabla^2\langle\hat{u}(\mathbf{x})\rangle = p\langle\hat{u}(\mathbf{x})\rangle \tag{15}$$

where p is defined by:

$$p = s + 3c \tag{16}$$

where $p << 1$ for long-times and diluteness of the spherical phase. Equation (15) constitutes the "mean-field" approximation. The mean-field approximation neglects all sphere-sphere and sphere-boundary interactions and retains only the screening effect of the spheres. For short times, reactant penetrates an order one volume of the domain thus sphere-interactions produce an order c effect and similarly, two-sphere interactions have an order c^2 effect. The previous steady-state results (I) indicate that the effect of sphere-boundary and two-sphere interactions are bounded by order $c \ln c$ and $c^{3/2} \ln c$ respectively.

The two-sphere analog of the foregoing procedure yields the next higher order truncation:

$$\nabla^2\langle\hat{u}(\mathbf{x}|\mathbf{x}_1)\rangle = p\langle\hat{u}(\mathbf{x}|\mathbf{x}_1)\rangle \tag{17}$$

The result is analogous to Equation (15) and is the mean-field approximation of the first conditionally averaged equation. Following this program retains the effect of sphere-boundary interactions neglected by the mean-field approximation but sphere-sphere interactions remain unaccounted. According to the above argument, the above truncation may be employed to obtain a uniformly valid solution to order c with order $c^{3/2} \ln c$ error.

5 Characteristic Times

Rescaling Equation (15) or (17) to balance the diffusive and dissipative terms defines the screening length:

$$L_s = a\| \ p^{-\frac{1}{2}}\| \tag{18}$$

where p is defined by (16) and L_s is the characteristic concentration decay length. In general, the screening length gives the characteristic decay length in response to a disturbance in the field and, in particular, gives the characteristic length for the decay of reactant concentration away from the boundary. The screening length is longest for long times and reaches its maximum value in the limit:

$$L_{s,\infty} = \lim_{s\to 0} \|a \ p^{-\frac{1}{2}}\| = a(3c)^{-\frac{1}{2}} \geq L_s \tag{19}$$

We define a frequency dependent "screening modulus":

$$\phi = L_c/L_s \equiv \left(\frac{L_c}{a}\right)\sqrt{p} \tag{20}$$

where L_c is a characteristic length for Ω ($e.g.$, $L_c = V^{1/3}$). The screening modulus, ϕ, determines the extent of reactant penetration into the domain. $\phi << 1$ implies that all the spheres in the domain are immersed in a uniform concentration field equal to unity and $\phi >> 1$ indicates significant "boundary screening": only spheres relatively near the boundary are exposed to significant reactant concentration. ϕ decreases with time, reaching a minimum value at steady-state:

$$\phi_\infty = L_c/L_{s,\infty} \equiv \left(\frac{L_c}{a}\right)\sqrt{3c} \leq \phi \tag{21}$$

which is the previously used, steady-state screening modulus (Eq. I.4.3). The frequency transition of ϕ determines the transition from high to low frequency

(short to long time) solution behavior. Equations (16) and (20) yield the "cross-over" frequency, s_c, given by:

$$\frac{s_c}{3c} = \frac{1}{\phi_\infty^2} + 1 \tag{22}$$

and a "cross-over" time, $t_c = s_c^{-1}$

$$t_c = \frac{1}{3c} \frac{\phi_\infty^2}{1 + \phi_\infty^2} \tag{23}$$

and upon rearrangement:

$$\frac{1}{t_c} = \frac{1}{t_D} + \frac{1}{t_S} \tag{24}$$

which is the (dimensionless) characteristic time for the process to reach steady-state. The quantities t_S and t_D are the characteristic times for the boundary-independent, local consumption of reactant and the purely diffusive process. The local consumption of reactant gives rise to screening, occurs on the time scale:

$$t_S = O\left(\frac{1}{3c}\right) \tag{25}$$

which is independent of the domain geometry (*e.g.*, Bixon and Zwanzig 1981). The diffusive time scale is approximately given by:

$$t_D = O\left(\frac{L_c}{a}\right)^2 \tag{26}$$

is independent of c but depends on the specific domain. E.g., for a sphere with normalized radius, R:

$$t_D = \left(\frac{R}{\pi}\right)^2 \qquad \text{sphere} \tag{27}$$

(Carslaw and Jaeger 1959). The result displayed in Eq. (24) indicates:

(i) The processes of local reactant consumption and macroscopic diffusive transport occur in parallel.

(ii) Screening reduces the time required to reach steady-state.

(iii) The overall characteristic time is given by $t_c = \min\left[t_D, (3c)^{-1}\right]$

6 Mean-Field Solution

In the present section, we shall obtain the mean-field solution for a spherical and semi-infinite domain. If Ω is a semi-infinite domain, the solution of (15) and (7) is:

$$\hat{u}_{mf}(\mathbf{x}) = \hat{f} \exp\left(-\sqrt{p}\, x\right) \tag{28}$$

where x is the distance from the plane boundary. The subscript, mf, replaces the angled brackets indicating that the result depends upon the mean-field approximation. The reactant flux is:

$$\hat{\mathbf{F}}_{mf} = \hat{f}\sqrt{p} \tag{29}$$

which is the largest flux for all bounded domains.

For a spherical domain, Ω, with normalized radius, R, the characteristic length of the domain is aR and the screening modulus is given by:

$$\phi = R\sqrt{p} \tag{30}$$

with steady-state ($s = 0$) limit:

$$\phi_\infty = \lim_{s\to 0} \phi = R\sqrt{3c} \tag{31}$$

In this case, Equations (15) and (7) yield:

$$\hat{u}_{mf}(\mathbf{x}) = \hat{f}\left[\frac{R\,\sinh(\sqrt{p}\,r)}{r\,\sinh(\phi)}\right] \tag{32}$$

$$\hat{\mathbf{F}}_{mf}(R) = \hat{f}\left[\sqrt{p}\coth\phi - \frac{1}{R}\right] \tag{33}$$

where r is the radial coordinate and is the distance from the center of the domain.

The leading order correction to the mean-field solution results from the interaction of the spheres with the boundary. In the following, the hierarchy is truncated at the next level thereby retaining this effect.

7 Solution to Order c

In the following, we improve upon the foregoing mean-field results and obtain a solution uniformly valid to order c. The solution of Equation (9) yields:

$$\langle\hat{\mathbf{F}}\rangle = \hat{\mathbf{F}}_0 + \frac{1}{S}\frac{3c}{4\pi}\int_\Omega \hat{u}_0(\mathbf{x}')\int_{\{\|\mathbf{x}'-\mathbf{x}_1\|=1\}\cap\bar{\Omega}} \frac{\partial}{\partial n}\langle u(\mathbf{x}'|\mathbf{x}_1)\rangle d\mathbf{x}_1 d\mathbf{x}' \qquad \mathbf{x}\in\partial\Omega \quad (34)$$

where $\langle\hat{\mathbf{F}}\rangle$ is the transient reactant flux on the boundary and $\hat{\mathbf{F}}_0(\mathbf{x})$ is the sink-independent contribution to the flux defined:

$$\hat{\mathbf{F}}_0 = -\frac{\partial}{\partial n}\hat{u}_0(\mathbf{x}) \qquad \mathbf{x}\in\partial\Omega \quad (35)$$

where $\hat{u}_0(\mathbf{x})$ is the homogeneous solution of (9) and (7) and is thus the solution to the problem in the dilute limit, $c = 0$. The reactant flux, $\langle\hat{\mathbf{F}}\rangle$, and the contribution, $\hat{\mathbf{F}}_0$, are independent of position on the boundary by the symmetry assumed above. Neglecting order $\sqrt{s}$ variations in $\hat{u}_0(\mathbf{x}')$ on the surface of the sphere at $\mathbf{x}_1$ (*cf.* Eq. 14) allows interchanging the order of integration:

$$\langle\hat{\mathbf{F}}\rangle = \hat{\mathbf{F}}_0 + \frac{3c}{S}\int_{\bar{\Omega}} \hat{u}_0(\mathbf{x}_1)\left[\frac{1}{4\pi}\int_{\|\mathbf{x}'-\mathbf{x}_1\|=1}\frac{\partial}{\partial n}\langle u(\mathbf{x}'|\mathbf{x}_1)\rangle d\mathbf{x}'\right] d\mathbf{x}_1 \qquad \mathbf{x}\in\partial\Omega \quad (36)$$

Equation (36) expresses the reactant flux into the domain in terms of the average flux into a single sphere which, in general, requires solution of (10) from the complete, coupled hierarchy. The above result is exact to $O(c\sqrt{s})$ but cannot be evaluated without truncating the hierarchy.

We shall employ Equation (17) to truncate the hierarchy thereby inducing an error of order $c^{3/2}\ln c$ according to the previous argument. The solution is inserted into (36) to yield the reactant flux directly without solving for the unconditionally averaged field, $\langle\hat{u}(\mathbf{x})\rangle$. The solution of (17) with boundary condition (7) is facilitated by the definition of a function $\hat{v}(\mathbf{x}|\mathbf{x}_1)$:

$$\hat{v}(\mathbf{x}|\mathbf{x}_1) = \left[\hat{u}_{mf}(\mathbf{x}) - \langle\hat{u}(\mathbf{x}|\mathbf{x}_1)\rangle\right]/\hat{u}_{mf}(\mathbf{x}_1) \quad (37)$$

where $\hat{u}_{mf}(\mathbf{x})$ and $\langle\hat{u}(\mathbf{x}|\mathbf{x}_1)\rangle$ satisfy the mean-field equations (15) and (17) respectively. By linearity, $\hat{v}(\mathbf{x}|\mathbf{x}_1)$ is also a solution of Equation (17) satisfying boundary conditions:

$$\hat{v}(\mathbf{x}|\mathbf{x}_1) = 0 \qquad \mathbf{x} \in \partial\Omega \tag{38}$$

$$\hat{v}(\mathbf{x}|\mathbf{x}_1) = 1 \qquad \|\mathbf{x} - \mathbf{x}_1\| = 1 \tag{39}$$

where we have neglected local gradients of $\hat{u}_{mf}(\mathbf{x})$ at $\mathbf{x}_1$ which are $O(\sqrt{p})$ according to the argument which follows. $\nabla\hat{u}_{mf}(\mathbf{x})$ satisfies the mean-field equation which is elliptic and by an appropriate maximum principle, each component of $\nabla\hat{u}_{mf}(\mathbf{x})$ attains a maximum on the boundary of $\partial\Omega$. The component of $\nabla\langle\hat{u}(\mathbf{x})\rangle$ normal to the boundary is bounded by $\sqrt{p}$ (Eq. 29) and Eq. (7) implies that tangential components of $\nabla\langle\hat{u}(\mathbf{x})\rangle$ are zero on the boundary. Therefore, each component of $\nabla\langle\hat{u}(\mathbf{x})\rangle$ is bounded by $\sqrt{p}$. Expressing the solution (36) in terms of $\hat{v}(\mathbf{x}|\mathbf{x}_1)$ yields:

$$\langle\hat{\mathbf{F}}\rangle = \hat{\mathbf{F}}_0 + 3c\mathbf{B} \tag{40}$$

where $\mathbf{B}$ is given by:

$$\mathbf{B} = \frac{1}{S}\int_{\bar{\Omega}} \hat{u}_0(\mathbf{x}_1)\hat{u}_{mf}(\mathbf{x}_1)\mathbf{H}(\mathbf{x}_1)d\mathbf{x}_1 \tag{41}$$

$$\mathbf{H}(\mathbf{x}_1) = \frac{1}{4\pi}\int_{\|\mathbf{x}-\mathbf{x}_1\|=1} \frac{\partial}{\partial n}\hat{v}(\mathbf{x}|\mathbf{x}_1)d\mathbf{x} \tag{42}$$

The quantity $\mathbf{B}$ is the contribution to the net flux resulting from the presence of reactive sinks in the domain. Equation (40) indicates that the flux can be calculated to order c if $\mathbf{B}$ is determined to order unity. In the appendix, we develop the general approximation:

$$\mathbf{B} = \frac{1}{S}\int_{\bar{\Omega}}\Big[\hat{u}_0(\mathbf{x}_1)\hat{u}_{mf}(\mathbf{x}_1)\left[(1+\sqrt{p}) + \mathbf{H}^{(1)}(\mathbf{x}_1)\right] + \mathbf{J}(\mathbf{x}_1)\Big]d\mathbf{x}_1 + O(\sqrt{p}\ln p) \tag{43}$$

The quantities: $(1+\sqrt{p})$ and $\mathbf{H}^{(1)}(\mathbf{x}_1)$ are the exact contributions to $\mathbf{H}(\mathbf{x}_1)$ resulting from the incident field and first reflection disturbance induced by the boundary.

$\mathbf{J}(\mathbf{x}_1)$ is the approximate contribution from the second and all higher-order reflections with the boundary as obtained by solution of Laplace's equation. Inserting the (43) into (40) yields the solution which may be written as the sum of four distinct contributions:

$$\hat{\mathbf{F}} = \hat{\mathbf{F}}_0 + \hat{\mathbf{F}}_{1a} + \hat{\mathbf{F}}_{1b} + \hat{\mathbf{F}}_{1c} + O(c\sqrt{p}\ln p) \tag{44}$$

where we have dropped the angled brackets on $\langle\hat{\mathbf{F}}\rangle$; the configurationally averaged reactant flux is henceforth assumed. The quantities: $\hat{\mathbf{F}}_{1a,b,c}$ reflect the reactivity of the spheres in the domain. The reactivity induced by the incident reactant field results in the contribution $\hat{\mathbf{F}}_{1a}$. The primary correction to the mean-field solution lies in the contributions $\hat{\mathbf{F}}_{1b}$ and $\hat{\mathbf{F}}_{1c}$ which result from the boundary-sphere interaction. Specifically, $\hat{\mathbf{F}}_{1b}$ results from the additional sphere reactivity induced by the first reflection disturbance and $\hat{\mathbf{F}}_{1c}$ from all higher-order reflections with the boundary. The sink-dependent contributions are explicitly given by:

$$\hat{\mathbf{F}}_{1a} = 3c(1+\sqrt{p})\frac{1}{S}\int_{\Omega}\hat{u}_0(\mathbf{x}_1)\hat{u}_{mf}(\mathbf{x}_1)d\mathbf{x}_1 - 3c \tag{45}$$

$$\hat{\mathbf{F}}_{1b} = \frac{3c}{S}\int_{\bar{\Omega}}\hat{u}_0(\mathbf{x}_1)\hat{u}_{mf}(\mathbf{x}_1)\mathbf{H}^{(1)}(\mathbf{x}_1)d\mathbf{x}_1 \tag{46}$$

$$\hat{\mathbf{F}}_{1c} = \frac{3c}{S}\int_{\bar{\Omega}}\mathbf{J}(\mathbf{x}_1)d\mathbf{x}_1 \tag{47}$$

Subtraction of the quantity $3c$ is a consequence of the hard-sphere distribution: sphere centers are excluded from the volume within one sphere radius of the boundary. This excluded hard-sphere volume is also responsible for restricting the range of integration on Ω to the subset $\bar{\Omega}$ in the expressions for $\hat{\mathbf{F}}_{1b}$ and $\hat{\mathbf{F}}_{1c}$.

In the long time limit ($s \to 0$), Equations (45)-(47) reduce to the previous steady-state results (Eqs. I.6.13-15). At short times ($s >> 3c$), the reactant concentration reaches only spheres which lie in an order one volume near the boundary and thus sinks in the domain contribute to the net reactant flux at order c. The

sink-independent contribution, $\hat{\mathbf{F}}_0$, is order one and dominates but tends to zero for long times where it is sub-dominant to the reactant flux resulting from the spherical sinks. The error term in the solution is order $c^{3/2}\ln c$ for long times ($s << 3c$) and is order $c\ \sqrt{s}\ln s$ for $s = O(1)$. The result is valid for all symmetric bounded or semi-infinite domains.

8 Spherical and Semi-Infinite Domains

In the present section, the foregoing procedure is applied to determine the reactant flux into both a semi-infinite and spherical domain. For a semi-infinite domain, $\hat{u}_{mf}(\mathbf{x})$ is given by (28) and $\hat{u}_0(\mathbf{x})$) is obtained in the dilute limit, $c = 0$. Inserting these functions into expressions (35) and (45) yields:

$$\hat{\mathbf{F}}_0 = -\hat{f}\frac{d}{dx}\, e^{-\sqrt{s}\ x}\Big|_{x=0} = \sqrt{s}\hat{f} \tag{48}$$

$$\hat{\mathbf{F}}_{1a} = 3c\hat{f}(1+\sqrt{p})\int_0^\infty e^{-\sqrt{s}\ x}e^{-\sqrt{p}\ x}dx - 3c = 3c\hat{f}\left[\frac{1+\sqrt{p}}{\sqrt{s}+\sqrt{p}} - 1\right] \tag{49}$$

The first reflection disturbance, $\mathbf{H}^{(1)}(\mathbf{x}_1)$, is determined by the "method of images" (Jackson, 1962) and inserted into (46) yielding the exponential integral:

$$\hat{\mathbf{F}}_{1b} = 3c\hat{f}\int_1^\infty e^{-\sqrt{s}\ x}\frac{e^{\ -3\sqrt{p}\ x}}{2x}dx \approx -\frac{3c}{2}\hat{f}\left[\ln(\sqrt{s}+3\sqrt{p})+\gamma\right] + O(c\ \sqrt{p}) \tag{50}$$

We obtain the exact solution to Laplace's equation in bi-spherical co-ordinates (Jeffery 1912) yielding $\mathbf{L}(\mathbf{x}_1)$ defined by (A.3). The first reflection disturbance for Laplace's equation is determined by the method of images and combined with (A.7) and (47) to obtain:

$$\hat{\mathbf{F}}_{1c} = 3c\hat{f}\int_1^\infty \mathbf{J}(x)dx = 3c(0.47472\cdots) \tag{51}$$

Inserting (48)-(51) into Eq. (54) yields the transient reactant flux into a semi-infinite domain with boundary condition given by (7):

$$\hat{\mathbf{F}} = \hat{f}\left[\sqrt{s} + 3c\frac{1+\sqrt{p}}{\sqrt{s}+\sqrt{p}} - 3c - \frac{3c}{2}\left[\ln(\sqrt{s}+3\sqrt{p}) + \gamma\right] + 3c(0.47472) + O(c\sqrt{p}\ln p)\right] \tag{52}$$

In the following section, we shall consider the transient reactant flux resulting from a unit step change in boundary concentration. In this case, $\hat{f} = s^{-1}$. The previous steady-state result, (Eq. I.7.5) is recovered in the long-time limit:

$$\lim_{s\to 0} s\hat{\mathbf{F}} = \mathbf{F}_\infty = \sqrt{3c} - \frac{3c}{4}\ln 3c - 3c\left(\frac{1}{2}\ln 3 + \frac{1}{2}\gamma - 0.47472\right) + O(c^{3/2}\ln c) \tag{53}$$

Next we analyze the more general case of a spherical domain with dimensionless radius R. In this case, angular integration yields 4π, and the surface area is $4\pi R^2$ yielding a multiplicative factor $1/R^2$ for each of required quadratures. In this case, $\hat{u}_{mf}(\mathbf{x})$ is given by (32) and $\hat{u}_0(\mathbf{x})$ by setting $c = 0$. Eqs. (35) and (45), become:

$$\hat{\mathbf{F}}_0 = \hat{f}\left[\frac{d}{dr}\frac{\sinh(\sqrt{s}\,r)}{\sinh(\sqrt{s}\,R)}\frac{R}{r}\right]\Bigg|_{r=R} = \hat{f}\left[\sqrt{s}\coth(\sqrt{s}R) - \frac{1}{R}\right] \tag{54}$$

$$\begin{aligned}\hat{\mathbf{F}}_{1a} &= \hat{f}\left[\frac{3c}{R^2}(1+\sqrt{p})\int_0^R \left(\frac{\sinh(\sqrt{s}\,r)}{\sinh(\sqrt{s}\,R)}\frac{R}{r}\right)\left(\frac{\sinh(\sqrt{p}\,r)}{\sinh(\sqrt{p}\,R)}\frac{R}{sr}\right) r^2 dr - 3c\right] \\ &= \hat{f}(1+\sqrt{p})\left[\sqrt{p}\,\coth(\sqrt{p}R) - \sqrt{s}\,\coth(\sqrt{s}R)\right] - 3c\hat{f}\end{aligned} \tag{55}$$

The method of images can again be used to determine the first reflection disturbance and Equation (46) becomes:

$$\hat{\mathbf{F}}_{1b} = \frac{3c\hat{f}}{R^2}\int_0^{R-1}\left(\frac{\sinh(\sqrt{s}\,r)}{\sinh(\sqrt{s}\,R)}\frac{R}{r}\right)\left(\frac{\sinh(\sqrt{p}\,r)}{\sinh(\sqrt{p}\,R)}\frac{R}{r}\right)\left(\frac{R}{R^2-r^2}\right)\exp\left(-\sqrt{p}\,\frac{R^2-r^2}{r}\right) r^2 dr \tag{56}$$

The exact solution to Laplace's equation is available in bi-spherical coordinates and is inserted into (A.7) with the first reflection disturbance for Laplace's equation and the result into (57) yielding:

$$\hat{\mathbf{F}}_{1c} = \frac{3c\hat{f}}{R^2}\int_0^{R-1}\mathbf{J}(r)r^2 dr \tag{57}$$

Equations (55)-(58) are evaluated numerically for fixed R, and summed to yield the transient reactant flux into a spherical domain resulting from a boundary value given by (7). The reactant flux resulting from a unit step change in boundary concentration is considered below. It can be similarly shown that the previous steady-state result (Eq. I.7.6-8) is recovered by the limiting process shown in (54).

9 Numerical Solution

We shall now present a numerical investigation of the above solutions for a unit step change in reactant concentration on the boundary ($\hat{f} = s^{-1}$). In compliance with the diluteness assumption, we restrict our attention to volume fractions in the range: $0.001 \leq 3c \leq 0.1$. For practical purposes, we are interested in $N >> 1$ and shall take $N = 10$ as a lower bound. Eqs. (1) and (2) yield the relationship: $N = cR^3$ which provides $R = 32$ as a lower bound for volume fractions in the above range. Results are presented for $R = 32$ and for a semi-infinite domain ($R \to \infty$). For the spherical domain, the steady-state screening modulus, (31), assumes the values: $\phi_\infty^2 = 1, 10, 100$ corresponding to the volume fractions $3c = 0.001, 0.01, 0.1$. The semi-infinite domain corresponds to the limiting case, $\phi_\infty^2 \to \infty$.

Figures 1 and 2 show the (dimensionless) reactant flux for both domains parametric in (dimensionless) time and volume fraction respectively. The results indicate that at short times, the flux exhibits algebraic decay and is almost independent volume fraction. This observation reflects the domination at short times by the sink-independent flux, $\mathbf{F}_0$, which is given by $(\pi t)^{-\frac{1}{2}}$ for short times. The flux into the semi-infinite domain exceeds the solution for a spherical domain (c fixed) and that the difference between the two solutions increases with time and inversely with ϕ_∞. Fig 1. indicates that for $\phi_\infty^2 = 100$, the spherical and semi-infinite domain solutions

are approximately equal for all times.

According to Eqs. (24)-(27), the characteristic time, t_c, is approximately 100 for the spherical domain and 1000 for the semi-infinite domain for $3c = 0.001$. At the higher concentrations, $3c = 0.01$ and 0.1, the transition is predicted to occur at approximately $t_c = 200$ and 10 for both domains. These estimates are in approximate agreement with the numerical results depicted in Fig. 1. The steady-state ($t \to \infty$) solutions shown in Figure 2 coincide with (I). For fixed time and volume fraction, the reactant flux for (finite) $R > 32$ lies between the values computed for $R = 32$ and a semi-infinite ($R \to \infty$) domain. Thus, the results displayed in Figs. 1 and 2 provide bounds for the flux with R in the range: $32 \leq R \leq \infty$.

Figure 3 displays the relative correction to the mean-field solution and thus, the significance of treating sphere-boundary interactions. The effect is a 4%-16% enhancement of the predicted reactant flux for long times but is negligible at short times. The time required to reach the steady-state correction is rather independent of volume fraction. The steady value is obtained very gradually for the semi-infinite domain, much slower than the characteristic time predicted by (23). The characteristic time required for the solution of the spherical domain to attain the steady mean-field correction seems to be correlated with the diffusive time, (27). The correction increases monotonically in time and volume fraction.

10 Conclusions

A detailed analysis has been presented for determining the transient reactant flux into a material containing reactive, randomly-located, spherical particles. The local reaction and macroscopic diffusion processes occur in parallel. A long-time asymp-

totic solution was obtained valid to order c for bounded and semi-infinite domains. Explicit consideration is given to the sphere-boundary interactions which include long-range reflection disturbances induced by the boundary and the short-range, hard-sphere interaction between the spheres and the boundary. These interactions dominate the effect of two-sphere interactions which affect the solution at order $c^{3/2} \ln c$. The solution reduces to a previously obtained, steady-state solution on a characteristic time scale of $t_c = \min [t_D, (3c)^{-1}]$. Numerical results were given for spherical and semi-infinite domains. A comparison with the simpler, mean-field analysis indicates that, in the range of parameter values considered, the present analysis produces a moderate enhancement of the predicted flux at long times and a smaller correction at short times.

11 Acknowledgements

This work was made possible through a fellowship from the LINK foundation.

12 Notation

SYMBOL	DESCRIPTION
Roman Symbols	
a	sphere radius
$\mathbf{B}$	defined by Equation (51)
c	volume fraction of particulate phase
D	diffusivity of supporting matrix
f	boundary concentration
$\mathbf{F}$	total dimensionless reactant flux
$\mathbf{F}_0$	sink-independent contribution to reactant flux (Equation 42)
$\mathbf{F}_{1a}$	sink reactivity induced by incident field (Equation 55)
$\mathbf{F}_{1b}$	reactivity enhancement by first reflection disturbance (Equation 56)
$\mathbf{F}_{1c}$	reactivity enhancement by higher-order reflections (Equation 57)
$\mathbf{H}$	defined by Equation (52)
$\mathbf{H}^{(1)}$	defined by Equation (A.5)
$\mathbf{J}$	defined by Equation (A.7)
$\mathbf{L}$	defined by Equation (A.3)
L_c	characteristic dimension of domain
L_s	characteristic screening length
n	sphere center density
N	total number of spheres in domain
p	defined by Equation (16)
R	domain radius normalized by sphere radius, a
s	dimensionless frequency variable

S	surface area of domain boundary
t	dimensionless time
t_S	characteristic reaction time (dimensionless)
t_D	characteristic diffusive time (dimensionless)
u	dimensionless concentration
V	domain volume
y	reactant concentration
y_e	reactant concentration on sphere surfaces

Greek Symbols

Ω	domain
$\bar{\Omega}$	restricted domain (Equation (9))
$\partial\Omega$	domain boundary
ϕ	screening modulus (Equation (20))

subscripts

mf	mean-field result
∞	steady-state value
0	initial value

superscripts

$\hat{}$	Laplace transform of quantity
$'$	dimensional quantity

13 References

1. Bixon, M. and Zwanzig, R. (1981) Diffusion in a medium with static traps. *J. Chem. Phys.* **75** (5), 2354.

2. Brinkman, H. C. (1947) A calculation of the viscous force exerted by a flowing fluid on a dense swarm of particles. *Appl. Sci. Res. A* **1**, 27.

3. Carslaw, H.C. and Jaeger, J.C. (1959) *Conduction of Heat in Solids.* Oxford: Clarendon Press.

4. Felderhof, B.U. and Deutch J.M. (1976) Concentration dependence of the rate of diffusion-controlled reactions. *J. Chem. Phys.* **64** (11), 4551.

5. Felderhof, B.U. (1977) Frequency-dependent rate coefficient in diffusion-controlled reactions. *J. Chem. Phys.* **66** (10), 4385.

6. Felderhof, B.U., Deutch J.M. and Titulaer, U.M. (1982) Diffusion and absorption in a medium with spherical sinks. *J. Chem. Phys.* **76** (8), 4178.

7. Happel, J. and Brenner, H. (1965) *Low Reynolds Number Hydrodynamics.* New York: Prentice Hall.

8. Hinch, E.J. (1977) An averaged-equation approach to particle interactions in a fluid suspension. *J. Fluid Mech.***83**, 695.

9. Jackson, J.D. (1962) *Classical Electrodynamics.* New York: John Wiley & Sons, Inc.

10. Jeffery, G. B. (1912) On the form of the solution of Laplace's equation suitable for problems relating two spheres. *Proc. R. Lond. A***87**, 109.

11. Loewenberg, M. and Gavalas, G.R. (1988) Steady-state reactant flux into a medium containing spherical sinks. (I) *Chem. Eng. Sci.* In Press.

12. Mattern, K. and Felderhof, B.U. (1986) Rate of diffusion-controlled reactions in a random array of monopole sinks. *Physica* **135A**, 505.

13. Mattern, K. and Felderhof, B.U. (1987) Rate of diffusion-controlled reactions in a random array of spherical sinks. *Physica* **147A**, 1.

14. Muthukumar, M. (1982) Concentration dependence of diffusion-controlled processes among static traps. *J. Chem. Phys.* **76** (5), 2667.

15. Smoluchowski, M. V. (1916) Drei Vortrage uber Diffusion Brownische Bewegung und Koagulation von Kolloidteilchen. *Phys. Z.* **17**, 557.

16. Tokuyama, M., Cukier, R.I. (1982) Dynamics of diffusion-controlled reactions among stationary sinks: scaling expansion approach. *J. Chem. Phys.* **76**, (12), 6202.

17. Ziman, J.M. (1979) *Models of Disorder.* Cambridge: Cambridge University Press.

Appendix: Approximation of B

In the following, we derive an order one approximation for $\mathbf{B}$ by an extension of a previous argument used for the steady-state problem (I). $\mathbf{B}$ is given by (41) which requires $\mathbf{H}(\mathbf{x}_1)$ defined by Equation (42). The limit: $\|p\| \to 0$ requires both $c \to 0$ and $\|s\| \to 0$. In this limit, the diffusion equation (9) and the mean-field equation (15) reduce to Laplace's equation which implies that $\hat{u}_0(\mathbf{x}_1)$ and $\hat{u}_{mf}(\mathbf{x}_1)$ are harmonic, satisfy (7) and thus:

$$\lim_{p\to 0} \hat{u}_0(\mathbf{x}_1) = 1 \tag{A.1}$$

$$\lim_{p\to 0} \hat{u}_{mf}(\mathbf{x}_1) = 1 \tag{A.2}$$

We shall define $\mathbf{L}(\mathbf{x}_1)$ by Equation (42) for the case where $\hat{v}(\mathbf{x}|\mathbf{x}_1)$ satisfies Laplace's equation:

$$\mathbf{L}(\mathbf{x}_1) \equiv \lim_{p\to 0} \mathbf{H}(\mathbf{x}_1) \tag{A.3}$$

Combining Equations (A.1)-(A.3), suggests the following approximation of (41) for $\mathbf{B}$:

$$\mathbf{B} \approx \lim_{p\to 0} \frac{1}{S} \int_{\bar{\Omega}} \hat{u}_0(\mathbf{x}_1)\hat{u}_{mf}(\mathbf{x}_1)\mathbf{H}(\mathbf{x}_1)d\mathbf{x}_1 = \frac{1}{S} \int_{\bar{\Omega}} \mathbf{L}(\mathbf{x}_1)d\mathbf{x}_1 \tag{A.4}$$

which requires that the above limit exist. The above result is generally valid for contributions to $\mathbf{H}(\mathbf{x}_1)$ resulting from the second and all higher-order reflections with the boundary. The strength of these reflections decays sufficiently fast to allow integration on all bounded or semi-infinite domains with $p \equiv 0$. For these terms, the error induced by (A.4) is uniformly small, as shown below. However, the contributions to $\mathbf{H}(\mathbf{x}_1)$ resulting from the incident field and first reflection disturbance generally diverge upon integration in the limit $p \to 0$ rendering (A.4) invalid. The approximation is remedied by subtracting the portion of $\mathbf{H}(\mathbf{x}_1)$ resulting from

the incident field and first reflection disturbance and calculating its contribution to $\mathbf{B}$ exactly. The contribution from the remaining, convergent portion of the integrand can be found to order one using (A.4). Assuming the existence of a regular perturbation solution for $\mathbf{H}(\mathbf{x}_1)$:

$$\mathbf{H}(\mathbf{x}_1) = \sum_{k=0}^{\infty} \mathbf{H}^{(k)}(\mathbf{x}_1) \tag{A.5}$$

where $\mathbf{H}^{(k)}(\mathbf{x}_1)$ is the contribution to $\mathbf{H}(\mathbf{x}_1)$ from the k^{th} reflection with the boundary. The existence of an analogous solution for $\mathbf{L}(\mathbf{x}_1)$ is also assumed with $\mathbf{L}^{(k)}(\mathbf{x}_1)$ analogously defined. The foregoing argument suggests the revised approximation:

$$\mathbf{B} \simeq \frac{1}{S} \int_{\bar{\Omega}} \left[\hat{u}_0(\mathbf{x}_1) \hat{u}_{mf}(\mathbf{x}_1) \left[(1 + \sqrt{p}) + \mathbf{H}^{(1)}(\mathbf{x}_1) \right] + \mathbf{J}(\mathbf{x}_1) \right] d\mathbf{x}_1 \tag{A.6}$$

which we claim is valid to order one for all domains considered. The quantity $(1+\sqrt{p})$ is the boundary-independent contribution from the incident field, $\mathbf{H}^{(1)}(\mathbf{x}_1)$ results from the first reflection disturbance and $\mathbf{J}(\mathbf{x}_1)$ is the $p = 0$ approximation for the remaining portion of the integrand in Equation (41) obtained according to (A.4):

$$\mathbf{J}(\mathbf{x}_1) = \sum_{k=2}^{\infty} \mathbf{L}^{(k)}(\mathbf{x}_1) = \mathbf{L}(\mathbf{x}_1) - \left[1 + \mathbf{L}^{(1)}(\mathbf{x}_1) \right] \tag{A.7}$$

where $\mathbf{L}^{(0)}(\mathbf{x}_1)$ is the contribution from the incident field and is equal to unity and $\mathbf{L}^{(1)}(\mathbf{x}_1)$ is the first reflection disturbance. As shown previously (I, Appendix D), the error induced by Equation (A.6) is largest for a semi-infinite domain. In this case, it can be shown that the error introduced to $\mathbf{B}$ by substituting $\mathbf{L}^{(2)}(\mathbf{x}_1)$ for $\mathbf{H}^{(2)}(\mathbf{x}_1)$ is $O(c^{1/2} \ln c)$ for $s \leq O(3c)$ and $O(\sqrt{c})$ for the substitution of all higher-order reflections. Therefore, Eq. (A.6) determines $\mathbf{B}$ to order one for all bounded or semi-infinite domains considered herein at long times ($s \leq O(3c)$).

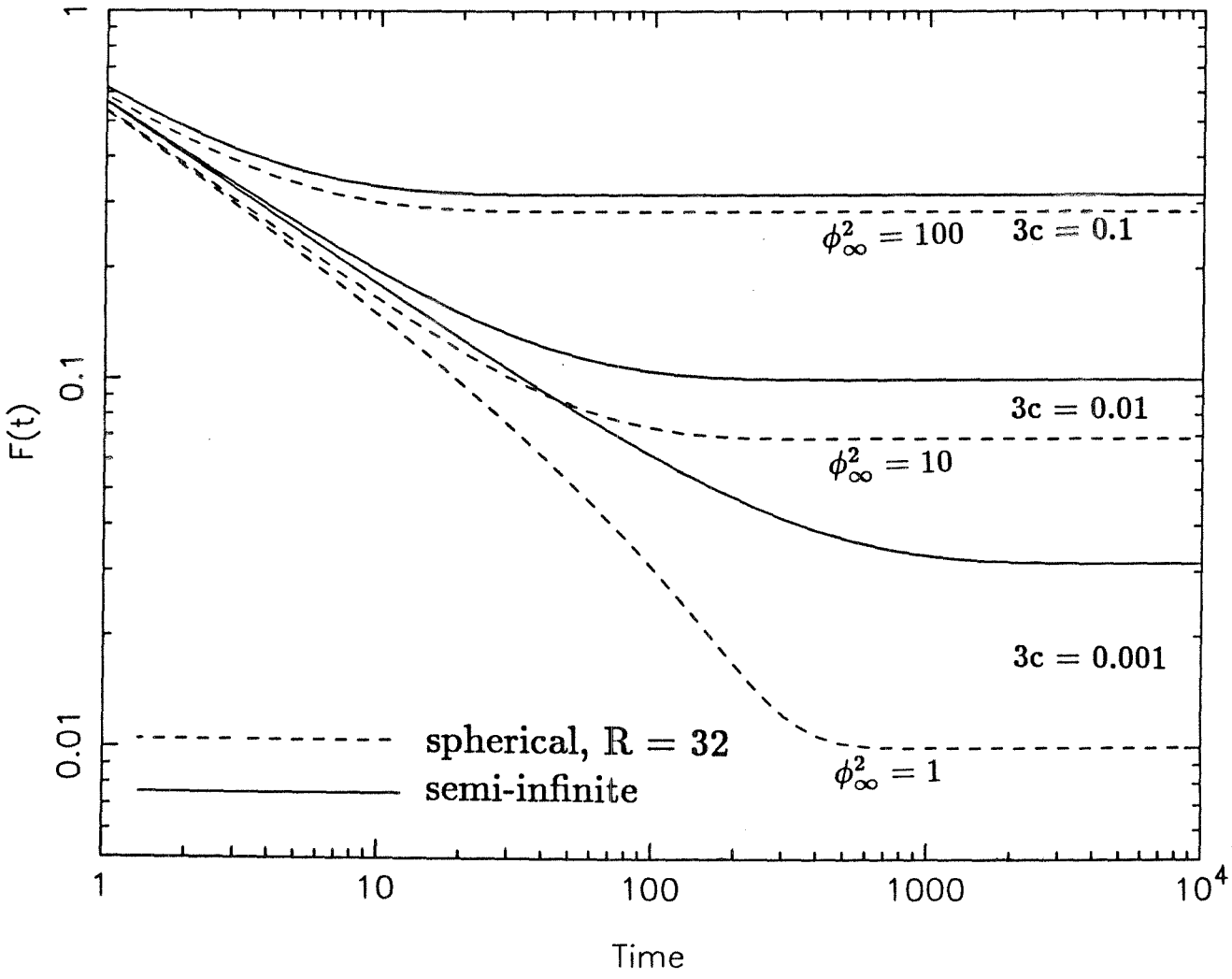

Figure 1: Dimensionless reactant flux versus time.

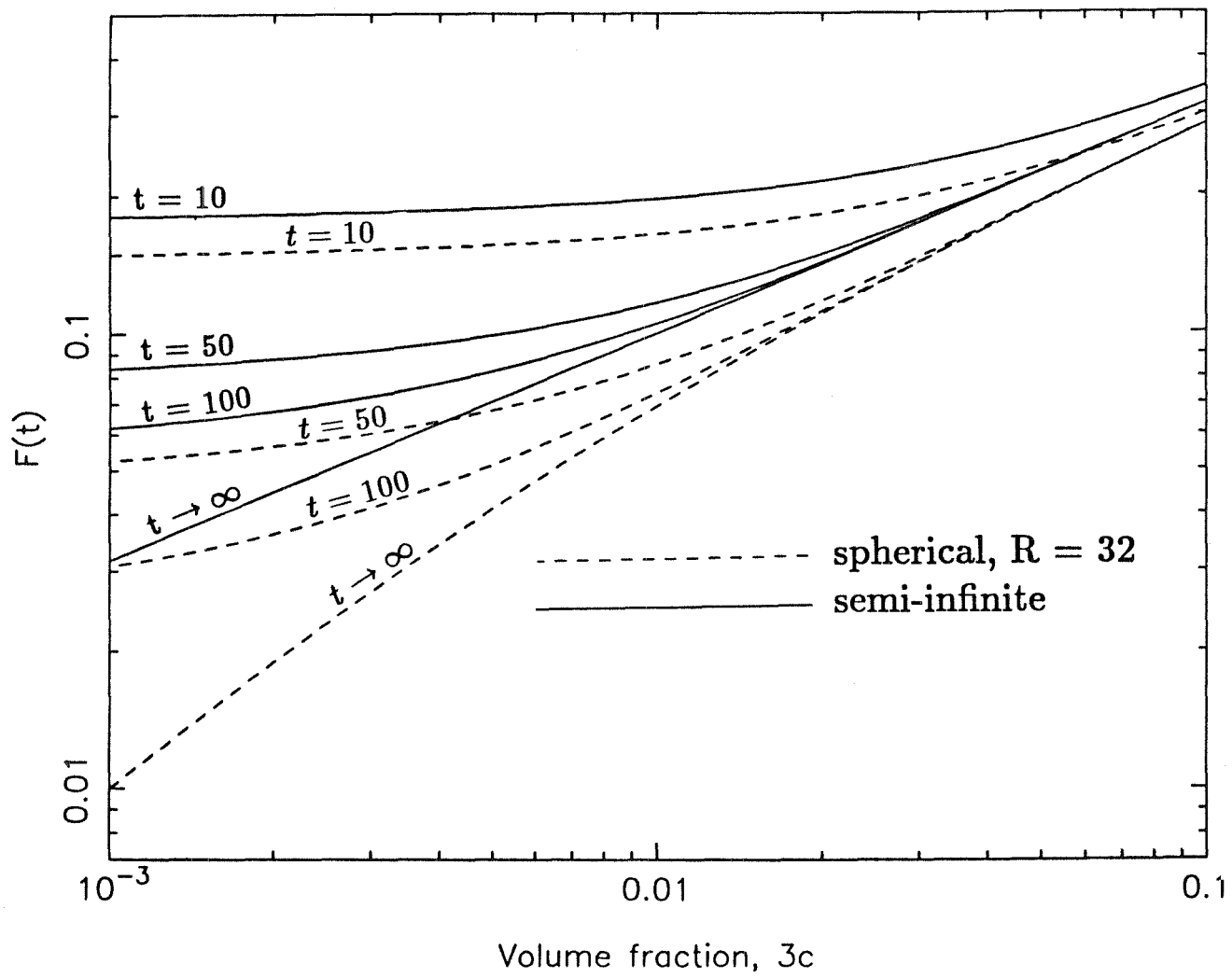

Figure 2: Dimensionless reactant flux versus volume fraction.

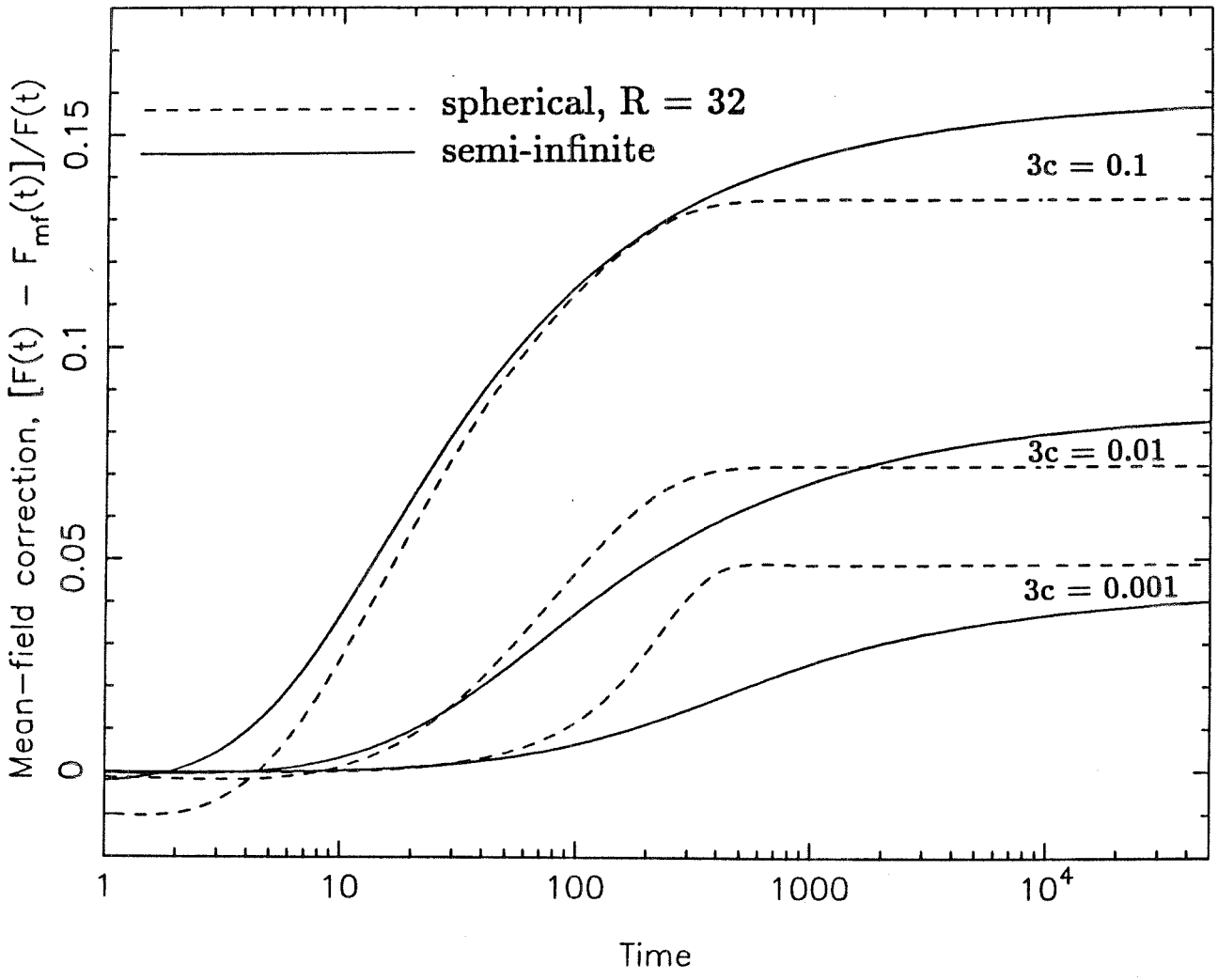

Figure 3: Mean-field correction versus time.

CHAPTER 7

Time Dependent, Diffusion-Controlled Reactions: The Influence of Boundaries

Time-Dependent, Diffusion-Controlled Reactions: The Influence of Boundaries

M. Loewenberg and G. R. Gavalas
Department of Chemical Engineering 206-41
California Institute of Technology
Pasadena, California 91125

Abstract

A configurational averaging procedure is presented for the analysis of diffusion-controlled reactions in a medium containing a hard-sphere distribution of spherical sinks. The hierarchy of equations produced from the averaging procedure is truncated assuming low concentration of sinks. The method is shown to reproduce previous results for the decay of an initially uniform distribution of reactant in an unbounded medium and is subsequently applied to determine the reactant flux on the boundary of a semi-infinite domain. In the latter problem, the boundary has a significant effect which cannot be accounted for by the usual rate coefficient.

1 Introduction

The problem of interest involves a two-phase system consisting of a continuous phase containing discrete particles acting as sources or sinks of some chemical species. The continuous phase permits diffusion of this species but is inert to chemical reaction. Such a situation is frequently encountered in problems such as the evaporation or condensation of sprays, growth of colloidal particles, suspension polymerization and fluorescence quenching. This problem was first studied by Smoluchowski[1] who considered the two-step process of slow diffusive transport followed by the rapid reaction of two chemical species. One of the species was assumed to be much more massive and was treated as a stationary, spherical sink.

Much of the recent work has focused on the steady problem in which reactant is supplied by a distant boundary. Felderhof and Deutch sought an effective rate coefficient which accounted for interactions between competing sinks at dilute sink volume fractions[2]. Muthukumar employed multiple scattering techniques to determine the rate coefficient[3] and diffusion coefficient[4] at arbitrary volume fractions of mono pole sinks. More recently, Mattern and Felderhof[5,6] used a cluster expansion approach to re-derive and discuss discrepancies among previous results.

In the present work, we are concerned with the time-dependent problem. Felderhof determined a frequency-dependent rate coefficient and demonstrated the necessity for including "retardation" effects in the treatment of multi-sink interactions.[7] Bixon and Zwanzig[8] explored the transient problem employing a multiple scattering approach to derive a configurationally averaged Green's function to first order in sink density. Felderhof, Deutch and Titulaer[9] modified the results of a multiple scattering analysis to account for the instantaneous absorption of reactant created within the sinks. Tokuyama and Cukier[10] employed a scaling expansion approach to

derive a local damping equation in space and time. They showed that the reaction-diffusion process cannot be cast in conventional local form due to long-range spatial correlations for long times.

The general approach followed in the above papers is the derivation of an averaged rate of reactant consumption which could be a function of position if the concentration field was initially non-uniform. In this paper, we have two objectives. The first is to develop an alternative and, we believe, simpler analytical solution of the unsteady problem. The second is to extend the analysis to domains with a boundary. The analysis is based on configurational averaging initially formulated by Hinch[11] which we have previously applied to the steady problem.[12] The boundary introduces disturbances in the concentration field that cannot be properly described as a simple boundary condition to a differential equation.

2 Problem Formulation

The dimensionless equations which describe the reactant concentration in a domain, Ω, containing a suspension of perfect spherical sinks imbedded in an inert matrix material are:

$$\nabla^2 U(\mathrm{x},t) - \frac{\partial}{\partial t} U(\mathrm{x},t) = 0 \tag{1}$$

for points in the matrix and,

$$U(\mathrm{x},t) = 0 \tag{2}$$

for points lying within the spheres. These equations have been cast in dimensionless form using: $\mathrm{x} = \mathrm{x}'/a$, and $t = Dt'/a^2$ where a is the radius of the equisized spheres and D is the constant matrix diffusivity. In general, (1) and (2) are solved subject to an initial distribution of reactant, $U(\mathrm{x},0) = U_i(\mathrm{x})$, and a prescribed boundary condition, $U(\mathrm{x},t) = G(\mathrm{x},t)$ for x on the boundary, $\partial\Omega$. Transforming the equations

yields:

$$\nabla^2 u(\mathbf{x}) - s u(\mathbf{x}) = -U_i(\mathbf{x}) \tag{3}$$

$$u(\mathbf{x}) = 0 \tag{4}$$

$$u(\mathbf{x}) = g(\mathbf{x}) \qquad \mathbf{x} \in \partial\Omega \tag{5}$$

where $u(\mathbf{x})$ and $g(\mathbf{x})$ are the Laplace transforms of $U(\mathbf{x},t)$ and $G(\mathbf{x},t)$; s is (dimensionless) frequency.

The spheres are distributed according to a hard-sphere potential with sphere center density, n. The volume fraction of the spherical phase, $c = \frac{4\pi}{3}a^3 n$, is assumed small. Equations (3) and (4) are configurationally averaged to yield the infinite hierarchy of coupled equations:[11,12]

$$\nabla^2 u_0(\mathbf{x}) - s u_0(\mathbf{x}) = -(1-c)U_i(\mathbf{x}) + 3cB_1(\mathbf{x}) \tag{6}$$

$$\nabla^2 u_1(\mathbf{x}) - s u_1(\mathbf{x}) = -(1-c)U_i(\mathbf{x}) + 3cB_2(\mathbf{x}) \qquad \|\mathbf{x}-\mathbf{x}_1\| > 1 \tag{7}$$

$$\nabla^2 u_2(\mathbf{x}) - s u_2(\mathbf{x}) = -(1-c)U_i(\mathbf{x}) + 3cB_3(\mathbf{x}) \qquad \|\mathbf{x}-\mathbf{x}_1\|,\ \|\mathbf{x}-\mathbf{x}_2\| > 1 \tag{8}$$

$$\vdots$$

where $u_N(\mathbf{x})$ is the configurationally averaged concentration field with sphere centers fixed at $\mathbf{x}_1, \mathbf{x}_2, \mathbf{x}_3, \cdots \mathbf{x}_N$. The factor $(1-c)$ reflects the absence of reactant within the sinks. The quantity, $B_N(\mathbf{x})$ is defined by:

$$B_N = \frac{1}{4\pi} \int_{\{\|\mathbf{x}-\mathbf{x}_N\|=1\}\cap\Omega_{N-1}} \frac{\partial}{\partial n} u_N(\mathbf{x}) d\mathbf{x}_N \tag{9}$$

which is essentially the average rate of reactant consumption by a sink at $\mathbf{x}$ given sinks fixed at $\mathbf{x}_1, \mathbf{x}_2, \mathbf{x}_3, \cdots \mathbf{x}_{N-1}$. The restricted domain Ω_N is the allowed portion of the domain for sphere centers consisting of the domain Ω less the excluded hard-sphere volume in the neighborhood of the boundary, $\partial\Omega$, and N spheres fixed at $\mathbf{x}_1, \mathbf{x}_2, \mathbf{x}_3, \cdots \mathbf{x}_N$. All averaged equations are subject to boundary condition (5) on

$\partial\Omega$ and (4) on all fixed sphere surfaces. Short-range correlations between the spheres which are induced by the hard-sphere potential[13] have been neglected throughout the foregoing averaging procedure which is valid for dilute volume fractions.[11] An effective rate coefficient can be defined,

$$ku_0(\mathbf{x}) = B_1(\mathbf{x}) \tag{10}$$

implying that the governing equation for the configurationally averaged concentration field may be cast in local form. This assumption is only valid far away from the domain boundary as discussed below.

The hierarchy must be truncated to permit solution of the unconditionally averaged field. The truncated hierarchy is solved in reverse order: the equation with the most spheres fixed is solved first because it is decoupled from the others; its solution provides the forcing term for the next equation. The procedure is continued until the unconditionally averaged field, u_0, is found.

The hierarchy is exploiting the assumption of diluteness ($c << 1$) and the physics of screening: far from a fixed sphere, its influence is "screened" by the presence of the intervening sinks in the material.[14] For large separation, $\|\mathbf{x} - \mathbf{x}_1\| >> L_s$:

$$u_1(\mathbf{x}) \sim u_0(\mathbf{x}) \tag{11}$$

where L_s is the "screening length" which is defined below. Using diluteness, $c << 1$, Equation (7) is approximated by:

$$\nabla^2 u(\mathbf{x})_1 - su(\mathbf{x})_1 = -(1-c)U_i(\mathbf{x}) \tag{12}$$

which is solved subject to boundary condition, (4) and the screening relation, (11) by elementary methods to obtain:

$$B_1 = u_0(\mathbf{x}) \tag{13}$$

which according to (10) is equivalent to the Smoluchowski result,[1] $k_S = 1$. Boundary condition (5) has been neglected in favor of (11). The $\sqrt{s}$ term which correlates with the short time scale, a^2/D, is omitted from (13) and will be throughout consistent with the approach of Felderhof.[7] Inserting the result into (6) yields the "mean-field" truncation:

$$\nabla^2 u_0(\mathbf{x}) - p u_0(\mathbf{x}) = -(1-c)U_i(\mathbf{x}) \tag{14}$$

where $p = s + 3c$ which is small for $t >> 1$ and $c << 1$. By analogy to the foregoing procedure, higher-order truncations are obtained:

$$\nabla^2 u_1(\mathbf{x}) - p u_1(\mathbf{x}) = -(1-c)U_i(\mathbf{x}) \tag{15}$$

$$\nabla^2 u_2(\mathbf{x}) - p u_2(\mathbf{x}) = -(1-c)U_i(\mathbf{x}) \tag{16}$$

Truncation (14) retains the screening effect of the spheres but neglects all direct sphere-sphere and sphere-boundary interactions. Truncation (15) retains sphere-boundary interactions and (16) includes two-sphere interactions. Rescaling Eqs. (14)-(16) to balance the diffusive and dissipative terms defines a screening length, $L_s = a|\, p^{-\frac{1}{2}}|$.

3 Decay of a Uniform Distribution of Reactant

In this section, we consider the decay of an initially uniform distribution of reactant in an infinite medium of reactive spheres. Accordingly, $U_i(\mathbf{x}) = 1$, and u_0 and B_1 are spatially invariant.

We will truncate the hierarchy with Eq. (16) and use the commonly employed, approximation:[7]

$$\begin{aligned} B_2(\mathbf{x}) &= \frac{1}{4\pi}\int_{\{\|\mathbf{x}-\mathbf{x}_2\|=1\}} \frac{\partial}{\partial n} u_2(\mathbf{x}_2)\, d\mathbf{x}_2 \qquad \mathbf{x} \in \Omega_1 \\ &= 0 \qquad\qquad\qquad\qquad\qquad\qquad\qquad\quad \mathbf{x} \notin \Omega_1 \end{aligned} \tag{17}$$

We can then write:

$$\begin{aligned} B_2(r) &= B_1\left[1-Q(r)\right] && r>2 \\ &= 0 && r<2 \end{aligned} \tag{18}$$

where $r=\|\mathbf{x}-\mathbf{x}_1\|$ and $Q(r)$ is the reduction in sink strength resulting from two-sphere interactions. Solving (16) and (4) up to two reflection disturbances yields:[15]

$$Q(r)=\frac{\mathrm{e}^{-\sqrt{p}\,r}}{r}-\frac{\mathrm{e}^{-\sqrt{p}\,r}}{r^2} \tag{19}$$

Eq. (7) becomes:

$$\begin{aligned} \frac{1}{r^2}\frac{d}{dr}\left(r^2\frac{du_1}{dr}\right)-su_1 &= -(1-c)+3cB_1\left[1-\frac{\mathrm{e}^{-\sqrt{p}\,r}}{r}+\frac{\mathrm{e}^{-\sqrt{p}\,r}}{r^2}\right] \qquad r>2 \\ &= -(1-c) \qquad\qquad 1<r<2 \end{aligned} \tag{20}$$

which is solved for B_1:

$$B_1=\frac{1-c}{s}\left[1+3c\{\frac{1}{s}-\frac{1}{\sqrt{s}+\sqrt{p}}-\ln(\sqrt{s}+\sqrt{p})-\gamma_E-\ln 2\}\right]^{-1} \tag{21}$$

where short-time $\sqrt{s}$ behavior is neglected and $\gamma_E=0.57722\cdots$ is Euler's constant. Inserting this result into (6) yields:

$$-su_0=-(1-c)+3c\frac{1-c}{s}\left[1+3c\{\frac{1}{s}+\frac{1}{\sqrt{s}+\sqrt{p}}+\ln(\sqrt{s}+\sqrt{p})+\gamma_E+\ln 2\}\right]^{-1} \tag{22}$$

Then according to (10), we can express the solution in terms of an effective rate constant, k:

$$u_0=\frac{1-c}{s+3ck} \tag{23}$$

given by:

$$k=\left[1-3c\{\frac{1}{\sqrt{s}+\sqrt{p}}+\ln(\sqrt{s}+\sqrt{p})+\gamma_E+\ln 2\}\right]^{-1}+O(c^{3/2}\ln c) \tag{24}$$

which differs from Felderhof's solution:[7]

$$k_F = \left[1 - 3c\{\frac{1}{\sqrt{s}+\sqrt{p}} + \ln(\sqrt{s}+\sqrt{p}) + \gamma_E + \ln 3\}\right]^{-1} + O(c^{3/2}\ln c) \qquad (25)$$

only in the order c term. The reason for the discrepancy is unclear. In the long-time ($s \to 0$) limit, these rate constants yield:

$$k_\infty = 1 + \sqrt{3c} + \frac{3c}{2}\ln 3c + 3c\,(1 + \gamma_E + \ln 2) \qquad (26)$$

$$k_{\infty,F} = 1 + \sqrt{3c} + \frac{3c}{2}\ln 3c + 3c\,(1 + \gamma_E + \ln 3) \qquad (27)$$

both of which differ slightly from the steady-state rate constant determined previously by Felderhof and Deutch:[2]

$$k_{\infty,FD} = 1 + \sqrt{3c} + \frac{3c}{2}\ln 3c + 3c\,(1 + \gamma_E + \ln 6) \qquad (28)$$

where the dipole contribution has been omitted from their solution[2] for the sake of comparison. The steady-state rate constant has been determined by others[3–6] and the different results discussed.[5] In the case of an initial uniform distribution of reactant, Bixon and Zwanzig's solution[8] reduces to:

$$k_{BZ} = 1 + \sqrt{s} \qquad (29)$$

which is obtained by neglecting two-sphere interactions ($Q = 0$) and retaining the $\sqrt{s}$ term in the solution of (20). At steady-state, $k_{\infty,BZ} = 1$ which coincides with Smoluchowski's solution.

The decay of an initially uniform distribution of reactant in an unbounded, dilute suspension of reactive spherical sinks is given by inversion of (23). The above solutions (with rate constants: k, k_F, k_{BZ} and k_S) all decay exponentially for short times,

$$U \sim U_F \sim U_{BZ} \sim U_s = (1-c)\mathrm{e}^{-3ct} \qquad 3ct << 1 \qquad (30)$$

but differ substantially in their long-time behavior. The Smoluchowski solution is given by (30) for all times which differs markedly from the long-time ($3ct >> 1$) algebraic decay exhibited by the other solutions:

$$U_{BZ} \sim \frac{1-c}{6c} \frac{1}{\sqrt{\pi t^3}} \tag{31}$$

$$U = U_F \sim \frac{1-c}{6c} \frac{1-\sqrt{3c}}{\sqrt{\pi t^3}} \tag{32}$$

This result implies that, at long times, the relative offset, $(U_F - U_{BZ})/U_F$, attains the value: $\left[-\sqrt{3c}/\left(1-\sqrt{3c}\right)\right]$.

Figure 1. displays $U(t)$ for a sphere volume fraction of 0.01. The transition from exponential to algebraic decay is apparent. The remaining curves show the difference between the above solutions and U_F. The difference between U_{BZ} and U_F results from neglecting two-sphere interactions thus demonstrating their significance. Initially, two-sphere interactions reduce the rate at which reactant is consumed thus, $U_F > U_{BZ}$ for short times. Two-sphere interactions appear to retard the transition from exponential to algebraic decay; during the transition, the relative difference between these two solutions changes sign and, at long times, $U_F < U_{BZ}$. Figure 1. predicts that the relative offset of the Bixon-Zwanzig solution is approximately -21% as quantitatively asserted by Eqs. (31) and (32). The relative difference between U_S and U_F diverges at $3ct \approx 1$ thus marking the transition from exponential to algebraic decay in the solution derived herein as well as in the solutions of Felderhof and Bixon-Zwanzig. Figure 1. shows that the deviation of our solution (relative to U_F) is uniformly small ($\leq 3\%$) and tends to zero at both short and long times in agreement with Eqs. (30) and (32). Apparently, the present approach closely reproduces the results obtained by Felderhof.[7]

4 Reactant Flux into a Semi-infinite Domain

In this section, we determine the transient reactant flux on the boundary, $x = 0$, of a semi-infinite domain. We shall consider the case in which reactant concentration is initially absent from the domain ($U_i(\mathbf{x}) = 0$). The boundary condition, $G(\mathbf{x}, t)$, is assumed to be a slowly-varying function of time and independent of position. Thus, the average concentration field, u_0, and sink strength, B_1, depend only on x, the distance normal to the boundary.

In the presence of boundaries, treating direct two-sphere interactions is very tedious, hence we shall truncate the hierarchy at an earlier stage, employing Eqs. (15) and (17):

$$\begin{aligned} B_1(x) &= u_0(x)\,[1 + Q(x)] \qquad && x > 1 \\ B_1(x) &= 0 && x < 1 \end{aligned} \tag{33}$$

where $Q(x)$ is the sink strength enhancement induced by the boundary at $x = 0$. Solving (15) by the method of reflections[15] yields:

$$Q(x) = \frac{\mathrm{e}^{-2\sqrt{p}\ x}}{2x} + J(x;p) \tag{34}$$

where $J(x;p)$ is the contribution from the second and all higher-order reflections with the boundary. Eq. (6) becomes:

$$\begin{aligned} u_0''(x) - p u_0(x) &= 3c u_0(x) \left[\frac{\mathrm{e}^{-2\sqrt{p}\ x}}{2x} + J(x;p)\right] \qquad && x > 1 \\ u_0''(x) - s u_0(x) &= 0 && 0 < x < 1 \end{aligned} \tag{35}$$

which must satisfy (5) and is solved by the following perturbation scheme for $|p| << 1$ which implies diluteness since $c \leq |p|$. Introducing the scaled independent variable, $\tilde{x} = x\sqrt{p}$, Eq. (35) becomes:

$$u''(\tilde{x}) - u(\tilde{x}) = \frac{3c}{\sqrt{p}} u(\tilde{x}) \left[\frac{\mathrm{e}^{-2\tilde{x}}}{2\tilde{x}} + O(\frac{\sqrt{p}}{\tilde{x}^2})\right] \qquad \tilde{x} > \sqrt{p} \tag{36}$$

$$u''(\tilde{x}) - \frac{s}{p}u(\tilde{x}) = 0 \qquad 0 < \tilde{x} < \sqrt{p}$$

where the subscript, 0, indicating conditional average has been dropped and is heretofore implied. Deriving the first two terms in a regular perturbation yields the uniformly valid approximation:

$$u(x) = g\ \mathrm{e}^{-\sqrt{p}x}\left[1 + \frac{3c}{4\sqrt{p}}\{E_1(2\sqrt{p}x) - \mathrm{e}^{2\sqrt{p}x}E_1(4\sqrt{p}x) - \ln 2\} + O(c)\right] \tag{37}$$

where $E_1(x)$ is the exponential integral. Then, assuming that $G(t)$ attains a constant steady-state value, G_∞, the steady-state ($s \to 0$) concentration field is:

$$U_\infty(x) = G_\infty\ \mathrm{e}^{-\sqrt{3c}\ x}\left[1 + \frac{\sqrt{3c}}{4}\{E_1(2\sqrt{3c}\ x) - \mathrm{e}^{2\sqrt{3c}\ x}E_1(4\sqrt{3c}\ x) - \ln 2\} + O(c)\right] \tag{38}$$

which, far from the boundary, relaxes to:

$$U_\infty(x) = G_\infty\ \mathrm{e}^{-\sqrt{3c}\ x}\left[1 - \frac{\sqrt{3c}}{4}\ln 2\right] \qquad \sqrt{3c}x >> 1 \tag{39}$$

The reactant flux on the boundary is obtained by differentiation of (37):

$$\begin{aligned} f = -\frac{du}{dx}\Big|_{x=0} &= g\left[\sqrt{p} + \frac{3c}{4}\{E_1(2\sqrt{p}) + E_1(4\sqrt{p}) - \ln 2\} + O(c)\right] \\ &= g\left[\sqrt{p} - \frac{3c}{4}\ln p - 3c\left(\ln 2 + \frac{1}{2}\gamma\right) + O(c)\right] \end{aligned} \tag{40}$$

The result given by Eq. (40) is accurate to order $c \ln c$ but can be refined to $O(c)$ by manipulating Eq. (35) to yield the implicit relation:

$$f = g\sqrt{p} + 3c\int_1^\infty \mathrm{e}^{-\sqrt{p}x}u(x)\left[\frac{\mathrm{e}^{-2\sqrt{p}\ x}}{2x} + J(x;p)\right]dx \tag{41}$$

When the first term of Eq. (37) is inserted into the integral of Eq. (41), the following result is obtained:

$$f = g\left[\sqrt{p} + \frac{3c}{4}\{E_1(2\sqrt{p}) + E_1(4\sqrt{p}) - \ln 2\} + 3cj + O(c^{3/2}\ln c)\right] \tag{42}$$

which reproduces the $O(c \ln c)$ solution and an additional term, $g(3cj)$, resulting from the contribution of higher-order reflections with the boundary. $J(x;p)$ is continuous and bounded uniformly by $O(x^{-2})$ as $x \to \infty$. Therefore, the improper integral of J on $[1,\infty)$ converges uniformly in p as $p \to 0$ which permits the limiting process:

$$j = \frac{1}{g} \lim_{p \to 0} \int_1^\infty \mathrm{e}^{-\sqrt{p}x} u(x) J(x;p) dx = \int_1^\infty J(x;0) dx = 0.47472 \cdots \tag{43}$$

The quantity $J(x,0)$ is known exactly from the solution of Laplace's equation in bispherical coordinates[16] and the integration is performed numerically. In the low-frequency limit ($s \to 0$), Eq. (42) reduces to:

$$F_\infty = G_\infty \left[\sqrt{3c} - \frac{3c}{4} \ln 3c - 3c \left(\ln 2 + \frac{1}{2}\gamma - j \right) + O(c^{3/2} \ln c) \right] \tag{44}$$

which nearly reproduces the recently-obtained steady-state solution of Loewenberg and Gavalas:[11]

$$F_{\infty,LG} = G_\infty \left[\sqrt{3c} - \frac{3c}{4} \ln 3c - 3c \left(\frac{3}{4} \ln 3 + \frac{1}{2}\gamma - j \right) + O(c^{3/2} \ln c) \right] \tag{45}$$

The discrepancy between expressions (44) and (45) is similar to that found between k and k_F and cannot be readily explained. In deriving the steady-state result, Loewenberg and Gavalas demonstrated that two-sphere interactions affect the solution at $O(c^{3/2} \ln c)$, a result assumed to hold in the present, time-dependent situation for $3ct >> 1$. For short times, two-sphere interactions have a smaller, order c^2 effect. Thus, in the context of this problem, the omitted two-sphere interactions have a uniformly higher-order effect than the sphere-boundary interactions which are treated above.

According to (10) and (33) we can identify a rate coefficient:

$$\begin{aligned} k(x) &= 1 + \frac{\mathrm{e}^{-2\sqrt{p}x}}{2x} + J(x;p) \qquad x > 1 \\ &= 0 \qquad\qquad\qquad\qquad\quad x < 1 \end{aligned} \tag{46}$$

which is specific to the boundary considered in this problem indicating that the bulk equations depend on the choice of boundary. Therefore, application of an effective rate coefficient which treats two-sphere interactions and is derived for the boundary-free problem would be inconsistent.

To assess the significance of sphere-boundary interactions, the above results are compared with the Smoluchowski solution which neglects all interactions except screening. The quantities u_S and f_S are obtained by solving Eq. (14):

$$u_S = g\ \mathrm{e}^{-\sqrt{p}\ x}\ ; \qquad f_S = g\sqrt{p} \tag{47}$$

which at steady-state, reduce to:

$$U_{\infty,S} = G_\infty\ \mathrm{e}^{-\sqrt{3c}\ x}\ ; \qquad F_{\infty,S} = G_\infty\sqrt{3c} \tag{48}$$

Eqs. (40) and (47) indicate the sphere-boundary interactions affect the reactant flux at order $c \ln c$. A comparison of Eqs. (39) and (48) indicate that the relative far-field ($\sqrt{3c}x >> 1$) depletion at steady-state which results from sphere-boundary interactions is $O(\sqrt{c})$.

As an illustration, we shall consider the transient reactant flux resulting from a unit step change in reactant concentration with sphere volume fraction, $c = 0.01$. Thus, $G(t)$ is given by the Heaviside function which has the transform, $g = 1/s$, and the steady-state value, $G_\infty = 1$. For short times, the solution is dominated by sink-independent algebraic decay:

$$F \sim \frac{1}{\sqrt{\pi t}} \qquad 3ct << 1 \tag{49}$$

and attains the steady value, F_∞, at $3ct \approx O(1)$ as shown in Figure 2. The remaining curve shows $(F - F_S)/F$ and demonstrates that sphere-boundary interactions enhance the reactant flux and become most significant at long times. According

to (39) and (48), sphere-boundary interactions deplete the steady-state, far-field concentration by about 3%, but enhance the steady-state reactant flux by approximately 10% as indicated in Figure 2. For the parameters used in this example, the steady-state flux, F_∞, deviates from the previous result, $F_{\infty,LG}$, by about 2%.

5 Conclusions

A configurational averaging approach was developed to analyze diffusion-controlled reactions. This approach reproduces previous results for the case of an unbounded medium. The calculated reactant concentration exhibits exponential decay initially and slow $t^{-3/2}$ decay for $3ct >> 1$. Two-sphere interactions were included and their effect shown to be order $\sqrt{c}$ for long times. The configurational averaging technique was then used to determine the time-dependent reactant flux in a medium with a macroscopic boundary. The presence of the boundary affects the averaged equations which govern the bulk concentration field. Thus, an effective rate coefficient cannot be consistently applied. The analysis shows that the boundary induces an order $c \ln c$ enhancement of the reactant flux and an order $\sqrt{c}$ depletion to the steady-state, far-field. An illustration shows that although the effect of sphere-boundary interactions on the far field is small, the effect on the reactant flux on the boundary is more significant. This flux algebraically approaches a steady-state value in close agreement with a previous result. In general, it appears that the configurational averaging approach is simpler than previous approaches and is well suited to treat bounded domains.

6 Acknowledgements

This work was made possible through a fellowship from the LINK foundation.

7 References

1. M.V. Smoluchowski, Phys. Z. **17**, 557 (1916).

2. B.U. Felderhof and J.M. Deutch, J. Chem. Phys. **64**, 4551 (1976).

3. M. Muthukumar and R.I. Cukier, J. Stat. Phys. **26**, 453 (1981).

4. M. Muthukumar, J. Chem. Phys. **76**, 2667 (1982).

5. K. Mattern and B.U. Felderhof, Physica **135A**, 505 (1986).

6. K. Mattern and B.U. Felderhof, Physica **147A**, 1 (1987).

7. B.U. Felderhof, J. Chem. Phys. **66**, 4385 (1977).

8. M. Bixon and R. Zwanzig, J. Chem. Phys. **75**, 2354 (1981).

9. B.U. Felderhof, J.M. Deutch and U.M. Titulaer, J. Chem. Phys. **76**, 4178 (1982).

10. M. Tokuyama and R.I. Cukier, J. Chem. Phys. **76**, 6202 (1982).

11. M. Loewenberg and G.R. Gavalas, Chem. Eng. Sci., In Press.

12. E.J. Hinch, J. Fluid Mech. **83**, 695 (1977).

13. J.M. Ziman, *Models of Disorder.* Cambridge: Cambridge University Press (1979).

14. H.C. Brinkman, Appl. Sci. Res. A **1**, 27 (1947).

15. J.D. Jackson, *Classical Electrodynamics* New York: John Wiley & Sons, Inc (1962).

16. G.B. Jeffery, Proc. R. Lond. A **87**, 109 (1912).

8 Figure Captions

1. Decay of an initially uniform distribution of reactant, U, with sphere volume fraction, $c = 0.01$:(———).
   Normalized differences between various solutions: $(U_F - U)/U_F$ (———); $(U_F - U_{BZ})/U_F$(– · – · –); $(U_F - U_S)/U_F$(· · · · · ·).

2. Reactant flux, F, into a semi-infinite medium resulting from a step change in the boundary concentration with sphere volume fraction, $c = 0.01$ (———).
   The relative effect of sphere-boundary interactions: $(F - F_S)/F$(· · · · · ·).

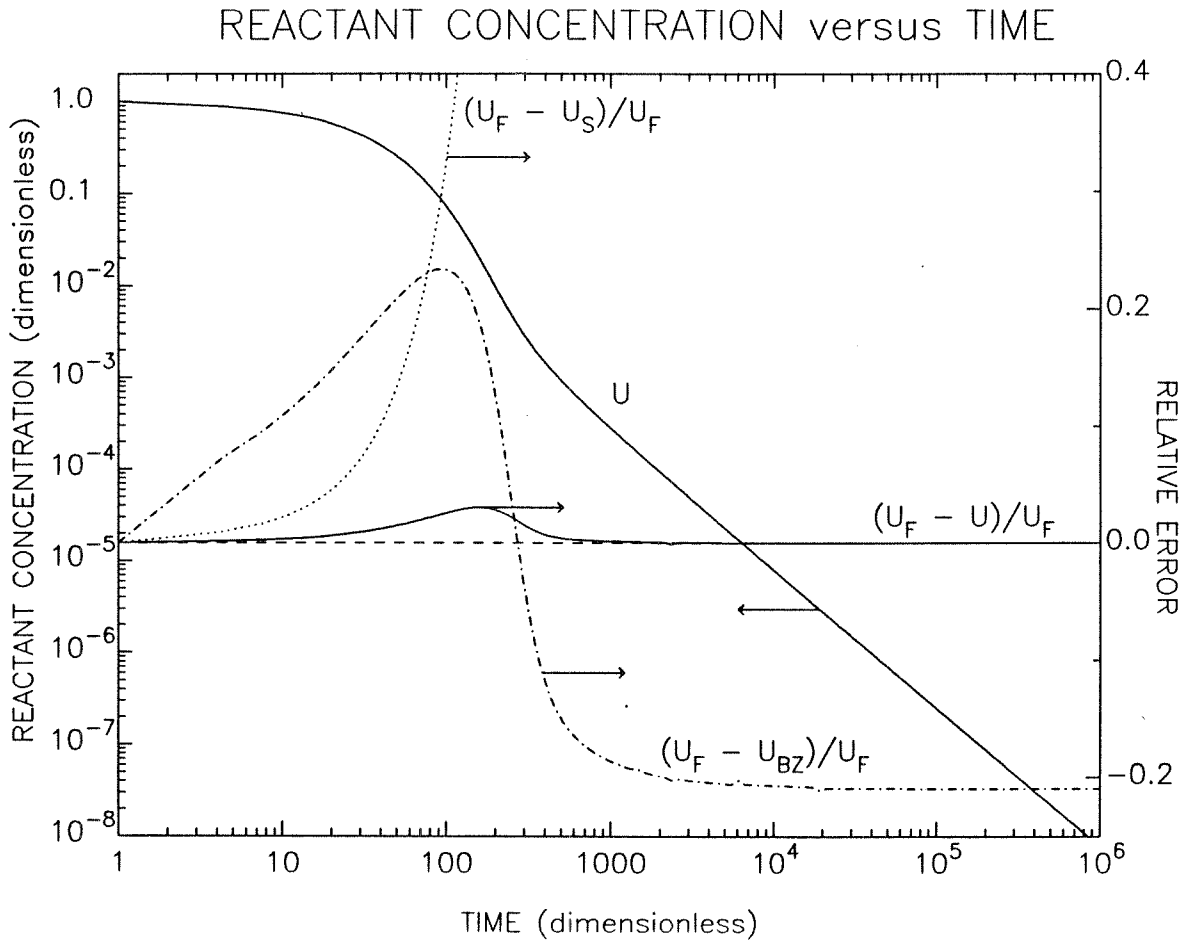

Figure 1: Decay of an initially uniform distribution of reactant, U, with $c = 0.01$. Error relative to Felderhof's solution: $(U_F - U)/U_F$ (———); $(U_F - U_{BZ})/U_F$(– · – · –); $(U_F - U_S)/U_F$(· · · · · ·)

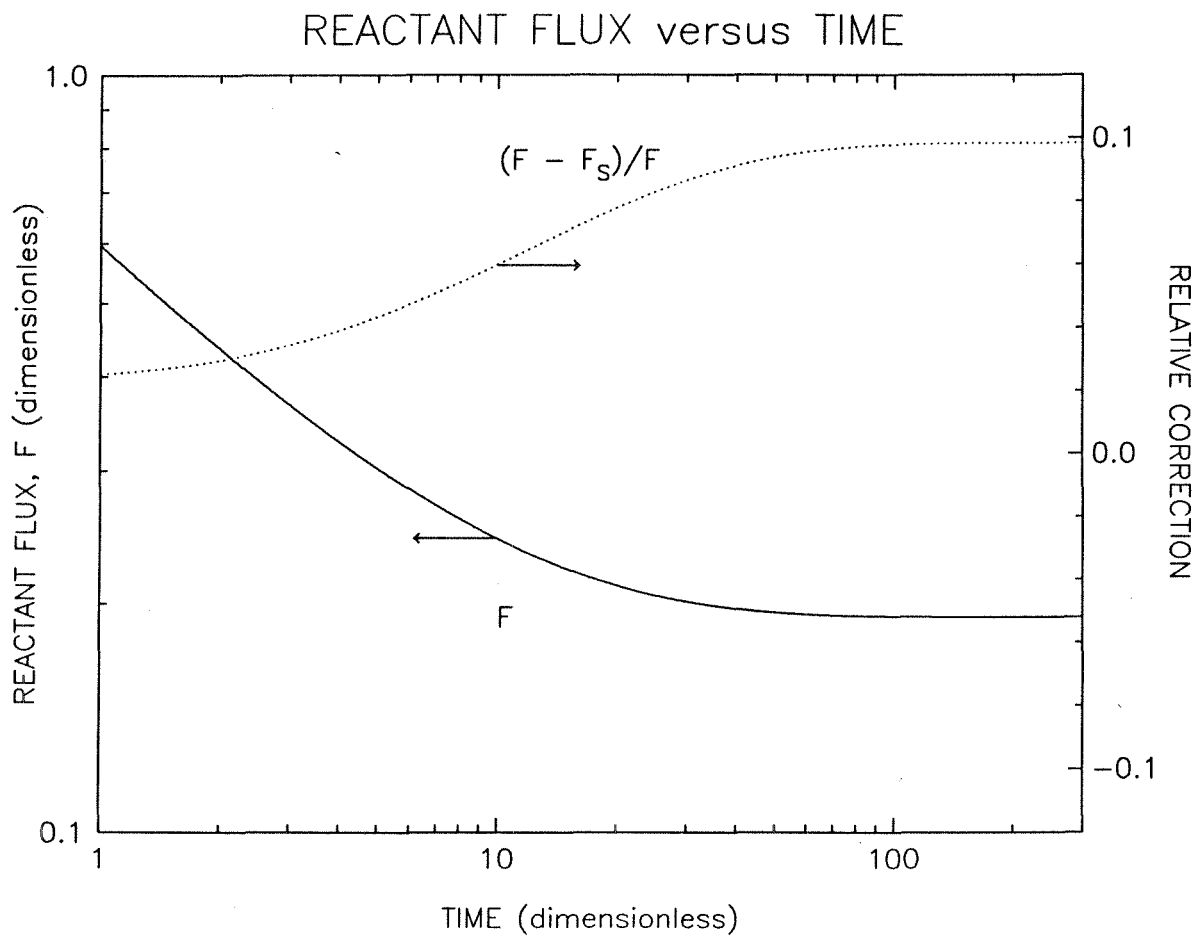

Figure 2: Reactant flux, F, into a semi-infinite medium resulting from a step change in the boundary concentration with sphere volume fraction, $c = 0.01$: (———). The relative effect of sphere-boundary interactions, $(F - F_S)/F$: (·····)

CHAPTER 8

Reaction and Diffusion in a Random, Porous Material

Reaction and Diffusion in a Random, Porous Material

M. Loewenberg and G. R. Gavalas
Department of Chemical Engineering 206-41
California Institute of Technology
Pasadena, California 91125

Abstract

A detailed analysis is presented for the theoretical treatment of the combined diffusion and reaction process which occurs in reactive, porous materials. A bimodal pore size distribution is assumed with a random, isotropic distribution of equisized, cylindrical macropores. A configurational averaging procedure is developed to address the finite size and detailed distribution of macropores. A hierarchy of coupled equations is produced which is later truncated assuming low macropore void volume. The microporous material is described as a continuum with a local diffusion coefficient and homogeneous, first-order rate constant. The present analysis is valid for diffusion-controlled conditions in which reactant penetration is on the same order as the size of the macropores. In the diffusion-controlled limit, the results reduce to those obtained by a simpler, single pore model described within. The results are qualitatively different than those obtained by a continuum description of the material.

1 Introduction

The study of reaction and diffusion in porous materials is important because of its obvious relevance to a variety of important technological problems including coal combustion and heterogeneous catalysis. Significant progress has been made since the pioneering work of Thiele (1939) who introduced the concept of an effectiveness factor that relates the observed rate of chemical reaction to the maximal rate that would occur in the absence of diffusional limitations. A single pore model was used in which the radius of the cylindrical pore was taken as the hydraulic radius of the pores in the catalyst. The object of predicting the rate of chemical reaction under conditions in which mass transport effects are significant has continued to be a central goal in studies involving heterogeneous reaction and diffusion.

Intraparticle mass transport has often been analyzed with pseudo-homogeneous differential equations. Such an approach ignores all details of the particle structure which, under some conditions, is adequate. However, in certain situations, details of the material microstructure become important. These conditions typically arise during the pulverized combustion of softening coals which tend to form cenospheres during heatup. Figure 1a. shows a bimodal pore size distribution for a cenosphere formed from PSOC-1451 bituminous coal char (Northrop 1988). Under the high-temperature conditions pertinent to pulverized coal combustion, oxygen penetration is on the order of a micron which, according to the figure, is the size of the larger pores in the char (Loewenberg 1988). In this context, a continuum treatment is inappropriate.

The pore size distribution of commercial catalysts are often bimodal, a consequence of their construction, typically from the compression of fine powders, consisting of small microporous particles, to form catalyst pellets (Satterfield p. 114,

1980). Figure 1b. depicts the bimodal pore size distribution of a commercial catalyst used for the water-gas shift reaction (Bohlbro, 1966). The proper analysis of heterogeneous reaction and diffusion in materials with a bimodal pore size distribution was addressed by Mingle and Smith (1961) through the introduction of a microeffectiveness factor to account for the reaction and diffusion within the small particles of the powder precursor. The microeffectiveness factor was obtained by an analysis of the transport within the microporous particles and inserted into a differential equation describing the bulk transport within the pellet. The overall effectiveness factor is a product of the macro- and microeffectiveness factors. This approach was subsequently employed by several other workers including Carberry (1962), Tartarelli (1971), and Örs and Doğu (1979).

Random pore models have been developed to describe the pore structure of char particles. A pore tree model was developed by Simons (1979) which describes the pore structure by trees emanating from the particle surface to its interior. Random capillary models have been developed by Gavalas (1980) and Bhatia and Perlmutter (1980). These models assume a random, isotropic distribution of cylindrical pores and implicitly account for various important details of the microstructure such as pore overlap.

In this paper, we analyze the reaction-diffusion processes that are relevant under diffusion-controlled conditions in which reactant concentration gradients have a length scale comparable to the size of the largest voids in the material. Under these conditions, the details of the macropore distribution become important. The detailed microstructure of the material is addressed according to the approach of Hinch (1977), using a configurational averaging procedure which is developed within. A hierarchy of coupled equations is produced which is truncated assuming a low macropore void volume. In the diffusion-controlled limit, the results reduce

to those obtained by a simple, single pore model described within. The results are qualitatively different than those obtained by a continuum description of the material that is valid under complimentary conditions in which there is a disparity between the length scales for the pore structure and the concentration profile (kinetic control).

2 Formulation

We envisage diffusion and chemical reaction in a porous material with reactant supplied at the boundary. A first-order surface reaction occurs at uniformly-distributed, constant-activity sites. Thus, the reacting material is assumed isothermal. A bimodal distribution of pore sizes is assumed in which the micropores are in the Knudsen size range (small compared with the mean free path). Diffusion in the macropores may occur via Knudsen, bulk, or a combination of both mechanisms. This situation is depicted by the pore size distributions shown in Figs. 1a and b. The macropore network is described by a random, isotropic distribution of monodisperse, cylindrical voids with radius, a, and void volume, ϵ_2. The void volume of the micropores is ϵ_1 and the total voidage is given by: $\epsilon_T = \epsilon_1 + \epsilon_2$. The microporous structure is described by a continuum with a local diffusion coefficient and homogeneous, first-order rate constant.

The effective diffusivity within the microporous material is given by:

$$D_1 = \frac{\epsilon_1}{\tau(1-\epsilon_2)} D_K \tag{1}$$

where $\epsilon_1/(1-\epsilon_2)$ is the void fraction per volume of microporous material and τ is the tortuosity of the micropore structure (Satterfield p.40, 1970). D_K is the Knudsen diffusion coefficient which is proportional to the micropore radius (Knudsen 1909). The effective diffusivity of the microporous material may be an order

of magnitude smaller than the diffusion coefficient within a micropore and easily two orders of magnitude smaller than the diffusion coefficient in the macropores, D_2. Under diffusion-controlled conditions, the macropores significantly enhance reactant transport into the material but the micropores supply the majority of the pore surface area for reaction.

The (homogeneous) reaction rate constant characterizing the microporous material is given by (Satterfield p.131, 1970):

$$k_1 = \frac{S k_S}{1 - \epsilon_2} \tag{2}$$

where k_S is a first-order surface rate coefficient which is constant by the assumption that the material is isothermal. $S/(1-\epsilon_2)$ is the local pore surface (per volume of microporous material). Eqs. (1) and (2) specify the continuum which will be used to describe the micropore structure.

According to the continuum description of the microporous matrix, the reactant concentration in this phase of the material is described by:

$$D_1 \nabla^2 C(\mathrm{x}) - k_1 C(\mathrm{x}) = 0 \tag{3}$$

However, in the macropores, which are inert to chemical reaction, the concentration profile satisfies Laplace's equation:

$$\nabla^2 C(\mathrm{x}) = 0 \tag{4}$$

The binary diffusivity within the macropores, D_2, may be given by a bulk diffusion coefficient for sufficiently large pores or by:

$$\frac{1}{D_2} = \frac{1}{D_K} + \frac{1 - y_A \left(1 + \frac{N_B}{N_A}\right)}{D_{\mathrm{b}}} \tag{5}$$

which was derived independently by Evans *et al.* (1961), Scott and Dullien (1962), and Rothfield (1963) for pores in the transition regime where both Knudsen and

bulk mechanisms are important. The quantities N_A and N_B denote molar flows of the gaseous species A and B and y_A specifies the composition of the binary mixture. D_b is the bulk diffusion coefficient. Stefan flow important for non-equimolar ($N_B \neq -N_A$) bulk diffusion at higher concentrations is neglected according to the approach of Wakao and Smith (1964); (Hill p.434, 1977), which eliminates composition dependence.

The governing equations are cast in dimensionless form using the macropore radius, a, and boundary concentration value (assumed constant) as characteristic values for length and concentration. We shall assume some domain, Ω, with a boundary, $\partial\Omega$, and characteristic length, L. Eqs. (3) and (4) become:

$$\nabla^2 C(\mathrm{x}) - \phi^2 C(\mathrm{x}) = 0 \qquad \text{microporous matrix} \tag{6}$$

$$\nabla^2 C(\mathrm{x}) = 0 \qquad \text{macropores} \tag{7}$$

$$C(\mathrm{x}) = 1 \qquad \text{on boundary : } \mathrm{x} \in \partial\Omega \tag{8}$$

where ϕ is a microscale Thiele modulus based on the macropore radius:

$$\phi = a\sqrt{\frac{k_1}{D_1}} \tag{9}$$

which is related to a macroscale Thiele modulus, based on the characteristic length of the domain:

$$\Phi = L\phi \tag{10}$$

and

$$L = \frac{V}{A} \tag{11}$$

where V and A are the normalized volume of the domain, Ω, and area of the boundary, $\partial\Omega$ according to the approach of Aris (1957). Continuity of reactant concentration and flux yield smoothness requirements for $C(\mathrm{x})$ on the macropore

surface:

$$\lim_{\|\delta\|\to 0}\left[C(\mathbf{x}+\delta)-C(\mathbf{x})\right] = 0 \tag{12}$$

$$\lim_{\|\delta\|\to 0^+}\left[\nabla C(\mathbf{x}+\delta)\cdot\mathbf{n}-\alpha\nabla C(\mathbf{x}-\delta)\cdot\mathbf{n}\right] = 0 \tag{13}$$

having defined:

$$\alpha \equiv \frac{D_2}{D_1} \tag{14}$$

3 Configurational Averaging

In this section, the result of configurationally averaging the governing equations is presented. The overall rate is given by:

$$R^T = R_\mathrm{b} + R_\mathrm{p} \tag{15}$$

where:

$$R_\mathrm{b} = -\frac{\partial}{\partial n}C_0(\mathbf{x})\bigg|_{\mathbf{x}\in\partial\Omega} \tag{16}$$

$$R_\mathrm{p} = \epsilon_2\alpha\int_0^{\frac{\pi}{2}}\int_{\rho_1\le 1}\left[\nabla C_1(\mathbf{x})\cdot\mathbf{n}\right]\sin\theta_1 d\hat{\mathbf{x}}_1 d\theta_1\bigg|_{\mathbf{x}\in\partial\Omega} \tag{17}$$

where R_p results from the consumption of reactant within the macropores and R_b describes the consumption of reactant at the boundary, $\partial\Omega$. The functions $C_0(\mathbf{x})$ and $C_1(\mathbf{x})$ are obtained by configurationally averaging Eqs. (6)-(8) resulting in an infinite hierarchy of coupled equations. The derivation assumes $\alpha >> 1$ and neglects intersections between the macropores which is valid for $\epsilon_2 << 1$. Closure relations, valid under the latter assumption, are used to truncate the hierarchy. The resulting (closed) set of configurationally averaged equations is:

$$\nabla^2 C_0(\mathbf{x}) - \phi^2 C_0(\mathbf{x}) = -\phi^2 C_\infty(\mathbf{x}) \tag{18}$$

$$\nabla^2 C_1(\mathbf{x}) - \phi^2 C_1(\mathbf{x}) = -\phi^2 C_\infty(\mathbf{x}) \qquad \rho_1 > 1 \tag{19}$$

$$\nabla^2 C_1(\mathbf{x}) = 0 \qquad \rho_1 < 1 \tag{20}$$

$$C_0(\mathbf{x}) = C_1(\mathbf{x}) = 1 \qquad \text{on boundary : } \mathbf{x} \in \partial\Omega \tag{21}$$

where $C_\infty(\mathbf{x})$ is given by:

$$C_\infty(\mathbf{x}) = \epsilon_2 A_1(\mathbf{x}) + \frac{2\epsilon_2}{\phi^2} B_1(\mathbf{x}) \tag{22}$$

As shown below, $C_\infty(\mathbf{x})$ describes the bulk concentration field except in the region close to the boundary. $A_1(\mathbf{x})$ and $B_1(\mathbf{x})$ are defined by:

$$A_1(\mathbf{x}) = \frac{1}{\pi} \int_0^{\frac{\pi}{2}} \int_{\rho_1 \le 1} C_1(\mathbf{x}) d\hat{\mathbf{x}}_1 \sin\theta_1 d\theta_1 \tag{23}$$

$$B_1(\mathbf{x}) = \int_0^{\frac{\pi}{2}} \lim_{\delta \to 0+} \frac{1}{2\pi} \int_{\rho_1 = 1} -\frac{\partial}{\partial n} C_1(\mathbf{x}) \Big|_{\rho_1 = 1+\delta} d\hat{\mathbf{x}}_1 \sin\theta_1 d\theta_1 \tag{24}$$

where the normal derivative in the definition of $B_1(\mathbf{x})$ is evaluated on the external surface of the pore as indicated. These expressions indicate that $C_0(\mathbf{x})$ is coupled to the conditionally averaged concentration field, $C_1(\mathbf{x})$. $A_1(\mathbf{x})$ is the average concentration within the macropores; its presence on the right hand side of Eqs. (18) and (19) reflects the reduction in the bulk reactivity resulting from the inert volume introduced by the macropores. $B_1(\mathbf{x})$ is the source term which results from the reactant supplied to the material through the macropores.

4 Approximations

In this section, approximations are developed that are used to obtain the solution to (18)-(21). It is convenient to define cylindrical coordinates oriented with respect to a specified pore axis: $\mathbf{x} = (\rho_1, \varphi_1, \xi_1)$ as defined in the appendix, where ξ_1 is the distance from the boundary along the specified pore axis. These coordinates

are dipicted in Figures 2a-c. As discussed in the appendix, a reference plane (for a random, isotropic material) may be arbitrarily specified by a unit vector, **e**. A unit vector, $\mathbf{q}_1$, in the ξ_1-direction specifies the orientation of a particular pore axis with respect to **e**. The coordinate ρ_1 is the radial distance from the specified pore axis and φ_1 is an azimuthal angle. The following restrictions will be imposed:

(i) The void volume of the macropores is small; $\epsilon_2 << 1$.

(ii) The Thiele modulus, based on the macropore radius, is restricted by the inequality:
$\phi^2 \ln \phi >> 2\epsilon_2$.

(iii) The ratio of the diffusion coefficient in the macropores, D_2, to the effective diffusivity of the micropores, D_1, is large; $\alpha \geq \epsilon_2^{-1}$.

(iv) The number of macropores is large: $L >> 1$; thus, the macroscale Thiele modulus is large; $\Phi >> 1$.

Under these conditions, as shown below, the intrapore concentration field is approximately axial, and the external field is approximately radial to the pore axis:

$$C_1(\mathrm{x}) = U_1(\xi_1;\theta_1) \qquad \rho_1 < 1 \tag{25}$$

$$C_1(\mathrm{x}) = V_1(\rho_1;\theta_1) \qquad \rho_1 > 1 \tag{26}$$

and when valid, these assumptions reduce definitions (17), (23) and (24) to:

$$A_1(\mathrm{x}) = \int_0^{\frac{\pi}{2}} U_1(\xi_1;\theta_1)\sin\theta_1 d\theta_1 \tag{27}$$

$$B_1(\mathrm{x}) = \int_0^{\frac{\pi}{2}} -\frac{d}{d\rho_1}V_1(\rho_1;\theta_1)\bigg|_{\rho_1=1} \sin\theta_1 d\theta_1 \tag{28}$$

$$R_\mathrm{p} = \epsilon_2\alpha\int_0^{\frac{\pi}{2}} -\frac{d}{d\xi_1}U_1(\xi_1;\theta_1)\bigg|_{\xi_1=0} [\mathbf{q}_1\cdot\mathbf{e}]\sin\theta_1 d\hat{\mathrm{x}}_1 d\theta_1$$

$$= \epsilon_2 \alpha \int_0^{\frac{\pi}{2}} -\frac{d}{d\xi_1} U_1(\xi_1;\theta_1)\Big|_{\xi_1=0} \cos\theta_1 \sin\theta_1 d\theta_1 \tag{29}$$

where the latter result is obtained using the relation: $\mathbf{q}_1 \cdot \mathbf{e} = \cos\theta_1$. Assumption (iv) is a practical consideration which implies:

$$C^0(\mathbf{x}) \sim \mathrm{e}^{-\phi z} \qquad \Phi >> 1 \tag{30}$$

where z is distance normal to the boundary and $C^0(\mathbf{x})$ is the homogeneous solution of (18) or, equivalently, the bulk concentration field in the limit $\epsilon_2 \to 0$. Similarly:

$$R_0 = \phi \qquad \Phi >> 1 \tag{31}$$

$$\eta_0 = \frac{1}{\Phi} \qquad \Phi >> 1 \tag{32}$$

are the overall rate and effectiveness factor for $\epsilon_2 \to 0$.

5 Solution Procedure

In this section, intermediate results are obtained which are used in the following sections to obtain the bulk concentration field and overall rate. Using (26), Eq. (19) becomes:

$$\frac{1}{\rho_1}\frac{d}{d\rho_1}\left(\rho_1 \frac{dV_1}{d\rho_1}\right) - \phi^2 V_1 = -\phi^2 C_\infty(\mathbf{x}) \qquad \rho_1 \geq 1 \tag{33}$$

which must satisfy the boundary conditions:

$$V_1(\rho_1;\theta_1) = U_1(\xi_1;\theta_1) \qquad \rho_1 = 1 \tag{34}$$

$$V_1(\rho_1;\theta_1) = C_\infty(\mathbf{x}) \qquad \rho_1 \to \infty \tag{35}$$

where the first follows from continuity on the pore surface, Eq. (12); the second is obtained by a relation similar to (A.54). Eqs. (33)-(35) are readily solved to yield:

$$-\frac{d}{d\rho_1} V_1(\rho_1;\theta_1)\Big|_{\rho_1=1} = \phi Q(\phi)\left[U_1(\xi_1;\theta_1) - C_\infty(\mathbf{x})\right] \tag{36}$$

where:

$$Q(\phi) = \frac{K_1(\phi)}{K_0(\phi)} \tag{37}$$

and K_0 and K_1 are the zeroeth- and first-order modified Bessel functions of the second kind. The function $Q(\phi)$ has the asymptotic behavior:

$$\begin{aligned} Q(\phi) &\sim 1 && \phi >> 1 \\ Q(\phi) &\sim -\frac{1}{\phi \ln \phi} && \phi << 1 \end{aligned} \tag{38}$$

Inserting (36) into (28) yields:

$$B_1(\mathbf{x}) = \phi Q(\phi) \left[A_1(\mathbf{x}) - C_\infty(\mathbf{x}) \right] \tag{39}$$

which, when combined with (22), yields:

$$B_1(\mathbf{x}) = \phi Q(\phi) A_1(\mathbf{x}) \left[1 - \Pi \right] \tag{40}$$

$$C_\infty(\mathbf{x}) = \Pi A_1(\mathbf{x}) \tag{41}$$

with Π given by:

$$\Pi = \epsilon_2 \left[\frac{\phi + 2Q(\phi)}{\phi + 2\epsilon_2 Q(\phi)} \right] \tag{42}$$

According to the definition of $A_1(\mathbf{x})$ and boundary condition (21), $A_1(\mathbf{x}_0) = 1$ for all $\mathbf{x}_0$ on the boundary of the domain and

$$C_\infty(\mathbf{x}_0) = \Pi \qquad \mathbf{x}_0 \in \partial\Omega \tag{43}$$

Eq. (41) indicates that Π may be interpreted as a partitioning parameter describing the distribution of reactant between the reactive, microporous material and the inert macropores (away from the boundary). It is the ratio of the bulk concentration to the average intrapore value and lies in the range: $1 \geq \Pi \geq \epsilon_2$, where the limiting cases, $\Pi = \epsilon_2$ and $\Pi = 1$, correspond to negligible and complete (local) penetration

of the micropores respectively. According to assumption (ii) and Eq. (38), Π and $C_\infty(\mathbf{x})$ are order ϵ_2 for the conditions considered herein.

A local effectiveness factor is defined:

$$\begin{aligned} \eta_{\text{loc}} &= \frac{2\epsilon_2 B_1(\mathbf{x})}{\phi^2(1-\epsilon_2)A_1(\mathbf{x})} \\ &= \frac{2\epsilon_2 Q(\phi)}{\phi}\left(\frac{1-\Pi}{1-\epsilon_2}\right) \qquad (44) \\ &\sim \frac{2\epsilon_2}{\phi} \qquad \phi >> 1 \qquad (45) \end{aligned}$$

which is the ratio of the volumetric rate at which reactant is supplied by the macropores to the microporous matrix to the maximum rate that corresponds to a locally uniform reactant concentration profile ($\Pi = 1$).

Integration of (20) over the cross section of a macropore in conjunction with assumption (iii) and boundary condition (13) yields the differential equation describing the concentration profile within the macropore (Hill pp. 439-442, 1977):

$$\pi\alpha\frac{d^2U_1}{d\xi_1^2} + r(\xi_1;\theta_1) = 0 \qquad (46)$$

where $r(\xi_1;\theta_1)$ is the consumption of reactant per unit length within the macropore:

$$\begin{aligned} r = -2\pi\frac{d}{d\rho_1}V_1(\rho_1;\theta_1)\Big|_{\rho_1=1} &= \pi\alpha\beta^2\phi^2[U_1(\xi_1;\theta_1) - C_\infty(\mathbf{x})] \\ &= \pi\alpha\beta^2\phi^2 U_1(\xi_1;\theta_1) + O(\epsilon_2) \qquad (47) \end{aligned}$$

having defined:

$$\beta^2 = \frac{2Q(\phi)}{\phi\alpha} << 1 \qquad (48)$$

where the inequality follows from assumptions (ii) and (iii). Thus, (46) becomes:

$$\frac{d^2U_1}{d\xi_1^2} - (\beta\phi)^2 U_1 = O(\epsilon_2) \qquad (49)$$

which is solved in conjunction with boundary conditions:

$$U_1(0) = 1 \tag{50}$$

$$\frac{d}{d\xi_1}U_1(l_p) = 0 \tag{51}$$

where the former boundary condition is implied by (21). The quantity, l_p, in the latter boundary condition is the half-length of an individual macropore which depends on the geometry of Ω and the orientation of the pore axis; *e.g.*,

$$l_p = \frac{b}{\cos\theta_1} \qquad \text{slab with half-thickness, } b \tag{52}$$

$$= b\cos\theta_1 \qquad \text{sphere with radius, } b$$

where the reference plane has implicitly been taken tangent to the boundary as shown in Figures 3a and b. The solution of this boundary value problem is:

$$U_1(\xi_1;\theta_1) = \frac{\cosh\beta\phi\,(l_p-\xi_1)}{\cosh\beta\phi l_p} + O(\epsilon_2) \tag{53}$$

$$\sim e^{-\beta\phi\xi_1} \qquad \beta\Phi >> 1 \tag{54}$$

$$\sim 1 \qquad \beta\Phi << 1 \tag{55}$$

Inserting the result into (29) yields:

$$R_p = \epsilon_2\alpha\beta\phi\int_0^{\frac{\pi}{2}} \tanh\beta\phi l_p\ \cos\theta_1\sin\theta_1 d\theta_1 \tag{56}$$

$$= \epsilon_2\alpha\beta\phi\int_1^{\infty} \tanh(\beta\Phi t)\frac{dt}{t^3} \qquad \text{(slab)} \tag{57}$$

$$= \epsilon_2\alpha\beta\phi\int_0^{1} \tanh(3\beta\Phi t)\ t dt \qquad \text{(sphere)} \tag{58}$$

$$\sim \frac{1}{2}\epsilon_2\alpha\beta\phi \qquad \beta\Phi >> 1 \tag{59}$$

where (52) was used to obtain (57) and (58).

A macropore effectiveness factor is defined by:

$$\eta_p = \frac{R_p}{R_p^{max}} \tag{60}$$

where, $R_{\mathrm{p}}^{\max}$ is the maximum rate of reactant consumption by the macropores in the material for a fixed local effectiveness factor, η_{loc}, which corresponds to: $U_1(\xi_1;\theta_1) = A_1(\mathbf{x}) = 1$. $R_{\mathrm{p}}^{\max}$ can be expressed:

$$R_{\mathrm{p}}^{\max} = r_{\max}\frac{l_{\mathrm{p}}^{T}}{A} \tag{61}$$

where $r_{\max}$ is the maximum rate of reactant consumption per unit length of macropore, l_{p}^{T} is the total length of macropores in the domain, and A is the area of the boundary defined by Eq. (11). Inserting $U_1(\xi_1;\theta_1) = 1$ into (47) yields:

$$r_{\max} = \pi\alpha\beta^2\phi^2 \tag{62}$$

Neglecting macropore intersections, the total macropore length per unit external area is given by:

$$\frac{l_{\mathrm{p}}^{T}}{A} = \frac{v_2}{\pi A} = \frac{\epsilon_2 L}{\pi} \tag{63}$$

where $v_2 = \epsilon_2 V$ is the volume of macropores with dimensionless cross sectional area, π. Employing (44) and combining the above results yields:

$$R_{\mathrm{p}}^{\max} = \epsilon_2\alpha\beta^2\phi^2 L = \frac{\eta_{\mathrm{loc}}R^{\max}}{1-\Pi} \tag{64}$$

where $R^{\max}$ is the maximum overall rate:

$$R^{\max} = \phi^2\frac{V}{A}(1-\epsilon_2) = \phi\Phi(1-\epsilon_2) \tag{65}$$

which is used to define the overall effectiveness factor in Eq. (74). Combining (60) and (64) yields:

$$\frac{R_{\mathrm{p}}}{R^{\max}} = \frac{\eta_{\mathrm{loc}}\eta_{\mathrm{p}}}{1-\Pi} \tag{66}$$

6 Bulk Concentration Field

In this section, the bulk concentration is obtained for the case: $\Phi >> 1$ in accordance with assumption (iv). The homogeneous solution of (18) is given by (30). In the regime $\beta\Phi >> 1$, the intrapore concentration is given by (54) and:

$$A_1(z) = \int_0^{\frac{\pi}{2}} \exp\left(-\frac{\beta\phi z}{\cos\theta_1}\right) \sin\theta_1 d\theta_1 = \mathrm{e}^{-\beta\phi z} - \beta\phi z E_1(\beta\phi z) \tag{67}$$

$$C_\infty(z) = \Pi\left[\mathrm{e}^{-\beta\phi z} - \beta\phi z E_1(\beta\phi z)\right] \qquad \beta\Phi >> 1 \tag{68}$$

where $\xi_1 \cos\theta_1 = z$, by taking the reference plane tangent to the boundary as shown in Figure 3c, $E_1(x) = \int_x^\infty \mathrm{e}^{-t}/t \; dt$ is the exponential integral, and $C_\infty(0) = \Pi$ by (43). Inserting (68) into (18) yields, after some algebra:

$$C_0(z) = \mathrm{e}^{-\phi z}(1-\Pi) + C_\infty(z) \tag{69}$$
$$+\Pi\beta\left[e^{-\phi z}\int_0^{\phi z} \sinh t \, \frac{e^{-\beta t}}{t} \, dt + \sinh\phi z E_1(1+\beta)\phi z\right] \qquad \beta\Phi >> 1$$

which has the asymptotic behavior:

$$C_0(z) \sim e^{-\phi z}(1-\Pi) + \Pi + O\left(\epsilon_2 \beta \ln\beta\right) \qquad \beta\phi z << 1 \tag{70}$$

$$C_0(z) \sim C_\infty(z) + O\left(\epsilon_2\beta^2\right) \qquad \phi z >> 1 \tag{71}$$

In the regime $\beta\Phi << 1$, the intrapore concentration equals unity, according to (55). Then, according to (27) and (41), $A_1(\mathbf{x}) = 1$ and $C_\infty(\mathbf{x}) = \Pi$. Inserting this result into (18) and solving indicates that $C_0(\mathbf{x})$ is given by (70). Eqs. (68), (70) and (71) may be combined to yield:

$$C_0(z) = \mathrm{e}^{-\phi z}(1-\Pi) + \Pi\left[\mathrm{e}^{-\beta\phi z} - \beta\phi z E_1(\beta\phi z)\right] \qquad \beta << 1 \tag{72}$$

which is uniformly valid in $\beta\Phi$, for $\beta << 1$ and $\Phi >> 1$. The result indicates that the bulk concentration is described by the slowly varying function, $C_\infty(z)$, except

near the boundary, where the reactant concentration decreases (exponentially) from the boundary value $C_0(0) = 1$ to $O(\epsilon_2)$ on the (normalized) length scale, ϕ^{-1}. Similarly, bulk concentration gradients are $O(\beta\phi)$ except in the region near the boundary ($z = O(\phi^{-1})$), where gradients are $O(\phi)$.

According to boundary condition (13), the bulk concentration gradients induce an order $\beta\phi\alpha^{-1}$ intrapore gradient which, by assumption (iii), is small compared to the axial intrapore gradients which are $O(\beta\phi)$ according to (49). By assumptions (ii) and (iii), $\beta << 1$; thus, bulk concentration gradients are small compared with the radial gradient external to a macropore which, according to (33), is order ϕ. These results do not apply in the region $z = O(\phi^{-1})$ which, according to assumption (iv), is a comparably small portion of the domain. These observations demonstrate that the simplifications displayed in Eqs. (25) and (26) follow from assumptions (i)-(iv) as claimed.

7 Effectiveness Factor

In this section, the overall reaction rate, given by the concentration flux on the boundary, is determined. Inserting (70) into (16) and the result into (15) yields:

$$R^T = \phi(1 - \Pi) + R_{\rm p} = R_0(1 - \Pi) + R_{\rm p} \tag{73}$$

where R_0 is the overall rate for $\epsilon_2 = 0$, given by (31). The form of the overall rate indicates that reactant consumption at the boundary occurs in parallel with consumption by the macropores. The factor, $1 - \Pi$, is a reduction in the rate of reactant consumption at the boundary which results from the introduction of inert void volume ($\epsilon_2 \neq 0$); the macropores allow greater reactant penetration and thus

reduce the gradient at the boundary. An effectiveness factor is defined:

$$\eta_T = \frac{R^T}{R^{\max}} \tag{74}$$

where $R^{\max}$ is given by (65). Combining (66) and (73), yields:

$$\eta_T = \frac{1}{\Phi}\left(\frac{1-\Pi}{1-\epsilon_2}\right) + \frac{R_{\rm p}}{R^{\max}} = \eta_0\left(\frac{1-\Pi}{1-\epsilon_2}\right) + \frac{\eta_{\rm loc}\eta_{\rm p}}{1-\Pi} \tag{75}$$

where the product, $\eta_{\rm loc}\eta_{\rm p}$, is similar in form to the results of Mingle and Smith (1961) from an analysis incorporating micro- and macroeffectiveness factors. The above result has the asymptotic behavior:

$$\eta_T \sim \frac{1}{\Phi}\left(\frac{1-\Phi}{1-\epsilon_2} + \frac{\epsilon_2}{1-\epsilon_2}\frac{2Q(\phi)}{\phi}\right) \qquad \beta\Phi << 1 \tag{76}$$

$$\sim \frac{1}{\Phi}\left(\frac{1-\Phi}{1-\epsilon_2} + \frac{\epsilon_2}{1-\epsilon_2}\frac{\alpha\beta}{2}\right) \qquad \beta\Phi >> 1 \tag{77}$$

$$\sim \frac{1}{\Phi}\left(1 + \frac{\epsilon_2}{1-\epsilon_2}\sqrt{\frac{\alpha}{2\phi}}\right) \qquad \beta\Phi >> 1\,, \quad \phi >> 1 \tag{78}$$

having taken $\eta_{\rm p} = 1$ for $\beta\Phi << 1$ and $R_{\rm p}$, given by (59), for $\beta\Phi >> 1$. The latter result indicates that the enhancement to the overall rate, resulting from the macropores in the material, vanishes as $\phi^{-1/2}$ for $\phi \to \infty$.

8 Comparison with other Models

In this section, we compare the present results with those obtained by a continuum description of the material and a single pore model.

8.1 continuum description

A continuum approach is suitable if changes in reactant concentration occur on a length scale much larger than the diameter of a macropore. This situation is encountered for $\phi << 1$, contrary to assumption (ii), used to obtain the results in

the preceding section. Under these conditions, the partitioning parameter, Π, and local effectiveness, $\eta_{\rm loc}$, are approximately unity. According to the continuum treatment, Eqs.(6) and (7) are replaced by a single (dimensionless) differential equation describing the bulk concentration field (Satterfield p.131, 1970):

$$\nabla^2 C(\mathbf{x}) - \phi_c^2 C(\mathbf{x}) = 0 \tag{79}$$

where ϕ_c is the Thiele modulus for the continuum based on the macropore radius:

$$\phi_c = a\sqrt{\frac{k_c}{D_c}} \tag{80}$$

where k_c and D_c are pseudo-homogeneous transport coefficients that characterize the continuum. An effective diffusivity is given by the parallel pore model developed by Johnson and Stewart (1965):

$$D_c = \frac{1}{\tau}\left[\epsilon_1 D_K + \epsilon_2 D_2\right] = D_1\left[1 - \epsilon_2 + \frac{\epsilon_2}{\tau}\alpha\right] \tag{81}$$

The homogeneous rate constant is given by:

$$k_c = S k_S = k_1(1-\epsilon_2) \tag{82}$$

where k_1 is defined by (2). Inserting these transport coefficients into (80) yields:

$$\phi_c = \phi\sqrt{\frac{\tau(1-\epsilon_2)}{\tau(1-\epsilon_2)+\epsilon_2\alpha}} >> \beta\phi \tag{83}$$

where the inequality holds under the conditions described by assumptions (i)-(iii). Solving (79) subject to boundary condition (8) yields:

$$C(z) = \mathrm{e}^{-\phi_c z} \tag{84}$$

$$R^T = \frac{D_c}{D_1}\phi_c = \phi\sqrt{(1-\epsilon_2)^2 + \epsilon_2(1-\epsilon_2)\tau^{-1}\alpha} \tag{85}$$

$$\eta_T \sim \frac{1}{\Phi}\sqrt{1 + \frac{\epsilon_2}{1-\epsilon_2}\,\frac{\alpha}{\tau}} \tag{86}$$

where $\Phi >> 1$ has been assumed. The predicted concentration field exhibits simple, exponential decay, in contrast to the more complex behavior depicted by Eq. (72). Comparing (83) with (72) indicates that the continuum treatment predicts shallower reactant penetration. The discrepancy arises from the fact that reactant can penetrate the material rapidly through the macropores, a feature neglected by treating the material as a homogeneous continuum. Inspection of the effectiveness factor displayed in (86) reveals that it exceeds the the values predicted by (76) and (77) for $\tau = O(1)$. In particular, the above result indicates that the macropores in the material enhance the effectiveness factor by a multiplicative constant in the limit $\phi \rightarrow \infty$, contrary to the result displayed in (78).

8.2 single pore model

A single pore model is relevant in the complimentary regime, where the reactant concentration field is attenuated on a length scale much smaller than the spacing between the macropores. This situation is realized for $\phi >> 2$ as shown below, which is consistent with assumptions used in the present work, although more restrictive. Eqs. (25) and (26) are assumed to hold. In this case, the macropores behave independently of each other. The boundary conditions (34) and (35) for the concentration field external to a macropore become:

$$V_1(\rho_1;\theta_1) = U_1(\xi_1;\theta_1) \qquad \rho_1 = 1 \tag{87}$$

$$V_1(\rho_1;\theta_1) = 0 \qquad \rho_1 \rightarrow \infty \tag{88}$$

Solving Eq. (33) subject to these boundary conditions indicates that the previously-obtained equations, (49)-(51), govern the intrapore concentration ($\rho_1 < 1$). The concentration field in the microporous material is approximately given by $C^0(\mathrm{x})$.

Taking a volume average yields the approximate bulk concentration field:

$$C(z) = \mathrm{e}^{-\phi z}(1-\epsilon_2) + \epsilon_2 A_1(z) \tag{89}$$

where $A_1(z)$ is the average intrapore concentration defined by (27) and is given by (67) for $\beta\Phi >> 1$, and $A_1(z) = 1$ for $\beta\Phi << 1$. For $\beta << 1$, these solutions may be combined to yield:

$$C_0(z) = \mathrm{e}^{-\phi z}(1-\epsilon_2) + \epsilon_2\left[\mathrm{e}^{-\beta\phi z} - \beta\phi z E_1(\beta\phi z)\right] \qquad \beta << 1 \tag{90}$$

which coincides with (72) for $\Pi \approx \epsilon_2$. Eqs. (38) and (42) indicate: implies:

$$\Pi = \epsilon_2\left[1 + O\left(\frac{2}{\phi}\right)\right] \qquad \phi >> 1 \tag{91}$$

Inserting (88) into (28) and the result into (44) yields:

$$\eta_{\mathrm{loc}} = \frac{2\epsilon_2 Q(\phi)}{\phi(1-\epsilon_2)} \tag{92}$$

thus (64) and (66) become:

$$R_{\mathrm{p}}^{\max} = \epsilon_2\alpha\beta^2\phi^2 L = \eta_{\mathrm{loc}} R^{\max} \tag{93}$$

$$\frac{R_{\mathrm{p}}}{R^{\max}} = \eta_{\mathrm{loc}}\eta_{\mathrm{p}} \tag{94}$$

The overall rate is given by (15) with R_{p} given by (56)-(59) and R_{b} given by:

$$R_{\mathrm{b}} = R_0(1-\epsilon_2) \tag{95}$$

where $(1-\epsilon_2)$ is the volume fraction of microporous material in the domain and the area fraction on the boundary. Thus, the overall rate is given by:

$$R^T = \phi(1-\epsilon_2) + R_{\mathrm{p}} \tag{96}$$

and the effectiveness factor is:

$$\eta_T = \frac{1}{\Phi} + \frac{R_{\mathrm{p}}}{R^{\max}} = \eta_0 + \eta_{\mathrm{loc}}\eta_{\mathrm{p}} \tag{97}$$

which has the asymptotic behavior:

$$\eta_T \sim \frac{1}{\Phi}\left(1+\frac{\epsilon_2}{1-\epsilon_2}\frac{2Q(\phi)}{\phi}\right) \qquad \beta\Phi << 1 \tag{98}$$

$$\sim \frac{1}{\Phi}\left(1+\frac{\epsilon_2}{1-\epsilon_2}\frac{\alpha\beta}{2}\right) \qquad \beta\Phi >> 1 \tag{99}$$

$$\sim \frac{1}{\Phi}\left(1+\frac{\epsilon_2}{1-\epsilon_2}\sqrt{\frac{\alpha}{2\phi}}\right) \qquad \beta\Phi >> 1\,, \quad \phi >> 1 \tag{100}$$

where the results coincide with (76)-(78) for $(1-\Pi)/(1-\epsilon_2) \rightarrow 1$ which, according to (91), occurs for $\phi >> 2$. Comparing Eqs. (72) and (76)-(78) with Eqs. (90) and (98)-(100) indicates that, for ϕ in the interval defined by:

$$\phi^2 \ln\phi >> 2\epsilon_2\,, \qquad \phi \leq O(1) \tag{101}$$

the earlier, more detailed analysis offers an order ϵ_2 correction to the single pore model described above. For $\phi >> 2$, the results of the two analyses are in agreement. The difference between the two models is illustrated by the behavior of the quantity $(1-\Pi)/(1-\epsilon_2)$ which is shown in Figure 4. The results indicate that the more detailed analysis offers a modest correction to the the single pore model in the regime defined by (101).

9 Conclusions

A detailed analysis has been presented for reaction in a random, porous material under diffusion-controlled conditions. The pore structure is assumed bimodal with a random, isotropic network of monodisperse cylindrical voids. The macropores are considered to be immersed in a mean-field which is collectively determined from the reactant flux from the macropores in the material. In the diffusion-controlled limit, described by $\phi >> 2$, this interaction between the macropores vanishes and

the results coincide with those of a simple, single pore model described within. Under the (diffusion-controlled) conditions considered, the results are qualitatively different from those obtained by a continuum description of the material which is valid in the complimentary, kinetically-limited regime.

10 Acknowledgement

This work was made possible through a fellowship from the LINK foundation.

11 Nomenclature

SYMBOL	DESCRIPTION
Roman Symbols	
a	radius of macropores
A	area of domain boundary
A_1	average intrapore concentration defined by (23)
B_1	source of reactant from macropore defined by (24)
C_0	configurationally averaged reactant concentration
C^0	average concentration field with $\epsilon_2 = 0$
C_1	conditionally averaged concentration field
C_∞	ambient concentration away from boundary defined by (22)
D_1	diffusivity of microporous material
D_2	diffusion coefficient in macropores
D_K	Knudsen diffusion coefficient
$\mathbf{e}$	reference vector
k_S	intrinsic surface reaction rate constant
k_1	homogeneous rate constant describing microporous material
l	length of a macropore
L	characteristic length of domain, (V/A)
$\mathbf{q}_\mathrm{i}$	orientation of i^{th} pore axis
$Q(\phi)$	defined by (37)
R^T	overall rate, $R^T = R_\mathrm{b} + R_\mathrm{p}$
R_p	reactant consumption within macropores
R_b	reactant consumption at boundary
R_0	overall rate for $\epsilon_2 = 0$

$R^{\max}$	maximum overall rate
$R_{\mathrm{p}}^{\max}$	maximum consumption within macropores
S	local pore surface area (per unit volume)
$U_1(\xi_1;\theta_1)$	reactant concentration within a macropore
$V_1(\rho_1;\theta_1)$	reactant concentration external to a macropore
V	volume of domain

Greek Symbols

α	ratio: D_2/D_1
β	defined by (48)
ϵ_1	void volume of micropores
ϵ_2	void volume of macropores
ϕ	local Thiele modulus based on macropore radius, a
Φ	macroscale Thiele modulus based on characteristic length, L
Ω	domain
$\partial\Omega$	domain boundary
Π	partitioning parameter defined by (42)
θ_{i}	orientation angle for $\mathbf{q}_{\mathrm{i}}$, Fig. (2)
φ_{i}	orientation angle for $\mathbf{q}_{\mathrm{i}}$, Fig. (2)
η_T	overall effectiveness factor
η_{loc}	local effectiveness factor
η_{p}	macropore effectiveness factor
η_0	overall effectiveness factor for $\epsilon_2 = 0$
ρ_{i}	radial distance from i^{th} pore axis
ξ_{i}	distance from boundary along i^{th} pore axis

12 References

Aris, R., "On shape factors for irregular particles–I. The steady problem. Diffusion and reaction." *Chem. Eng. Sci.*, **6**, 262 (1957).

Bhatia, S.K. and D.D. Perlmutter, "A random pore model for fluid-solid reactions: I. Isothermal, kinetic control." *A.I.Ch.E. J.*, **26**, 379 (1980).

Bohlbro, H., *An Investigation on the Kinetics of the Conversion of Carbon Monoxide with Water Vapour over Iron Oxide Based Catalysts*, Gjellerup, Copenhagen (1966).

Carberry, J.C., "The micro-macro effectiveness factor for the reversible catalytic reaction." *A.I.Ch.E. J.*, **8**, 557 (1962).

Evans, R.B., G.M. Watson and E.A. Mason, "Gaseous diffusion in porous media at uniform pressure." *J. Chem. Phys.*, **35**, 2076 (1961).

Gavalas, G.R., "A random capillary model with application to char gasification at chemically controlled rates." *A.I.Ch.E. J.*, **26**, 577 (1980).

Hill, C.G., *An Introduction to Chemical Engineering Kinetics & Reactor Design*, John Wiley & Sons, New York (1977).

Hinch, E.J., "An averaged-equation approach to particle interactions in a fluid suspension." *J. Fluid Mech.*, **83**, 695 (1977).

Johnson, M.F.L. and W.E. Stewart, "Pore structure and gaseous diffusion in solid catalysts." *J. Catalysis*, **4**, 248 (1965).

Kendall, M.G. and P.A.P. Moran, *Geometrical Probability*, Charles Griffin, London (1963).

Knudsen, M., "Die Gesetze der Molekularströmung und der inneren Reibungsströmung der Gase durch Röhren." *Ann. Phys.*, **28**, 75 (1909).

Loewenberg, M., "Reaction and diffusion in random microstructured materials." Ph.D. thesis, Caltech (1988).

Loewenberg, M. and G.R. Gavalas, "Steady-state reactant flux into a medium containing spherical sinks." *Chem. Eng. Sci.* In press (1988).

Mingle, J.O. and J.M. Smith, "Effectiveness factors for porous catalysts." *A.I.Ch.E. J.*, **7**, 243 (1961).

Northrop, P.S. "A fundamental study of char combustion: changes in particle morphology during combustion." Ph.D. thesis, Caltech (1988).

Örs, N. and T. Doğu, "Effectiveness of bidisperse catalysts." *A.I.Ch.E. J.*, **25**, 723 (1979).

Reed, T.M. and K.E. Gubbins, *Applied Statistical Mechanics.* Mcgraw-Hill, New York (1973).

Rothfield, L.B. "Gaseous counter-diffusion in catalyst pellets." *A.I.Ch.E. J.*, **9**, 19 (1963).

Satterfield, C.N., *Heterogeneous Catalysis In Practice*, Mcgraw-Hill, New York (1980).

Satterfield, C.N., *Mass Transfer In Heterogeneous Catalysis*, M.I.T. Press, Cambridge (1970).

Scott, D.S. and Dullien, F.A.L., "Diffusion of ideal gases in capillaries and porous solids." *A.I.Ch.E. J.*, 8, 113 (1962).

Tartarelli, R. and M. Capovani, "Zeroth-order reactions in heterogeneous catalysis." *A.I.Ch.E. J.*, **17**, 246 (1971).

Thiele, E.W., "Relation between catalytic activity and size of particle." *Ind. Eng. Chem.*, **31**, 916 (1939).

Wakao, N. and J.M. Smith, "Diffusion and reaction in porous catalysts." *Ind. Eng. Chem.*, **3**, 123 (1964).

13 List of Figures

1. Bimodal pore size distributions for: (a) PSOC-1451 coal derived char (Northrop 1988) and (b) $Fe_3O_4-CrO_3$ catalyst (Bohlbro 1966).

2. Coordinate system. (a) two-dimensions, (b) three-dimensions, and (c) cylindrical coordinates oriented with pore axis. $\mathbf{x}$ is an arbitrary field point, θ_i is the angle between reference plane (defined by $\mathbf{e}$) and orientation plane (defined by $\mathbf{q}_i$). Pore axis intersects reference plane at $\mathbf{x}_i$ and orientation plane (ξ_i =constant) at $\hat{\mathbf{x}}_i$. ξ_i is an axial coordinate (distance from the boundary) in the $\mathbf{q}_i$−direction. ρ_i is a radial coordinate; $\rho_i = 1$ defines macropore surface. Azimuthal angle, φ_i is defined in the plane ξ_i =constant.

3. Orientation of reference vector, $\mathbf{e}$ for (a) slab, (b) spherical and (c) semi-infinite geometries.

4. Behavior of $(1 - \Pi)/(1 - \epsilon_2)$ where Π is defined by (42).

Appendix: Configurational Averaging

In this appendix, a derivation of the material properties and configurationally averaged equations is presented. Although the approach has been used elsewhere (*e.g.*, Hinch 1977, Loewenberg and Gavalas 1988), a self-contained development is useful. In the first subsection, fundamental relationships relevant for averaging are developed and the void volume of the macropore network is related to the statistics that describe its distribution. In the second subsection, useful expressions are derived for the reactant flux, bulk rate and overall rate. In the last subsection, the configurationally averaged equations are derived.

1 Void Volume

In this subsection, the void volume for a random, isotropic distribution of cylindrical micropores is determined and the methods which are developed will prove useful in the following derivations. A pore axis is specified by its intersection with a fixed plane, the angle with respect to the normal direction and an azimuthal angle in the plane (Kendall and Moran 1963). For a random, isotropic material, intersections with the plane are independent of angular distribution. Furthermore, intersections with the reference plane are distributed according to a Poisson process with mean λ independent of the reference orientation.

1.1 General: $\epsilon_2 = O(1)$

The void volume may be interpreted as the configurational average of a function $E(\mathbf{x})$ defined by:

$$\begin{aligned} E(\mathbf{x}|\mathrm{C}_N) &= 1 \qquad \mathbf{x} \text{ in macropore} \\ &= 0 \qquad \mathbf{x} \text{ in microporous matrix} \end{aligned} \tag{A.1}$$

where C_N is a configuration of the pore axes in the material given by the set of position vectors: $\{\mathbf{r}_1, \cdots, \mathbf{r}_N\}$. The position vectors are explicitly given by $\mathbf{r}_\mathrm{i} = (\mathbf{x}_\mathrm{i}, \mathbf{q}_\mathrm{i})$, where $\mathbf{x}_\mathrm{i}$ is the intersection of the i^{th} pore axis with an arbitrary reference plane with normal vector $\mathbf{e}$, and $\mathbf{q}_\mathrm{i}$ is a unit vector parallel to the i^{th} axis. The orientation vector, $\mathbf{q}$, is described by two independent angles, (θ, φ), where θ is defined by: $\mathbf{q}_\mathrm{i} \cdot \mathbf{e} = \cos\theta_\mathrm{i}$, and φ is an azimuthal angle. We shall also define a coordinate, ξ_i, which is the distance along the i^{th} pore axis measured from its intersection with the boundary. The plane: $(\hat{\mathbf{x}} - \mathbf{x}) \cdot \mathbf{q}_\mathrm{i} = 0$ (constant ξ_i) is normal to the i^{th} pore axis and contains the point $\mathbf{x}$ which lies in the reference plane defined by $\mathbf{e}$. The point $\hat{\mathbf{x}}_\mathrm{i}$ denotes the intersection with the i^{th} axis and is the point on the i^{th} axis closest to $\mathbf{x}$. These coordinates are depicted in Figures 2a-c. In terms of the foregoing notation, $E(\mathbf{x})$ can be compactly expressed in terms of Heaviside functions:

$$E(\mathbf{x}|\mathrm{C}_N) = 1 - \prod_{\mathrm{i}=1}^{N} H(\rho_\mathrm{i} - 1) \tag{A.2}$$

where $\rho_i = \|\hat{\mathbf{x}}_\mathrm{i} - \mathbf{x}\|$ is the (minimum) distance between the i^{th} pore axis and $\mathbf{x}$. The void volume of the macropores is given by:

$$\epsilon_2 = \langle E(\mathbf{x}) \rangle_0 = 1 - \left\langle \prod_{\mathrm{i}=1}^{N} H(\rho_\mathrm{i} - 1) \right\rangle_0 \tag{A.3}$$

where the subscript 0 denotes an unconditionally averaged quantity. The pore axes are identical and uncorrelated; thus, we can write:

$$\epsilon_2 = 1 - \langle H(\rho_1 - 1)\rangle_0^N$$

or equivalently,

$$\epsilon_2 = 1 - [1 - \langle H(1 - \rho_1)\rangle_0]^N \tag{A.4}$$

The configurational average is given explicitly by an $N-$fold integration of each pore axis specification weighted by a configurational probability, $P(\mathbf{C}_N)$, thus:

$$\langle H(1 - \rho_1)\rangle_0 = \frac{1}{N!}\int_{T^N} H(1 - \rho_1)P(\mathbf{C}_N)d\mathbf{C}_N \tag{A.5}$$

where T is the individual pore specification space given by $T = \Re^2 \times [0, \frac{\pi}{2}] \times [0, 2\pi]$, where $\mathbf{x}_i \in \Re^2$, $\theta_i \in [0, \frac{\pi}{2}]$ and $\varphi_i \in [0, 2\pi]$. Angular integration is restricted to the upper hemisphere to prevent double-counting; each (θ, φ) in the upper hemisphere corresponds to an equivalent, diametrically opposed pair in the lower hemisphere. The configurational probability distribution function is normalized by (Reed and Gubbins 1973):

$$\int_{T^N} P(\mathbf{C}_N)d\mathbf{C}_N = N! \tag{A.6}$$

A conditional probability distribution function can be defined:

$$P(\mathbf{C}_N|\mathbf{r}_1)P(\mathbf{r}_1) = P(\mathbf{C}_N)$$

$$\int_{T^{N-1}} P(\mathbf{C}_N|\mathbf{r}_1)d\mathbf{C}_{N-1} = (N-1)! \tag{A.7}$$

and a doubly conditional probability distribution function can be defined

$$P(\mathbf{C}_N|\mathbf{r}_1, \mathbf{r}_2)P(\mathbf{r}_2|\mathbf{r}_1) = P(\mathbf{C}_N|\mathbf{r}_1)$$

$$\int_{T^{N-2}} P(\mathbf{C}_N|\mathbf{r}_1, \mathbf{r}_2)d\mathbf{C}_{N-2} = (N-2)! \tag{A.8}$$

Inserting the conditional probability into (A.5) and integrating over $\mathbf{r}_2, \cdots, \mathbf{r}_N$ yields:

$$\langle H(1-\rho_1)\rangle_0 = \frac{1}{N}\int_T H(1-\rho_1)P(\mathbf{r}_1)d\mathbf{r}_1 \qquad (A.9)$$

Since the distribution of pore axis intersections with the reference plane is independent of the angular distribution, the pore axis probability distribution is separable: $P(\mathbf{r}_1) = P(\mathbf{x}_1)P(\mathbf{q}_1)$, where $P(\mathbf{x}_1)$ is given by the normalized Poisson mean number density: $P(\mathbf{x}_1) = a^2\lambda$. The isotropic angular distribution is obtained by requiring that $\mathbf{q}_1$ be uniformly distributed on a unit sphere and normalized to unity on the upper hemisphere (Gavalas 1980), which implies: $P(\mathbf{q}_1) = (\mathbf{q}_1 \cdot \mathbf{e})/\pi = \cos\theta_1/\pi$, indicating that the distribution is axisymmetric. Thus, the pore axis distribution is given by:

$$P(\mathbf{r}_1) = \frac{a^2}{\pi}\lambda\cos\theta_1 \qquad (A.10)$$

Inserting the distribution into (A.9), yields:

$$\langle H(1-\rho_1)\rangle_0 = \frac{a^2\lambda}{N\pi}\int_0^{2\pi}\int_0^{\frac{\pi}{2}}\int_{\Re^2} H(1-\rho_1)\cos\theta_1\sin\theta_1 d\mathbf{x}_1 d\theta_1 d\varphi_1 \qquad (A.11)$$

The Jacobian for the change of variables: $\mathbf{x}_1 \rightarrow \hat{\mathbf{x}}_1$ is:

$$\left|\frac{\partial \mathbf{x}_1}{\partial \hat{\mathbf{x}}_1}\right| = [\mathbf{q}_1 \cdot \mathbf{e}]^{-1} = \frac{1}{\cos\theta_1} \qquad (A.12)$$

which can be deduced from Fig. 1. Changing variables and integrating to eliminate the Heaviside function yields:

$$\langle H(1-\rho_1)\rangle_0 = \frac{a^2\lambda}{N\pi}\int_0^{2\pi}\int_0^{\frac{\pi}{2}}\int_{\rho_1\leq 1}\sin\theta_1 d\hat{\mathbf{x}}_1 d\theta_1 d\varphi_1 = \frac{2\pi a^2\lambda}{N} \qquad (A.13)$$

Inserting this result into (A.4) and taking the limit $N \rightarrow \infty$, produces the desired result:

$$\epsilon_2 = 1 - \lim_{N\rightarrow\infty}\left[1 - \frac{2\pi a^2\lambda}{N}\right]^N = 1 - \mathrm{e}^{-2\pi a^2\lambda} \qquad (A.14)$$

1.2 Approximation for $\epsilon_2 << 1$

Neglecting pore intersections allows the approximation:

$$\prod_{i=1}^{N} H(\rho_i - 1) \approx 1 - \sum_{i=1}^{N} H(1 - \rho_i) \tag{A.15}$$

Inserting this approximation into (A.3) yields:

$$\epsilon_2 = \sum_{i=1}^{N} \langle H(1 - \rho_i) \rangle_0 \tag{A.16}$$

By the indistinguishability and independence of the pores, we can write:

$$\epsilon_2 = N \langle H(1 - \rho_1) \rangle_0 \tag{A.17}$$

Then, employing (A.13) yields

$$\epsilon_2 \approx 2\pi a^2 \lambda \tag{A.18}$$

which by inspection of (A.14), is valid for $\epsilon_2 << 1$.

2 Reactant Flux and Reaction Rate

In this section we obtain expressions for the configurationally averaged concentration flux, overall rate, effective diffusivity and volumetric reaction rate.

2.1 Reactant Flux

Fick's law is written in a generalized form describing the reactant flux for every arbitrary x in the domain:

$$\mathbf{F} = -D(\mathbf{x}|\mathbf{C}_N) \nabla C(\mathbf{x}|\mathbf{C}_N) \tag{A.19}$$

where $\mathbf{C}_N$ is a particular configuration of the pore axes as defined above. The generalized diffusivity, $D(\mathbf{x}|\mathbf{C}_N)$, is a scalar quantity based on the assumption that

the macropore distribution is isotropic and is defined by:

$$D(\mathbf{x}|\mathbf{C}_N) = 1 \qquad \mathbf{x} \text{ in microporous matrix} \tag{A.20}$$

$$= \alpha \qquad \mathbf{x} \text{ in macropore}$$

which can be expressed in terms of Heaviside functions:

$$D(\mathbf{x}|\mathbf{C}_N) = \alpha + (1-\alpha)\prod_{\mathrm{i}=1}^{N} H(\rho_\mathrm{i} - 1)$$

$$\approx 1 + (\alpha - 1)\sum_{\mathrm{i}=1}^{N} H(1-\rho_\mathrm{i}) \tag{A.21}$$

where the latter equality follows from approximation (A.15). Inserting this expression into (A.19) and configurationally averaging yields:

$$\langle \mathbf{F} \rangle_0 = \nabla \langle C(\mathbf{x}) \rangle_0 + (\alpha - 1)\sum_{\mathrm{i}=1}^{N} \langle H(1-\rho_\mathrm{i}) \nabla C(\mathbf{x}|\mathbf{C}_N) \rangle_0 \tag{A.22}$$

where $\langle C(\mathbf{x}) \rangle_0$ denotes the configurationally averaged concentration. The result relies on the commutability of configurational averages with linear operators. The term within the sum is explicitly given by an $N-$fold integration over the individual pore specification space, T, weighted by a configurational probability: $P(\mathbf{C}_N) = P(\mathbf{C}_N|\mathbf{r}_\mathrm{i})P(\mathbf{r}_\mathrm{i})$ which are defined by (A.5)-(A.7). Accordingly, we write:

$$\sum_{\mathrm{i}=1}^{N} \langle H(1-\rho_\mathrm{i}) \nabla C(\mathbf{x}|\mathbf{C}_N) \rangle_0 = \frac{1}{N!}\sum_{\mathrm{i}=1}^{N} \int_{T^N} H(1-\rho_\mathrm{i}) \nabla C(\mathbf{x}|\mathbf{C}_N) P(\mathbf{C}_N|\mathbf{r}_\mathrm{i}) P(\mathbf{r}_\mathrm{i}) d\mathbf{r}_\mathrm{i} d\mathbf{C}_{N-1} \tag{A.23}$$

Then, performing all but the i^{th} integration for each term in the sum yields:

$$\sum_{\mathrm{i}=1}^{N} \langle H(1-\rho_\mathrm{i}) \nabla C(\mathbf{x}|\mathbf{C}_N) \rangle_0 = \frac{1}{N}\sum_{\mathrm{i}=1}^{N} \int_T H(1-\rho_\mathrm{i}) \nabla \langle C(\mathbf{x}|\mathbf{r}_\mathrm{i}) \rangle P(\mathbf{r}_\mathrm{i}) d\mathbf{r}_\mathrm{i} \tag{A.24}$$

where $\langle C(\mathbf{x}|\mathbf{r}_\mathrm{i}) \rangle$ is the conditionally averaged concentration field with a pore specified by $\mathbf{r}_\mathrm{i}$. The pore axes are identical and hence each term in the resulting sum is the same, allowing its summation:

$$\sum_{\mathrm{i}=1}^{N} \langle H(1-\rho_\mathrm{i}) \nabla C(\mathbf{x}|\mathbf{C}_N) \rangle_0 = \int_T H(1-\rho_1) \nabla \langle C(\mathbf{x}|\mathbf{r}_1) \rangle_0 P(\mathbf{r}_1) d\mathbf{r}_1 \tag{A.25}$$

Then, making the change of variables: $\mathbf{x}_1 \rightarrow \hat{\mathbf{x}}_1$ defined by (A.12) and integrating to eliminate the heaviside function:

$$\sum_{i=1}^{N} \langle H(1-\rho_i)\nabla C(\mathbf{x}|\mathbf{C}_N)\rangle_0 = \int_0^{2\pi}\int_0^{\frac{\pi}{2}}\int_{\rho_1\leq 1} \nabla\langle C(\mathbf{x}|\mathbf{r}_1)\rangle \frac{P(\mathbf{r}_1)}{\cos\theta_1}\sin\theta_1 d\hat{\mathbf{x}}_1 d\theta_1 d\varphi_1 \tag{A.26}$$

Inserting the random, isotropic pore distribution, Eq. (A.10), and integrating yields:

$$\sum_{i=1}^{N} \langle H(1-\rho_i)\nabla C(\mathbf{x}|\mathbf{C}_N)\rangle_0 = \frac{\epsilon_2}{\pi}\int_0^{\frac{\pi}{2}}\int_{\rho_1\leq 1} \nabla\langle C(\mathbf{x}|\mathbf{r}_1)\rangle \sin\theta_1 d\hat{\mathbf{x}}_1 d\theta_1 \tag{A.27}$$

Inserting this result into (A.22) yields the configurationally averaged reactant flux:

$$\langle \mathbf{F}\rangle_0 = \nabla\langle C(\mathbf{x})\rangle_0 + \epsilon_2\alpha\frac{1}{\pi}\int_0^{\frac{\pi}{2}}\int_{\rho_1\leq 1} \nabla\langle C(\mathbf{x}|\mathbf{r}_1)\rangle \sin\theta_1 d\hat{\mathbf{x}}_1 d\theta_1 \tag{A.28}$$

having made the approximation: $\alpha - 1 \approx \alpha$.

2.2 Overall Rate

The overall reaction rate is given by the normal component of the reactant flux evaluated on the boundary, $\partial\Omega$. The component of flux in the direction of the normal vector, $\mathbf{n}$, is obtained from a scalar product with Eq. (A.28):

$$F_n \equiv \langle \mathbf{F}\rangle_0 \cdot \mathbf{n} = \nabla\langle C(\mathbf{x})\rangle_0 \cdot \mathbf{n} + \frac{\alpha}{\pi}\int_0^{\frac{\pi}{2}}\int_{\rho_1\leq 1} [\nabla\langle C(\mathbf{x}|\mathbf{r}_1)\rangle \cdot \mathbf{n}]\sin\theta_1 d\hat{\mathbf{x}}_1 d\theta_1 d\varphi \tag{A.29}$$

and the overall rate is given by evaluation of this expression on the boundary, $\partial\Omega$, as displayed by Eqs. (15)-(17), where the compact notation defined by (A.53) is employed.

2.3 Bulk Reaction Rate

Following the approach used to determine the average flux, we write a reaction term valid everywhere in the domain in terms of a generalized rate coefficient:

$$R(\mathbf{x}, \mathbf{C}_N) = K(\mathbf{x}|\mathbf{C}_N)C(\mathbf{x}|\mathbf{C}_N) \tag{A.30}$$

where

$$K(\mathbf{x}|\mathbf{C}_N) = \phi^2 \qquad \mathbf{x} \text{ in microporous matrix} \tag{A.31}$$

$$= 0 \qquad \mathbf{x} \text{ in macropore}$$

which can be exactly expressed as a continued product of Heaviside functions, or by invoking (A.15), approximately expressed as:

$$K(\mathbf{x}|\mathbf{C}_N) \approx \phi^2 \left[1 - \sum_{i=1}^{N} H(1-\rho_i)\right] \tag{A.32}$$

Inserting into (A.30) and configurationally averaging yields:

$$\langle R(\mathbf{x})\rangle_0 = \phi^2\langle C(\mathbf{x})\rangle_0 - \phi^2 \sum_{i=1}^{N}\langle H(1-\rho_i)C(\mathbf{x}|\mathbf{C}_N)\rangle_0 \tag{A.33}$$

The summation can be simplified by the same procedure as used in the previous subsection to obtain (A.28) from (A.22). The result is:

$$\langle R(\mathbf{x})\rangle_0 = \phi^2\langle C(\mathbf{x})\rangle_0 - \phi^2 \frac{\epsilon_2}{\pi} \int_0^{\frac{\pi}{2}} \int_{\rho_1 \le 1} \langle C(\mathbf{x}|\mathbf{r}_1)\rangle \sin\theta_1 d\hat{\mathbf{x}}_1 d\theta_1 \tag{A.34}$$

3 Configurational Averaged Equations

The solution of the configurationally averaged equations developed in this section is required to evaluate the above expressions for the overall rate and effective diffusivity.

3.1 Configurationally Averaged Equation

In this subsection, we combine results from the previous section in order to obtain the configurationally averaged equations. Equations (6) and (7) are replaced by a generalized conservation equation:

$$\nabla \cdot \mathbf{F}(\mathrm{x}|\mathrm{C}_N) \quad - \quad R(\mathrm{x}|\mathrm{C}_N) = 0 \tag{A.35}$$

which is configurationally averaged to yield:

$$\nabla \cdot \langle \mathbf{F}(\mathbf{x}) \rangle_0 \quad - \quad \langle R(\mathbf{x}) \rangle_0 = 0 \tag{A.36}$$

where the quantities: $\langle \mathbf{F}(\mathbf{x}) \rangle_0$ and $\langle R(\mathbf{x}) \rangle_0$ are given by Eqs. (A.28) and (A.34). Performing the required divergence operation in conjunction with Eqs. (7) and (13), yields:

$$\nabla \cdot \langle \mathbf{F} \rangle_0 = \nabla^2 \langle C(\mathbf{x}) \rangle_0 + \epsilon_2 \lim_{\delta \to 0+} \frac{1}{\pi} \int_0^{\frac{\pi}{2}} \int_{\rho_1 = 1+\delta} [\nabla \langle C(\mathbf{x}|\mathbf{r}_1) \rangle \cdot \mathbf{n}] \, \sin\theta_1 d\hat{\mathbf{x}}_1 d\theta_1 \tag{A.37}$$

where the normal derivative, $\nabla \langle C(\mathbf{x}|\mathbf{r}_1) \rangle \cdot \mathbf{n}$, is evaluated on the exterior surface of the macropore as indicated. Inserting this result and Eq. (A.34) into (A.35) yields the configurationally averaged equation:

$$\nabla^2 \langle C(\mathbf{x}) \rangle_0 - \phi^2 \langle C(\mathbf{x}) \rangle_0 = \tag{A.38}$$

$$\epsilon_2 \lim_{\delta \to 0+} \frac{1}{\pi} \int_0^{\frac{\pi}{2}} \int_{\rho_1 = 1+\delta} \frac{\partial}{\partial n} \langle C(\mathbf{x}|\mathbf{r}_1) \rangle \, \sin\theta_1 d\hat{\mathbf{x}}_1 d\theta_1 - \epsilon_2 \phi^2 \frac{1}{\pi} \int_0^{\frac{\pi}{2}} \int_{\rho_1 \leq 1} \langle C(\mathbf{x}|\mathbf{r}_1) \rangle \sin\theta_1 d\hat{\mathbf{x}}_1 d\theta_1$$

The solution must satisfy the configurationally averaged boundary condition:

$$\langle C(\mathbf{x}) \rangle_0 = 1 \qquad \text{on boundary}: \ \mathbf{x} \in \partial\Omega \tag{A.39}$$

which is obtained by configurationally averaging (8). The above boundary value problem is evidently coupled to the conditionally averaged equation through integrals on the RHS (right-hand side) which involve the conditionally averaged concentration, $\langle C(\mathbf{x}|\mathbf{r}_1)$.

3.2 Conditionally Averaged Equation

In this section, the conditionally averaged equation is determined by a conditional average of the generalized conservation equation, (A.35):

$$\nabla \cdot \langle \mathbf{F}(\mathbf{x}) \rangle_1 \quad - \quad \langle R(\mathbf{x}) \rangle_1 = 0 \tag{A.40}$$

where $\langle \mathbf{F}(\mathbf{x}) \rangle_1$ and $\langle R(\mathbf{x}) \rangle_1$ are conditionally averaged quantities which are obtained below.

3.2.1 Conditionally Averaged Flux

Inserting (A.21) into (A.19) and conditionally averaging yields:

$$\langle \mathbf{F} \rangle_1 = \nabla \langle C(\mathbf{x}|\mathbf{r}_1) \rangle + (\alpha - 1) \sum_{i=2}^{N} \langle H(1-\rho_i) \nabla C(\mathbf{x}|\mathbf{C}_N) \rangle_1 \qquad \rho_1 > 1 \qquad (A.41)$$

$$= \alpha \nabla \langle C(\mathbf{x}|\mathbf{r}_1) \rangle \qquad \rho_1 < 1 \qquad (A.42)$$

In this case, the term within the sum is given by an $(N-1)-$fold integration over the pore specification space, T, weighted by the conditional probability: $P(\mathbf{C}_N|\mathbf{r}_1) = P(\mathbf{C}_N|\mathbf{r}_1, \mathbf{r}_i) P(\mathbf{r}_i|\mathbf{r}_1)$ given by (A.7) and (A.8). Thus:

$$\sum_{i=2}^{N} \langle H(1-\rho_i) \nabla C(\mathbf{x}|\mathbf{C}_N) \rangle_1 =$$

$$\frac{1}{(N-1)!} \sum_{i=2}^{N} \int_{T^{N-1}} H(1-\rho_i) \nabla C(\mathbf{x}|\mathbf{C}_{N-1}) P(\mathbf{C}_N|\mathbf{r}_1, \mathbf{r}_i) P(\mathbf{r}_i|\mathbf{r}_1) d\mathbf{r}_i d\mathbf{C}_{N-2} \qquad (A.43)$$

which is analogous to (A.23). Performing all but the i^{th} integration for each term in the sum yields:

$$\sum_{i=2}^{N} \langle H(1-\rho_i) \nabla C(\mathbf{x}|\mathbf{C}_N) \rangle_1 = \frac{1}{N-1} \sum_{i=2}^{N} \int_T H(1-\rho_i) \nabla \langle C(\mathbf{x}|\mathbf{r}_1, \mathbf{r}_i) \rangle P(\mathbf{r}_i|\mathbf{r}_1) d\mathbf{r}_i \qquad (A.44)$$

where $\langle C(\mathbf{x}|\mathbf{r}_1, \mathbf{r}_i) \rangle$ is the doubly conditional averaged concentration field with pores specified by $\mathbf{r}_1$ and $\mathbf{r}_i$. Using the indistinguishability of the unspecified pore axes $(i \neq 1)$, we can perform the sum yielding:

$$\sum_{i=2}^{N} \langle H(1-\rho_i) \nabla C(\mathbf{x}|\mathbf{C}_N) \rangle_1 = \int_T H(1-\rho_2) \nabla \langle C(\mathbf{x}|\mathbf{r}_1, \mathbf{r}_2) \rangle P(\mathbf{r}_2|\mathbf{r}_1) d\mathbf{r}_2 \qquad (A.45)$$

Since the pores are uncorrelated, $P(\mathbf{r}_2|\mathbf{r}_1) = P(\mathbf{r}_2)$, which is given by (A.10). Thus, the method used to evaluate the RHS of (A.25) may be applied to the above RHS

and the result inserted into (A.41) to yield:

$$\langle \mathbf{F} \rangle_1 = \nabla \langle C(\mathbf{x}|\mathbf{r}_1) \rangle + \epsilon_2 \alpha \frac{1}{\pi} \int_0^{\frac{\pi}{2}} \int_{\rho_2 \leq 1} \nabla \langle C(\mathbf{x}|\mathbf{r}_1, \mathbf{r}_2) \rangle \sin\theta_2 d\hat{\mathbf{x}}_1 d\theta_2 \qquad \rho_1 > 1 \tag{A.46}$$

having approximated $\alpha - 1 \approx \alpha$. Incorporating Eqs. (7) and (13), the divergence of $\langle \mathbf{F} \rangle_1$ is given by:

$$\nabla \cdot \langle \mathbf{F} \rangle_1 = \nabla^2 \langle C(\mathbf{x}|\mathbf{r}_1) \rangle \; + \tag{A.47}$$

$$\epsilon_2 \lim_{\delta \to 0+} \frac{1}{\pi} \int_0^{\frac{\pi}{2}} \int_{\rho_2 = 1+\delta} \left[\nabla \langle C(\mathbf{x}|\mathbf{r}_1, \mathbf{r}_2) \rangle \cdot \mathbf{n} \right] \sin\theta_2 d\hat{\mathbf{x}}_2 d\theta_2 \qquad \rho_1 > 1$$

$$\nabla \cdot \langle \mathbf{F} \rangle_1 = \nabla^2 \langle C(\mathbf{x}|\mathbf{r}_1) \rangle = 0 \qquad \rho_1 < 1$$

3.2.2 Conditionally Averaged Reaction Rate

Similarly, inserting (A.32) into (A.30) and conditionally averaging yields:

$$\langle R(\mathbf{x}) \rangle_1 = \phi^2 \langle C(\mathbf{x}|\mathbf{r}_1) \rangle - \phi^2 \sum_{\mathrm{i}=1}^{N} \langle H(1-\rho_{\mathrm{i}}) C(\mathbf{x}|\mathbf{C}_N) \rangle_1 \tag{A.48}$$

where the term involving the summation is evaluated by the procedure used above to yield:

$$\langle R(\mathbf{x}) \rangle_1 = \phi^2 \langle C(\mathbf{x}|\mathbf{r}_1) \rangle - \phi^2 \frac{\epsilon_2}{\pi} \int_0^{\frac{\pi}{2}} \int_{\rho_2 \leq 1} \langle C(\mathbf{x}|\mathbf{r}_1, \mathbf{r}_2) \rangle \sin\theta_2 d\hat{\mathbf{x}}_2 d\theta_2 \tag{A.49}$$

3.2.3 Conditionally Averaged Equation

The desired conditionally averaged equation is now be obtained by inserting (A.47), (A.49) into (A.40):

$$\nabla^2 \langle C(\mathbf{x}|\mathbf{r}_1) \rangle - \phi^2 \langle C(\mathbf{x}|\mathbf{r}_1) \rangle = \tag{A.50}$$

$$\epsilon_2 \lim_{\delta \to 0^+} \frac{1}{\pi} \int_0^{\frac{\pi}{2}} \int_{\rho_2 = 1+\delta} \frac{\partial}{\partial n} \langle C(\mathbf{x}|\mathbf{r}_1, \mathbf{r}_2) \rangle \sin\theta_2 d\hat{\mathbf{x}}_2 d\theta_2 \; -$$

$$\epsilon_2 \phi^2 \frac{1}{\pi} \int_0^{\frac{\pi}{2}} \int_{\rho_1 \leq 1} \langle C(\mathbf{x}|\mathbf{r}_1, \mathbf{r}_2) \rangle \sin\theta_2 d\hat{\mathbf{x}}_2 d\theta_2 \qquad \rho_1 > 1$$

$$\nabla^2 \langle C(\mathbf{x}|\mathbf{r}_1) \rangle = 0 \qquad \rho_1 < 1 \tag{A.51}$$

where a conditional average of (8) yields:

$$\langle C(\mathbf{x}|\mathbf{r}_1) \rangle = 1 \qquad \text{on boundary : } \mathbf{x} \in \partial\Omega \tag{A.52}$$

The resulting boundary value problem is evidently coupled to the doubly conditional averaged concentration field: $\langle C(\mathbf{x}|\mathbf{r}_1, \mathbf{r}_2) \rangle$. As may now be clear, the foregoing conditional averaging procedure can be repeated indefinitely to produce an infinite hierarchy of coupled equations with an additional specified pore axis at each level.

3.3 Truncation of Hierarchy

It is convenient to introduce the compact notation:

$$C_0(\mathbf{x}) \equiv \langle C(\mathbf{x}) \rangle, \qquad C_1(\mathbf{x}) \equiv \langle C(\mathbf{x}|\mathbf{r}_1) \rangle, \qquad C_2(\mathbf{x}) \equiv \langle C(\mathbf{x}|\mathbf{r}_1, \mathbf{r}_2) \rangle \tag{A.53}$$

Far from a fixed pore axis, the doubly conditional averaged concentration field must tend to the first conditionally averaged field:

$$\lim_{\rho_2 \to \infty} C_2(\mathbf{x}) = C_1(\mathbf{x}) \tag{A.54}$$

The development contained in this appendix relies upon Eq. (A.15) which is valid for $\epsilon_2 << 1$. Under this condition, the above expression becomes a reasonable approximation everywhere in the material:

$$C_2(\mathbf{x}) \approx C_1(\mathbf{x}) \qquad \epsilon_2 << 1 \tag{A.55}$$

which implies that the RHS of (A.51) is approximately equal to the RHS of (A.38). Using this approximation, the foregoing hierarchy is truncated to yield the closed set of equations (18)-(21).

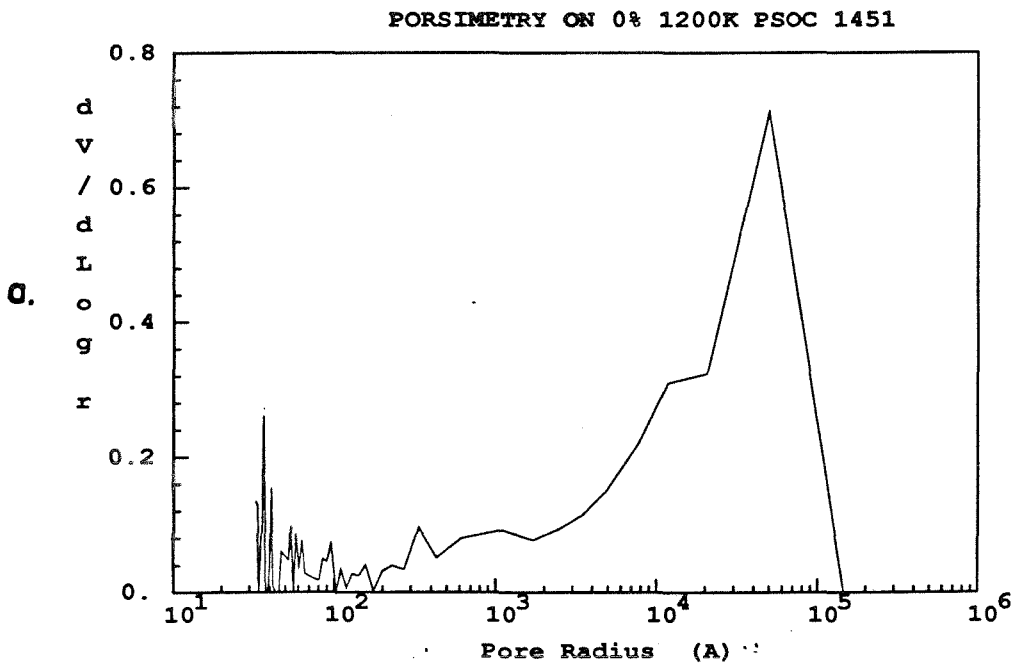

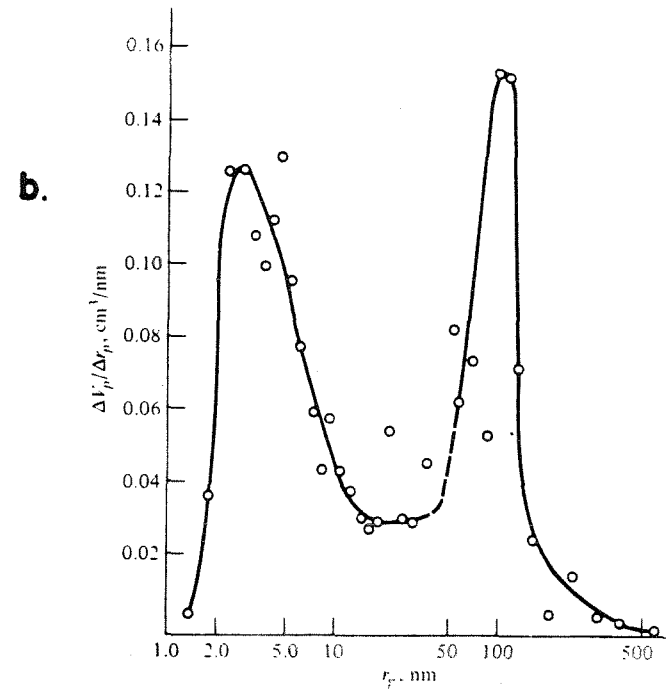

Figure 5.5 Pore-size distribution for a commercial Fe_3O_4–Cr_2O_3 catalyst. (*Bohlbro, 1966, p. 14.*)

Figure 1: Bimodal pore size distributions for: (a) PSOC-1451 coal derived char Northrop (1988) and (b) $Fe_3O_4-CrO_3$ catalyst (Bohlbro 1966).

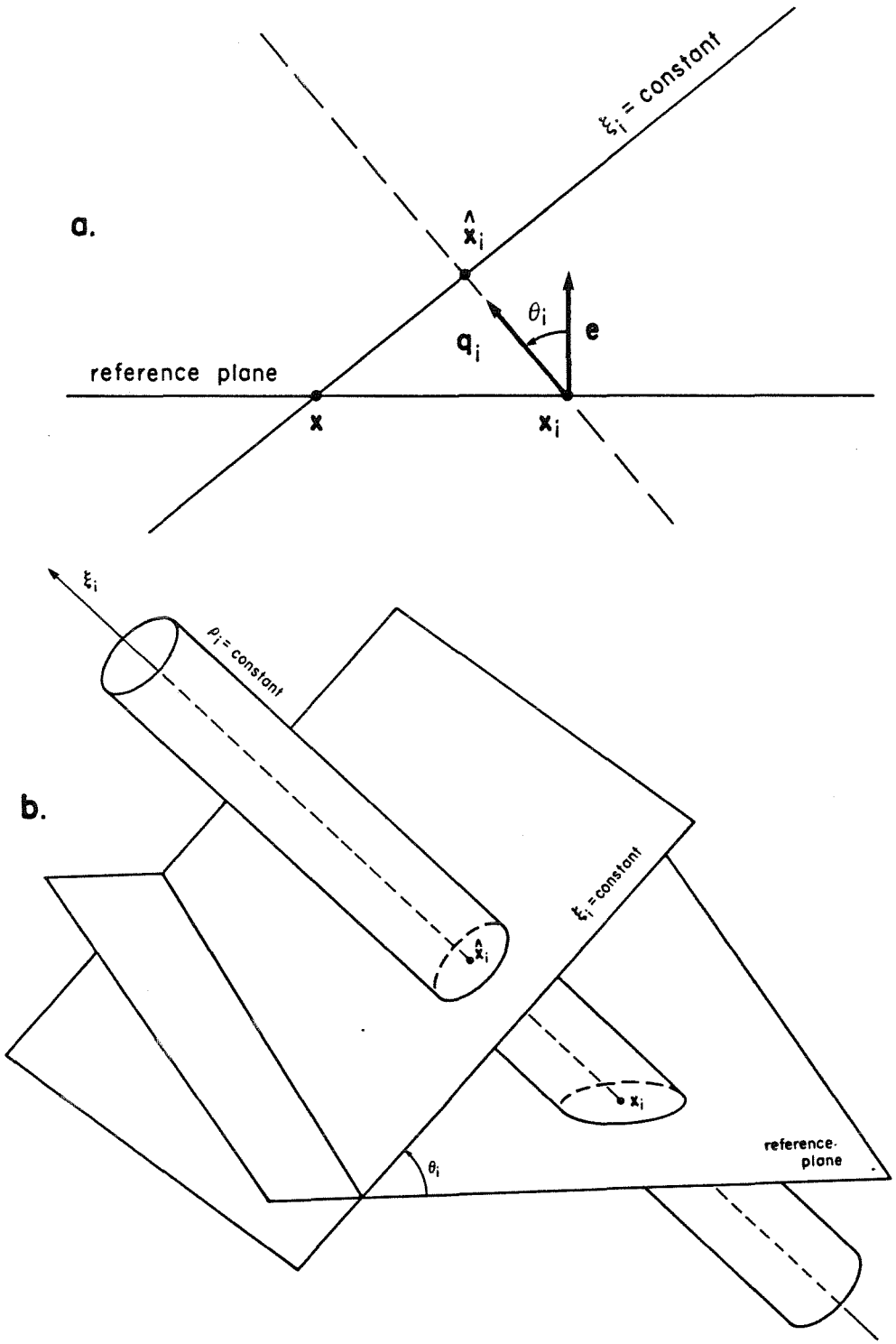

Figure 2: Coordinate system: (a) two-dimensions (b) three-dimensions (c) cylindrical coordinates oriented with pore axis.

c.

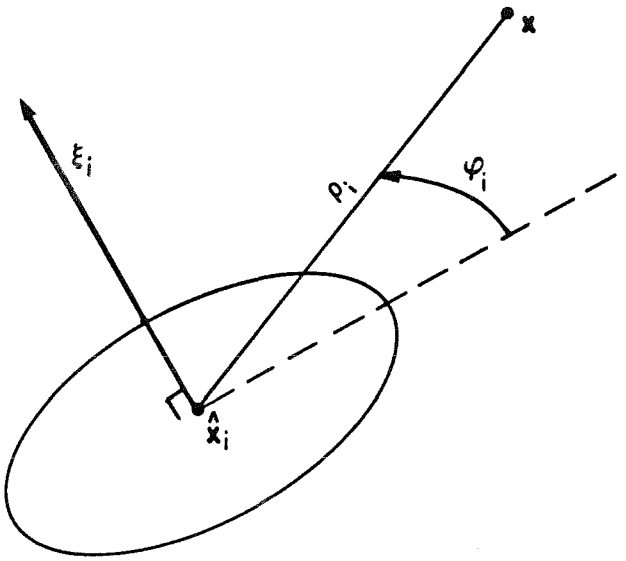

$\mathbf{x}$ is an arbitrary field point, θ_i is the angle between reference plane (defined by $\mathbf{e}$) and orientation plane (defined by $\mathbf{q}_i$). Azimuthal angle, φ_i is defined in the plane ξ_i =constant. Pore axis intersects reference plane at $\mathbf{x}_i$ and orientation plane (ξ_i =constant) at $\hat{\mathbf{x}}_i$. ξ_i is an axial coordinate (distance from the boundary) in the $\mathbf{q}_i$−direction. ρ_i is a radial coordinate; $\rho_i = 1$ defines macropore surface.

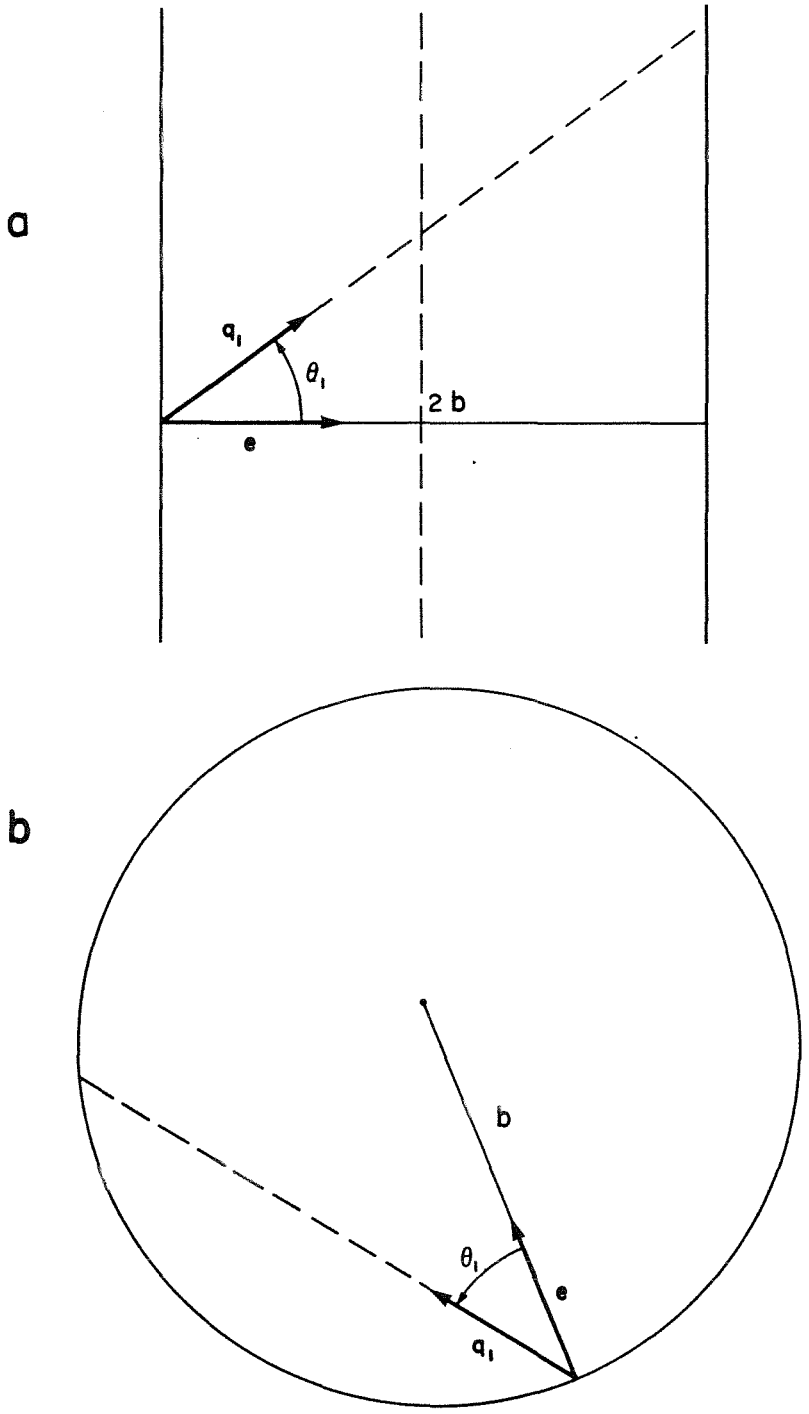

Figure 3: Orientation of reference vector, **e** for (a) slab, (b) spherical, and (c) semi-infinite geometries.

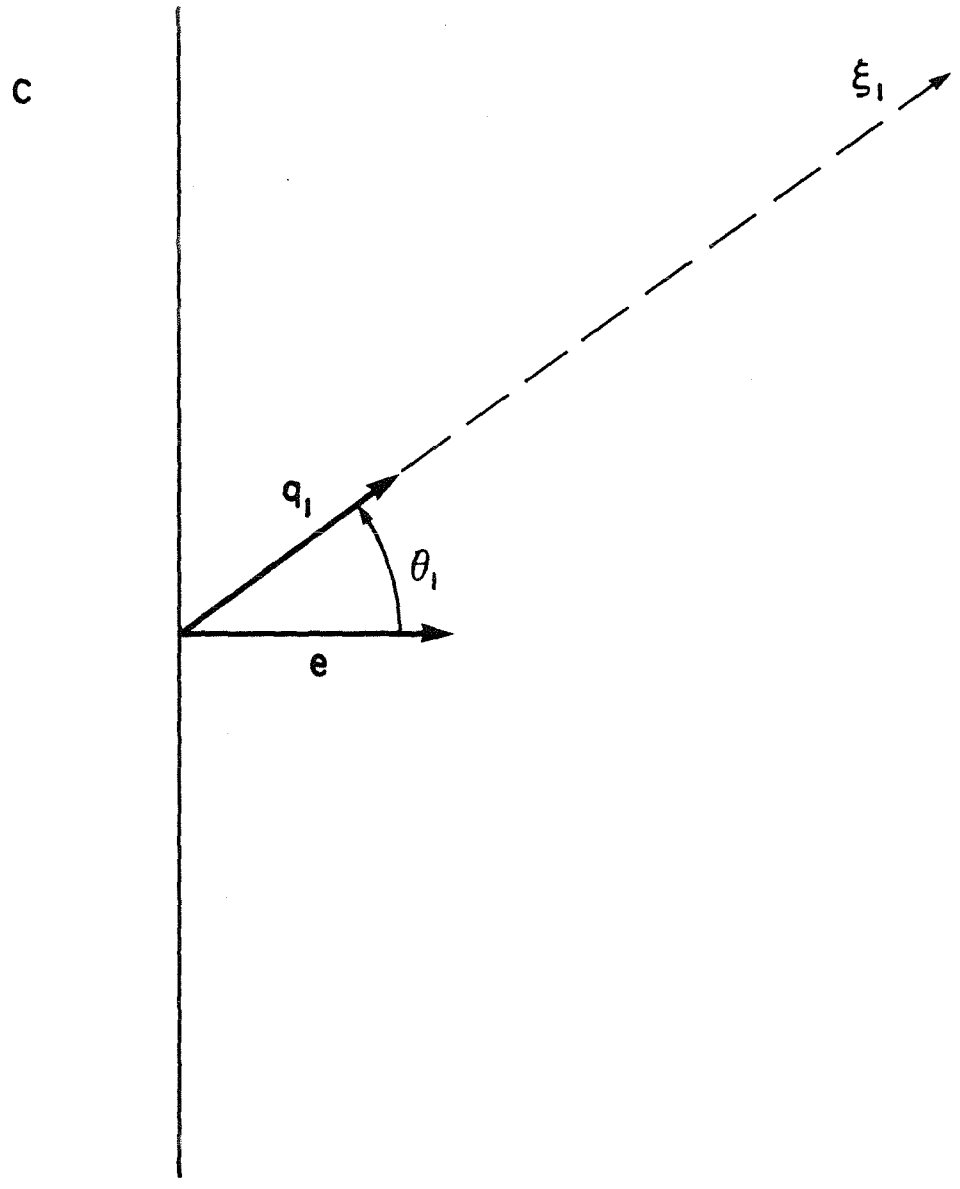
C
ξ_1
q_1
θ_1
e

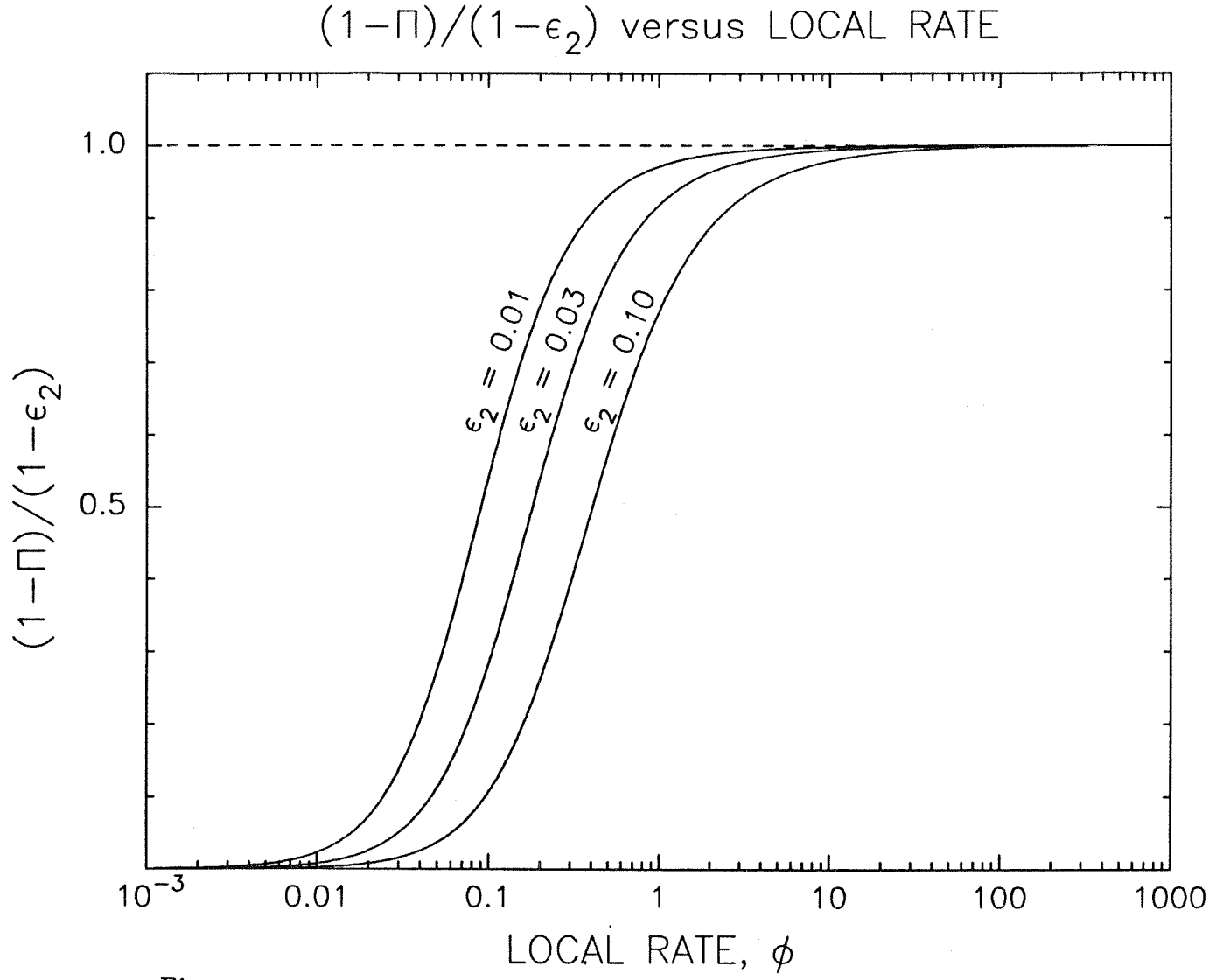

Figure 4: Behavior of $(1 - \Pi)/(1 - \epsilon_2)$ where Π is defined by Eq. (42).

CHAPTER 9

Summary

Summary

A detailed conclusion is contained within each chapter, hence only the general results from the thesis as a whole are put forth in this section. The thrust of the present work has been an improved understanding of the influence of microstructure in problems involving heterogeneous reaction and diffusion.

The first part of this thesis is concerned with char combustion. A simplified single-particle char combustion model was developed for application in situations which permit a continuum description of the porous char structure. The model accounts for intraparticle pore diffusion and pore evolution coupled to gas-phase heat and mass transport. An efficient algorithm, based on this combustion model, was developed for the prediction of char oxidation rates from particle combustion data. The combustion model and the algorithm for estimating kinetic parameters were applied to, and to some extent verified by, combustion data gathered from well-defined laboratory combustion experiments (Levendis and Flagan 1988).

The most significant contribution of this thesis is contained in the latter portion which focuses on a theoretical approach for the study of diffusion reaction processes in microstructured materials. A detailed analysis is presented for determining the reactant flux into a medium containing a dilute suspension of reactive, spherical particles under both steady and transient conditions. The governing equations were configurationally averaged to produce an infinite hierarchy of coupled, conditionally averaged equations which is truncated using the physical considerations of screening and diluteness. The detailed influence of the macroscopic boundary was given explicit consideration. An asymptotic solution was obtained valid for dilute volume fractions of the reactive particles. The results are contrasted with those obtained by a mean-field analysis (Quann and Sarofim 1982).

The same methodology is subsequently applied to the well-known problem of the decay of an initially uniform distribution of reactant in an infinite medium of spherical sinks. The results provide a useful comparison with other theoretical work (Felderhof and Deutch 1976, Felderhof 1977, Bixon and Zwanzig 1981) indicating that the present methodology faithfully reproduces recent results on this problem by a seemingly simpler, more physical approach.

Typically, the porous structure of char is adequately described by a continuum as assumed throughout most of the char combustion study contained herein. A notable counterexample is cenosphere combustion discussed at the beginning of this work. The microstructure of the char cannot be rationally considered as a continuum under conditions realized in practice. In the last chapter of this thesis, this problem is reconsidered.

The configurational averaging approach developed in the context of ash vaporization is applied to reaction and diffusion in a random, porous material with a bimodal pore size distribution. The detailed distribution of cylindrical macropores is treated under diffusion-controlled conditions which are pertinent to cenosphere combustion. An asymptotic solution, valid for low macropore void volume, was analytically obtained. In the diffusion-controlled limit, the results reduce to those obtained by a simpler, single pore model.

References

1. Bixon, M. and Zwanzig, R. (1981) Diffusion in a medium with static traps. *J. Chem. Phys.* **75** (5), 2354.

2. Felderhof, B.U. and Deutch, J.M. (1976) Concentration dependence of the rate of diffusion-controlled reactions. *J. Chem. Phys.* **64**, (11), 4551-4558.

3. Felderhof, B.U. (1977) Frequency-dependent rate coefficient in diffusion-controlled reactions. *J. Chem. Phys.* **66** (10), 4385.

4. Levendis, Y.A. and Flagan, R.C. Synthesis, formation and characterization of glassy spheres of variable properties. submitted to *Carbon.*

5. Levendis, Y.A., Flagan, R.C. and Gavalas, G.R. Oxidation kinetics of monodisperse spherical, carbonaceous particles of variable properties. *Comb. & Flame* In Press.

6. Quann, R.J. and Sarofim, F., 1982, Vaporization of refractory oxides during pulverized coal combustion. *19^{th} Symposium (International) on Combustion, The Combustion Institute*, 1429-1440.

CHAPTER 10

Epilogue

Suggestions for Future Work:

Concentrated Systems

In this thesis, a methodology was developed for the analysis of reaction diffusion processes in microstructured materials and several problems have been studied. The details of the microstructure were addressed, however, the results were restricted to sparse structures. An important area which warrants further study is heterogeneous reaction problems in concentrated systems. A study of the ash vaporization problem in the regime of high inclusion volume fraction would be interesting and may have significant implications to the metabolic production rate of cells immobilized in a polymer gel (Karel *et al.* 1985). Similarly, a detailed study of reaction and diffusion in moderately porous solid has obvious relevance to char combustion and heterogeneous catalysis.

Theoretical studies of concentrated suspensions have a shorter history than that for dilute systems but a wealth of useful results are nevertheless available. The Hashin and Shtrikman (1962) variational bounds for the effective magnetic permeability (conductivity of a random composite material consisting of spherical inclusions of one material embedded in another are a well-known result for concentrated systems. By retaining more details of the microstructure, Torquato (1985) improved upon their results and developed tighter rigorous bounds for the effective conductivity. The development of rigorous upper and lower bounds has also been applied to diffusion-controlled reactions yielding approximate rate constants valid to arbitrary volume fraction (Rubinstein and Torquato).

The recent development of the effective continuum treatment by Chang *et al.* (1986) represents a complimentary (theoretical) approach for determining effective

transport properties of concentrated microstructured materials. Their approach requires a detailed distribution function but entirely avoids the necessity for the solution of complicated two-particle problems. Although a rigorous justification for this approach is not available, it appears to agree well with experiment.

Computer simulations provide a very useful tool which allows the analysis of microstructured problems without the need for an *ad hoc* closure assumption. Furthermore, simulations can be used to explore the implication of commonly employed approximations most notably the superposition approximation. In a study on the effective conductivity of concentrated suspensions, Bonnecaze (1987) employed the simulation procedure of Durlofsky *et al.* (1987). The results supported the earlier theoretical work of Sangani and Acrivos (1982) for regular arrays of spherical particles.

In addition to the foregoing theoretical approaches, useful supporting experiments may also be possible. An experiment pertinent to the ash vaporization problem may be conceived through the impregnation of porous particles with a volatile material. The mass flux of the volatile material from the particle can be directly and accurately measured using a thermogravimetric analyzer (TGA). An appropriate, well-defined chemical reaction suitable for a TGA experiment would obviously be a useful experiment in a study of heterogeneous reaction and diffusion in a porous solid.

1 References

1. Bonnecaze, R.T. (1987) A method for determining the effective conductivity of dispersions of particles. Master's Thesis.

2. Chang, E.Y., Yendler, B.S. and Acrivos, A., 1986, A model for estimating the effective thermal conductivity of a random suspension of spheres. *Proceedings of the SIAM Workshop on Multiphase Flow.*

3. Durlofsky, L., Brady, J.F. and Bossis, G. (1987) Dynamic simulation of hydrodynamically interacting particles. *J. Fluid Mech.* **180**, 21.

4. Hashin, Z. and Shtrikman, S. (1962) A variational approach to the theory of the effective magnetic permeability of multiphase materials. *J. Appl. Phys.* **33**, 10, 3125.

5. Karel, S.F., Libicki, S.B. and Robertson, C.R. (1985) The immobilization of whole cells: engineering principles. *Chem. Eng. Sci.* **40** (8), 1321.

6. Rubinstein, J. and Torquato, S. Diffusion-controlled reactions: mathematical formulation, variational principles, and rigorous bounds. *J. Chem. Phys.* In press.

7. Sangani,A.S. and Acrivos,A. (1982) The effective conductivity of a periodic array of spheres. *Proc. Roy. Soc.* A **386**, 263.

8. Torquato, S. (1985) Effective electrical conductivity of two-phase disordered composite media. *J. Appl. Phys.* **58** (10), 3790.

APPENDIX 1

Effects of the Catalytic Activity of Calcium in the Combustion of Carbonaceous Particles

Effects of the Catalytic Activity of Calcium in the Combustion of Carbonaceous Particles

Y. A. Levendis S. W. Nam* M. Loewenberg*

R. C. Flagan

G. R. Gavalas*

Departments of Environmental Engineering Science

and * Chemical Engineering

California Institute of Technology

Pasadena, California 91125

Abstract

The reactivity of calcium-laden carbonaceous particles to oxygen has been investigated. The chars particles used, were prepared from polyfurfuryl alcohol (PFA) and were spherical and monodisperse. Some experiments were also carried out with a HVA bituminous coal. Calcium was introduced by one of three different methods: precipitation of calcium carbonate, impregnation with calcium acetate, and calcium ion exchange. Electron microscopy indicated that the distribution of calcium was remarkably uniform in particles containing a bimodal distribution of micro- and transitional-pores, whereas for particles with micropores only the Ca concentration was high at the surface and low at the center. X-ray analysis indicated that the conversion of the carbonate to the

with micropores only the Ca concentration was high at the surface and low at the center. X-ray analysis indicated that the conversion of the carbonate to the oxide at temperatures below 1400 K takes place only after all carbon has been consumed. Calcium carbonate is the predominant species while carbon is still present in the sample. Combustion studies showed that the calcium catalyst promoted the overall as well as the intrinsic reaction rate at all temperatures investigated (600-3000 K) by up to two orders of magnitude. The effectiveness of the catalyst introduced by the different methods was comparable, with the calcium ion exchanged chars being, in general, the most reactive.

1 Introduction

Calcium enrichment of coals has been a subject of technological interest because it accelerates coal gasification[1-8] and has the potential of reducing sulfur emissions by retaining the sulfur within the ash[9]. A number of techniques of calcium introduction have been developed, ranging from mixing ground limestone with coal and subsequent injection of the mixed powder into the combustor[11], to incorporation of calcium within the coal matrix such methods as ion exchange [6,7,9,10,12,14], $CaCO_3$ precipitation[15], or impregnation[8]. The methods that introduce calcium inside the coal matrix, show considerable promise for capturing sulfur[12].

The introduction of minerals in the carbon matrix changes both the physical and the chemical structure of the particles and greatly affects the reactivity. Previous studies on the reactivity of coals and chars revealed that metals, metal salts and metal oxides catalyze the reaction of carbon with O_2, H_2O, H_2 and CO_2. Active metals include Au, Ni, Na, Ca, K, Ag, Cu, Co, Pb, Mn, and Fe[1-8,14, 16-20]. Calcium, in particular, has been the subject of numerous investigations, and its catalytic effects on carbon gasification are well established. Kinetic studies at low

to intermediate particle temperature (500-1600 K) have showed that the catalytic activity of calcium depends on its concentration[6,7], inclusion size[18,21], uniformity of dispersion[13] and chemical form[3,8]. Hence, char pre-treatment, pyrolysis conditions and maceral composition may influence the catalytic activity through their impact on the Ca-treatment process. It is of interest to note that, while for some lignite chars the reactivity increased monotonicaly with calcium loading[6], for others it saturated at a modest calcium loading (4 wt% Ca)[22].

The present investigation employs monodisperse, spherical glassy carbon chars, formed by pyrolysis of uniformly sized droplets of polyfurfuryl alcohol (PFA), to investigate the catalytic effects of calcium on the reactivity of carbon over a range of particle temperatures, with emphasis to high temperatures. The relative effectiveness of various Ca-treatment techniques was also examined. These char particles are ideal for this study because of their precisely known size (50 ± 1 μm in diameter) and shape, their well characterized physical and chemical nature[23], and their homogeneity and lack of residual mineral matter. Use of these synthetic chars for fundamental studies of the Ca-enhanced carbon reactivity overcomes some of the problems previously encountered with HCl-HF demineralized chars: (a) incomplete demineralization[6], (b) substantial alteration of the pore structure and apparent density (formation of cenospheres etc.)[3], and (c) deactivation of the calcium catalyst by residual chemisorbed clorine[6].

The synthetic chars selected for the present study were a plain PFA char containing only micropores and a high porosity (75% PFA - 25% carbon black) char containing both micro- and transitional pores. A HVA bituminous coal was also used to explore the influence of Ca on the combustion of natural fuels under similar conditions. Both the synthetic char and the coal particles were treated with calcium by: (i) precipitation of $CaCO_3$ within the pores of the chars, (ii) impregna-

tion with calcium acetate solution and (iii) calcium addition by ion exchange. The combustion of the calcium treated chars was studied by a number of techniques in the particle temperature ranges of 670-870 K, 1200-1500 K, and 1800-3000 K.

2 Experimental

2.1 *Production of Synthetic Chars.*

The glassy carbon materials used in this study were produced from a carbon yielding binder (polyfurfuryl alcohol) and a thinning and mixing agent (acetone). To obtain a high porosity char, carbon black particles, about 20 nm in diameter, were suspended in the polymer-acetone mixture to serve as pore forming agents. The mixtures were conducted at constant rate into an aerosol generator using a syringe pump and were subsequently sprayed into an externally heated thermal reactor. The full description of the atomization and the thermal reactor system is given elsewhere[23]. Following atomization, the uniform droplets were cured by heating to a maximum temperature of 650 K in an inert atmosphere. The resulting particles were collected by sedimentation at the bottom of the reactor. The total residence time in the reactor was approximately 4 s. To eliminate sticking of the collected particles, all materials underwent a second pyrolysis treatment for 1 hr at 800 K in a horizontal muffle furnace in N_2.

To differentiate the chars produced for the present study the following nomenclature will be used: (a) the plain polymer char will be labeled *low porosity* char since its porosity, ϵ, is $\sim$25%; (b) the char containing 25% carbon black filler will be termed *high porosity* char, $\epsilon = 48\%$; and (c) the coal will be referred to as PSOC-680.

Partial oxidation enlarges the fine pores and preferentially removes pore constrictions in the synthetic chars, thus, making the particle interior accessible to gases and liquids[23]. The calcium treatment processes were, therefore, facilitated by partial oxidation in air for 5 min at 800 K resulting at about 15% conversion. For this oxidation, the particles were spread in a thin layer inside porcelain boats, thereby minimizing bed diffusion resistance. The boats were then introduced into a hot muffle tube furnace for the 5 min. exposure.

2.2 *Calcium Treatment Techniques*

Calcium was added to the synthetic char by $CaCO_3$ precipitation, acetate impregnation, and calcium ion exchange. $CaCO_3$ precipitation involved the following ionic reactions:

$$Ca(CH_3COO)_2+H_2O+CO_2 = CaCO_3+2CH_3COOH \qquad \Delta H^0_{298} = 3.6\text{kcal/mole} \quad (1)$$

$$2CH_3COOH+Ca(OH)_2 = Ca(CH_3COO)_2+2H_2O \qquad \Delta H^0_{298} = -26.9\text{kcal/mole} \quad (2)$$

A small amount of char or coal was evacuated in a 10 ml reactor vessel at 70°C for 1 day. Carbon dioxide was then introduced into the reactor at room temperature and of 200 mbar pressure, and allowed to equlibrate with the char for 30 min. A slurry of calcium acetate solution in water and a predetermined amount of calcium hydroxide was introduced into the reactor which had been cooled in an ice bath for 10 min. in order to prevent desorption of CO_2 upon heating by the exothermic reaction (2). The char and the slurry mixture were stirred with a magnetic stirrer for 3 hrs, during which time the pH of the mixture dropped from 12.0 to 6.8, indicating that all of the $Ca(OH)_2$ had reacted. The char was then filtered, rinsed with distilled water, and dried at 80°C for 24 hrs.

Chars were impregnated with calcium acetate by the incipient wetness method. The char was evacuated at 70°C for 1 day. Calcium acetate solution (1 N) was then slowly added to incipient wetness while the sample was stirred vigorously. Since the synthetic char is not readily wetted, the chars were impregnated under vacuum. The treated sample was dried at 80°C. The procedure was repeated 3 times. After the third impregnation the sample was washed and dried.

Calcium ion exchange was performed in a 300 ml beaker placed in a water bath maintained at 50°C. The char samples were first mixed with 10 ml of distilled water for 10 min in the reactor to ensure that they were wetted thoroughly. Subsequently, 100 ml of 1 N calcium acetate solution, the pH of which was adjusted to 8.5 with calcium hydroxide, were added to the reactor. The temperature was kept at 50°C. The reactor was sealed quickly and the slurry was maintained at the initial pH value with continuous addition of 0.01 N $Ca(OH)_2$ solution. A stream of N_2 was used to purge the reactor of air in order to prevent the absorption of atmospheric CO_2 in the solution. At the end of the process the slurry was filtered and washed with distilled water. The treated char was then dried at 80°C for 24 hrs.

2.3 *Characterization of Chars*

2.3.1 *Physical Properties*

The total (internal and external) initial surface area of the chars was measured by N_2 adsorption at 77 K and CO_2 adsorption at room temperature. The results were analyzed by the BET theory and the Polanyi-Dubinin potential theory, respectively. It was found that the BET area of the low porosity char was 2 m^2/g After the partial oxidation, it increased to 300 m^2/g. The surface area, as measured by Medek's approximation to the Polanyi-Dubinin isotherm came out to be 59 m^2/g

before, and 560 m^2/g after partial oxidation. These values indicate the presence of a vast network of micropores in this char. The porosity of this char after partial oxidation, as measured by CO_2 adsorption was 27%, corresponding to a void volume of 0.22 cm^3/g. The porosity deduced from the helium and the apparent densities was lower, 25%. The apparent density, as measured by low pressure mercury intrusion, was 1.12 cm^3/g. The true density was found to be circa 1.5 cm^3/g using helium pycnometry. After calcium treatment the N_2 BET area came out to be 15, 16, and 20 m^2/g for the ion exchanged, the precipitated and the impregnated chars, respectively.

The initial N_2 BET surface area of the high porosity char was 184 m^2/g, its apparent and true densities were 0.88 cm^3/g and 1.45 cm^3/g, and the porosity was 40%. After the partial oxidation to about 15% burnout its total surface area rose to 230 m^2/g and the porosity to 48%. Calcium treatment reduced the areas to 80 and 75 m^2/g, for the ion exchanged and the precipitated chars, respectively.

2.3.2 *Calcium Distribution*

The effectiveness of the calcium treatment was assessed by measuring the calcium concentration as a function of distance from the surface of the particle. Samples of the various chars were cast in epoxy, polished in a *Buehler Minimet* automatic polisher, and gold coated for examination with a *CamScan* scanning electron microscope (SEM). Particles that had been sectioned near the middle, i.e. those with the largest diameters, were selected for analysis.

The calcium distribution was determined by energy dispersive spectroscopy (EDS) or, in the case of lower concentrations, with a *JEOL Superprobe 733* electron microprobe by wavelength dispersive spectroscopy (WDS).

Figure 1 shows Ca distributions (presented as mass percentage of CaO equiva-

lents) as a function of distance from the surface of the different chars. Each of the profiles shown is an average from three particles. The variability in calcium levels from particle to particle was small ($\pm$ 5%), indicating that the treatment processes are highly repeatable. Furthermore, the two analytical techniques (EDS and WDS) were in very good agreement in the regions where they overlapped. The calcium oxide is uniformly distributed in the high porosity chars that contain both both transitional- and micropores, since the calcium compounds penetrate readily into the interior of the particles. On the other hand, in the low porosity chars that contain only micropores, the penetration is not very effective and the concentration of calcium is high close to the surface and very low at the center. A comparison of the three methods of calcium addition indicates that, for the low porosity chars, ion exchange is the most effective; the calcium concentration is approximately constant in a 5μm thick outside layer. In the next 5μm the calcium level drops rapidly by two orders of magnitude. Thereafter, the level is again flat all the way to the center of the particle. Calcium carbonate precipitation results in a lower concentration everywhere with a thinner region (1-2μm) of constant concentration near the surface. As before, the concentration drops rapidly reaching a plateau at about 10μm from the surface. Calcium acetate impregnation method resulted in a distribution similar to that of $CaCO_3$ precipitation, except that in the latter method the calcium penetrated more effectively the region near the surface of the particle but more poorly the region close to the center.

The overall calcium loadings in the high and the low porosity chars treated by ion exchange are comparable, but for the chars treated by $CaCO_3$ precipitation the high porosity char had considerably higher loading than the low porosity char. In all cases, the partial oxidation pre-treatment increased the calcium loading of the particles by enlarging the pores and removing the pore constrictions, and by

enhancing the calcium exchange capability of the chars[24].

SEM-BSE (Back Scattered Electrons) was used as an additional technique to visually observe the calcium distribution in the particles. This method utilizes the dependence of the electron backscattering coefficient on the mean atomic number of the material, $\bar{Z}$, to distinguish elements with different $\bar{Z}$. Micrographs of sections through calcium treated glassy carbon particles shown in Fig. 2 reveal the spatial variation of composition. Examination of Fig. 2 reveals, qualitatively, the same features regarding the radial distribution of calcium as the analyses above. The bright color in the periphery of the particles results from high concentrations of calcium. The particle depicted in Fig. 2a is calcium ion exchanged, while that in Fig. 2b contains precipitated $CaCO_3$. The concentrated (bright) regions near the particle surface graphically illustrate the concentration profile of Fig. 1. Figures 3a and b depict high porosity particles that have been treated by ion exchange and $CaCO_3$ precipitation respectively. These particles are uniformly bright, as expected for the uniform distribution of calcium in these chars.

The distribution of calcium in the particles is also illustrated by the ash residue after complete combustion. Ashing experiments were performed in air at 800 K. The ash residue from the combustion of low porosity particles containing precipitated $CaCO_3$ consists of thin bubble-like shells while the residue of the ion exchanged low porosity particles has the form of thick rough shells, shown in Fig. 4 a and b. The high porosity synthetic chars produce compact ash residues reminiscent of coal ash. Polished sections of these ash residues, shown in Fig. 5.

2.4 *X-ray Diffraction*

X-ray diffraction studies of low porosity chars treated with calcium by the ion exchange and precipitation methods were conducted in a *Siemens D500/501* diffrac-

tometer at 40kV, 30mA using Ni filtered CuKα radiation. No Ca diffraction peaks were observed in the x-ray diffraction (XRD) patterns of the calcium loaded chars, presumably because of the small size of the crystallites and the high degree of dispersion[6]. Oxidation of the chars resulted in different XRD patterns depending on the soaking temperature and atmosphere. Samples of chars that were partially burned at 1400 K in 4% O_2 for 2 s exhibited both $CaCO_3$ and CaO peaks, as shown in Fig. 6. The calcium ion exchanged sample showed particularly strong $CaCO_3$ peaks. Ash produced after complete combustion at 1400 K in 4% O_2 possessed only CaO peaks. Samples pyrolyzed at 1400 K in N_2 exhibited weak CaO peaks only. Finally, complete oxidation at low temperatures (773 K, air) resulted in both CaO and $CaCO_3$ peaks. Therefore, as previously observed in XRD of lignites[8] crystals of CaO appear to form during pyrolysis of chars at elevated temperatures. During oxidation, however, calcium carbonate is the predominant product in the presence of CO_2. After all carbon is consumed, the $CaCO_3$ transforms to CaO, at a rate which increases with temperature. The conversion of $CaCO_3$ to CaO at temperatures above 1100 K is expected to proceed even in the presence of carbon and thence, CO_2. The fact that this was not seen for the ion exchanged chars at 1400 K presently, is probably due to carbonate regeneration at the cooler region of the sampling probe of the furnace used for the oxidation[25].

The average crystallite size for $CaCO_3$ produced in combustion at 1400 K, estimated from the 3/4 peak width of the (104) diffraction line[28] was 22 nm in fair agreement with results obtained elsewhere[9]. The large crystallite size suggests that the calcium carbonate might have plugged some of the pores in the chars during combustion.

2.5 *Combustion Experiments*

The combustion of the chars was studied in a drop tube furnace and a thermogravimetric analyzer.

2.5.1 *Pyrometry*

The chars were burned at moderate (1200-1500 K) and high particle temperatures (1800-3000 K) in an externally heated, laminar flow (drop-tube) furnace[25]. Particle temperatures were measured by near-infrared two color pyrometry for particles that burned at temperatures that were significantly higher than the wall temperature or inferred from heat balance calculations for particles that oxidized at temperatures close to the wall temperature. The combustion apparatus and the pyrometer are described in[25]. The experiments were conducted at a constant furnace wall temperature of 1470 K, either in air or pure oxygen. Using the pyrometer to view the particles along the axis of the reactor, the entire temperature-time histories of individual burning particle were observed. Typical profiles are shown in Figures 7-11.

In Fig. 7a temperature-time traces of several high-porosity calcium-free particles burning in O_2 are superimposed. The average maximum temperature was about 2600 K, and the mean burnout time was 14 ms. The combustion behavior of similar size particles to which calcium was added by ion exchange is shown in Fig. 7b. The maximum temperatures were about 2900 K and mean burnout time was of 11.5 ms. Figure 7c shows traces from combustion of high porosity particles in which $CaCO_3$ had been precipitated. Again the profiles are rather flat, the average maximum temperatures are 2800 K and the average burnout time was 12 ms. Thus, calcium addition has a modest effect on reducing the burnout time and increasing

the combustion temperature of particles.

Figure 8 shows the temperature history of high porosity particles burning in air. Again particles treated by both ion exchange and precipitation behave similarly. The particles burn for 25 to 30 ms in a luminous mode, and the average temperatures are in the vicinity of 2000 K. This combustion behavior is strikingly different from the behavior of plain PFA char calcium-free particles. Under identical conditions, the latter particles burned slowly in a non-luminous mode at temperatures close to that of the reactor wall, with about 2 sec being required for complete combustion.

Combustion of low-porosity particles reveals similar features to the combustion of high porosity particles. The presence of calcium reduces burnout times and increases particle combustion temperatures. Figure 9 depicts combustion of low porosity particles in O_2. The untreated particles burn at an average temperature of 2200 K and a burnout time of approximately 22 ms (Fig. 9a). The calcium treated particles burned faster, $\approx$12.5 ms, and hotter, $\approx$2500 K (Fig. 9b and c). The combustion behavior of particles containing calcium seemed to be independent of the method of calcium treatment. Combustion in air, however, revealed large differences in the manner in which the particles burned. The untreated char particles did not ignite and burned slowly at temperatures between those of the gas and the wall, and the conversion at the end of the 2 sec residence time in the combustion chamber was only 60%[25]. On the contrary, the particles that had been treated by acetate impregnation ignited and burned in an average of 30 ms at a temperature of 1900-2000 K (Fig. 10a). Some particles that were ion exchanged or precipitated ignited and burned in about 25 ms and circa 1900 K (Fig. 10b), while others burned slowly at a lower temperature. This behavior suggests that the particles so treated were at the verge of ignition. Had the oxygen concentration been a little higher they might too have ignited[25].

A few combustion experiments were conducted in air using the PSOC-680 coal. The combustion behavior of the untreated coal is contrasted to the behavior of $CaCO_3$ precipitated coal in Fig. 11 a and b. The untreated coal particles readily ignited in air unlike the synthetic Ca-free chars. The difference is due to the higher reactivity possessed by coal char by virtue of its different pore structure as well as its content of heteroatoms and minerals. The burnout times for the coal char particles were about 35 ms with the average temperatures of 2000 K. The particle temperatures were surprisingly uniform (except for one trace) although the burnout times varied. Early in the combustion of these particles, a distinct temperature peak lasting only 1-2 ms was observed, probably caused by the combustion of evolving volatiles. Introduction of $CaCO_3$, by precipitation, accelerated the combustion. The resulting burnout times were of order 15 ms (Fig. 11b). The particle temperatures exhibited large scatter and on the average they were somewhat higher than those of the untreated particles.

2.5.2 *Moderate Temperatures*

Combustion experiments at lower particle temperatures where ignition occurred without a temperature jump were also conducted in the same drop tube furnace, by lowering the oxygen partial pressure, P_{O_2}[25]. At P_{O_2} lower than $\approx$7% and at a combustor wall temperature range of 1200-1500 K the particles did not ignite, but rather burned slowly at approximately the wall temperature in a non-luminous mode. Combustion rates were deduced from particle size reduction and/or sample mass and density change. The calcium laden chars were again significantly more reactive than the untreated chars. For example, at T_W = 1250 K, T_{gas} = 1225 K , P_{O_2} = 0.04, and residence time t = 2 s, the conversion of 50μm PFA particles was 22% while the conversion of calcium ion exchanged PFA particles was 85%. Under

the same conditions, the conversion of $CaCO_3$ precipitated particles was 68%.

2.5.3 *Low Temperatures (TGA)*

Experiments were conducted in a *DuPont* model *951* thermogravimetric analyzer (TGA) at temperatures ranging between 650-850 K. The samples were heated in nitrogen at 30 K/min until the final temperature was reached. The gas flow rates were kept at 100 cm^3/min STP for all runs. Small sample quantities (1 mg) were spread in a thin layer (1 or 2 monolayers) on the balance pan to minimize diffusional resistance in the particle layer. To ensure that the measured rates are free of diffusional limitations, film diffusion, layer diffusion, and particle pore diffusion were examined separately as outlined elsewhere[27]. For combustion of the low porosity ion exchanged particles at 800 K, which involves the strongest diffusion limitations in this section of our investigation, the modified layer Thiele modulus[26] at 25% conversion was of order 10^{-2}, indicative of uniform oxygen concentration in the particle layer. The particle Thiele modulus, Φ, was about 0.9, and the effectiveness factor, η, was a little below unity suggesting complete intraparticle penetration. Therefore, it may be concluded that the particles were burning approximately under the kinetic regime I [27] of combustion. One should be cautious, however about assessing the intraparticle penetration of the oxidizer gas in these calcium treated microporous chars since, the pore structure is not well characterized and Ca crystallites might be blocking some of the pores. Furthermore, the fact that the reaction rate was found, in the present experiments, to be independent of particle size is not sufficient to ascertain the absence of pore diffusion limitations for microporous chars in general[13]. An apparent reaction rate per instantaneous mass of carbon,

R_m can be defined by:

$$R_m = -\frac{1}{m - m_{ash}} \frac{dm}{dt} \tag{3}$$

where m is the instantaneous total mass. Figures 12-14 show the apparent reaction rates for glassy carbons and coal chars at 673, 773 and 873 K as functions of conversion (burnout). The conversion, X, at any given time, is given by,

$$X = \frac{m_{initial} - m}{m_{initial} - m_{ash}}. \tag{4}$$

Figures 12a and b show the apparent rate of low porosity particles burning at 673 and 773 K, respectively. The rates of the calcium treated chars appear to be higher than those of the untreated PFA particles by up to two orders of magnitude. The rate of the Ca-free PFA chars is roughly constant with conversion, the initial transient being due to the changing gas composition over the bed, from N_2 to 21% O_2–79% N_2 upon admission of air. The rate of the Ca-treated PFA chars is initially high up to a certain conversion, but subsequently falls to values roughly two times the rate of the plain PFA char. The rate plots can be correlated with the calcium concentration and distribution inside the char particles. The ion exchanged chars that possessed the highest concentration and penetration of calcium exhibited the highest reactivity. In those chars the calcium concentration falls sharply at 6-7 μm below the surface; this Ca-rich outside layer, however, contains roughly 60% of the carbon mass and corresponds to the high rate portion of the rate curve (up to 60% conversion). The calcium precipitated and impregnated particles showed similar behavior but since both the penetration and concentration of calcium is lower the high rate region extends only to 30% conversion. This is somewhat lower than the conversion of 40-50% calculated on the basis of the calcium concentration distribution. This discrepancy may be due to the different form of the calcium compound. The precipitated $CaCO_3$ may cease to catalyze the carbon gasification

when it loses contact with the adjacent carbon matrix even if there is still unburned carbon in the vicinity. The difference in the dispersion and chemical form of the calcium additive is also responsible for the large disparity in the rate of oxidation, with the chemically bound calcium added by ion exchange being the most reactive. However, in this case it is difficult to separate the effects of the concentration and the chemical form of the catalyst.

The combustion behavior of high porosity particles is shown in Fig. 13a and b at temperatures of 773 and 873 K, respectively. The rates are overall higher than those of the low porosity chars (compare Figs 12b with 13a) due primarily to the existence of transitional "feeder"[1] pores. The calcium laden particles again exhibit higher rates with the calcium ion exchanged particles exhibiting the highest. In all but one case, the rates are monotonicly increasing with conversion reflecting the constant calcium distribution in the particles and the progressive opening and enlarging of pores with burnout. The only case that exhibits an anomalous behavior inasmuch as it undergoes a maximum in rate is the calcium ion exchanged char at 773 K. The cause of this behavior is uncertain.

Coal oxidation at 773 K in air is depicted in Fig. 14. The rate of untreated coal appears to be higher than the rate of the glassy carbons as was observed at the high temperature experiments. This rate exhibits a maximum at about 20% conversion. This behavior may be explained on the grounds of preferential combustion of thin walls between transitional pores. Both calcium laden chars exhibit overall higher rates without undergoing an early maximum in rate. The rate drop at high conversions (circa 80%) may be due to burnout of all carbon in proximity to the catalyst, and/or existence of small regions where the catalyst had not penetrated since, the coal had not been subjected to any pyrolysis or preoxidation prior to calcium addition.

3 Estimation of Rate Parameters

3.1 *Medium and High Temperatures*

Kinetic rate parameters were estimated using the approach of Loewenberg and Levendis[29] for particle temperatures at or above 1200 K. Their approach applies to the case in which particle combustion occurs at nearly constant temperature and apparent density. These conditions were observed for combustion at particle temperatures at or above 1200-1300 K. The apparent rate is assumed to be first-order in oxygen concentration: $F_p^T = k_a(T_p)C_s$. The analysis involves the solution of the pseudosteady film transport equations to obtain an apparent rate constant and particle temperature, (k_a, T_p) in terms of the observed burnout time, conversion and initial particle radius for each temperature-time trace. An Arrhenius plot of these quantities yields estimates for the observed activation energy, E_a, and pre-exponential factor, A_a.

It has been suggested that under low-temperature conditions, calcium enrichment promotes the reaction to CO_2[30,31]

$$C + O_2 = CO_2 \tag{5}$$

However, this effect is expected to diminish at particle temperatures above 1300 K[30]. An approximate analysis of the possibility of CO_2 formation was conducted by assuming that Eq.(5) is the only heterogeneous reaction (equilibrium chemistry). The resulting particle temperature calculated under these assumptions exceeded the observed values by as much as 1000 K at the highest temperatures. Thus, it was concluded that the most significant heterogeneous reaction at these temperatures is the oxidation of carbon to carbon monoxide:

$$C + \frac{1}{2}O_2 = CO \tag{6}$$

a conclusion which is in agreement with other investigators.[33] Assuming that CO is the only heterogeneous reaction product, burning only in the free stream, yielded particle temperatures within 100 K of the experimental values. An Arrhenious plot of the estimated apparent rate coefficient is shown in Fig. 15 for the two synthetic chars used. The estimated rates of the calcium laden particles are one order of magnitude higher than those of the untreated chars at all but the highest temperatures. At the highest temperature region, above approximately 2600 K, the apparent rate of the calcium treated chars is lower than the rate at 2000 K. This negative temperature dependence could be due to thermal rearrangement of the carbon matrix and decline of the number of active sites [25,32] and/or due to a decrease in the effectiveness of the catalyst.

Intrinsic rate parameters may be related to the estimated apparent rate parameters[29]:

$$E_{in} = 2E_a \tag{7}$$

$$A_{in} = 2bJ\left(\frac{\sigma_T A_a}{\sigma_{a,0}}\right)^2 \tag{8}$$

where the intrinsic rate is given by: $R_{in} = k_{in}(T_p)C$ and J is a physical factor which depends only on the particle structure[35]:

$$J = \int_0^{q^*} \frac{\epsilon(q) - \epsilon_0}{\delta_e(q)} dq \tag{9}$$

where ϵ and δ_e are the porosity and effective diffusivity, respectively and q is the length by which the local surface has receded by oxidation. Calcium enriched chars exhibited a substantial loss of BET surface area. For the high porosity char which exhibited uniform calcium penetration, it was assumed that calcium treatment resulted in:

1. a spatially uniform distribution of plugged pores

2. unblocked pores the same size as in the untreated material

3. preferential plugging of smaller pores

Based on these three assumptions, the BET surface area of the calcium treated high porosity chars may be related to their void volume distribution which allows evaluation of the physical factor, J. This procedure, in combination with Eqs. (7) and (8), allows estimation of the intrinsic rate. This procedure is only applicable to the high porosity chars which acquired uniform calcium penetration from treatment. It cannot be applied to the low porosity particles which exhibit spatially non-uniform calcium enrichment. For the high porosity chars, using the measured BET area at 10-15% burnoff (1500 K) as the initial area we calculated an intrinsic rate constant, k_i, of 0.05 gm/cm^2 s atm at T_p = 2000 K, twenty times higher than the rate of the untreated char. The calculated intrinsic rate of the calcium treated chars is comparable to the intrinsic rate of coal chars reported by Smith[34].

3.2 *Low Temperatures*

Apparent reaction rates per unit weight of material, R_m, plotted against burnout were presented previously. [1] Intrinsic rates were calculated as:

$$R_i = \frac{R_m}{\eta \gamma \sigma_a A_{tot}} \tag{10}$$

where A_{tot} is the total surface area, here taken as the N_2 BET area at 77 K, γ is the characteristic dimension of the particle (ratio of particle volume to external area), and σ_a is the apparent density of the particle. For comparison purposes, the reactivities of the chars were contrasted at 20% burnout, where the apparent

[1] The apparent rate per unit mass, R_m is related to the apparent rate per unit external area, R_a by: $R_a = R_m \gamma \sigma_a$.

rate of most chars had reached a plateau. The apparent and intrinsic reaction rate constants k_m and k_i respectively, can be calculated by dividing R_m and R_i by the surface oxygen concentration (for first order kinetics). For combustion in Regime I [29], assumed at these low temperatures, the surface oxygen concentration is equal to the ambient. The estimated rate parameters for these chars are shown in Fig.16. The N_2 BET surface areas for these chars at 20% conversion were 320 m^2/g for the low porosity char and 35 to 55 m^2/g for the calcium treated chars. The area of the high porosity char at 20% burnout was about 380 m^2/g, while that of the calcium treatment chars was between 140 and 150 m^2/g. The areas vary little with combustion temperature in the range of 673-873 K.

The apparent rate constant, k_m, increases with addition of calcium by up to two orders of magnitude for the low porosity and up to five times for the high porosity char, Fig.16a. The latter is apparently more reactive than the former in the pure form but less reactive when both are loaded with calcium. The enhanced reactivity of the high porosity char can be attributed to the network of transitional "feeder" pores, however, this advantage is lost at the presence of calcium where the overwhelming effect of catalysis renders the low porosity particles containing 2.5-3.5 wt% Ca more reactive than the high porosity chars containing 1.5 wt% Ca. This reasoning is valid only if we assume the existence of some pore diffusion limitations in the low porosity materials and hence, preferential burning in the outside Ca-rich layer of the particles first. The intrinsic reaction rate constant, k_i, follows similar trends, Fig. 16b. Here the differences between the various chars become even more pronounced by removal of the offsetting effect of reduced total surface areas. It can be noted that both the apparent and intrinsic activation energies E_a and E_i, of the chars appears to decrease with Ca-loading. Comparison with data elsewhere[35] suggests that the calcium laden chars appear to be apparently more reactive by

4-8 times and intrinsicaly more reactive by more than an order of magnitude than porous brown coal char. The calcium laden chars were also found to be one to two orders of magnitude more reactive than three HVA Bituminous coals tested under identical conditions in the same apparatus[27] even if the unladen glassy carbon chars were less reactive.

4 Conclusions

Monodisperse synthetic char and coal particles have been treated with calcium using the following methods: (i) precipitation of CaO_3 within the pores of the chars, (ii) impregnation with calcium acetate solution and (iii) calcium addition by ion exchange. The distribution of calcium inside low porosity synthetic chars was high in the vicinity of the surface and low at the center. A steep fall in concentration occurs at 2 to 6 μm depth below the surface depending on the method of calcium treatment; the ion exchange method produces the deeper penetration. The calcium concentration in the high porosity chars was very uniform throughout the char particles. X-ray diffraction show that at combustion temperatures below 1400 K calcite seems to be the predominant form of calcium at the presence of carbon and CO_2.

Combustion experiments revealed that the presence of calcium enhances the particle temperature and reduces the burnout time. The carbon reactivity was enhanced at all temperatures examined in the range of 600-3000 K, however, the difference in combustion rates was more pronounced in the low to intermediate temperature region (650-2000 K) rather than at the very high temperatures where the pure carbon kinetics exhibit a plateau. The biggest gains were recorded for the intrinsic rate of the chars since, despite of the reduction of total surface area by Ca-

induced plugging of pores the chemical kinetics were promoted. All forms of calcium introduction, both physical and chemical attachment, enhanced the combustion rate with the calcium ion exchanged chars (chemically bound) being general the most effective in catalyzing the carbon gasification in the examined temperature region (650 - 3000 K).

5 References

1. Jenkins, R. G., Nandi, S. P. and Walker, P. L., Jr. *Fuel* **52**, 288, 1973.

2. Hippo, E. J. and Walker, P. L., Jr. *Fuel* **54**, 245, 1975.

3. Tomita, A., Mahajan, O. P. and Walker, P. L., Jr. *Fuel* **56**, 137, 1977.

4. Linares-Solano, A., Mahajan, O. P. and Walker, P. L., Jr. *Fuel* **58**, 327, 1979.

5. Takarada, T., Tamai, Y, Tomita, A. *Fuel* **64**, 1438, 1985.

6. Hengel, T. D. and Walker, P. L., Jr. *Fuel* **63**, 1214, 1984.

7. Linares-Solano, A., Hippo, E. J. and Walker, P. L., Jr. *Fuel* **65**, 776, 1986.

8. Ohtsuka, Y. and Tomita, A. *Fuel* **65**, 1653, 1986.

9. Schafer, H. N. S. *Fuel* **49**, 197, 1970.

10. Case, P. L., Heap, M. P., McKinnon, C. N. Pershing, D. W. and Rayne, R. *Am. Chem. Soc. Div. Fuel Chem. Prepr.* **27**(1), 158, 1982.

11. Freund, H. and Lyon R. K. *Comb. & Flame* **45**, 191, 1982. And references therein.

12. Chang, K. K., Flagan, R. C., Gavalas G. R. and Sharma P. K. *Fuel* **65**, 75, 1986.

13. Radovic, L. R., Walker, P. L., Jr and Jenkins R. G. *Fuel* **62**, 209, 1983.

14. Jones, M. L., McCollor, D. P. and Weber, B. J. "Combustion behavior of ion exchanged coal chars. " Presented at the Fall 1987 Meeting of the Western States Section of the Combustion Institute. Hawai, November 1987.

15. Sharma, P. K., Gavalas, G. R. and Flagan R. C. *Fuel* **66**, 207, 1987.

16. Marsh, H. and Adair, R. R. *Carbon* **13**, 327, 1975.

17. Letort, M. and Martin, G. *Bull. Soc. Chim. France* **14**, 400, 1947.

18. Walker, P. L., Jr., Shelef, M. and Anderson R. A. *Chemistry and Physics of Carbon* (Edited by P. L. Walker), Vol. 4 p. 287. Edward Arnold, London, 1968.

19. Tudenheim, W. M. and Hill, G. R. *Ind. Engng. Chem.* **47**, 2129, 1955.

20. Turkdogan, E. T. and Vinters, J. V. *Carbon* **10**, 97, 1972.

21. Oya A. and Marsh, H. *Jour. of Mater. Sci.* **17**, 309, 1982.

22. Hippo, E. J., Jenkins, R. G. and Walker, P. L. Jr. *Fuel* **58** 338, 1979.

23. Levendis, Y. A. and Flagan, R. C. Submitted to *Carbon*, 1988.

24. Kalema, W. S. "A Study of Coal Oxidation" *PhD Thesis*, California Institute of Technology, 1984.

25. Levendis, Y. A., Flagan, R. C. and Gavalas G. R. Submitted to *Comb. & Flame*, 1988.

26. Weitz, P. B. and Prater C. D. *Advan. Catalysis* **6**, 143, 1954.

27. Mulcahy, M. F. R. and Smith, I. W. *Rev. Pure and Appl. Chem.* **19**, 81, 1969.

28. Short, M. A. and Walker, P. L. Jr. *Carbon* **1**, 3, 1963.

29. Loewenberg, M., Levendis, Y. A. Submitted to *Comb. & Flame*, 1988.

30. Young, B. C. and Niksa, S. *Fuel* **67**, 155, 1988.

31. Field, M. A., Gill, D. W., Morgan, B. B., and Hawksley, P. G. W. *Combustion of Pulverized Coal*, BCURA, Leatherhead, p. 189, 1967. And references therein.

32. Nagle, J. and Strickland-Constable, R. F. *Proceed. of the Fifth Carbon Conf.* 1:154, Pergamon Press, Oxford (1961).

33. Smith, I. W. *Nineteenth Symposium (International) on Combustion* The Combustion Institute, Pittsburgh, PA, 1045-1065, 1982. And references therein.

34. Smith, I. W. and Tyler, R. J. Comb. Sci. and Tech. **9**, 87, 1974.

35. Gavalas, G.R. *Comb. Sci. Tech.* **24**, 197, 1981.

6 Notation

SYMBOL	DESCRIPTION	UNITS
a	particle radius	cm
A_a	apparent pre-exponential factor	g/cm^2 s (atm)^n
A_{in}	intrinsic pre-exponential factor	g/cm^2 s (atm)^m
A_{tot}	specific total area	m^2/g
b	stoichiometric coefficient	(=1/24)
C_∞	ambient oxygen concentration	g/cm^3
C_s	oxygen concentration at particle surface	g/cm^3
E_a	apparent activation energy	kcal/g
E_{in}	intrinsic activation energy	kcal/g
F_p^T	total mass flux; apparent rate	g/cm^2-sec
ΔH	enthalpy of reaction	kcal/mole
k_i	intrinsic rate coefficient	g/(cm^{2}sec(atm)^m)
m	mass of carbon	g
P_{O_2}	ambient partial pressure of oxygen	
q	local structural variable	cm
r	radial distance	cm
r_p	pore radius	cm
R_a	apparent reaction rate	g/cm^2-sec
R_m	apparent reaction rate	g/g-sec
R_i	intrinsic reaction rate	g/cm^2-sec
T_g	ambient temperature	K
T_p	particle temperature	K
X	conversion	

δ_e	effective intraparticle diffusion coefficient	cm^2/s
ϵ	total porosity	
η	effectiveness factor	
Φ	Thiele modulus	

7 List of Figures

TABLE I

Physical Properties of Partially Oxidized Chars before Calcium Treatment

CHAR	Low Porosity plain polymer	High Porosity polymer + 25% carbon black
Apparent Density (g/cm^3)	1.12	0.75
Helium Density (g/cm^3)	1.5	1.45
Porosity	25%	48%
Average Pore Diameter	$\approx$ 15Å	150Å and 15Å bimodal
BET area (m^2/g)	300	184
CO_2 area at 298 K (m^2/g)	560	-

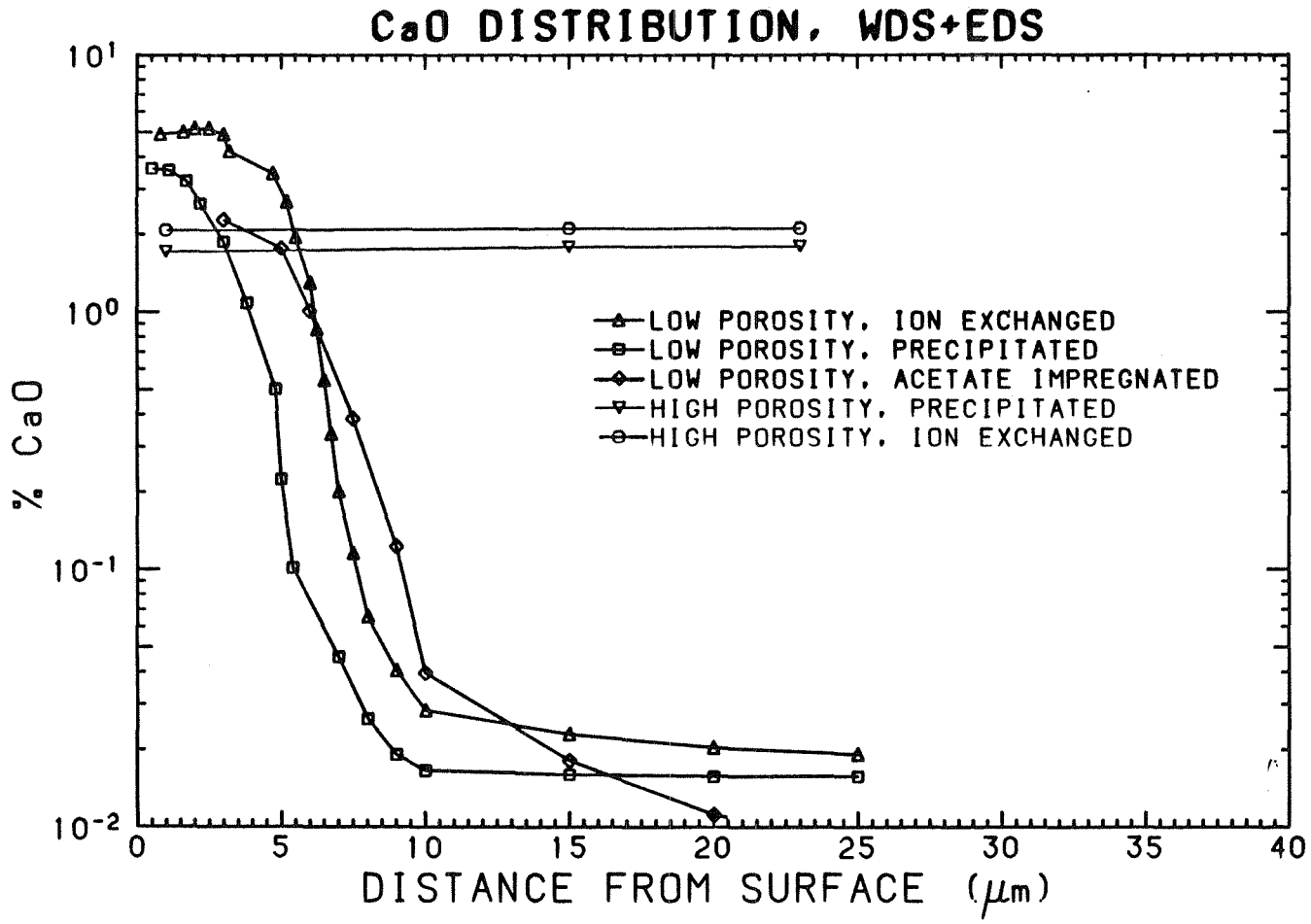

Figure 1: Distribution of calcium in CaO equivalents along the radius of calcium treated synthetic chars

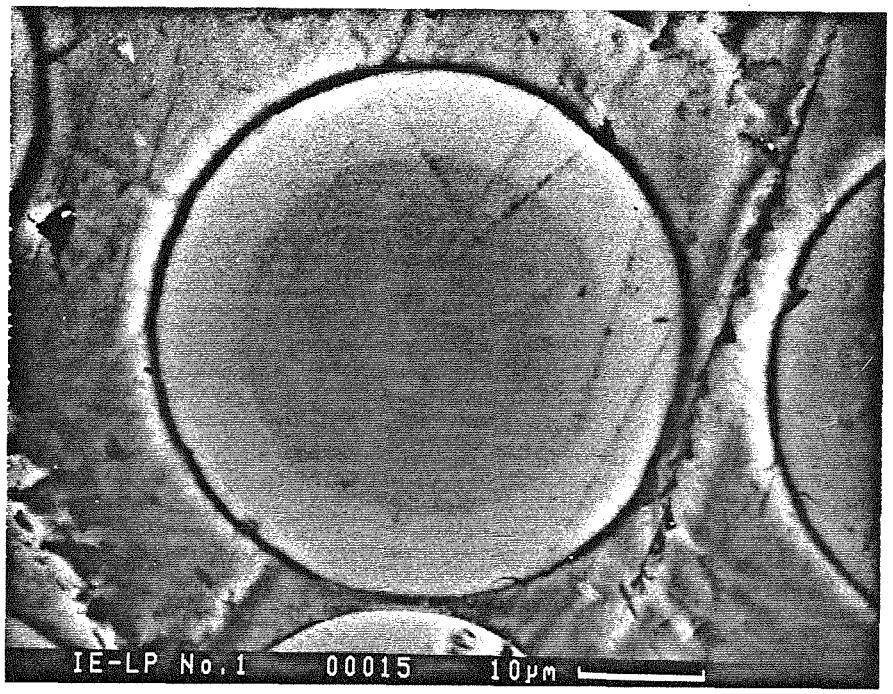

a

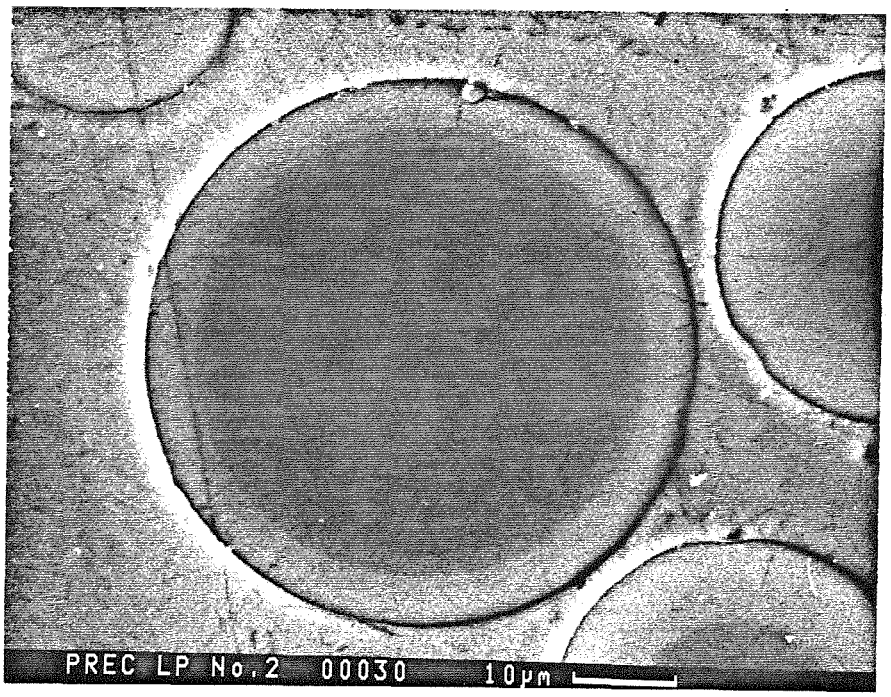

b

Figure 2: SEM-BSE micrographs of sections through calcium treated synthetic char particles (a) low porosity ion exchanged (b) low porosity $CaCO_3$ precipitated

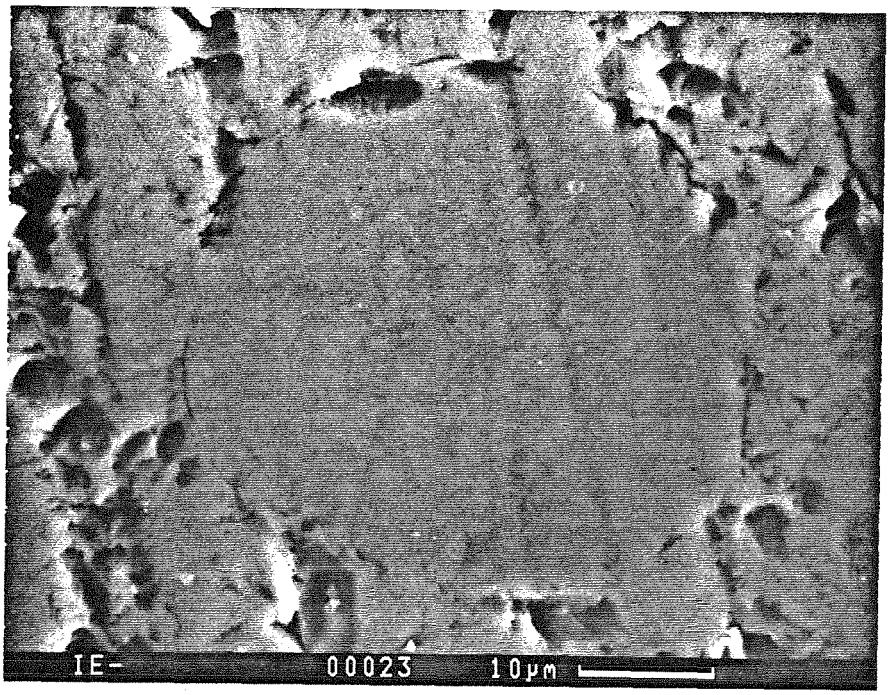

a

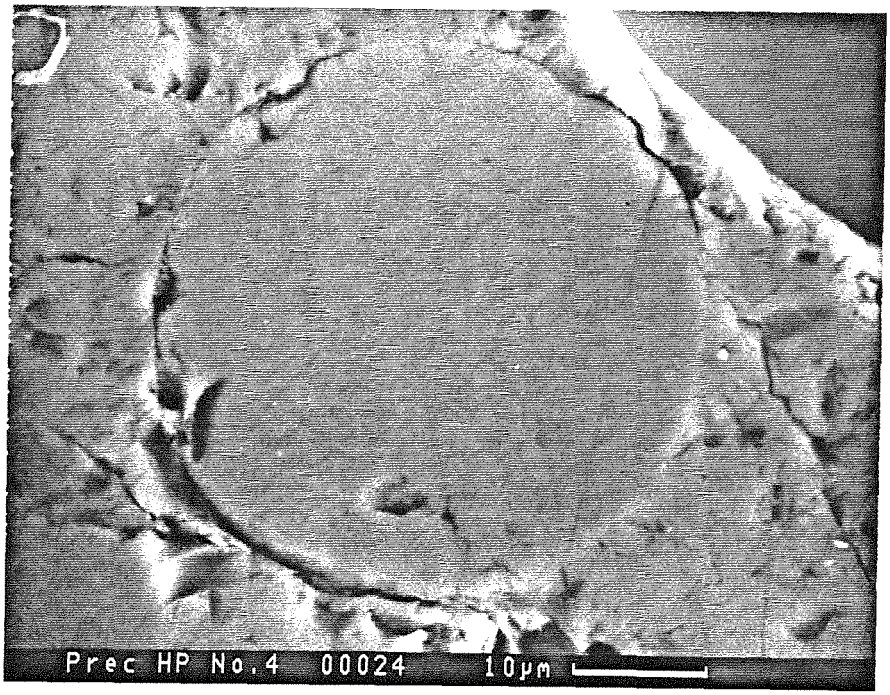

b

Figure 3: (a) high porosity ion exchanged (b) high porosity $CaCO_3$ precipitated.

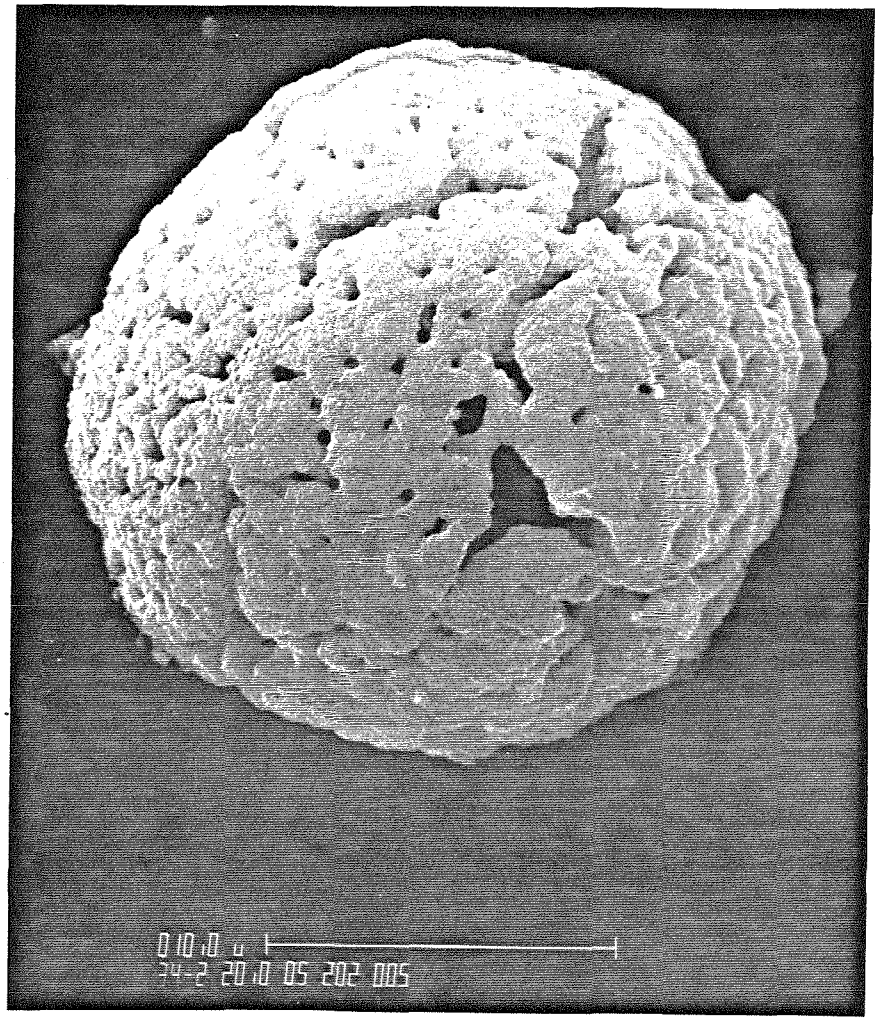

a

Figure 4: SEM-SE micrographs of residual ash after complete combustion of low porosity synthetic char particles in air at 800 K. The particles were treated with ion exchanged calcium: (a) outside view (b) inside view.

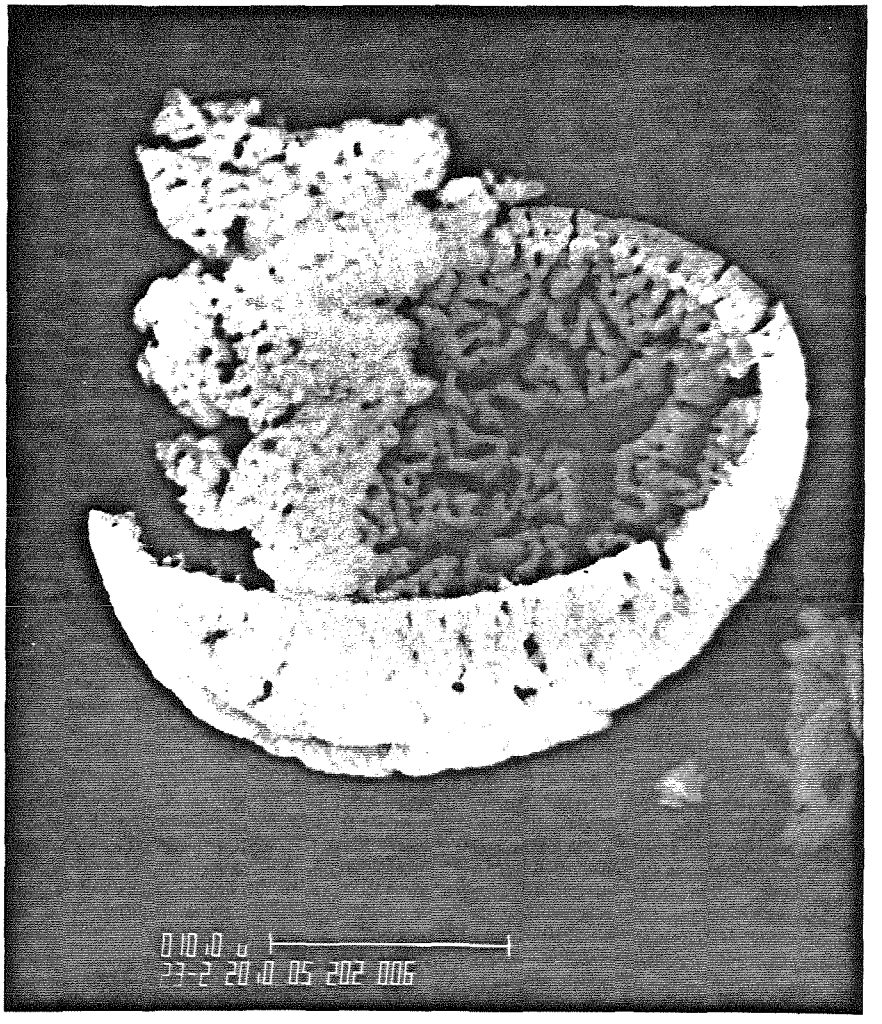

b

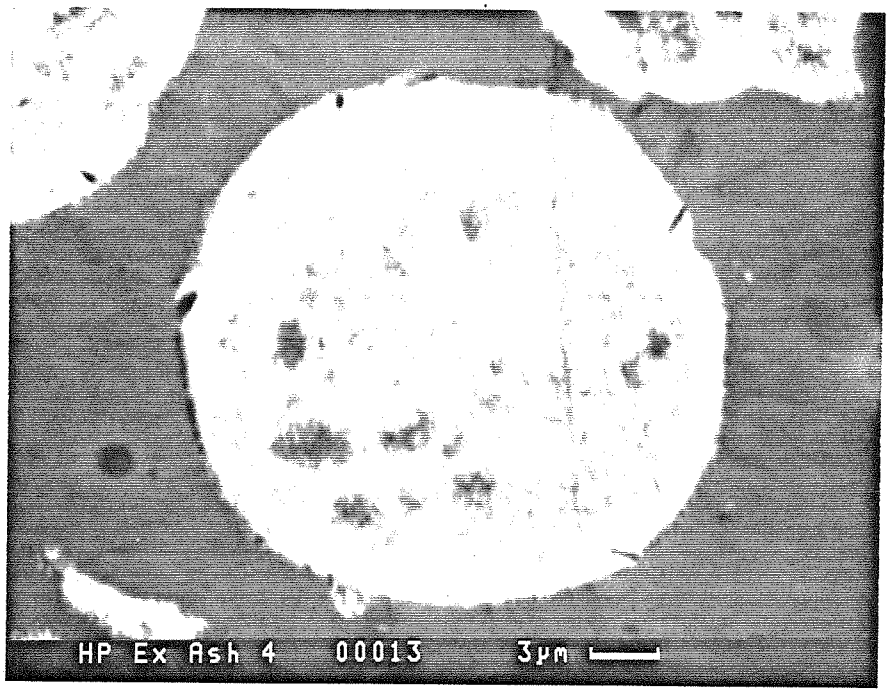

Figure 5: SEM micrographs of polished sections of ash particles resulting from combustion of high porosity chars.

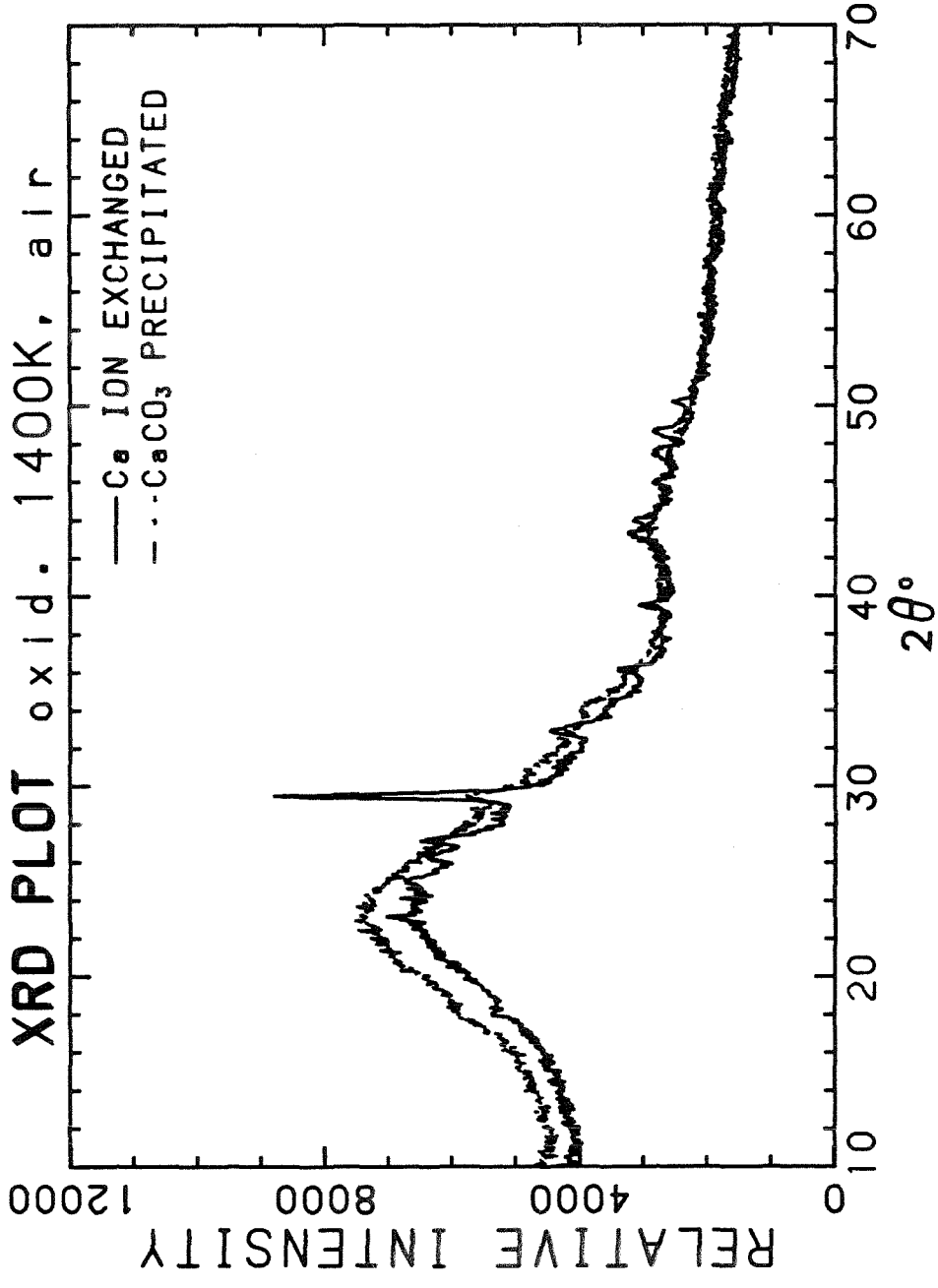

Figure 6: XRD profiles of partially burned low porosity chars at T_W = 1400 K, P_{O_2} = .04, 2 ms.

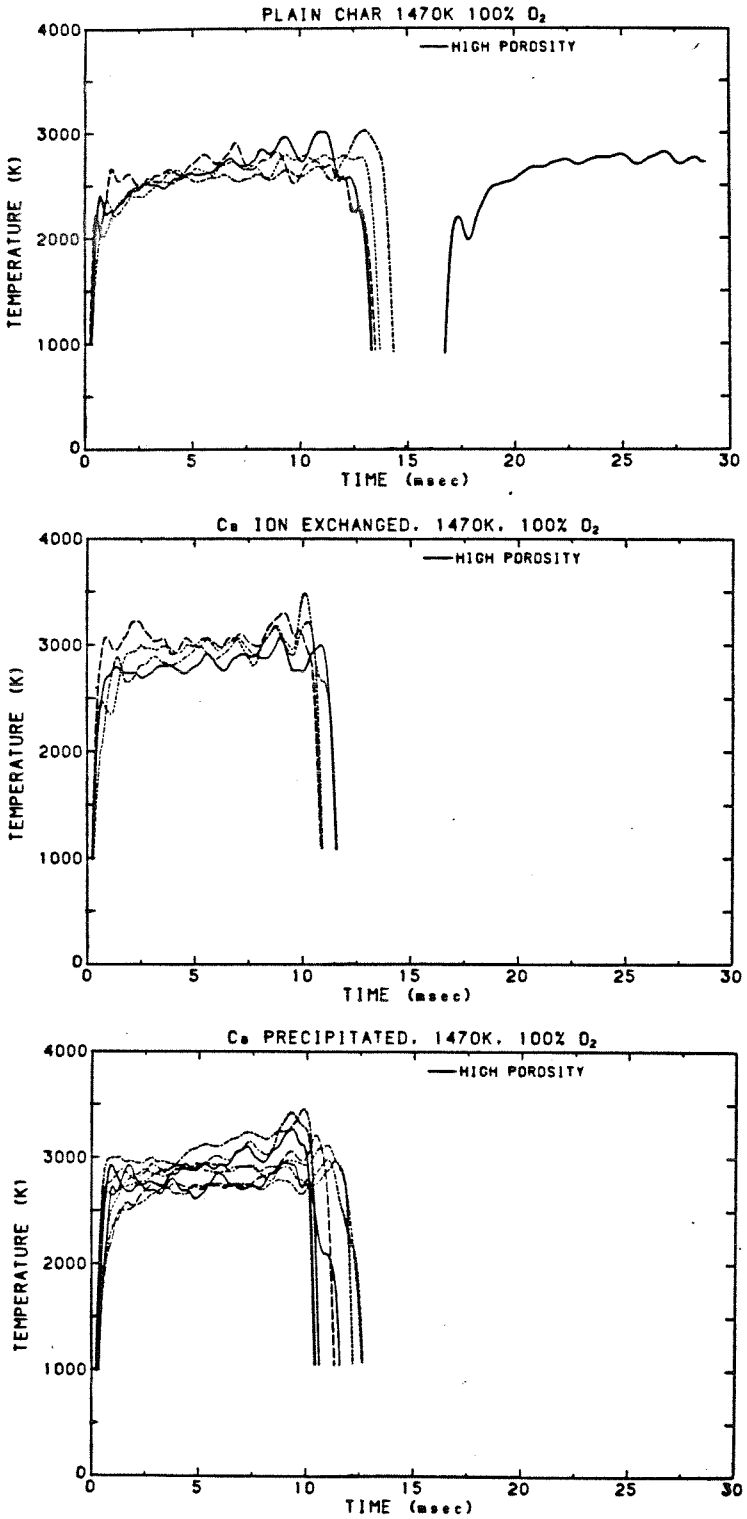

Figure 7: Temperature-time profiles of high porosity particles burning in O_2: (a) plain char, (b) ion exchanged, (c) $CaCO_3$ precipitated.

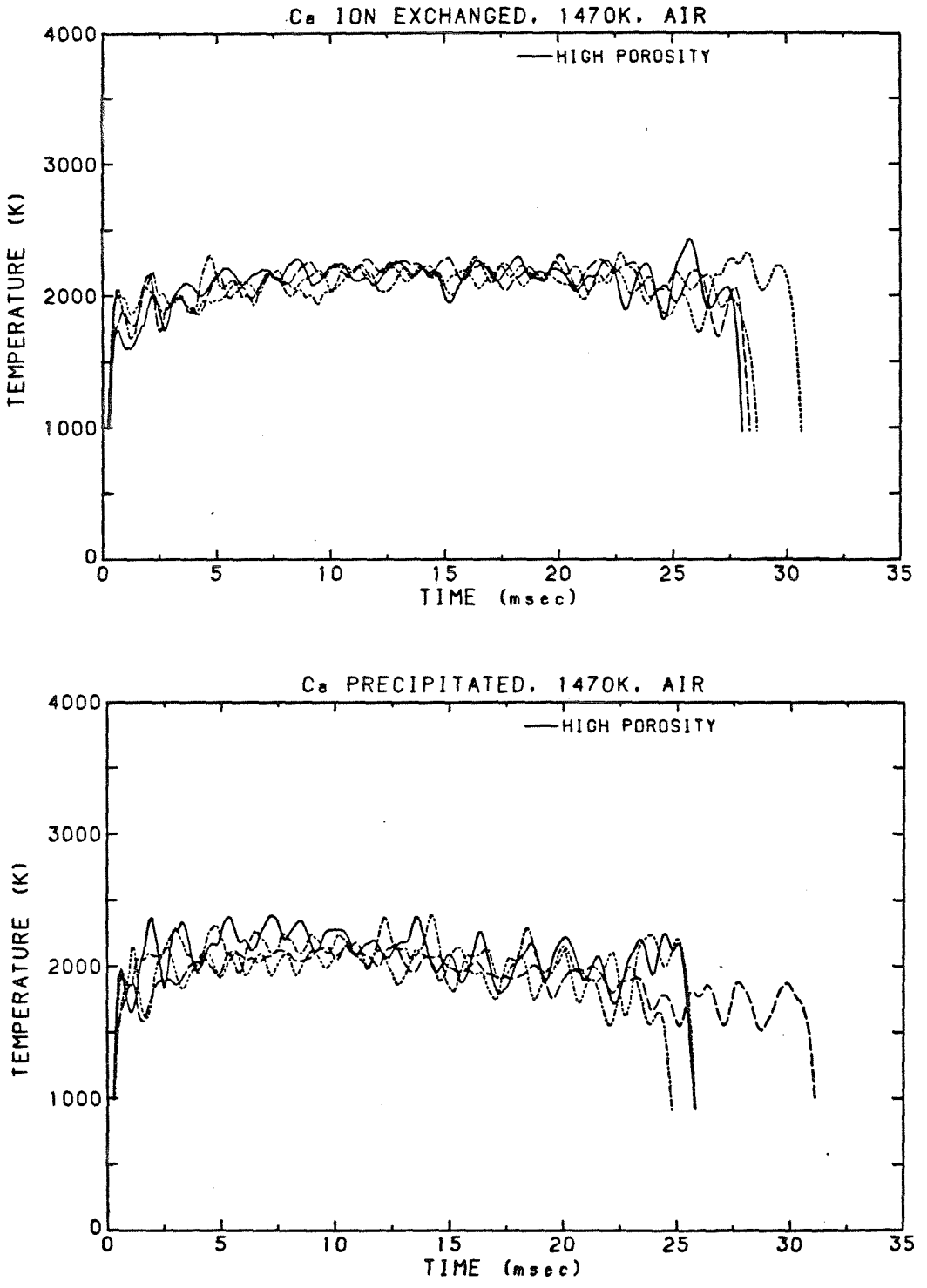

Figure 8: Temperature-time profiles of high porosity particles burning in air: (a) ion exchanged, (b) $CaCO_3$ precipitated.

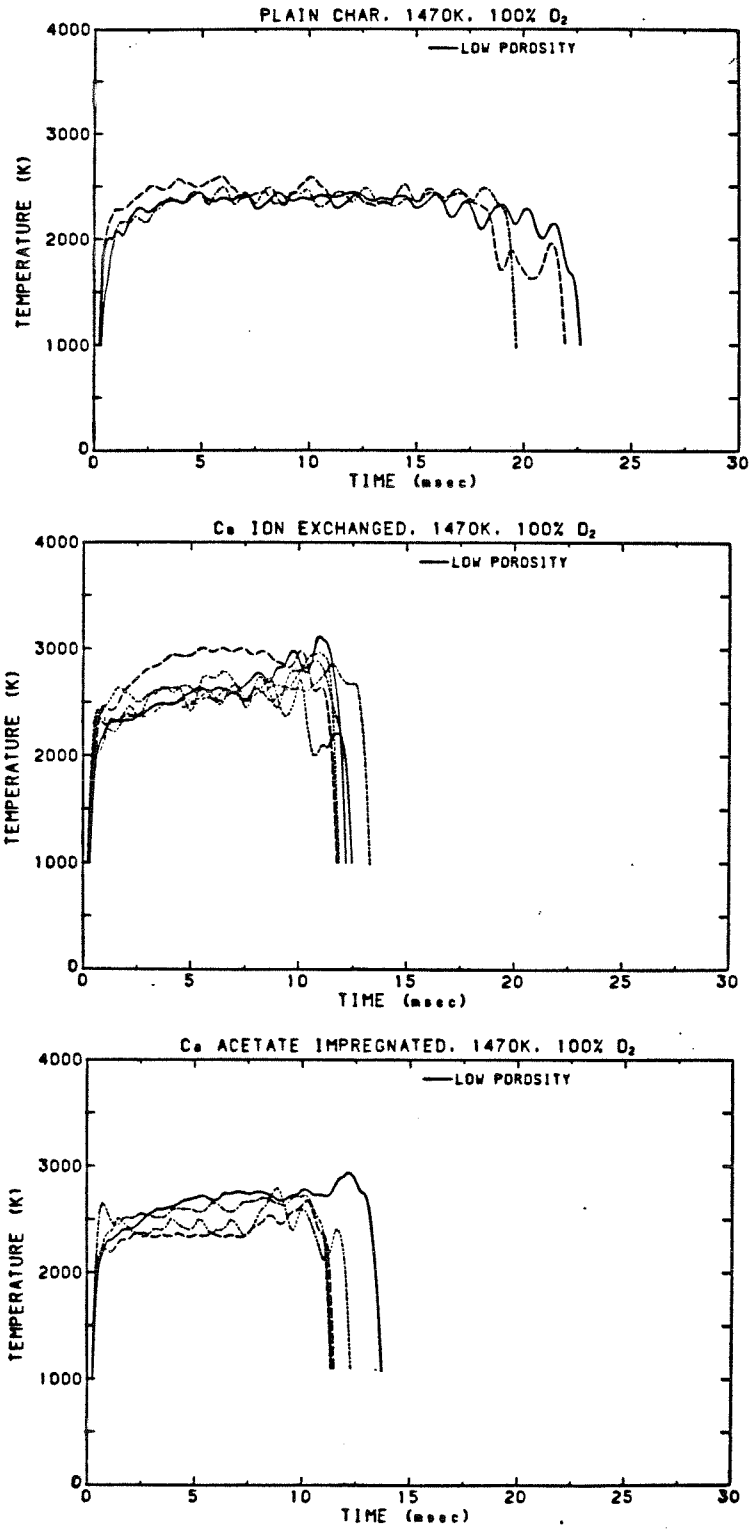

Figure 9: Temperature-time profiles of low porosity particles burning in O_2: (a) plain char, (b) ion exchanged, (c) calcium acetate impregnated.

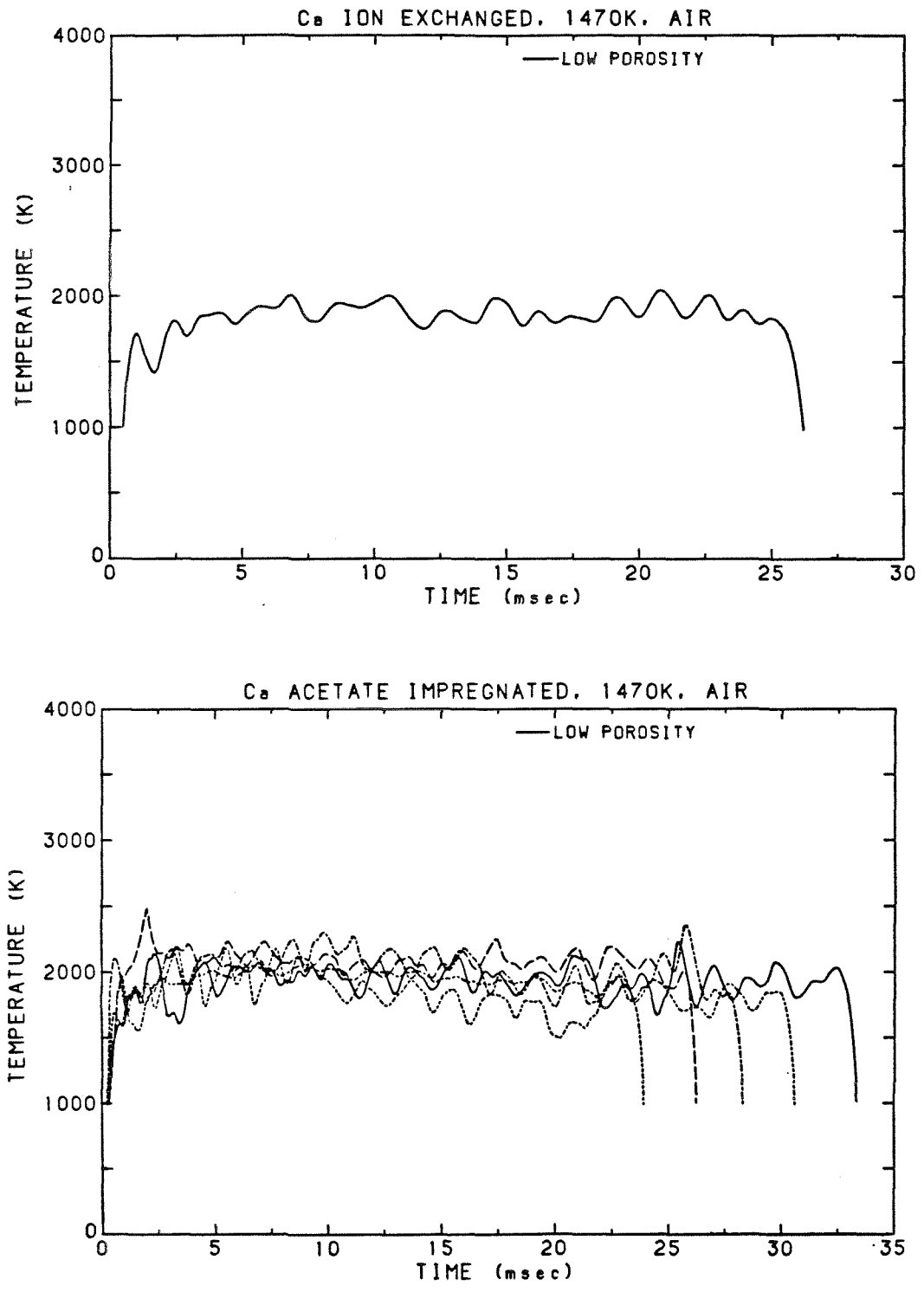

Figure 10: Temperature-time profiles of low porosity particles burning in air: (a) ion exchanged, (b) calcium acetate impregnated.

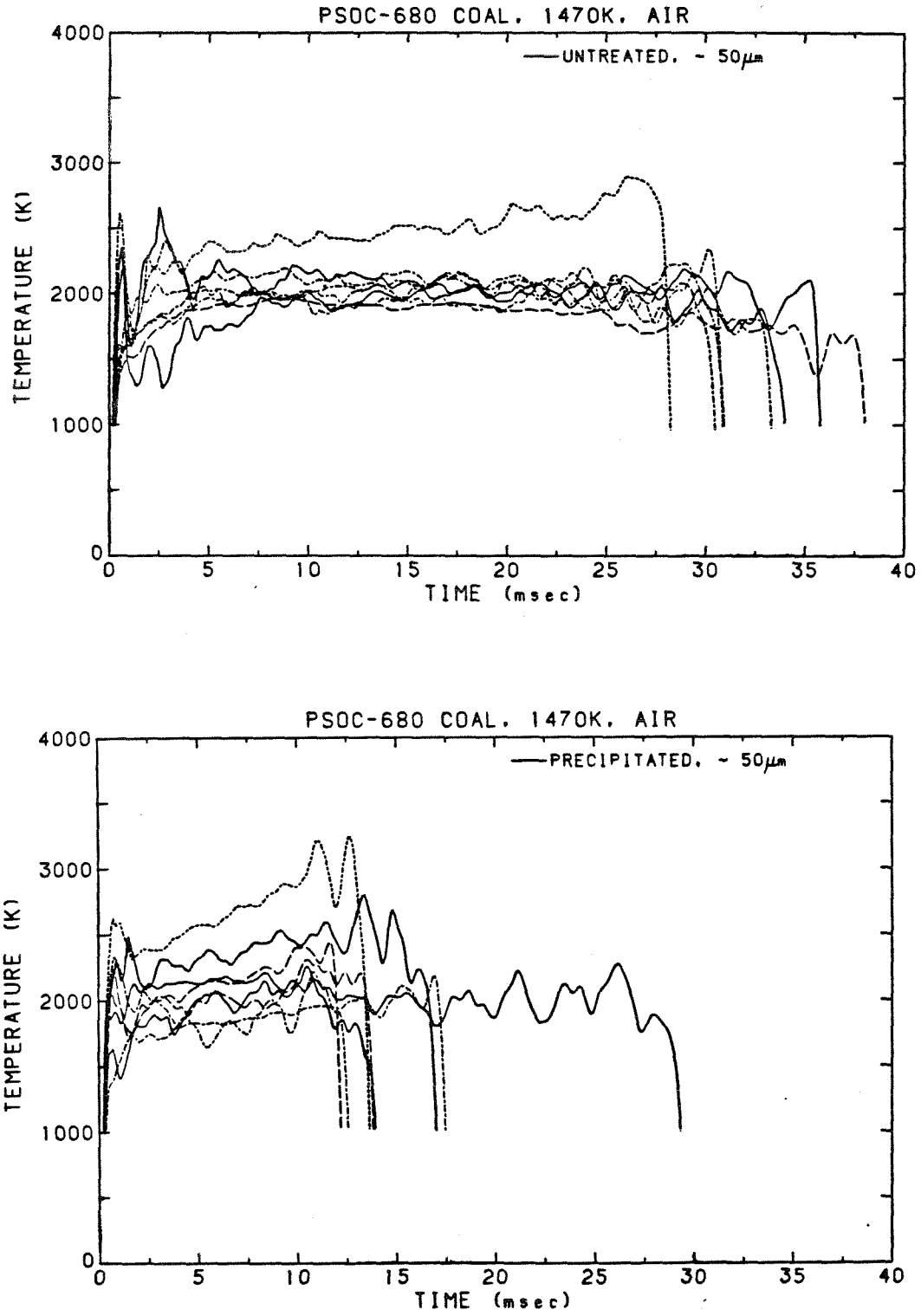

Figure 11: Temperature-time profiles of PSOC-680 coal particles burning in air: (a) untreated coal, (b) $CaCO_3$ precipitated.

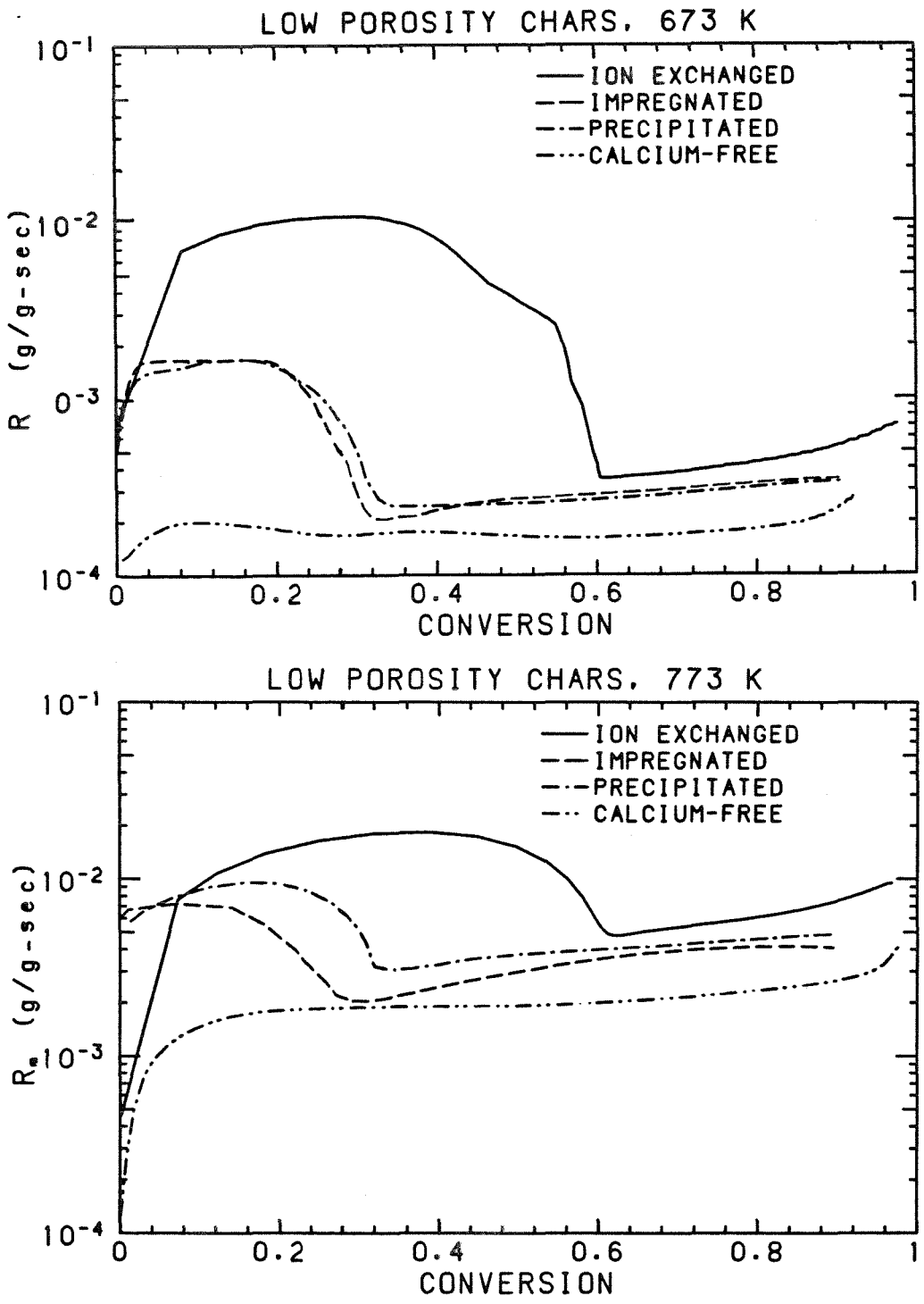

Figure 12: Reaction rate R_m vs. burnoff for TGA combustion of low porosity chars at (a) 673 K and (b) 773 K.

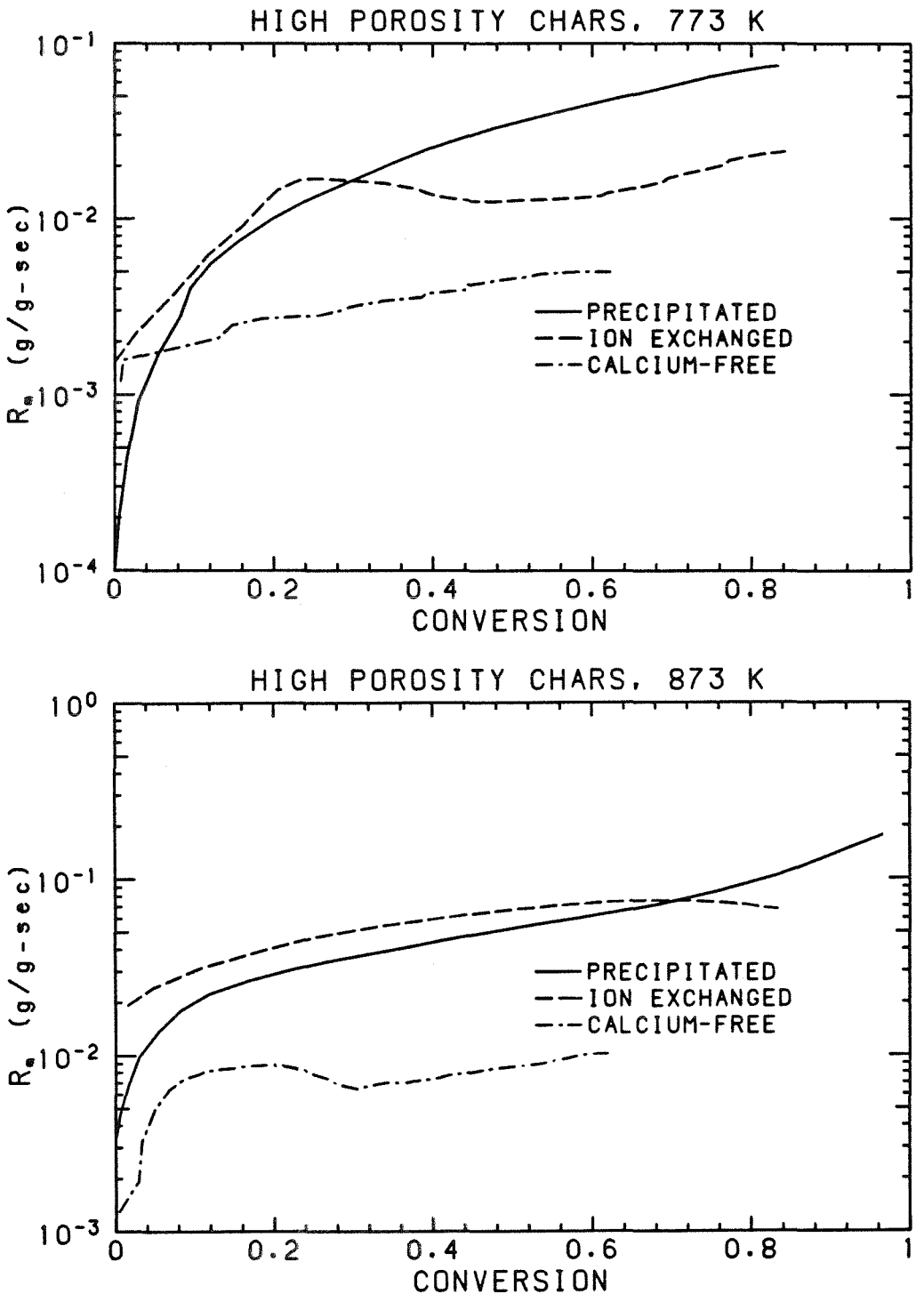

Figure 13: Reaction rate R_m vs. burnoff for TGA combustion of high porosity chars at (a) 773 K and (b) 873 K.

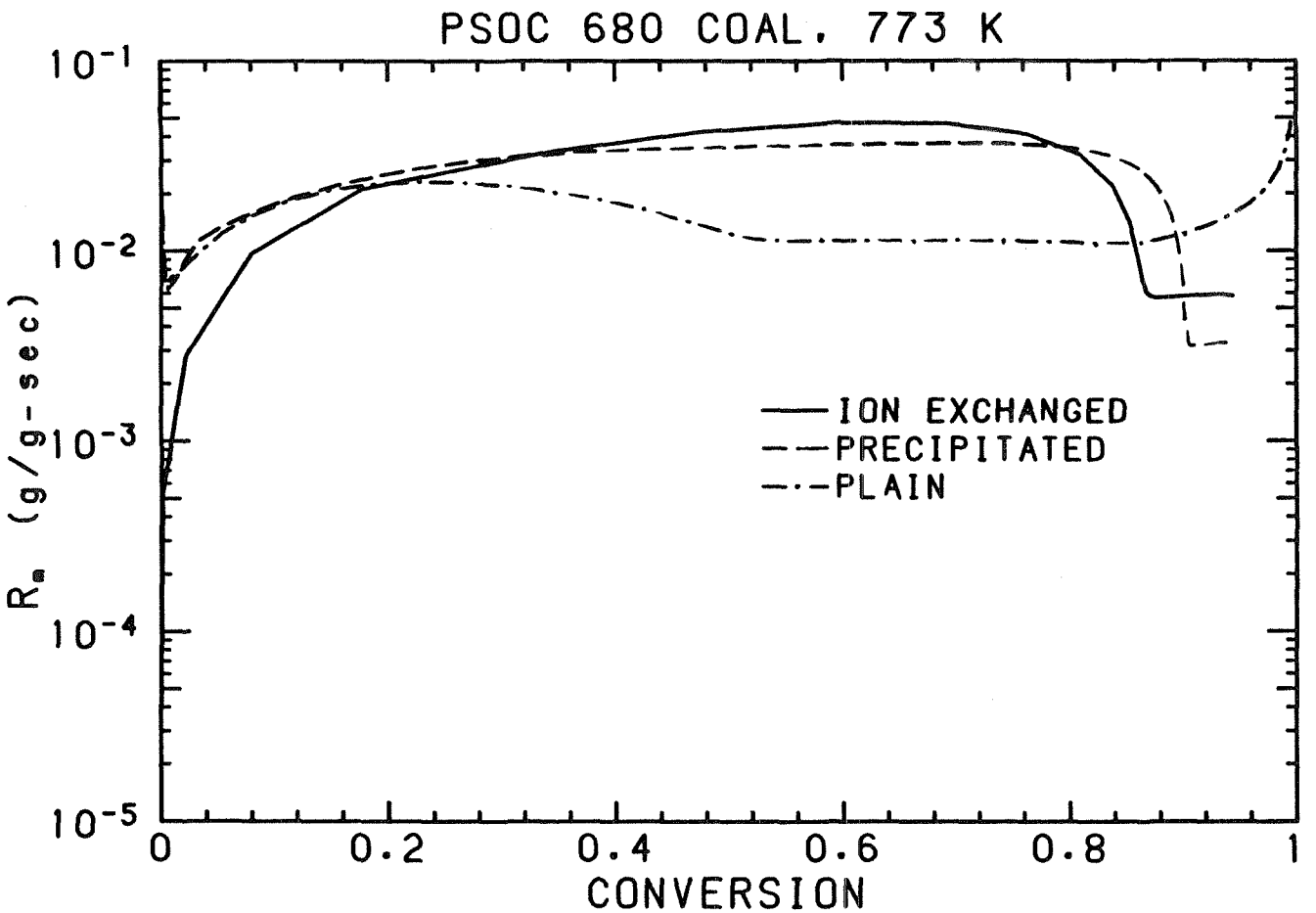

Figure 14: Reaction rate R_m vs. burnoff for TGA combustion of PSOC-176 coal-char at 773 K.

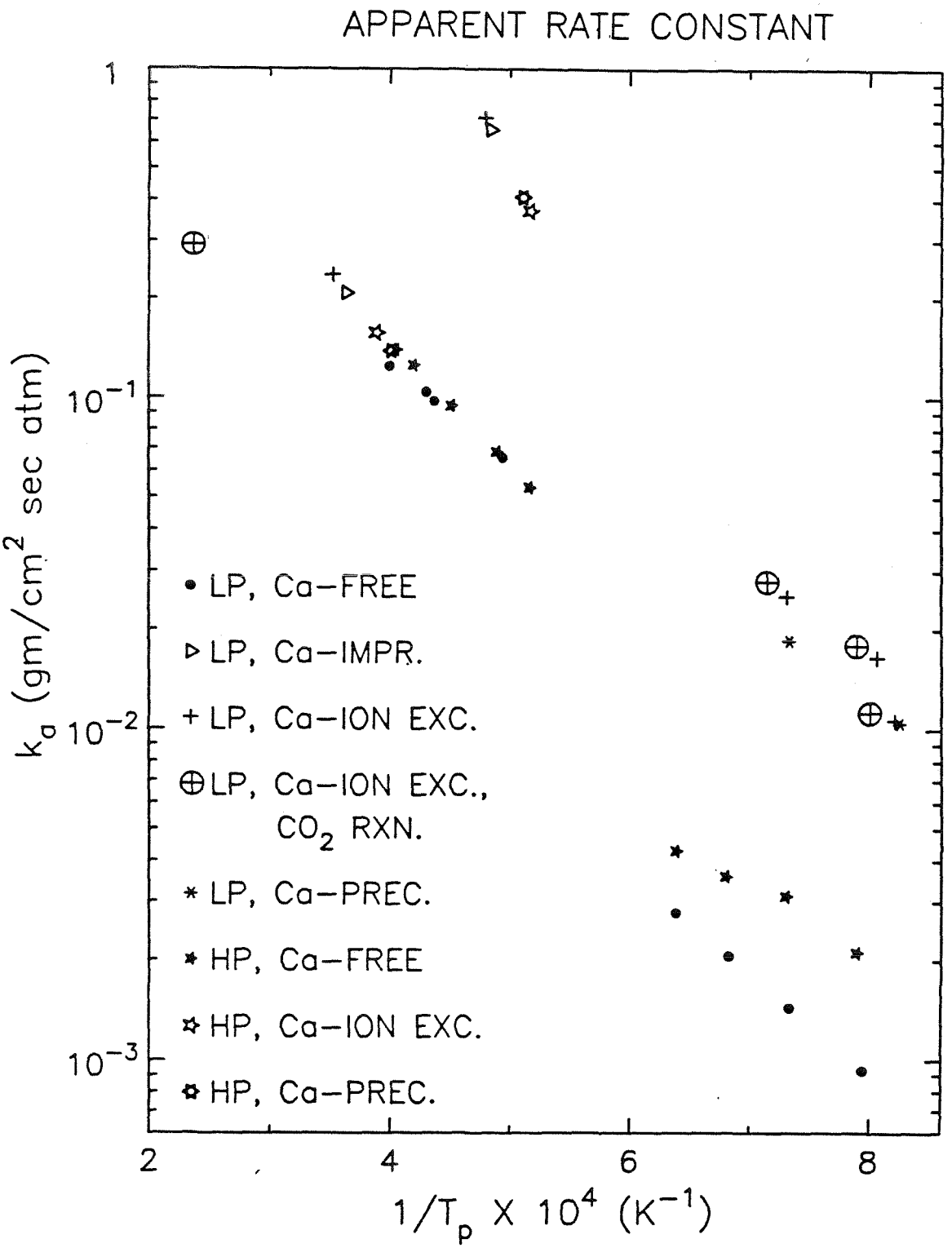

Figure 15: Apparent reaction rate coefficient k_a at intermediate to high temperatures, both low porosity (LP) and high porosity chars (HP).

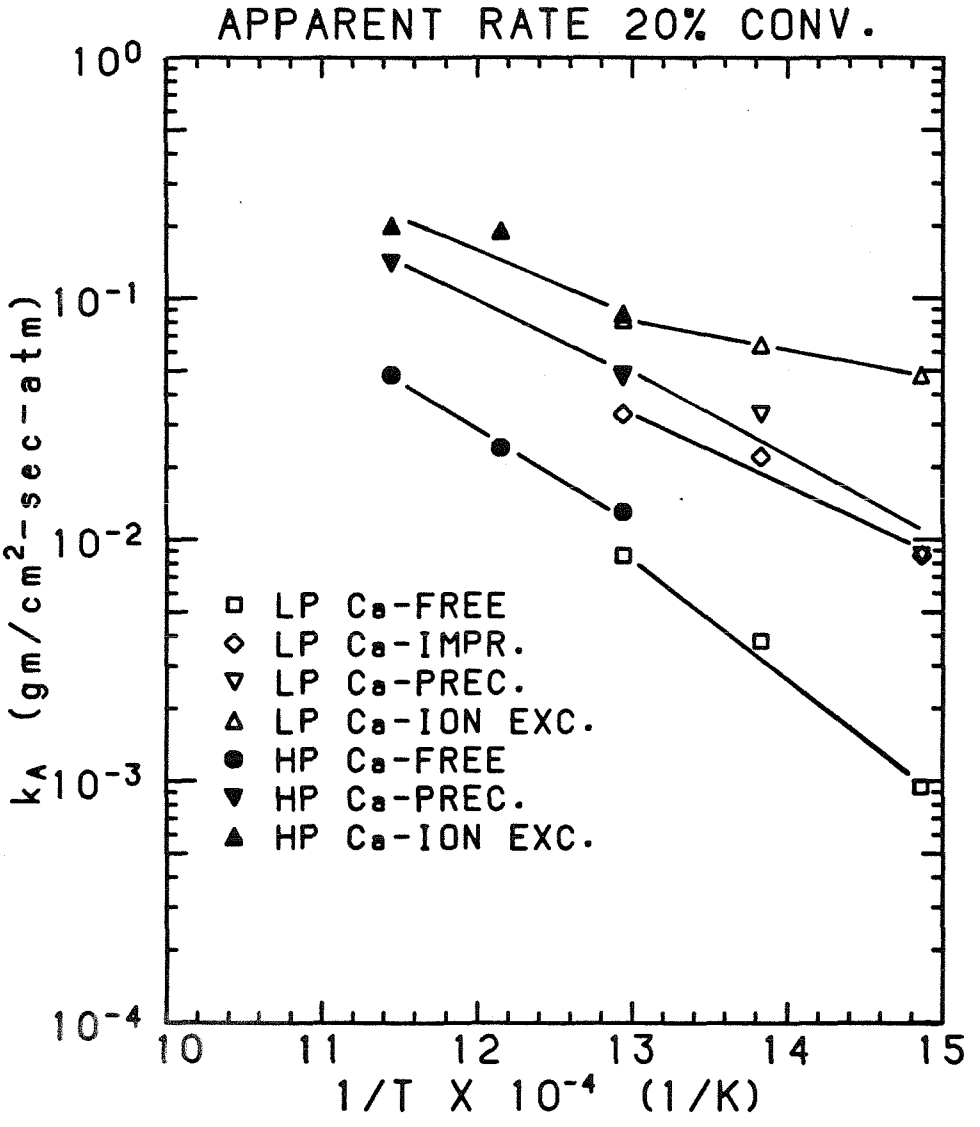

Figure 16: Apparent reaction rate coefficient k_m at low temperatures, both low porosity (LP) and high porosity chars (HP).

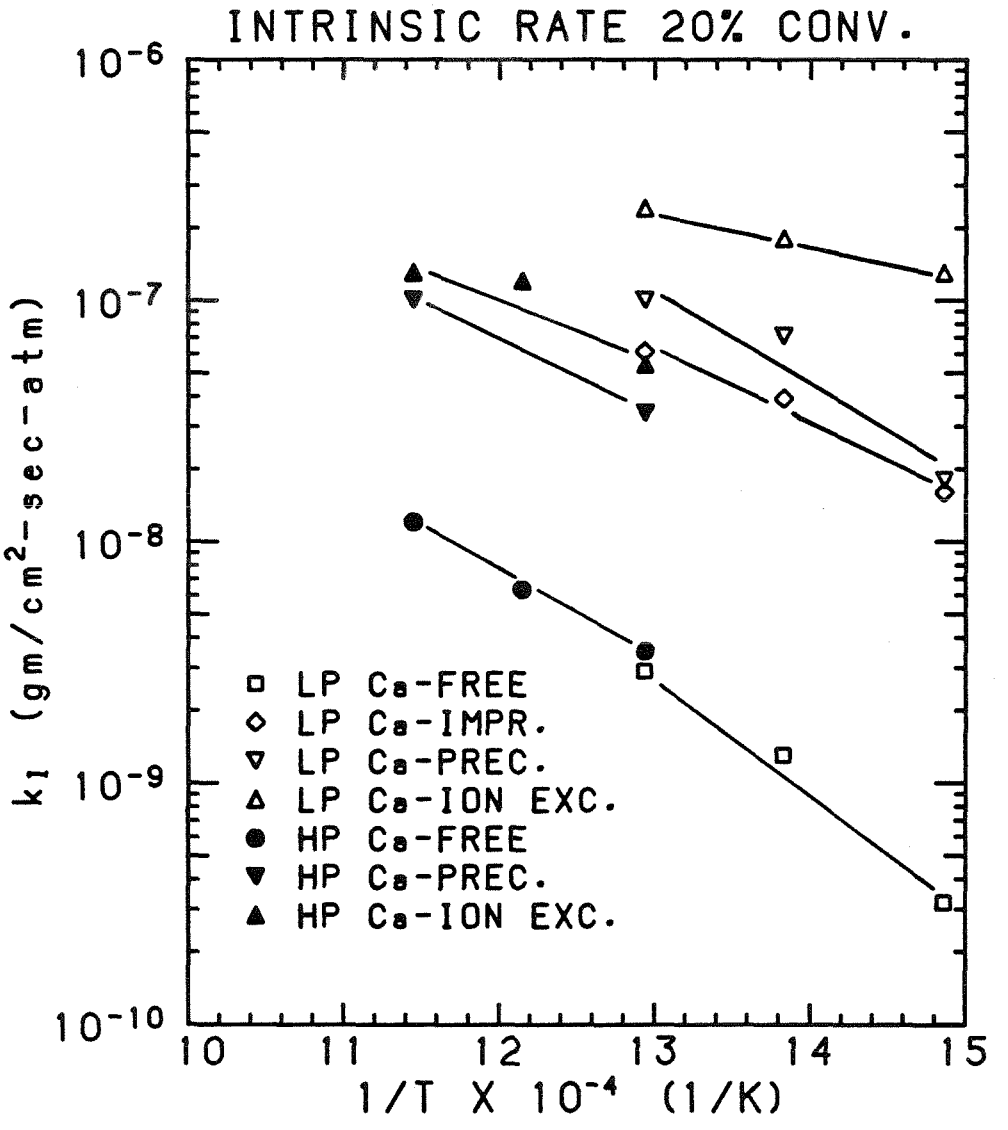

Figure 17: Intrinsic reaction rate coefficient k_i at low temperatures, both low porosity (LP) and high porosity chars (HP).